



Delft University of Technology

## From sequentially linear analysis to incremental sequentially linear analysis

### Robust algorithms for solving the non-linear equations of structures of quasi-brittle materials

Yu, Chenjie

#### DOI

[10.4233/uuid:b20beffc-f69f-4723-9c91-77da79861f62](https://doi.org/10.4233/uuid:b20beffc-f69f-4723-9c91-77da79861f62)

#### Publication date

2019

#### Document Version

Final published version

#### Citation (APA)

Yu, C. (2019). *From sequentially linear analysis to incremental sequentially linear analysis: Robust algorithms for solving the non-linear equations of structures of quasi-brittle materials*. [Dissertation (TU Delft), Delft University of Technology]. <https://doi.org/10.4233/uuid:b20beffc-f69f-4723-9c91-77da79861f62>

#### Important note

To cite this publication, please use the final published version (if applicable).

Please check the document version above.

#### Copyright

Other than for strictly personal use, it is not permitted to download, forward or distribute the text or part of it, without the consent of the author(s) and/or copyright holder(s), unless the work is under an open content license such as Creative Commons.

#### Takedown policy

Please contact us and provide details if you believe this document breaches copyrights.  
We will remove access to the work immediately and investigate your claim.

# **FROM SEQUENTIALLY LINEAR ANALYSIS TO INCREMENTAL SEQUENTIALLY LINEAR ANALYSIS**

**ROBUST ALGORITHMS FOR SOLVING THE NON-LINEAR  
EQUATIONS OF STRUCTURES OF QUASI-BRITTLE MATERIALS**

**Chenjie Yu**



# **FROM SEQUENTIALLY LINEAR ANALYSIS TO INCREMENTAL SEQUENTIALLY LINEAR ANALYSIS**

**ROBUST ALGORITHMS FOR SOLVING THE NON-LINEAR  
EQUATIONS OF STRUCTURES OF QUASI-BRITTLE MATERIALS**

## **Proefschrift**

ter verkrijging van de graad van doctor  
aan de Technische Universiteit Delft,  
op gezag van de Rector Magnificus prof. dr. ir. T.H.J.J. van der Hagen,  
voorzitter van het College voor Promoties,  
in het openbaar te verdedigen op vrijdag 3 mei 2019 om 12.30 uur

door

**Chenjie Yu**

Master of Science in Architectural and Civil Engineering,  
South China University of Technology, Guangzhou, P.R. China,  
geboren te Wuhan, P.R. China.

Dit proefschrift is goedgekeurd door de  
promotor: Prof. dr. ir. J.G. Rots  
copromotor: Dr. ir. P.C.J. Hoogenboom

Samenstelling promotiecommissie:

Rector Magnificus, voorzitter  
Prof. dr. ir. J.G. Rots Technische Universiteit Delft  
Dr. ir. P.C.J. Hoogenboom  
Technische Universiteit Delft

*Onafhankelijke leden:*

Prof. dr. T. Jefferson Cardiff University  
Prof. ir. S.N.M. Wijte  
Technische Universiteit Eindhoven  
Dr. J. Alfaiate Institute Superior Tecnico  
Prof. dr. ing. habil. J. Ozbolt  
Universität Stuttgart  
Prof. dr. ir. L.J. Sluys Technische Universiteit Delft  
Prof. dr. ir. Z. Li Technische Universiteit Delft, reservelid

*Keywords:* Structural mechanics, Computational mechanics, Fracture mechanics, Quasi-brittle materials, Incremental, Saw tooth model, Sequentially linear analysis (SLA), Smeared crack model, Damage model, Strong discontinuity, Newton-Raphson (N-R) method, Piecewise, Iterative, Implicit, Explicit, Masonry, Concrete

*Printed by:* Ipkamp Printing, The Netherlands

Copyright © 2019 by Chenjie Yu

All rights reserved. This copy of the thesis has been supplied on condition that anyone who consults it is understood to recognize that its copyright rests with its author and that no quotation from the thesis and no information derived from it may be published without the author's prior consent.

ISBN 978-94-028-1476-7

An electronic version of this dissertation is available at  
<http://repository.tudelft.nl/>.

*To my parents*

谨以此书献给我的父母



# CONTENTS

<b>Summary</b>	<b>xi</b>
<b>Samenvatting</b>	<b>xv</b>
<b>Symbols and Abbreviations</b>	<b>xix</b>
<b>1 Introduction</b>	<b>1</b>
1.1 Overview . . . . .	1
1.2 Research objectives . . . . .	3
1.3 Research contributions . . . . .	4
1.4 Thesis outline . . . . .	5
<b>2 Literature review</b>	<b>9</b>
2.1 Failure mechanics . . . . .	9
2.1.1 Cracking concepts in finite element analysis . . . . .	9
2.1.2 Constitutive models . . . . .	12
2.1.3 Multiscale modelling . . . . .	13
2.2 Incremental iterative solution procedures . . . . .	14
2.3 Snap-back and bifurcation points . . . . .	16
2.4 Sequentially linear analysis . . . . .	17
2.5 Other methods to improve robustness for quasi-brittle non-linear analysis . . . . .	21
2.6 Discussion . . . . .	24
<b>3 Improvements to SLA</b>	<b>25</b>
3.1 SLA procedure . . . . .	25
3.2 Saw-tooth model . . . . .	26
3.3 Material model . . . . .	30
3.4 Failure criterion . . . . .	31

3.5	The critical element and load factor . . . . .	34
3.6	Stiffness reduction of orthotropic damage . . . . .	36
3.7	Approximation of principal direction Young's moduli . . . . .	42
3.8	Discussion . . . . .	45
<b>4</b>	<b>Improvements to non-proportional loading in SLA</b>	<b>47</b>
4.1	Algorithm principle . . . . .	48
4.2	Proposed non-proportional loading procedure in SLA . . . . .	48
4.3	Calculation of initial-load factor $v$ . . . . .	49
4.4	Test case of a simply supported concrete beam . . . . .	51
4.5	Material properties and FEM model . . . . .	53
4.6	Analysis and comparison of the results . . . . .	54
4.7	Test case of increased prestress . . . . .	60
4.8	Discussion . . . . .	62
<b>5</b>	<b>Incremental sequentially linear analysis (ISLA)</b>	<b>65</b>
5.1	Introduction . . . . .	65
5.2	Load control . . . . .	67
5.3	Load scaling control . . . . .	68
5.3.1	Damage control method . . . . .	69
5.3.2	Load and damage control method . . . . .	70
5.4	Unified framework . . . . .	72
5.5	Computation process . . . . .	74
5.6	Comparison of SLA and ISLA . . . . .	85
5.7	Discussion . . . . .	85
<b>6</b>	<b>Elaboration of Load scaling control in ISLA</b>	<b>89</b>
6.1	Damage control method . . . . .	90
6.2	Load and damage control method . . . . .	91
6.3	Parameter determination for load and damage control . . . . .	95
6.3.1	Stiffness reduction factor study . . . . .	95
6.3.2	Linear function parameter study . . . . .	96
6.3.3	Exponential function parameter study . . . . .	97

6.4	Single element uniaxial tensile test for a loading schedule . . . . .	98
6.4.1	Damage control method test . . . . .	99
6.4.2	Load and damage control . . . . .	100
6.5	Optimization . . . . .	105
6.6	Discussion . . . . .	107
<b>7</b>	<b>Validation of ISLA for proportional loading</b>	<b>109</b>
7.1	Material properties and FEM Model . . . . .	110
7.2	Damage control for the scaled force test . . . . .	112
7.3	Load control for the imposed displacement test . . . . .	114
7.4	Load control for the imposed force test . . . . .	125
7.5	Load and damage control for the scaled force test . . . . .	131
7.6	Load control for snap-back behaviour test . . . . .	141
7.7	Discussion . . . . .	143
<b>8</b>	<b>Validation of ISLA for non-proportional loading</b>	<b>145</b>
8.1	Comparison for low prestress . . . . .	147
8.2	Comparison for medium prestress . . . . .	148
8.3	Comparison for high prestress . . . . .	151
8.4	Discussion . . . . .	154
<b>9</b>	<b>Extension of ISLA to geometrical non-linearity</b>	<b>157</b>
9.1	Indirect displacement control in load and damage control . . . . .	158
9.2	Masonry wall out-of-plane bending test . . . . .	159
9.2.1	Modelling approach . . . . .	159
9.2.2	Test results . . . . .	163
9.3	Discussion . . . . .	168
<b>10</b>	<b>Extension of ISLA to transient analysis</b>	<b>171</b>
10.1	Implementation . . . . .	171
10.2	FEM model and Material properties . . . . .	176
10.3	Test results . . . . .	177
10.4	Discussion . . . . .	184

<b>11 Application of ISLA at the structural level</b>	<b>187</b>
11.1 Masonry facade subjected to dead load and settlement . . . . .	187
11.1.1 Modelling approach . . . . .	188
11.1.2 Test results for the load control method . . . . .	189
11.1.3 Test results for the load and damage control method . . . . .	194
11.1.4 Comparison of orthotropic and isotropic damage models . . . . .	202
11.2 Masonry house subjected to dead load and pushover . . . . .	204
11.2.1 Modelling approach . . . . .	205
11.2.2 Test results . . . . .	206
11.3 Discussion . . . . .	214
11.3.1 Masonry facade subjected to dead load and settlement . . . . .	214
11.3.2 Masonry house subjected to dead load and pushover . . . . .	215
<b>12 Conclusions and future work</b>	<b>217</b>
12.1 Conclusions . . . . .	217
12.2 Further work . . . . .	224
<b>Bibliography</b>	<b>229</b>
<b>Acknowledgements</b>	<b>245</b>
<b>A Extension of ISLA to proportional cyclic loading for brittle materials</b>	<b>249</b>
<b>B Coupled damage-plastic material model in ISLA for proportional loading</b>	<b>277</b>
<b>Curriculum Vitæ</b>	<b>309</b>
<b>List of Publications</b>	<b>311</b>

# SUMMARY

The Newton-Raphson method (N-R) has been widely used in nonlinear FEM analysis of quasi brittle materials, such as masonry, concrete and reinforced and prestressed concrete. However, the robustness of the N-R method is still a serious issue when bifurcation, snap-back or divergence problems arise. In order to enhance the robustness of solving non-linear problems, a total approach with secant stiffness and an “event-by-event” damage model was introduced by sequentially linear analysis (SLA). The incremental-iterative procedure, adopted in nonlinear finite element analysis, is replaced by a sequence of scaled linear finite element analyses with decreasing secant stiffness, corresponding to local damage increments. However, SLA has difficulties in dealing with non-proportional loading as well as the cases in which the displacement history matters, such as geometrically non-linear analysis, transient analysis and cyclic analysis with plastic unloading, since the damage history is traced in SLA rather than the displacement history.

SLA is improved in this thesis, and an orthotropic damage model has been introduced for SLA based on the rotating smeared crack model to eliminate the difficulty of choosing a proper shear retention function. A new algorithm for applying non-proportional load has been implemented in SLA, which is naturally suitable for different element types (2D and 3D) and failure criteria without extra modifications.

In this work, a new method, incremental sequentially linear analysis (ISLA), is proposed and based on a combination of the N-R method and SLA. This method is incremental, as each increment starts and ends with an equilibrium state. The solution search path follows damage cycles sequentially with secant stiffness, which traces both damage history (explicit) and displacement history (implicit). A utilisation value is determined at the local level by the stress state and the failure surface of an element with the elastic material properties. A utilisation function  $\mu$  is defined as the largest utilisation value of all elements, which is a function of the load factors and the stiffness matrix  $K$  at the global level. An equilibrium is reached when  $\mu \leq 1$ .

Due to the stiffness reduction, the internal forces are updated based on the displacements of the previous load step and the algorithm reaches a temporary equilibrium state. Afterwards, the incremental load is applied, and a linear analysis is performed for the current load step. Three control methods have been proposed: load control, damage control and load and damage control. In load control, every load step can contain one increase or decrease of the load and several reductions of Young's modulus of various elements; in damage control, every load step can contain one reduction of Young's modulus and several changes of the load; and, in load and damage control, every load step can contain several changes of the load and several reductions of Young's modulus of various elements. It is suggested to use the load control method for the displacement loads and the load and damage control method for the force loads to trace the post-peak behaviour. The currently proposed version of ISLA uses two types of material models: the damage model (secant unloading) and the coupled damage-plastic model (plastic unloading). Furthermore, it employs the rotating smeared crack model (the damage model) and the Mohr-Coulomb criterion with tension cut-off.

A first advantage of ISLA is that it is better suited to handle cases of non-proportional loading, due to the incremental approach. This is demonstrated by four examples of non-proportional loading: a concrete beam with both prestress and vertical load; out-of-plane bending of a masonry wall with overburden; a differential settlement test on a pre-loaded masonry façade and a 3D pushover analysis of a masonry house. The results of ISLA are discussed and compared against SLA, the total approach of which is known to have more difficulties in handling non-proportional loads.

Apart from the non-proportional loading, ISLA can be naturally extended from geometrically linear analysis to geometrically non-linear analysis due to the incremental procedure. Indirect displacement control with the control point is introduced in load and damage control to avoid or pass localized failure process zones for geometrically non-linear analysis. This is demonstrated by the example of out-of-plane bending of a masonry wall, which is pushed post-peak until full failure.

Additionally, ISLA is extended to transient analysis. Due to the stiffness sensitivity in transient analysis, a modified damage control method in which the equilibrium states are searched for every stiffness reduction until the load factor reaches

the value of the current load step is introduced. The potential of ISLA for transient analysis is then indicated for a simple multi-degree of freedom concrete problem.

In addition, there is potential for extending ISLA to cyclic analysis. Two types of unloading paths are considered, namely unloading with the secant stiffness (the damage model) and with the non-secant stiffness (the plastic model). These are demonstrated by the examples of cyclic (unloading with the secant stiffness) and repeating (unloading with the non-secant stiffness) loading of a notched concrete beam. However, non-proportional loading is not considered. ISLA determines only loading and unloading state changes at the global level to avoid iterations at the local level, which may cause divergence or bifurcations.

ISLA is robust since all physical non-linearity is linearized in damage cycles with the explicit secant stiffness of the damaged elastic material model (saw-tooth model). This has been demonstrated by checking that the performance of the load control, damage control and load and damage control methods have been tested at the structural level for the cases of proportional and non-proportional loading mentioned above. For the snap-backs in the quasi-static brittle problems, the load control and load and damage control methods have both been shown to perform successfully. For the displacement history, the load control method jumps over snap-backs while the load and damage control method follows snap-backs. For the damage history, both methods trace the damage process cycle-by-cycle during snap-backs. This proposed method can be easily implemented into commercial software.



# SAMENVATTING

De Newton-Raphson methode (N-R) wordt algemeen gebruikt in niet-lineaire eindige-elementenberekeningen van quasi brosse materialen, zoals metselwerk, beton, gewapend beton en voorgespannen beton. Echter, de robuustheid van de N-R methode is nog steeds een belangrijk probleem in het geval van bifurcaties, snap-back of divergentie. Voor het verbeteren van de robuustheid van het oplossen van niet-lineaire problemen is de sequentiële lineair analyse (SLA) geïntroduceerd met een niet-incrementele aanpak, secant-stijfheid en een schademodel gebaseerd op opeenvolgende gebeurtenissen. De incrementele-iteratieve procedure toegepast bij niet-lineaire eindige-elementenberekeningen, is vervangen door een opeenvolging van geschaalde lineaire eindige-elementenberekeningen met afnemende secant-stijfheid, overeenkomend met lokale schade-incrementen. Echter, SLA kan moeilijk omgaan met belastingen die na elkaar optreden en met situaties waarin de verplaatsingsgeschiedenis een rol speelt, zoals geometrisch niet-lineaire berekeningen, dynamische berekeningen en cyclische berekeningen met plastisch ontlasten. Dit wordt veroorzaakt doordat de schadegeschiedenis wordt bijgehouden in plaats van de verplaatsingsgeschiedenis.

In dit proefschrift is SLA verbeterd en is orthotrope schade geïntroduceerd in SLA gebaseerd op het roterende uitgesmeerde scheurmodel. Dit laatste voorkomt het probleem dat een geschikte functie moet worden gekozen voor de schuifspanning in de scheuren (shear retention). Een nieuw algoritme voor belastingen die na elkaar optreden is geïmplementeerd in SLA welke van nature geschikt is voor verschillende elementtypen (2D en 3D) en faalcriteria zonder extra aanpassingen.

In dit werk is een nieuwe methode, genaamd incrementele sequentiële lineaire analyse (ISLA) voorgesteld die gebaseerd is op een combinatie van de N-R-methode en SLA. Deze methode is incrementele waarbij elk increment begint en eindigt in een evenwichtstoestand. Opeenvolgende cycli met reducties van secantstijfheden produceren een pad dat zowel de schadegeschiedenis (expliciet) als de verplaats-

ingsgeschiedenis (impliciet) volgt. Een benuttingswaarde is bepaald op materiaal-niveau op basis van de spanningstoestand en het grensspanningsoppervlak van een element met elastische materiaaleigenschappen. Een benuttingsfunctie  $\mu$  is gedefinieerd als de grootste van de benuttingswaarden van alle elementen. Deze functie hangt af van de belastingfactoren en de stijfheidsmatrix  $K$  van de draagconstructie. Evenwicht is bereikt wanneer  $\mu \leq 1$ .

De stijfheidsreducties zorgen ervoor dat de interne krachten worden bijgewerkt uitgaande van de verplaatsingen van de vorige belastingstap waardoor het algoritme een tijdelijke evenwichtstoestand bereikt. Vervolgens wordt een belastingstap aangebracht en wordt een lineaire berekening uitgevoerd voor de huidig belastingstap. Drie sturingsmethoden worden voorgesteld: belastingsturing, schadesturing en belasting-en-schadesturing. Bij belastingsturing bevat elke belastingstap een toename of afname van de belasting en een aantal reducties van de elasticiteitsmoduli van een aantal elementen. Bij schadesturing bevat elke belastingstap een reductie van een elasticiteitsmodulus en een aantal veranderingen van de belasting. Bij belasting-en-schadesturing bevat elke belastingstap een aantal veranderingen van de belasting en een aantal reducties van de elasticiteitsmoduli van een aantal elementen. Het advies is om belastingsturing te gebruiken voor opgelegde verplaatsingen en belasting-en-schadesturing te gebruiken voor opgelegde krachten zodat het constructiedrag na de lastpiek kan worden gevuld. De huidige versie van ISLA gebruikt twee materiaalmodellen: ontladen volgens de secantstijfheid (schademodel) en ontladen volgens een andere dan de secant-stijfheid (gekoppelde schade-plasticiteitsmodel). Bovendien maakt het gebruik van roterende uitgesmeerde scheuren (schademodel) en het faalcriterium volgen Mohr-Coulomb met een extra begrenzing van de trekspanning (tension cut-off).

Het eerste voordeel van ISLA is dat het vanwege de incrementele aanpak geschikter is voor belastingen die na elkaar optreden. Dit is gedemonstreerd met vier voorbeelden: een betonnen ligger met zowel voorspanning als een verticale belasting, een muur van metselwerk met zowel een bovenbelasting in het vlak als een verticale belasting uit het vlak, een gevel van metselwerk met zowel een bovenbelasting als een zettingsverschil van de fundering en de driedimensionale situatie van een huis van metselwerk belast door zowel eigengewicht als een langzame horizontale verplaatsing die het omver duwt, om de weerstand tegen aardbeving-en

te onderzoeken (push-over analysis). De resultaten van ISLA zijn besproken en vergeleken met die van SLA. Van de laatstgenoemde niet-incrementele aanpak is bekend dat het minder geschikt is voor belastingen die na elkaar optreden.

Naast belastingen die na elkaar optreden, kan ISLA uitgebreid worden zodat geometrisch niet-lineaire berekeningen kunnen worden gemaakt. Dit is een natuur-lijke eigenschap van de incrementele procedure. De methode belasting-en-schadesturing is uitgebreid met een sturingspunt (indirecte verplaatsingssturing) waarmee gelokaliseerde scheurvorming kan worden vermeden of gevuld in geometrische niet-lineaire berekeningen. Dit is geïllustreerd met een metselwerk muur die uit het vlak belast wordt voorbij de lastpiek tot volledig bezwijken optreedt.

Ook is ISLA uitgebreid naar dynamische berekeningen in het tijdsdomein. Het blijkt dat de dynamische responsie zeer gevoelig is voor stijfheidsreducties. Daarom is een methode geïntroduceerd (gemodificeerde schadesturing) waarbij voor elke stijfheidsreductie de evenwichtstoestand wordt gezocht waarbij de belastingfactor de waarde van de huidige belastingstap heeft. De toekomstige mogelijkheden voor dynamische berekeningen met ISLA zijn onderzocht met een eenvoudig voorbeeld van een betonnen staaf gemodelleerd met een aantal massa's en niet-lineaire veren.

Daarnaast bestaat de mogelijkheid om ISLA uit te breiden naar cyclische berekeningen. Twee typen van onlasten zijn beschouwd, namelijk onlasten volgens de secantstijfheid (schademodel) en niet volgens de secantstijfheid (plastisch model). Deze typen zijn gedemonstreerd door voorbeelden van cyclische belasting (ontlasten volgens de secantstijfheid) en herhalende belasting (ontlasten niet volgens de secantstijfheid) van een betonnen ligger met een inkeping. Echter, in deze voorbeelden werden geen belastingen na elkaar aangebracht. In ISLA wordt de omschakeling in het materiaalmodel tussen belasten en onlasten bepaald op het niveau van de draagconstructie in plaats van op materiaalniveau. Hierdoor wordt vermeden dat extra iteraties op het materiaalniveau leiden tot divergentie of bifurcaties.

ISLA is robuust doordat alle fysische niet-lineariteiten worden gelineariseerd in schadestappen met de expliciete secantstijfheid van het beschadigde elastische materiaalmodel (zaagtandmodel). De robuustheid is gedemonstreerd door de prestaties van de belastingsturing, schadesturing and belasting-en-schadesturing te

controleren op het niveau van de draagconstructie voor belastingen die tegelijkertijd en na elkaar, zoals hierboven vermeld, worden aangebracht. Met betrekking tot snap-backs in quasi-statische brosse situaties is gedemonstreerd dat zowel belastingsturing als belasting-en-schadesturing uitstekend presteren. Met betrekking tot de verplaatsingsgeschiedenis springt belastingsturing over de snap-backs terwijl belasting-en-schadesturing de snap-backs volgt. Met betrekking tot de schadegeschiedenis volgen beide methoden het schadeproces in opeenvolgende stappen gedurende de snap-backs. ISLA kan eenvoudig geïmplementeerd worden in commercieel beschikbare software.

# SYMBOLS AND ABBREVIATIONS

## ROMAN SYMBOLS

$c$  Cohesion of the Mohr-Coulomb criterion

$C$  Variable in the Mohr-Coulomb criterion with tension cutting-off to calculate the load factor in SLA

[C] Material compliance matrix

$E$  Young's modulus.  $E_0$  is the initial value of Young's modulus.  $E_i$  represents Young's modulus in the orthotropic model, where  $i$  can be 1,2,3

$f'_c$  Damaged compressive strength of the Mohr-Coulomb criterion

$f_t$  Tension strength

$f'_t$  Damaged tension cutting-off strength

$f_{t2}$  Fictitious tensile strength of the Mohr-Coulomb criterion calibrated to obtain the correct shear failure

$f_{ts}$  Updated tension strength based on Saw tooth model

$F_{cur}$  Current load

$F_{ini}$  Initial load

$F_r$  Unbalance forces of control points in Load scaling

$F_{ref}$  Reference load

$G$  Shear modulus.  $G_0$  is the initial value of shear modulus.  $G_{ij}$  represents shear modulus in the orthotropic model, where  $i$  and  $j$  can be 1,2,3

$G_f$  Mode-I fracture energy

*h* Crack band width

*K* Current stiffness matrix

[*M*] Principal direction cosine matrix

*q* Load reduction factor in ISLA

*r* Convergence tolerance of  $\mu$  in ISLA

*r<sub>r</sub>* Convergence tolerance of unbalance forces control points in Load scaling

[*R*] Rotation matrix of the stress tensor to the principal directions

*S<sub>t</sub>* Saw tooth factor in the Saw tooth model

*t* Stiffness reduction factor

[*T*] Rotation matrix of the strain tensor to the principal directions

*u* Imposed displacements of control points in Load Scaling

*v* Initial load factor for non-proportional loading in SLA

## GREEK SYMBOLS

$\beta_{ij}$  Corresponding principal direction cosine

$\varepsilon'$  Uniaxial strain used to compute the principal direction Young's modulus

$\varepsilon_1$  Maximum principal strain

$\varepsilon_3$  Minimum principal strain

$\varepsilon_u$  Ultimate tensile strain

$\varepsilon_{us}$  Updated ultimate tensile strain based on Saw tooth model

$\lambda$  Load factor in SLA

$\lambda_{cur}$  Load factor of current load in ISLA

$\lambda_{ini}$  Load factor of initial load in ISLA

$\mu$  Utilisation function which is the largest utilisation value of all elements in ISLA

$\nu$  Poisson's ratio.  $\nu_0$  is the initial value of Poisson's ratio.  $\nu_{ij}$  represents Poisson's ratio in the orthotropic model, where  $i$  and  $j$  can be 1,2,3

$\sigma$  Normal stress in the Mohr-Coulomb criterion

$\sigma_1$  Maximum principal stress

$\sigma_3$  Minimum principal stress

$\tau$  Shear stress in the Mohr-Coulomb criterion

$\phi$  Internal friction angle of the Mohr-Coulomb criterion

## ABBREVIATIONS

CITA Continuous incremental-only tangential analysis

DOF Degree of freedom

IMPL – EX Implicit-explicit approach

ISLA Incremental sequentially linear analysis

GFEM Generalized finite element method

LATIN The large time increment method

MM Meshless method

MPM Material point method

NIEM Non-iterative energy based method

NR Newton–Raphson method

SDA Strong discontinuity approach

SLA Sequentially linear analysis

SUR Smooth unloading-reloading function approach

X – FEM Extended finite element method



# 1

## INTRODUCTION

### 1.1. OVERVIEW

To determine whether a designed engineering structure is safe, we compute its response due to loading. Modern computers and software can perform this computation quickly and with little human assistance. For example, the response of steel frame structures due to extreme wind load is routinely computed, including second-order effects, the formation of plastic hinges, buckling of members and, eventually, the beginning of collapse. Another example is the response of a reinforced concrete high-rise building due to an earthquake. To compute the response, dynamic non-linear analysis with beam elements and a hysteretic model of the beam-column joints is used.

However, for structures constructed of unreinforced masonry, unreinforced concrete or other quasi-brittle materials, the computation of response is very difficult. The classical constitutive models for quasi-brittle materials are plasticity models, damage models and coupled damage-plastic models, which are described later [1]. The classical algorithm for solving non-linear mathematical equations is the Newton-Raphson method (see Section 2.2). This method is robust if the load-displacement curve is continuous and smooth. However, for quasi-brittle materials,

many cracks occur and grow at every load increment, which creates many small, sharp peaks in the load-displacement curve. There is no consideration of the physical description of quasi-brittle materials, but the stress-strain equations are well-defined and the size effect is included. The problem is that algorithms for solving these equations often fail to find a solution. The negative tangent stiffness causes an ill-conditioned stiffness matrix when brittle material softens [2] [3][4]. In addition, two physical phenomena sometimes occur in non-linear analysis, namely that the solution can lack uniqueness and can be split into equally possible realities. This split is called a bifurcation. The solution to an increment can be a reduction in load and displacement, which is called snap-back. These phenomena need to be simulated correctly. The engineer responsible for such an analysis must steer the software to obtain accurate results. Computation is slow when crack explosive propagation, snap-back and bifurcation arise, and the results typically do not continue beyond the onset of failure. Moreover, the results are often unreliable.

Many improved solution methods have been proposed, divided by incremental and total approaches, such as the modified Newton-Raphson method with initial stiffnesses [5], the LATIN method [6][7][8] and sequentially linear analysis (SLA) [9]. SLA is an alternative to the Newton-Raphson method when bifurcation, snap-back or divergence problems arise. The incremental iterative procedure, adopted in non-linear finite element analysis, is replaced by a sequence of scaled linear finite element analyses with decreasing secant stiffness, corresponding to local damage increments, to find a solution to the equations for masonry and unreinforced concrete structures. The local damage increments are discretized "event-by-event" in the saw-tooth softening model [10][11].

In static structural analysis, loads are often applied together (proportional loading). However, the load order can be important, for example first prestress on a concrete beam and subsequent removal of the formwork, which activates self-weight. Other examples are pushover loading of a masonry wall with permanent overburden and wind load after snow load on a roof structure. In general, non-proportional loading is a situation in which some loads are kept constant while others vary over time. Unfortunately, original SLA can be used only when all loads are applied at the same time (proportional loading). Non-proportional loading was first and partly accomplished in 2008 [12]. Other limitations of the method are that it

cannot be easily used for large displacements (second-order effect), plastic deformation or dynamic behaviour due to the total approach of SLA. Therefore, incremental sequentially linear analysis (ISLA) is formulated in this thesis and in [13][14] to extend SLA to an incremental approach. ISLA is an incremental procedure with an iterative scheme and begins and ends with an equilibrium state. The solution search path follows damage steps sequentially with secant stiffness. A utilisation value is defined, which is determined at the local by the stress state and the failure surface of an element with the elastic material properties. A utilisation function is defined as the largest utilisation value of all elements (the utilisation value of the critical element), which is a function of the load factors and the stiffness matrix. When the utilisation function is larger than 1, the material is overloaded. When the utilisation function is smaller than 1, the material can carry more load. In this dissertation, SLA and ISLA have been programmed on top of the finite element program ANSYS. ANSYS has a scripting language APDL that can be used to run analyses, process results, modify stiffness, and continue with more analyses. This made it possible to explore many materials and loading ideas from which ISLA evolved.

Until recently, the computation of unreinforced masonry response was not an urgent problem because unreinforced masonry or unreinforced concrete were not used for structures that need to carry large loads. However, since 1986, earthquakes have occurred in East Groningen, the Netherlands due to gas extraction from deep, porous rocks. Gas extraction began in 1959 and considerable subsidence of the surface has occurred, but it was unexpected that parts of the porous rock would suddenly compact. Most houses, schools and churches in East Groningen are made of unreinforced masonry, which must now withstand Magnitude 4 earthquakes. This has created an urgent need for robust software to compute the response of unreinforced masonry and unreinforced concrete, not just in the linear design stage but up to failure and near-collapse.

## 1.2. RESEARCH OBJECTIVES

The aim of this thesis is to develop a robust approach for non-linear analysis that includes bifurcation, snap-back and convergence. This approach should be suitable for all types of materials, including quasi-brittle materials and plastic materials. The approach should be applicable for different element types (e.g., plane ele-

ments, shell elements and solid elements) and load cases (i.e., proportional or non-proportional loading). In addition, the approach should be easily extendible from static analysis to geometrically non-linear analysis and transient analysis. Moreover, the approach should consider not only damage but also plasticity. Last but not least, this approach must be validated on a simple, elemental level and on a complicated, structural level.

### 1.3. RESEARCH CONTRIBUTIONS

The contributions of this thesis are divided into improvements to SLA and the development of ISLA as well as plastic behaviour.

Improvements to SLA include:

- Introduction of a saw-tooth model governed by the stiffness reduction rather than the saw-tooth number.
- Introduction of an orthotropic damage model for SLA based on the rotating smeared crack model.
- Introduction of multiple failure criteria for SLA, so that the combination of tension, compression or shear failure can be modelled.
- Implementation of a new algorithm of SLA for analysing non-proportional load. The algorithm is a pre-procedure modification in original SLA rather than a post-procedure modification in [12]. It is naturally suitable for different element types and failure criterion without extra extensions. This algorithm can be easily programmed into any commercial software.

Development of ISLA includes:

- Formulation of ISLA, which follows an incremental procedure and ensures robustness. The solution search path follows damage steps sequentially with secant stiffness. An equilibrium is determined at the local by the stress state and the failure surface of an element with elastic material properties.
- Development of extended control procedures in ISLA, which is comparable with the arc-length method. These procedures consist of load control, damage control and the combination of these. In addition, indirect displacement

control loading has been implemented into ISLA. The procedures also preserve robustness.

- Extension of ISLA to geometrically non-linear analysis, transient analysis and proportional cyclic loading of quasi-brittle materials.
- Validation of ISLA at the large-scale structural level. For snap-back, the load control method and the load and damage control method both perform successfully.
- Introduction of a coupled damage-plastic model in ISLA and preliminary implementation of plasticity in cyclic loading.

## 1.4. THESIS OUTLINE

**Chapter 2** presents the state-of-the-art of fracture mechanics, damage theories and computational methods for quasi-brittle materials. The development of SLA and other related methods are described in terms of improvements of the standard Newton–Raphson method.

**Chapter 3** describes improvement of the constitutive properties in SLA. A saw-tooth model governed by stiffness reduction is developed for the softening material, and an orthotropic damage model based the multi-directional smeared crack is implemented. In addition, multiple failure criterion is formulated using the improved procedure to allow a combination of tension, compression and/or shear.

**Chapter 4** proposes an algorithm for non-proportional loading in SLA. The constant-load factor is applied and adjusted in the pre-procedure<sup>1</sup>. This algorithm is validated on a prestressed beam with point loading.

**Chapter 5** presents ISLA, which is an incremental procedure with an iterative scheme that begins and ends with an equilibrium state. The solution search path follows damage steps sequentially with secant stiffness. An equilibrium is determined at the local level by the stress state and the failure surface of an element with the elastic material properties. The history of displacement and forces on the global level is described during the ISLA procedure. This method is tested on a notched beam (proportional loading).

---

<sup>1</sup>The target is to keep the constant-load constant after the mapping back procedure, therefore the constant-load factor is not constant

**Chapter 6** elaborates load scaling control in ISLA, which includes the damage control method and the load and damage control method. Different searching strategies are proposed and compared in terms of computational accuracy and efficiency. The functions in this method are optimized, governed by utilisation values of ISLA.

**Chapter 7** shows and demonstrates the principle, algorithms and search paths of ISLA on a simply supported concrete notched beam (proportional loading). Three methods are compared, namely the load control method, damage control method and load and damage control method.

**Chapter 8** validates ISLA using a highly prestressed beam test (non-proportional loading), for which SLA suffers divergence problems. Global hardening behaviour and branch cracks are observed with a softening material model.

**Chapter 9** validates ISLA using geometrically non-linear analysis. ISLA is compared with the Newton–Raphson method using a masonry wall out-of-plane bending test. Crack propagation and ultimate displacement are observed by ISLA.

**Chapter 10** validates ISLA using transient analysis. A multiple degree-of-freedom system is used for testing. Several ways of updating the stiffness are investigated and compared between ISLA and the Newton–Raphson method. Several stiffness adjusting solutions are proposed and compared with the results of the Newton–Raphson method.

**Chapter 11** validates ISLA at the structural level, including the aspect of non-proportional loading. Two structural examples tested in the laboratory are selected, namely a masonry facade settlement test and a full-scale masonry house pushover test, which are compromise cases for SLA for the simulation of initial damage. This chapter compares the load control method and load and damage control method as well as the isotropic damage model and the orthotropic damage model.

**Chapter 12** summarizes key features of improved SLA and ISLA and proposes further work related to this method.

**Appendix A** validates ISLA using proportional cyclic loading of a quasi-brittle material, where a structure is governed by tensile failure and unloading behaviour follows secant stiffness. The correlative damage model is described and tested to simulate reverse loading behaviour between tension and compression.

**Appendix B** combines plasticity behaviour with the damage model (saw-tooth

model) in ISLA. This method is validated by an element compressive loading-unloading test and a notched beam tension loading-unloading test. Unloading with plastic deformation is combined with reverse loading at the element level.

Figure 1.1 shows the structure of the chapters of this thesis.

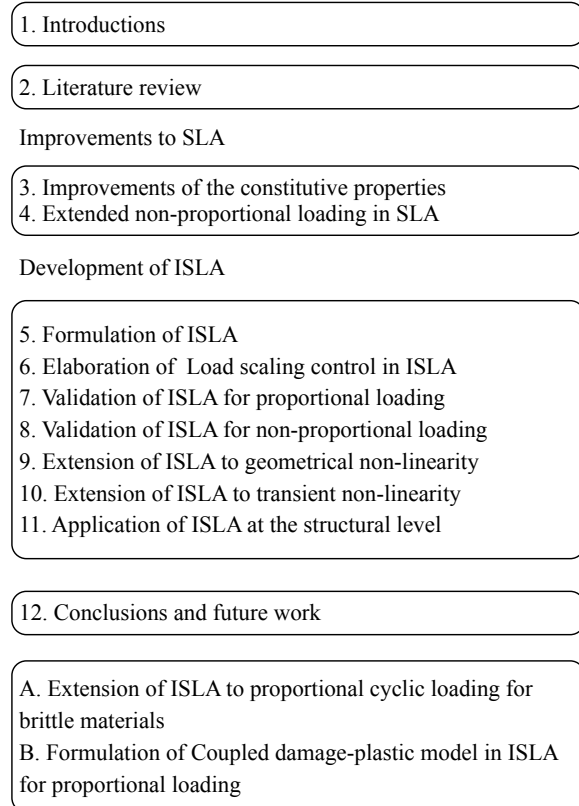


Figure 1.1: Structure of the chapters of this thesis



# 2

## LITERATURE REVIEW

Non-linear finite element analysis has become a common tool for studying the behaviour of masonry, reinforced concrete and prestressed concrete. Over the years, techniques for non-linear analysis have been enhanced significantly by improved constitutive models, improved solution procedures and extended finite element techniques. However, the robustness of the algorithms remains a serious issue, especially when cracking and crushing in real-world structures are being analysed.

This chapter presents the state-of-the-art of numerical modelling of fracture in quasi-brittle materials. Research on quasi-brittle materials can be divided into constitutive descriptions of failure and proposals for solving the governing non-linear equations. Section 2.1 discusses descriptions of failure and Sections 2.2 to 2.5 discuss solving the non-linear equations. A general framework can be found in [15].

### 2.1. FAILURE MECHANICS

#### 2.1.1. CRACKING CONCEPTS IN FINITE ELEMENT ANALYSIS

For quasi-brittle materials, there are three ways of representing cracks via finite element configurations, namely discrete crack models, smeared crack models and

lattice models.

In the discrete crack model [16][17], a crack occurs when the nodal force normal to the element boundaries is larger than the maximum tensile strength. New degrees of freedom (DOFs) at the location of this node are created, which disconnects the elements. The crack is regarded as a geometrical entity [18]. The main limitation is that the crack propagation is restricted to the mesh lines. Discrete crack models are improved with the possibility of remeshing [17] and the use of interface elements as predefined cracks [18].

In contrast, in smeared crack models [19], a cracked solid is regarded as a continuum and described by a stress-strain relation. One possibility is fixing the direction of the crack upon its initiation. This is called a fixed crack model. A recent fixed crack model is the crack band model [20], which was developed for mode-I fracture and extended with mode-II shear retention. Fracture energy was introduced in [21] and was used to obtain mesh-independence in [20]. A threshold angle has been introduced, which allows new cracks to form only when the angle between the current direction of the major principal stress and the normal direction to the existing cracks is exceeded, to avoid an ill-conditioned stiffness matrix [2][3][4].

As an alternative, the rotating smeared crack model was introduced [22]. This model allows cracks to rotate and describes the behaviour in terms of the rotating principal axes rather than the fixed crack axes. It eliminates the difficulty of choosing a proper shear retention function. It uses an implicit shear formulation that guarantees coaxiality between principal stress and principal strain [15]. The rotating crack model can be regarded as a fixed multiple crack model for a zero threshold angle [18].

In lattice models [23][24][25][26][27], the continuum is represented by a lattice of truss or beam elements. The micro structure of the material is simulated by assigning different properties to different truss or beam elements. An element is removed when a failure criterion is reached in the brittle material. SLA has similarities to the discretized lattice model method.

Afterwards, three developments have taken place, namely meshless methods, the extended finite element method (X-FEM) and strong discontinuity approaches (SDA). The main concept of these methods is that crack propagation is not restrained by the element mesh. The disadvantage of these methods is that they are

not as convenient as smeared approaches. Crack continuity algorithms become complex in 3D.

Meshless methods (MMs) have been described in [28][29]. In MMs, the approximation is constructed from nodes, only to overcome the difficulties of building approximation related to mesh dependency [29]. The element-free Galerkin method [30] is the first method developed on a global weak form, which requires only nodal data but is suitable for arbitrary shapes. The element-free Galerkin method is widely used for fluid, elasticity and heat conduction problems. The partition of unity finite element method (PUFEM) combines MMs and finite element methods, the shape function of which are based on Lagrange polynomials [31]. The generalized finite element method (G-FEM) enables a different partition of unities to be used for the usual approximation and so-called enrichment[32]. The material point method (MPM) [33][34][35] is also a Lagrangian particle-based method like MM, but it employs the grid as a temporary computational scratch pad instead of nodal data in MM.

X-FEM has been described in [36][37][38][39]. The displacement jump is incorporated as a discontinuous partition of unity so that the strain on both sides of a stress-free crack are fully decoupled and there are no incompatibilities between elements [40]. X-FEM can also be used to model reinforcements for quasi-brittle materials.

There is a family of methods called strong discontinuity approaches (SDAs). SDAs were introduced in [41][42][43][44]. The displacement jump is embedded in elements, which depends on the local stress or strain field instead of a priori defined paths [45]. Discontinuity, as an incompatible mode in the strain field, is included in the elements based on enhanced assumed strain (EAS) [46]. The discontinuity is defined by an internal element node in EAS. The method in [43] is extended from 2D to 3D for brittle fracture in [47]. In [45], shape functions are employed as partitions of unity to incorporate the discontinuity with extra DOFs at existing nodes. Therefore, this method is suitable for different types of elements and renders discontinuity continuous across element boundaries. Embedded discontinuity elements are adopted to simulate mode-I and mixed-mode fracture in [48]. Discontinuity can be non-homogeneous in each element by the formulation in [49]. Discontinuity is linked to the continuum constitutive model as a traction-displacement jump in

the continuum strong discontinuity approach (CSDA) [50][51][52]. Discontinuity is incorporated as a rigid body motion in the discrete strong discontinuity approach (DSDA) [53]. The corresponding stretching of discontinuity is also considered in the generalized strong discontinuity approach (GSDA) [54]. The distinction between X-FEM and SDAs were described in [40][55][56].

### 2.1.2. CONSTITUTIVE MODELS

The constitutive models of quasi-brittle materials describe softening for tension, hardening or softening for compression and cohesion softening, and Coulomb friction for shear. These can be divided into plasticity models, damage models, coupled damage-plasticity models [1] and total-strain-based models.

Plasticity models adopt the concept of the split of the total strain into elastic strain and accumulated plastic strain. Several plasticity models have been introduced based on distinctive yield functions, hardening and flow rules and can be found in [57]. The drawbacks of plasticity models are that they cannot describe stiffness reduction and recovery due to the opening and closing of cracks [58]. For concrete, softening plasticity models were developed by a composite yield function in [59][60]. For masonry, softening plasticity models were developed based on discrete concepts in [61] and smeared concepts in [62].

In continuum damage models, the elastic stiffness of the unloading branch is degraded. The degradation is composed of changes in the material at the micro structural level by scalar or tensor internal variables [63]. The models have been used for softening brittle materials [64]. The damage can be defined as one scalar variable [65][66][67], two scalar variables (tension and compression)[68][69][58], a vector [70] and a tensor (second-order [71] and higher order [72]). Continuum damage models vary in their definition (local and non-local damage models) and in ways of representing degradation (isotropic and orthotropic models).

In a local damage model, the description of the material response is based on one integration point. Isotropic damage models [68][73] assume the stiffness reduction is isotropic. Two scalar variables have been introduced to describe the tensile and compressive behaviours of brittle materials separately. Orthotropic damage models have been introduced to consider realistic damage behaviour. Microplane models consider the splitting in terms of volumetric and deviatoric

components[74][75]. The smeared crack model can be regarded as a form of an orthotropic local damage model with one scalar variable.

In a non-local damage model, the material response at a certain point is influenced by the stress in the surrounding region [76]. Non-local models have been used [77] to prevent element size dependency [78] of local damage models. A type of non-local model is gradient enhanced damage, in which the stress depends on the strain and the gradient of the strain [79]. Rather than the gradient damage models, phase field models [80] are adopted for fracture in a mathematically consistent manner with a small, but finite zone with sharp gradients [81]. The gradient damage models and the phase field models have been compared [82]. The issue of the broadening of the damage zone in the gradient damage models does not exist in the phase field models, however the computational robustness and the mode-II fracture simulation still need to be further investigated in the phase field models.

Coupled damage-plasticity models consider both stiffness degradation (damage theory) and irreversible deformations (plasticity theory). The plasticity model was combined with the isotropic damage model in [83][84] and with the orthotropic damage model in [85][86][87][88].

Total-strain-based models do not decompose the strain into an elastic part and a crack part, instead starting from the total strain and describing the material in terms of engineering stress-strain relations in either fixed crack axes or rotating principal axes [89]. Standard smeared crack models are based on total-strain concepts. The total strain is decomposed into a part of the crack and a part of the solid material to consider plasticity in [90][15][2].

### 2.1.3. MULTISCALE MODELLING

Multiscale approaches provide possibilities to link crack propagation at the macro level to failure behaviours at the meso or micro level for quasi-brittle materials [91][92][93]. A general framework to connect material properties at two physical levels was introduced in 1984 [94]. Multiscale methods consist of homogenisation methods and concurrent methods. Homogenisation methods are divided into analytical homogenisation, numerical homogenisation (unit-cell method), computational homogenisation ( $FE^2$  method) and space-time computational homogenisation.

Computational homogenisation [95][96][97][98][99][100] connects different levels by averaging computations at different levels, down-scaling of strains and up-scaling of stresses, and the tangent stiffness based on the Hill-Mandel condition [101][102]. The unit cell of the upper level (macro or meso) has been referred to as a representative volume element (RVE). The boundary value problem has been investigated and solved as the periodic boundary [95][96]. Existence and size determination of RVE was investigated in [103]. A failure zone averaging scheme has been introduced in terms of the size objectivity [104]. Similar with continuum damage models, local models (first-order) [95][105] and non-local models (second-order) [106][107] have been introduced in multiscale modelling.

## 2.2. INCREMENTAL ITERATIVE SOLUTION PROCEDURES

Non-linear equations can be solved by incremental iterative computational approaches based on the Newton–Raphson (N-R) method [5]. In the N-R method, the applied load is divided into small increments, and the displacement increment within each load increment is calculated by the tangent stiffness matrix as summarized in, for example [108][5][109]. The internal force can be computed from accumulated displacement, and the residual force vector can be determined by the difference between external and internal forces. When both the residual force and residual displacements errors are less than specified tolerances measured by Euclidean norms (L2), convergence is reached. If convergence criteria are not satisfied, the residual force vector is re-evaluated, the stiffness matrix is updated and thus a new iteration is performed. This iterative procedure continues until the solution converges and then the next load increment is applied [109].

The standard N-R scheme suffers from divergence problems for quasi-brittle materials. The load-displacement curves of quasi-brittle materials have many small peaks related to the initialization and growth of numerous cracks. These peaks are only visible if one zooms in on a curve that is computed with very small load increments. Further, sharp peaks may occur associated with the sudden development of major cracks or major crushing zones. Consequently, the tangent stiffness in the neighbourhood of these peaks has extreme variations and can lead to the divergence of N-R iterations at any load increment. The negative local tangent stiffness due to softening may give rise to ill-conditioning of the global system. Variations of the

scheme have been proposed to save computing time and to accelerate and improve robustness. These include the modified N-R method, the quasi N-R method, the accelerated N-R method and the line search algorithm [110] [5] [111]. The methods vary in robustness and efficiency. The modified N-R method computes and decomposes the tangential stiffness matrix only in the first iteration at the beginning of every load step while the full N-R method sets up and decomposes the tangent stiffness matrix in every iteration. The global tangent stiffness in the N-R method can be based on true negative softening stiffness at the local level or on the positive secant stiffness at the local level. The quasi N-R method updates the tangent stiffness matrix using the existing one, such that the stiffness in the subsequent iteration is computed based on a multi-dimensional secant approximation. A disadvantage of any variant of the N-R method is its limited radius of convergence. To enlarge this convergence radius, line search applies an improvement to the incremental displacement vector by scaling it with a multiplier so that the point of lowest potential energy along the search direction is obtained [110]. In the accelerated N-R method, the target function is modified from a linear approximation to a high-order approximation in such a way that it yields a faster rate of convergence.

In the standard N-R method, load increments are applied by prescribed forces or displacements, which is called load control. The arc-length control method is a modification of load control to trace post-failure behaviour numerically when a structure softens or snaps back [112][113][114][115]. The load increment parameter is regarded as an additional variable. The value is governed by a constraint equation on the incremental displacement [15]. The norm of the incremental displacement was adopted as the constraint equation in [116], which was linearised from a "spherical arch" to a "normal plane" in [117]. In the case of strong localization, the iterative plane in the standard arc-length method has been constructed from only a selected number of components to trace limit points and even very sharp snap-backs associated with localized failure instead of all DOFs [118][119]. A new constraint has been developed based on the energy release rate in terms of geometrically linear damage, geometrically linear plasticity and geometrically non-linear damage to improve the robustness of the arc length method in [120].

### 2.3. SNAP-BACK AND BIFURCATION POINTS

The N-R method may suffer from divergence at the global level due to softening and negative tangent stiffness, independent of the local constitutive model adopted [121]. This divergence often occurs at snap-back or bifurcation points.

Snap-back is a reduction of both load and displacement in the global load-displacement diagram. Studying fracture shows that a crack initiates, propagates and may either snap to a free surface or be arrested by reinforcing steel, where stresses are redistributed and a new crack or crushing may start. This is accompanied by decreases in the quasi-static load-displacement response [122]. It can be observed that after reaching a valley, a new ascending path may be found up to a new local peak when redistribution capacity is available. These peaks cannot be missed as they may be the global peak for structural failure. This abrupt changing response (snap-back) is difficult to trace although arc length and indirect control schemes provide possibilities [118]. Snap-backs have been successfully traced with examples of detailed meshes on relatively small specimens [15][123][124]. Further, fractures of indirect displacements have been reported with very brittle sharp snap-backs for large-scale structures such as a masonry facade subjected to settlement in [125][9][126] and for reinforced concrete problems in [121][127].

A bifurcation point is the point at which more equilibrium paths begin in the load-displacement solution domain [119][110]. The inclusion of non-linear terms in the kinematic description or the non-linearity of material models brings about bifurcations and alternative branches in many engineering fields[110]. Constitutive models have multiple equilibrium states for softening materials [110]. The existence of bifurcation points and multiple equilibrium branches results from a problem for the N-R procedure, in either its unmodified or its modified form [110]. [128] reported that an unperturbed analysis of the full specimen causes a bifurcation point with two post-bifurcation solutions (a symmetric one and a non-symmetric one). When alternative equilibrium states occur, the correct lowest equilibrium path can only be traced with an incremental iterative approach with imperfections and very small load steps [128].

## 2.4. SEQUENTIALLY LINEAR ANALYSIS

Sequentially linear analysis (SLA) is an alternative to the N-R method when bifurcation, snap-back or divergence problems arise [9]. The incremental iterative procedure, adopted in non-linear finite element analysis, is replaced by a sequence of scaled linear finite element analyses with decreasing secant stiffness, corresponding to local damage increments. A saw-tooth model discretizes material softening driven by damage and recomputes the load via scaling at the local level. The critical element is defined as the element for which the stress-strain state is closest to the failure surface. The load factor  $\lambda$  is defined as the ratio of the current strength and stress of the critical element. A linear analysis is conducted, the critical element is tracked, the stiffness and strength of the element are reduced according to the saw-tooth curve, scaling is performed by  $\lambda$  and the process is repeated. Compared to non-linear smeared crack models in incremental iterative settings, SLA has been shown to be robust and effective in predicting localizations, crack spacing and crack width as well as brittle shear behaviour [9]. The main features of SLA are a total approach with secant stiffness (load-unload method) at the global level and an “event-by-event” damage model (saw-tooth constitutive law) at the local level.

Different constitutive formulations, saw-tooth curves and strategies for non-proportional loading have been proposed in SLA. The saw-tooth model has been improved to make the results independent of the magnitude of the stiffness reduction in a step [10][11]. A regularization scheme provides mesh-size objectivity of the saw-tooth model, either saw-tooth tension softening for unreinforced material or saw-tooth tension stiffening for reinforced material. The scheme is similar to the one commonly used in the smeared crack framework, but both the initial tensile strength and the ultimate strain are rescaled. In this way, the dissipated fracture energy is invariant with respect not only to the mesh size, but also to the number of saw teeth adopted to discretize the softening branch.

The fixed smeared crack model has been implemented in SLA [12][129][130]. The crack orientation is fixed when the crack is initiated. Subsequently, the stiffness orthogonal to the fixed smeared crack ( $E_n$ ) is reduced while the elastic stiffnesses parallel to the crack ( $E_t$  and  $E_s$ ) are kept unaltered. The second and, in 3D, third cracks may occur orthogonal to the fixed crack. Poisson's ratios are assumed to be

reduced at an equal rate as the corresponding E-moduli:

$$\nu_{sn} = \nu_{tn} = \nu_0 \frac{E_n}{E_0} \quad \nu_{ns} = \nu_{ts} = \nu_0 \frac{E_s}{E_0} \quad \nu_{nt} = \nu_{st} = \nu_0 \frac{E_t}{E_0} \quad (2.1)$$

For shear behaviour, a constant or a variable shear retention relation can be included. A constant shear retention factor can result in stress locking [15] and unexpected large shear forces. The structural response can then be too strange and too stiff because of large shear planes, even when the crack is almost fully opened. These are not always correct and thus SLA with fixed smeared cracking has been improved with variable shear retention decreasing along with Young's modulus to reduce the mesh-directional bias for fixed smeared cracking [12][129][130]. Variable shear retention, which directly depends on the crack width and reduced material properties, is a better choice. In this way, completely opened cracks can no longer transfer shear forces. The possibility for variable shear retention is assumed to reduce the shear stiffness at a rate equal to the minimum of the corresponding Young's Moduli:

$$G_{ns} = \frac{\min(E_n, E_s)}{2(1 + \nu_0 \frac{\min(E_n, E_s)}{E_0})} \quad G_{st} = \frac{\min(E_s, E_t)}{2(1 + \nu_0 \frac{\min(E_s, E_t)}{E_0})} \quad G_{tn} = \frac{\min(E_t, E_n)}{2(1 + \nu_0 \frac{\min(E_t, E_n)}{E_0})} \quad (2.2)$$

In addition, Coulomb friction laws have been introduced in SLA as a tension-shear failure criterion for interface elements[131].

Various methods have been proposed to perform SLA with non-proportional loading. The method in [9][12] has been explained in combination with the fixed smeared crack model, and the method in [132] has been explained in combination with the rotating smeared crack model. The difficulty is to keep the initial-load constant when the current load is scaled.

In [9][12], non-proportional loading is described by the application of two load cases, an initial load  $F_{ini}$  that should be kept constant and a current load  $F_{ref}$  that is to be scaled according to damage propagation. Most of the procedure is the same as that for the proportional loading case, but specifically is as follows:

1. Apply the first load  $F_{ini}$ , calculate the stresses  $\sigma_{ini}$  and then remove load one.
2. Apply the second load  $F_{ref}$  as a reference load and calculate the stresses  $\sigma_{ref}$ .
3. Calculate the load multipliers  $\lambda$ , at which the maximum principal stress resulting from the combination of the first and second load such that  $(\sigma_{ini} + \sigma_{ref}\lambda)$  equals the current tensile strength  $f_{ti}^+$ .

4. Determine the critical integration point and calculate  $\lambda_{crit}$ .
5. Apply the critical load combination by scaling the reference  $F_{ref}$  with the critical load multiplier  $\lambda$  from  $(\sigma_{ini} + \sigma_{ref}\lambda_{crit})$  and obtain the current stress-strain state.
6. Remove all loads and update the stiffness and strength properties of the critical integration point according to the saw-tooth constitutive model.
7. Repeat this cycle of steps continuously, updating the properties of a single integration point after each cycle.

The non-proportional loading method in [9][12] has been improved by a constrained optimization suitable for large variety of non-proportional loading cases [131]. The strategy in [131] is that either the initial load is scaled or the last "successful" combination of the initial and reference load is scaled when an empty load factor is obtained, which means the initial load cannot be fully applied without damage initiation or extension. Recently, SLA has been extended to 3-D stress state for the fixed smeared crack model [133].

In [132], a factor  $v$  was introduced for the initial load  $F_{ini}$ . In every load cycle, the initial load is divided by  $v$  after which linear elastic analysis is performed and the total load, which includes the scaled initial load  $F_{ini}/v$  and the current load  $F_{ref}$ , is scaled by the load factor  $\lambda$ . The variable  $v$  is adjusted until  $v = \lambda$ , so at the end of each load cycle the initial load remains constant. The algorithm in [132] is suitable for both 2D and 3D stress state, which is also proposed in Chapter 4 of this thesis.

Compared with these two strategies of non-proportional loading, the algorithm selects the critical integration point, to which a damage increment is applied by extra stresses [9][12] or a varying initial-load factor [132].

Although the results of these methods are encouraging, non-proportional loading has limitations. The stresses may temporarily not satisfy the constitutive equations in [12]. It has been shown that the method fails when a large initial overburden force is applied [134]. In [131], the initial load was temporarily reduced, which can be regarded as switching from non-proportional loading to proportional loading. In [132], the initial-load factor was not obtained for certain cases, which are discussed in Chapter 4 and 8. Another limitation in [12] is that the work does not consider

the actual damage state caused by the current load for the initial load; however, the algorithm in [132] does consider this.

Due to difficulties with SLA, it has been extended to an incremental approach called incremental sequentially linear analysis (ISLA) [13].

## 2.5. OTHER METHODS TO IMPROVE ROBUSTNESS FOR QUASI-BRITTLE NON-LINEAR ANALYSIS

In addition to developing SLA, many other research directions are being explored to improve robustness and efficiency when solving non-linear problems with quasi-brittle materials.

The LATIN method [6][7][8] is a non-incremental iterative computational strategy applied over the entire time interval. Its main features are the separation of possibly non-linear local equations in space and time and possibly linear global equations in the spatial variable, a two-step iterative approach and an ad-hoc space-time global approximation. A difficulty is defining the search paths in the two-step scheme, which is currently guided by numerical parameters that do not have a clear physical meaning.

In the implicit-explicit approach (IMPL-EX), an explicit (non-iterative) scheme and implicit (iterative) scheme are combined [135][136]. IMPL-EX combines an implicit scheme of the stresses in the constitutive model with an explicit extrapolation of the involved internal variables. IMPL-EX consists of two stages. In a first stage, the stresses and the stress-like variable are explicitly calculated based on the stresses and the extrapolated values of the strain-like internal variable of the previous time step. In a second stage, the stresses and the extrapolated values of the strain-like internal variable are implicit. The length of the time step influences the accuracy of this method [109].

The predictive smooth unloading-reloading (SUR) approach is a non-linear incremental iterative N-R method [137]. The SUR approach employs a target function and a smooth unloading-reloading function related to a damage evolution parameter. The SUR function is used to compute an approximate tangent stiffness matrix. The damage evolution parameter governs the SUR function and is updated for every iteration from the last converged increment in each load or displacement increment. A converged value of the damage parameter is computed from the predictive function. The predictive SUR approach has been reported to be more efficient than the total load-unload method, but the convergence characteristics of the model are significantly affected by the form of the SUR function. Currently, this method uses an isotropic damage model.

Another method to improve robustness was developed in combination with the strong discontinuity approach [138]. Here, either a loading phase or an unloading phase is defined for each increment based on the assumption that the crack state is frozen when cracks suddenly propagate through several elements in one increment. An unloading phase is performed with the frozen crack state each time a segment of the crack is added in an element. In the case that the failure criterion is reached simultaneously in more than one element, the crack is added in the critical element.

Other improved approaches are the non-iterative energy-based method (NIEM) [139] and CITA [140], both of which adopt piece-wise linear continuum laws.

NIEM employs tangent stiffness to scale global load increments according to local discontinuity in the multi-linear stress-strain diagram[139][141]. When a bifurcation point is reached, it allows switching from an incremental to a total approach. The total approach is performed with the secant material stiffness whenever a critical bifurcation point is reached because it is impossible to incrementally determine the effective path. This secant stiffness is decreased by a constant stiffness reduction factor as in SLA. A disadvantage is that this stepwise reduction of the secant stiffness must be defined in advance without a clear meaning. To avoid this, the switch between an incremental and a total approach has been based on the use of an energy dissipation criterion rather than a predefined number of reductions of the secant stiffness. When NIEM switches to a total approach, the non-proportional loading issue remains. Recently, NIEM has been improved to deal with the non-proportional loading, and a fully incremental approach has been proposed to avoid this issue [142].

In continuous, incremental-only, tangential analysis (CITA) for the Newton-Raphson method [140], stiffness is calculated based on a piece-wise linear stress-strain curve tangential, which includes parts with negative values. The entire concrete softening failure procedure, including crack propagation, can be obtained because CITA introduces damage in steps. The CITA method limits the damage level to a single event to control the energy dissipation of a failing concrete structure when concrete is damaged due to tension softening, which is similar to the SLA method. However, CITA incrementally continues the analysis to the next event rather than completely unloading and re-loading the structure after each event us-

ing the current and subsequently updated secant stiffness as in SLA. Like NIEM, this method is thus primarily incremental and driven by tangent stiffness, rather than by total secant stiffness. CITA traces the displacement history and has been reported to be more efficient than the load-unload method. A negative tangent stiffness may still cause divergence problems, for example in the case of snap-backs and bifurcations.

The force-release method [143] extends saw-tooth constitutive laws to an incremental and non-iterative procedure, which has been proposed with a particular emphasis on non-proportional loading. The force-release method is based on released stress redistribution and keeps each step linear. After damage of the critical element, the force-release method involves conducting a sequentially linear redistribution process of stress release until a static equilibrium state is reached. The energy is redistributed with imposed displacement or force control loading. Therefore, the method does not follow snap-backs because the load increments are prescribed. In an attempt to follow snap-backs, the force-release method is combined with the load-unload method by introducing external load velocity and a ratio between out-of-balance forces and the external load increment [144]. The result is a range of possible solutions that depend on the choice of the introduced parameters. In addition, the difficulty of non-proportional loading remains when combining the load-unload method.

## 2.6. DISCUSSION

This chapter investigates many material models and solution methods for quasi-brittle materials. The three main problems considered in the literature discussed in the review are size dependency, mesh dependency and ill-conditioning related to softening. Three main objectives of previous research relate to accuracy, robustness and efficiency. Material models vary in terms of discrete versus continuum, local versus non-local, isotropic versus orthotropic, and plasticity versus damage. Solution methods range from incremental to total and from implicit to explicit schemes. The material models and solution methods are discussed independently but in fact they are dependent since some solution methods fit certain material models much better than others. They also influence the development of each other. Based on various assumptions, it can be seen that a new method often brings disadvantages along with advantages. From the author's point of view, none of these is perfect and the appropriate choice depends on the particular problems considered.

Although a number of related research directions have been recently explained to improve the robustness of quasi-brittle analysis, such as SLA, the LATIN method and IMPL-EX, there is a need to better combine the advantages of total approaches and incremental approaches while incorporating the features of orthotropic damage, softening and effects of permanent strains on unloading/reloading at the constitutive level. Various strategies focus on non-proportional loading in total approaches, but there is room for improvement. The incremental approach (incremental sequentially analysis) is developed based on experience with total-based SLA. The advantage of an incremental approach is the natural inclusion of non-proportional loading, effects of permanent strains on unloading/reloading, geometrically non-linear effects or transient effects. The final goal is to provide a general, robust and accurate solution for structural problems of quasi-brittle materials. The methods developed are validated against results from lab tests for both concrete and masonry. The examples focus on numerical stability and robustness, and aspects of size dependency and computation efficiency are of less concern.

# 3

## IMPROVEMENTS TO SLA

SLA has been implemented by many authors. The mathematical details vary from case to case. In this chapter, new equations for SLA are proposed. The material model is extended to Mohr-Coulomb with a tension cut-off. Both the tensile and compression strength can soften, and the softening relations are extended to piecewise linearities. The crack direction can rotate, instead of being fixed as previously assumed in SLA. The saw-tooth formulation is generalized to facilitate various options for stiffness reductions to obtain an accurate and smooth displacement-force diagram.

In this chapter, the implementation of SLA is elaborated from a fundamental point of view. This chapter is limited to proportional loading, and non-proportional loading is considered in the next chapter.

### 3.1. SLA PROCEDURE

The concepts and definitions have been explained in Section 2.4. The basic algorithm of SLA [11] is:

1. Apply a reference load  $F_{ref}$  to the structure.
2. Perform a linear elastic analysis.

3. Consider all elements and find the critical element and the load factor  $\lambda$  (this will be elaborated in section 3.4, 3.5, 3.7).
4. Reduce the stiffness and strength of the critical element based on the saw-tooth model (this is elaborated in section 3.6).
5. Scale all output results linearly by  $\lambda$ .
6. Restart at step 1 with the reduced stiffness and strength from the current cycle.

3

## 3.2. SAW-TOOTH MODEL

The local damage increments are discretized "event-by-event" in the saw-tooth softening model [10][11]. Each time the secant stiffness is reduced, the strength is also reduced at the local level. Figure 3.1 shows different shapes of the saw-tooth model. The objectivity of the saw-tooth model was shown in [10]. The initial tensile

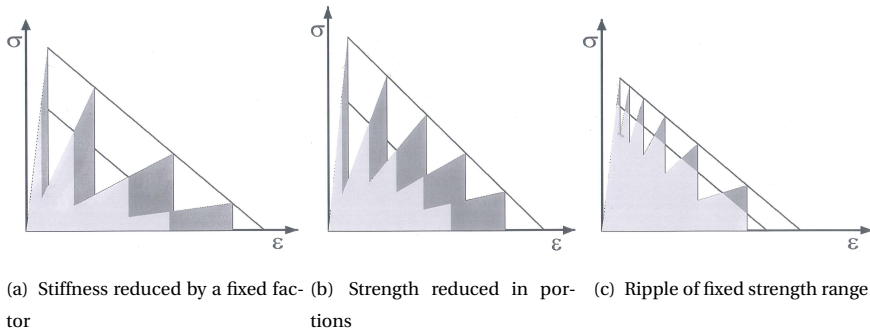


Figure 3.1: Saw-tooth models

strength or the ultimate strain are rescaled such that the fracture energy is invariant with respect not only to the mesh size but also to the number of saw teeth adopted to discretize the softening branch, which can make the fracture energy for SLA the same as that of a physical non-linear analysis and also improves computational efficiency [10].

In this section, a new formulation is proposed based on stiffness reduction, which is important for the rotating smeared crack model implemented in Section 3.6. Another advantage of this formulation compared to others is that a smooth diagram can be obtained. Eq. (3.1) is used to determine ultimate strain for different

element sizes.  $E = 30000$  MPa,  $f_t = 1.43$  MPa and  $\epsilon_u = 0.002$  are used as an example. The area under the diagram in Figure 3.2 represents the fracture energy  $G_f$  divided by the crack band width  $h$ , which is a discretization parameter associated with the size, orientation and integration scheme of the finite element. The saw-tooth model is adopted to determine the consecutive strength reduction in SLA.

$$G_f = \frac{f_t \epsilon_u h}{2} \quad (3.1)$$

As it is linear analysis, each cycle's fracture energy in SLA is written as

$$G_f = \frac{\epsilon_u f_t (K - Kt) h}{2K} \quad (3.2)$$

where  $K$  is current stiffness and  $t$  is the stiffness reduction factor,<sup>1</sup> which determines next cycle's stiffness.

The area representing the step reducing strength from B to D in Figure 3.3 is  $S_{ABC}$  instead of  $S_{ABD}$ , which indicates less fracture energy for SLA.

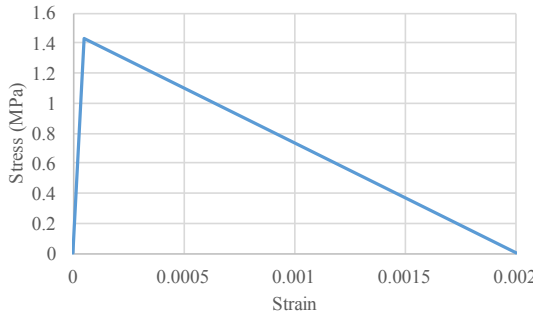


Figure 3.2: Material properties of concrete

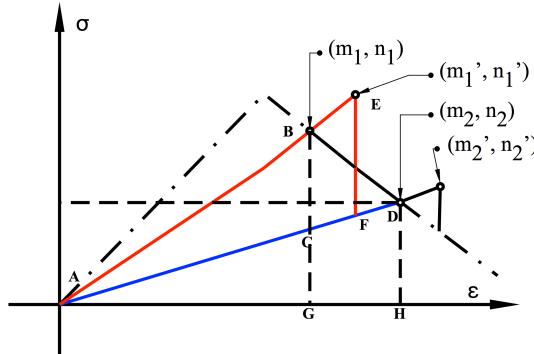
To make SLA's fracture energy the same as with non-linear analysis (Figure 3.3),

$$S_{AEF} = S_{ABD} \quad (3.3)$$

$$S_{ABD} = \frac{m_2}{m_1} S_{ABC} \quad (3.4)$$

$$S_{AEF} = \left( \frac{m'_1}{m_1} \right)^2 S_{ABC} \quad (3.5)$$

<sup>1</sup>Note that the value of the stiffness reduction factor is between 0 and 1. A large value of the stiffness reduction factor means a small stiffness reduction.



3

Figure 3.3: Saw-tooth model implementation

$$S_t = \frac{m'_1}{m_1} = \sqrt{\frac{m_2}{m_1}} \quad (3.6)$$

where  $S_t$  is the saw-tooth factor for one scaling, which is the ratio of the saw-tooth strength and the original material strength of a cycle. Eq. (3.6) provides an elegant way of implementing the saw-tooth model. It can be applied to any stiffness and stiffness reduction, which means it is versatile and essential to the present work.

The saw-tooth model can be simplified for the constant strength (concrete compressive plateau strength and steel material model without hardening behaviour),

$$m_2 = \frac{n_2}{Kt} = \frac{f_c}{Kt} \quad (3.7)$$

$$m_1 = \frac{n_1}{K} = \frac{f_c}{K} \quad (3.8)$$

so the saw-tooth factor is constant for each scaling cycle

$$S_t = \frac{m'_1}{m_1} = \frac{1}{\sqrt{t}} \quad (3.9)$$

For a non-linear stress-strain function  $n = f(m)$ , a similar formula can be obtained by removing the area of arch BID (Figure. 3.4).

$$S_{BID} = S_{GBDH} - S_{GBIDH} \quad (3.10)$$

$$S_{GBDH} = \frac{(m_2 - m_1)(n_2 + n_1)}{2} \quad (3.11)$$

$$S_{GBIDH} = \int_{m_1}^{m_2} f(m) dm \quad (3.12)$$

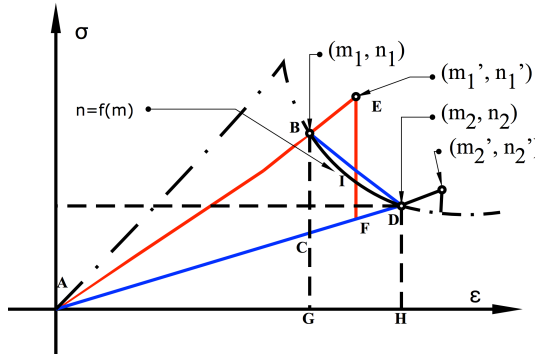


Figure 3.4: Saw-tooth model implementation

$$S_{ABC} = \frac{m_1 n_1 (1 - t)}{2} \quad (3.13)$$

$$S_{BID} = \frac{(m_2 - m_1)(n_2 + n_1) - 2 \int_{m_1}^{m_2} f(m) dm}{m_1 n_1 (1 - t)} S_{ABC} \quad (3.14)$$

$$\begin{aligned} S_{ABID} &= S_{ABD} - S_{BID} \\ &= \frac{m_2 n_1 (1 - t) - (m_2 - m_1)(n_2 + n_1) + 2 \int_{m_1}^{m_2} f(m) dm}{m_1 n_1 (1 - t)} S_{ABC} \end{aligned} \quad (3.15)$$

$$S_t = \frac{m'_1}{m_1} = \sqrt{\frac{m_2 n_1 (1 - t) - (m_2 - m_1)(n_2 + n_1) + 2 \int_{m_1}^{m_2} f(m) dm}{m_1 n_1 (1 - t)}} \quad (3.16)$$

For instance, the saw-tooth model for linear tension softening is shown in Figure 3.5. A 50% and 10% stiffness reduction are shown in the figure. The maximum strength for 50% stiffness reduction is 1.999 MPa while that for 10% stiffness reduction is 1.505 MPa. The saw-tooth factor  $S_t$  becomes increasingly smaller. The factor is almost 1 when the strain meets the ultimate strain. This also indicates that there is almost no overshoot when the stiffness reduction is sufficiently small. However, the small stiffness reduction influences calculation efficiency, so the concept of the saw-tooth factor is still worthwhile.

According to research results from [10], increasing only the strength for the saw-tooth model would overestimate the peak load while increasing only the ultimate strain would underestimate it. The best option is to increase both the strength as well as the ultimate strain for the saw-tooth model. The method to convert the original saw-tooth model to an optimized one is simple. Multiplying both strength

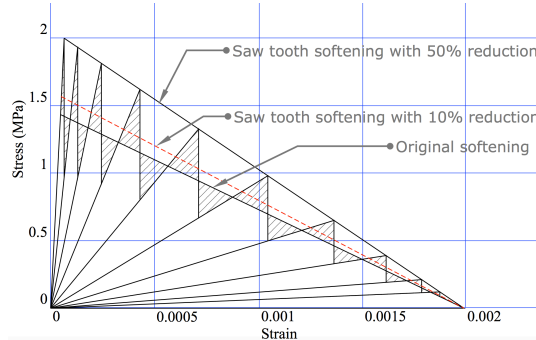


Figure 3.5: Saw-tooth model for tension softening comparing two reduction factors

and ultimate strain by  $\sqrt{S_t}$  instead of  $S_t$ , which is the original saw-tooth factor, keep  $G_f$  the same as the original (Eq. (3.17)).

$$G_f = \frac{(S_t f_t) \epsilon_u}{2h} = \frac{(\sqrt{S_t} f_t) (\sqrt{S_t} \epsilon_u)}{2h} \quad (3.17)$$

To make the saw-tooth factor equal to  $\sqrt{S_t}$  and leave  $G_f$  unchanged, both strength and ultimate strain need to be updated. The new equations are obtained by following Eqs(3.18) and (3.19).

$$f_{ts} = f_t \sqrt{S_t} \quad (3.18)$$

$$\epsilon_{us} = \epsilon_u \sqrt{S_t} \quad (3.19)$$

where  $f_{ts}$  and  $\epsilon_{us}$  are the updated strength and ultimate strain based on the saw-tooth model.  $S_t$  is derived from Eq (3.6).

The optimized saw-tooth model is shown in Figure 3.6.

### 3.3. MATERIAL MODEL

The previous SLA adopts a fixed crack model [11][12][129]. In a fixed crack model, the cracking directions are recorded at the onset of cracking and not updated during computations. The directions are  $n, s, t$  with  $n$  the normal direction to the crack and  $s, t$  the tangential directions to the fixed crack. Stiffnesses  $E_{nn}, E_{ss}, E_{tt}$  related to the cracking directional stresses  $\sigma_{nn}, \sigma_{ss}, \sigma_{tt}$  are recorded and reduced whenever the integration point is critical. In the present study, a rotating crack model is adopted in which the cracking directions are not recorded but recomputed

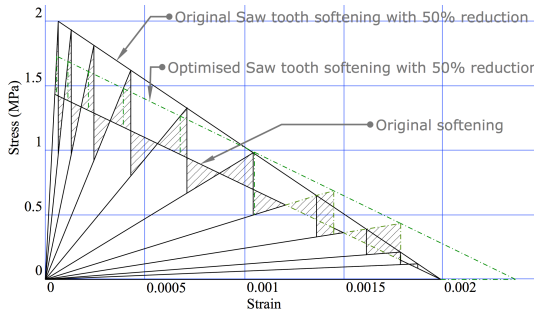


Figure 3.6: Optimized saw-tooth model for tension softening compared with the original model

during each cycle based on the principal directions. Stiffnesses  $E_1, E_2, E_3$  related to continuously rotating principal directional stresses are recomputed and reduced whenever the integration point is critical.

The reason for choosing a rotating crack formulation is that it reduces stress locking and possible stiff response. Such behaviour has been reported for fixed smeared cracks in the incremental iterative analysis, depending on the choice for shear retention along with the fixed crack plane. Another reason for choosing this model is to account for the possibility that the cracking direction can change based on principal directions. For the saw-tooth model of the rotating smeared crack, the stiffness and the strength are updated based on the recomputed principal directions.

### 3.4. FAILURE CRITERION

SLA can work for any failure criterion. In this work, two failure criteria are applied, firstly the Mohr-Coulomb criterion for a combination of compression and shear and secondly, the tension cut-off criterion for tensile cracking. Both of these are suitable for 3D stress situations. Figure 3.7 shows the failure surface of the Mohr-Coulomb criterion with tension cut-off, both in the  $\tau, \sigma$  plane (Figure 3.7(a)) and in the principal stress space (Figure 3.7(b)). The stresses are ordered  $\sigma_3 < \sigma_2 < \sigma_1$  in principal directions. Stresses  $\sigma_1$  and  $\sigma_3$  are the maximum and minimum principal stresses. Therefore,  $\sigma_2$  direction is not shown in Figure 3.7(b) for 3D stress situations because the failure surface cannot reach in this direction. For 2D stress situations,  $\sigma_2$  is zero. In the  $\tau, \sigma$  plane (shear stress and normal stress), the Mohr-Coulomb

criterion is described by the parameters  $c$  and  $\phi$ , namely cohesion and the angle of the internal friction. In the 3D principal stress space, the Mohr-Coulomb criterion can be characterized by the parameters  $f'_c$  and  $f_{t2}$ . In addition, the tension cut-off criterion is introduced and described by the "true" tensile strength  $f'_t$ .  $f_{t2}$  can be regarded as the fictitious tensile strength of the Mohr-Coulomb criterion, regarding the physical parameters  $c$  and  $\phi$ , and does not correspond to the actual tensile strength  $f'_t$ . Therefore, a tension cut-off criterion is added, as indicated in the two figures, described by the true tensile strength  $f'_t$ . For biaxial tension, the failure surface is determined by the tension cut-off criterion. For biaxial compression, the failure surface is determined by the Mohr-Coulomb criterion. For tension-compression, the failure surface is determined by the Mohr-Coulomb criterion or the tension cut-off criterion.

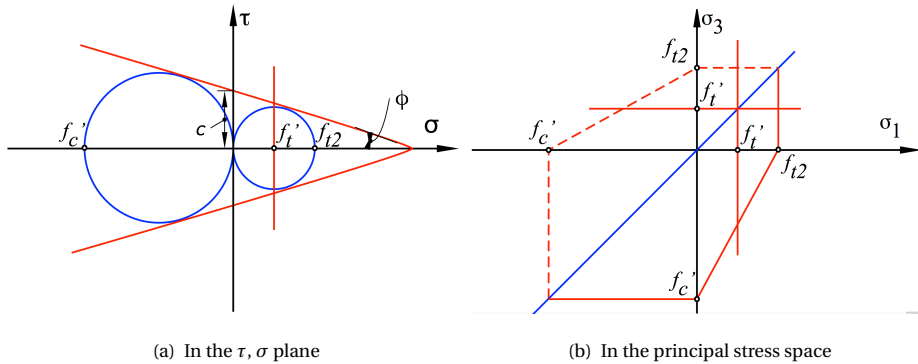


Figure 3.7: Failure surface of the Mohr-Coulomb criterion with tension cut-off

The Mohr-Coulomb criterion reads

$$\tau \leq c - \sigma \tan \phi \quad (3.20)$$

where

$$\sigma = \frac{\sigma_1 + \sigma_3}{2} + \frac{\sigma_1 - \sigma_3}{2} \sin \phi \quad (3.21)$$

$$\tau = \frac{\sigma_1 - \sigma_3}{2} \cos \phi \quad (3.22)$$

The substitution of (3.21) and (3.22) in (3.20) gives

$$\sigma_1 \frac{1 + \sin \phi}{2 \cos \phi} - \sigma_3 \frac{1 - \sin \phi}{2 \cos \phi} \leq 1 \quad (3.23)$$

If we define  $f'_c$  and  $f_{t2}$  as:

$$f'_c = \frac{2c \cos \phi}{\sin \phi - 1} \quad (3.24)$$

$$f_{t2} = \frac{2c \cos \phi}{\sin \phi + 1} \quad (3.25)$$

Then, the Mohr-Coulomb criterion can be written as

$$\frac{\sigma_1}{f_{t2}} + \frac{\sigma_3}{f'_c} \leq 1 \quad (3.26)$$

The tension cut-off criterion reads

$$\frac{\sigma_1}{f'_t} \leq 1 \quad (3.27)$$

The inclusion of load factor  $\lambda$  in (3.26) and (3.27) for the Mohr-Coulomb criterion with tension cut-off in SLA gives

$$\frac{\lambda \sigma_1}{f_{t2}} + \frac{\lambda \sigma_3}{f'_c} = 1 \quad (3.28)$$

$$\frac{\lambda \sigma_1}{f'_t} = 1 \quad (3.29)$$

The parameter  $f_{t2}$  of the Mohr-Coulomb criterion is assumed to be constant. The cut-off tension  $f'_t$  and compression part  $f'_c$  (negative value) of the Mohr-Coulomb criterion are not constant during a computation. They are updated based on the saw-tooth model of the rotating smeared crack model. Stiffnesses  $E_1$  and  $E_3$  are the maximum and minimum principal directional stiffnesses related to  $\sigma_1$  and  $\sigma_3$ . The maximum principal directional stiffness  $E_1$  is reduced when an element becomes critical with respect to the tension cut-off criterion. The minimum principal directional stiffness  $E_3$  is reduced when an element becomes critical with respect to the Mohr-Coulomb criterion. The tensile strength  $f'_t$  of the tension cut-off criterion is updated based on  $E_1$  and the material tensile stress-strain curve. The compressive strength  $f'_c$  of the Mohr-Coulomb criterion is updated based on  $E_3$  and the material compressive stress-strain curve. A bilinear hardening and linear softening curve is used for compression. This is an example of multi-linear stress-strain representation in SLA, which is detailed further in Section 3.5.

The tensile strength  $f_{t2}$  of the Mohr-Coulomb criterion is a fictitious value calibrated to obtain the correct shear failure.

$$\frac{f_{t2}}{f'_c} = \frac{\sin \phi - 1}{\sin \phi + 1} \quad (3.30)$$

$$\frac{f_{t2}}{f'_t} = \frac{\sin \phi - 1}{\rho(\sin \phi + 1)} \quad (3.31)$$

where  $\rho$  is the ratio of tensile and compressive strength.

3

In this study,  $\rho$  and  $\phi$  are assumed as  $-0.1$  and  $42^\circ$ , reflecting concrete and concrete-like materials, which implies that two times the tensile strength has been used for  $f_{t2}$ .

### 3.5. THE CRITICAL ELEMENT AND LOAD FACTOR

Scaling is defined here as reducing or enlarging the applied reference load by a factor  $\lambda$  to make the stresses just fulfil the material strength condition (unity check). The critical element is the element with the smallest  $\lambda$  of a cycle in SLA. Below are the equations for the intersection of two lines, derived with elementary mathematics.

$$e = \frac{(bc - ad)m}{(c - a)n - (d - b)m}, f = \frac{(bc - ad)n}{(c - a)n - (d - b)m} \quad (3.32)$$

$$\frac{n}{f} = \frac{c - a}{bc - ad}n - \frac{d - b}{bc - ad}m \quad (3.33)$$

In Figure 3.8, coordinate  $(m, n)$  represents a computed principal direction Young's

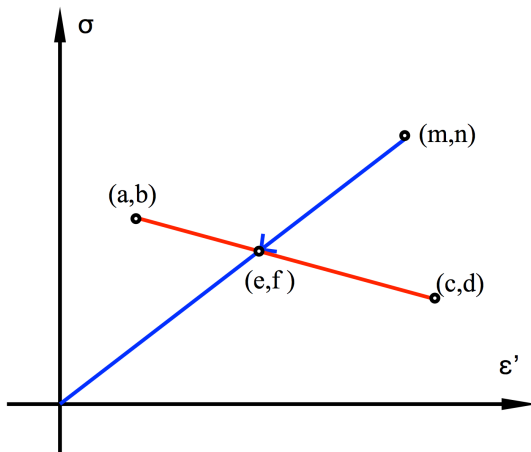


Figure 3.8: Elementary mathematics for calculating  $\lambda = \frac{f}{n}$

modulus from an SLA cycle for some material point. The ratio of  $\frac{n}{m}$  or  $\frac{f}{e}$  is the principal direction Young's modulus. We define  $\epsilon'_1 = \frac{\sigma_1}{E_1}$  etc. as uniaxial strain. Line  $(a, b) - (c, d)$  represents a part of a multi-linear material failure curve. Intersection  $(e, f)$  represents the failure situation. Ratio  $\frac{f}{n}$  represents the load factor  $\lambda$ . The computed strain-stress is scaled to the failure strain-stress. Equation (3.33) is used to calculate  $\lambda$ .

For the Mohr-Coulomb criterion, there are two situations in compression, namely branch 1 and branch 2 (Figure 3.9). For the tension criterion, there is only one softening branch to be considered (Figure 3.10).

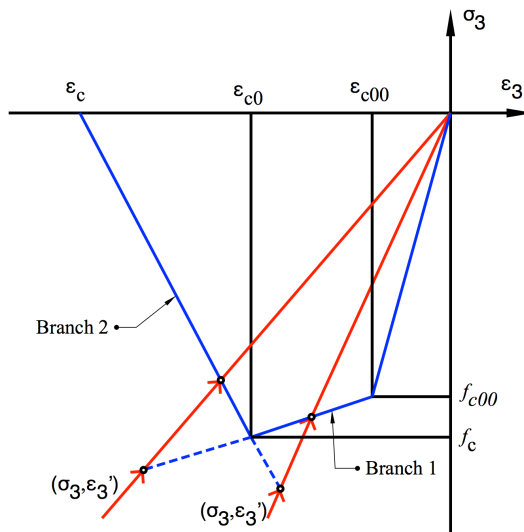


Figure 3.9: Scaling for the Mohr-Coulomb criterion

For compression of branch 1, the Mohr-Coulomb criterion (Eq. (3.28)) is evaluated by computing  $C_{c1}$ , which is  $\frac{1}{\lambda}$  for branch 1. Eq (3.33) is used to obtain

$$C_{c1} = \frac{\sigma_1}{f_{t2}} + c_1 \sigma_3 + c_2 \epsilon'_3 \quad (3.34)$$

where  $c_1 = \frac{\epsilon_{c0} - \epsilon_{c00}}{f_{c00} \epsilon_{c0} - f_c \epsilon_{c00}}$  and  $c_2 = \frac{f_{c00} - f_c}{f_{c00} \epsilon_{c0} - f_c \epsilon_{c00}}$ .

For compression of branch 2, the Mohr-Coulomb criterion (Eq. (3.28)) is evaluated by

$$C_{c2} = \frac{\sigma_1}{f_{t2}} + c_3 \sigma_3 + c_4 \epsilon'_3 \quad (3.35)$$

where  $c_3 = \frac{\epsilon_c - \epsilon_{c0}}{f_c \epsilon_c}$  and  $c_4 = \frac{f_c}{f_c \epsilon_c}$ .

The largest  $\frac{1}{\lambda}$  of branch 1 and branch 2 is the correct one,

$$C_{m-c} = \max(C_{c1}, C_{c2}) \quad (3.36)$$

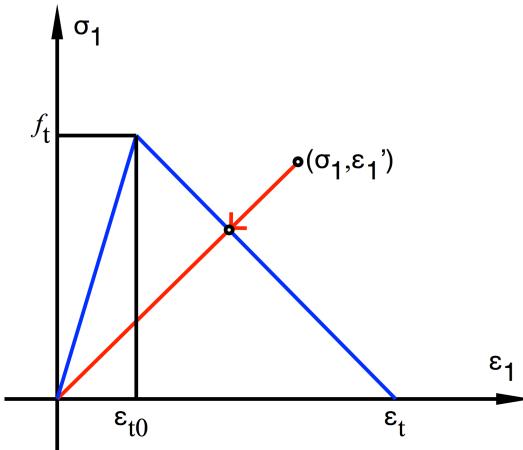


Figure 3.10: Scaling for tension cut-off

For tension, the tension cut-off criterion (Eq. (3.29)) is evaluated by computing  $C_t$

$$C_t = t_1 \sigma_1 + t_2 \epsilon'_1 \quad (3.37)$$

where  $t_1 = \frac{\epsilon_t - \epsilon_{t0}}{f_t \epsilon_t}$  and  $t_2 = \frac{f_t}{f_t \epsilon_t}$ .

The correct  $\frac{1}{\lambda}$  is the largest of the Mohr-Coulomb value  $C_{m-c}$  and the tension cut-off value  $C_t$ .

Note that the formulas for calculating the Mohr-Coulomb criterion can be used to include bilinear tension stiffening behaviour. Actually, the procedure for multi-linear behaviour is the same as for bilinear behaviour except for

$$C_{m-c} = \max(C_{c1}, C_{c2}, C_{c3} \dots) \quad (3.38)$$

## 3.6. STIFFNESS REDUCTION OF ORTHOTROPIC DAMAGE

In an isotropic damage model, stiffness is reduced in all directions, which is easy to implement but physically unrealistic. In contrast, in an orthotropic damage

model, stiffness in the fixed (fixed smeared crack) or the principal directions (rotating smeared crack) can be reduced to different degrees. To this end, the stiffness matrix needs to be transformed to the fixed or the principal directions, reduced and transformed back. In a publication [130] on orthotropic damage, as soon as load increments cause the principal stress to violate the tensile strength, a crack was initiated perpendicular to the direction of the critical principal stress. After crack initiation in this critical integration point, the crack direction is fixed (fixed crack model). However, in the present new orthotropic model, damage in each step is in one of the principal directions of the critical element, which means it can still carry loads in the other directions. The damage direction changes along with the principal direction step-by-step (rotating crack model). Below is the procedure to reduce one of the principal direction's Young's moduli and update relevant shear moduli and Poisson's ratios.

At any time, the following data can be retrieved through analysis. These are the critical element's stress state ( $\sigma_x, \sigma_y, \sigma_z, \sigma_{xy}, \sigma_{yz}$  and  $\sigma_{xz}$ ) and material properties ( $E_x, E_y, E_z, v_{xy}, v_{yx}, v_{yz}, v_{zy}, v_{xz}, v_{zx}, G_{xy}, G_{yz}$  and  $G_{xz}$ ).

Further, the principal direction cosine matrix  $[M]$  can be obtained for the stress state. The rows of this matrix are principal direction vectors.

$$[M] = \begin{bmatrix} \beta_{11} & \beta_{12} & \beta_{13} \\ \beta_{21} & \beta_{22} & \beta_{23} \\ \beta_{31} & \beta_{32} & \beta_{33} \end{bmatrix} \quad (3.39)$$

The rotation matrix  $[R]$  can be derived from the direction matrix  $[M]$ .

$$[\sigma_{i'j'}] = [M] [\sigma_{ij}] [M]^T \quad (3.40)$$

where  $\sigma_{i'j'}$  is the stress tensor in the principal directions and  $\sigma_{ij}$  is the stress tensor in the global direction. This can be written in Voigt notation as

$$\begin{bmatrix} \sigma_1 \\ \sigma_2 \\ \sigma_3 \\ 0 \\ 0 \\ 0 \end{bmatrix} = [R] \begin{bmatrix} \sigma_x \\ \sigma_y \\ \sigma_z \\ \sigma_{xy} \\ \sigma_{yz} \\ \sigma_{xz} \end{bmatrix} \quad (3.41)$$

where  $[R]$  is evaluated as

$$\begin{bmatrix} \beta_{11}^2 & \beta_{12}^2 & \beta_{13}^2 & 2\beta_{11}\beta_{12} & 2\beta_{12}\beta_{13} & 2\beta_{11}\beta_{13} \\ \beta_{21}^2 & \beta_{22}^2 & \beta_{23}^2 & 2\beta_{21}\beta_{22} & 2\beta_{22}\beta_{23} & 2\beta_{21}\beta_{23} \\ \beta_{31}^2 & \beta_{32}^2 & \beta_{33}^2 & 2\beta_{31}\beta_{32} & 2\beta_{32}\beta_{33} & 2\beta_{31}\beta_{33} \\ \beta_{11}\beta_{21} & \beta_{12}\beta_{22} & \beta_{13}\beta_{23} & \beta_{11}\beta_{22} + \beta_{21}\beta_{12} & \beta_{12}\beta_{23} + \beta_{22}\beta_{13} & \beta_{11}\beta_{23} + \beta_{21}\beta_{13} \\ \beta_{21}\beta_{31} & \beta_{22}\beta_{32} & \beta_{23}\beta_{33} & \beta_{21}\beta_{32} + \beta_{31}\beta_{22} & \beta_{22}\beta_{33} + \beta_{32}\beta_{23} & \beta_{21}\beta_{33} + \beta_{31}\beta_{23} \\ \beta_{11}\beta_{31} & \beta_{12}\beta_{32} & \beta_{13}\beta_{33} & \beta_{31}\beta_{12} + \beta_{11}\beta_{32} & \beta_{32}\beta_{13} + \beta_{12}\beta_{33} & \beta_{11}\beta_{33} + \beta_{31}\beta_{13} \end{bmatrix} \quad (3.42)$$

3

and  $[R]^{-1}$  is evaluated as

$$\begin{bmatrix} \beta_{11}^2 & \beta_{21}^2 & \beta_{31}^2 & 2\beta_{11}\beta_{21} & 2\beta_{21}\beta_{31} & 2\beta_{11}\beta_{31} \\ \beta_{12}^2 & \beta_{22}^2 & \beta_{32}^2 & 2\beta_{12}\beta_{22} & 2\beta_{22}\beta_{32} & 2\beta_{12}\beta_{32} \\ \beta_{13}^2 & \beta_{23}^2 & \beta_{33}^2 & 2\beta_{13}\beta_{23} & 2\beta_{23}\beta_{33} & 2\beta_{13}\beta_{33} \\ \beta_{11}\beta_{12} & \beta_{21}\beta_{22} & \beta_{31}\beta_{32} & \beta_{21}\beta_{12} + \beta_{11}\beta_{22} & \beta_{31}\beta_{22} + \beta_{21}\beta_{32} & \beta_{31}\beta_{12} + \beta_{11}\beta_{32} \\ \beta_{12}\beta_{13} & \beta_{22}\beta_{23} & \beta_{32}\beta_{33} & \beta_{22}\beta_{13} + \beta_{12}\beta_{23} & \beta_{32}\beta_{23} + \beta_{22}\beta_{33} & \beta_{32}\beta_{13} + \beta_{12}\beta_{33} \\ \beta_{11}\beta_{13} & \beta_{21}\beta_{23} & \beta_{31}\beta_{33} & \beta_{21}\beta_{13} + \beta_{11}\beta_{23} & \beta_{31}\beta_{23} + \beta_{21}\beta_{33} & \beta_{31}\beta_{13} + \beta_{11}\beta_{33} \end{bmatrix} \quad (3.43)$$

A similar procedure can be carried out for the strain tensor.

$$[\epsilon_{i'j'}] = [M] [\epsilon_{ij}] [M]^T \quad (3.44)$$

where  $\epsilon_{i'j'}$  is the strain tensor in the principal directions and  $\epsilon_{ij}$  is the strain tensor in the global direction. This matrix equation can also be written in engineering form.

$$\begin{bmatrix} \epsilon_1 \\ \epsilon_2 \\ \epsilon_3 \\ 0 \\ 0 \\ 0 \end{bmatrix} = [T] \begin{bmatrix} \epsilon_x \\ \epsilon_y \\ \epsilon_z \\ \gamma_{xy} \\ \gamma_{yz} \\ \gamma_{xz} \end{bmatrix} \quad (3.45)$$

The shear strains ( $\gamma_{xy}$ ,  $\gamma_{yz}$  and  $\gamma_{xz}$ ) are the engineering shear strains, which are twice

the tensor shear strains.  $[T]$  is evaluated as

$$\begin{bmatrix} \beta_{11}^2 & \beta_{12}^2 & \beta_{13}^2 & \beta_{11}\beta_{12} & \beta_{12}\beta_{13} & \beta_{11}\beta_{13} \\ \beta_{21}^2 & \beta_{22}^2 & \beta_{23}^2 & \beta_{21}\beta_{22} & \beta_{22}\beta_{23} & \beta_{21}\beta_{23} \\ \beta_{31}^2 & \beta_{32}^2 & \beta_{33}^2 & \beta_{31}\beta_{32} & \beta_{32}\beta_{33} & \beta_{31}\beta_{33} \\ 2\beta_{11}\beta_{21} & 2\beta_{12}\beta_{22} & 2\beta_{13}\beta_{23} & \beta_{11}\beta_{22} + \beta_{21}\beta_{12} & \beta_{12}\beta_{23} + \beta_{22}\beta_{13} & \beta_{11}\beta_{23} + \beta_{21}\beta_{13} \\ 2\beta_{21}\beta_{31} & 2\beta_{22}\beta_{32} & 2\beta_{23}\beta_{33} & \beta_{21}\beta_{32} + \beta_{31}\beta_{22} & \beta_{22}\beta_{33} + \beta_{32}\beta_{23} & \beta_{21}\beta_{33} + \beta_{31}\beta_{23} \\ 2\beta_{11}\beta_{31} & 2\beta_{12}\beta_{32} & 2\beta_{13}\beta_{33} & \beta_{31}\beta_{12} + \beta_{11}\beta_{32} & \beta_{32}\beta_{13} + \beta_{12}\beta_{33} & \beta_{11}\beta_{33} + \beta_{31}\beta_{13} \end{bmatrix} \quad (3.46)$$

3

and  $[T]^{-1}$  is evaluated as

$$\begin{bmatrix} \beta_{11}^2 & \beta_{21}^2 & \beta_{31}^2 & \beta_{11}\beta_{21} & \beta_{21}\beta_{31} & \beta_{11}\beta_{31} \\ \beta_{12}^2 & \beta_{22}^2 & \beta_{32}^2 & \beta_{12}\beta_{22} & \beta_{22}\beta_{32} & \beta_{12}\beta_{32} \\ \beta_{13}^2 & \beta_{23}^2 & \beta_{33}^2 & \beta_{13}\beta_{23} & \beta_{23}\beta_{33} & \beta_{13}\beta_{33} \\ 2\beta_{11}\beta_{12} & 2\beta_{21}\beta_{22} & 2\beta_{31}\beta_{32} & \beta_{21}\beta_{12} + \beta_{11}\beta_{22} & \beta_{31}\beta_{22} + \beta_{21}\beta_{32} & \beta_{31}\beta_{12} + \beta_{11}\beta_{32} \\ 2\beta_{12}\beta_{13} & 2\beta_{22}\beta_{23} & 2\beta_{32}\beta_{33} & \beta_{22}\beta_{13} + \beta_{12}\beta_{23} & \beta_{32}\beta_{23} + \beta_{22}\beta_{33} & \beta_{32}\beta_{13} + \beta_{12}\beta_{33} \\ 2\beta_{11}\beta_{13} & 2\beta_{21}\beta_{23} & 2\beta_{31}\beta_{33} & \beta_{21}\beta_{13} + \beta_{11}\beta_{23} & \beta_{31}\beta_{23} + \beta_{21}\beta_{33} & \beta_{31}\beta_{13} + \beta_{11}\beta_{33} \end{bmatrix} \quad (3.47)$$

Consequently, the element coordinate system is converted from the global direction to the principal directions.

The constitutive relation in the  $x, y, z$  directions is

$$\begin{bmatrix} \epsilon_x \\ \epsilon_y \\ \epsilon_z \\ \gamma_{xy} \\ \gamma_{yz} \\ \gamma_{xz} \end{bmatrix} = [C] \begin{bmatrix} \sigma_x \\ \sigma_y \\ \sigma_z \\ \sigma_{xy} \\ \sigma_{yz} \\ \sigma_{xz} \end{bmatrix} \quad (3.48)$$

where  $[C]$  is the compliance matrix, which is written as

$$\begin{bmatrix} \frac{1}{E_x} & -\frac{\nu_{xy}}{E_x} & -\frac{\nu_{xz}}{E_x} & 0 & 0 & 0 \\ -\frac{\nu_{yx}}{E_y} & \frac{1}{E_y} & -\frac{\nu_{yz}}{E_y} & 0 & 0 & 0 \\ -\frac{\nu_{zx}}{E_z} & -\frac{\nu_{zy}}{E_z} & \frac{1}{E_z} & 0 & 0 & 0 \\ 0 & 0 & 0 & \frac{1}{G_{xy}} & 0 & 0 \\ 0 & 0 & 0 & 0 & \frac{1}{G_{yz}} & 0 \\ 0 & 0 & 0 & 0 & 0 & \frac{1}{G_{xz}} \end{bmatrix} \quad (3.49)$$

The substitution of (3.41) and (3.45) in (3.48) gives

$$[T]^{-1} \begin{bmatrix} \epsilon_1 \\ \epsilon_2 \\ \epsilon_3 \\ 0 \\ 0 \\ 0 \end{bmatrix} = [C][R]^{-1} \begin{bmatrix} \sigma_1 \\ \sigma_2 \\ \sigma_3 \\ 0 \\ 0 \\ 0 \end{bmatrix} \quad (3.50)$$

3

which can be written as

$$\begin{bmatrix} \epsilon_1 \\ \epsilon_2 \\ \epsilon_3 \\ 0 \\ 0 \\ 0 \end{bmatrix} = [T][C][R]^{-1} \begin{bmatrix} \sigma_1 \\ \sigma_2 \\ \sigma_3 \\ 0 \\ 0 \\ 0 \end{bmatrix} \quad (3.51)$$

Consequently, the compliance matrix  $[C]'$  in the principal directions is

$$[C]' = [T][C][R]^{-1} \quad (3.52)$$

which is written as

$$[C]' = \begin{bmatrix} \frac{1}{E_1} & -\frac{\nu_{12}}{E_1} & -\frac{\nu_{13}}{E_1} & 0 & 0 & 0 \\ -\frac{\nu_{21}}{E_2} & \frac{1}{E_2} & -\frac{\nu_{23}}{E_2} & 0 & 0 & 0 \\ -\frac{\nu_{31}}{E_3} & -\frac{\nu_{32}}{E_3} & \frac{1}{E_3} & 0 & 0 & 0 \\ 0 & 0 & 0 & \frac{1}{G_{12}} & 0 & 0 \\ 0 & 0 & 0 & 0 & \frac{1}{G_{23}} & 0 \\ 0 & 0 & 0 & 0 & 0 & \frac{1}{G_{13}} \end{bmatrix} \quad (3.53)$$

The principal direction Young's moduli are reduced in  $[C]'$  by dividing  $C'[1,1]$  or  $C'[3,3]$  by the stiffness reduction factor <sup>2</sup>.

In every calculation step, the most loaded element is selected. Young's modulus of this element is reduced to, for example, 90% of its previous value. Elements with a stiffness smaller than a certain value, for example 0.01 N/mm<sup>2</sup>, are no longer

<sup>2</sup>Note that the value of the stiffness reduction factor is between 0 and 1. A large stiffness reduction factor value means a small stiffness reduction.

considered to prevent the same element stiffness from being reduced in every step. Data on the failure type is recorded for each computational step.

The reduced compliance matrix  $[C]''$  is rotated back to the element coordinate system by

$$[C]'' = [T]^{-1} [C]'' [R] \quad (3.54)$$

The elements of matrix  $[C]''$  are used to update the element material properties.

It can occur that the smallest and the largest principal stress value are almost the same. In this case either of these directions is the critical direction. The algorithm picks only one of these directions; it picks the one that is slightly larger. It can also occur that the principal directions interchange between the beginning and the end of a load step. This can happen if the principal stresses are approximately the same. If a purely rotating crack model were used, the material directions would rotate  $90^\circ$ , which clearly is not realistic. The proposed algorithm does not have this problem because it does not relate the stiffness to the local principal directions as in a purely rotating crack model. In every load step the algorithm makes updates to the stiffnesses in the global x, y, z coordinate system.

In addition, the fixed smeared crack model can be also used in this method. In this case, the damage direction is rotated at the initial damage stage. After the certain damage stage based on the maximum principal direction's angle or Young's moduli,  $[T]$  and  $[R]$  are no longer updated. Therefore, the damage direction is fixed. Young's moduli are updated following the previous procedure, but Poisson's ratios and shear moduli are updated according to Eq (2.1) and (2.2) by a reduced shear retention factor. A constant shear retention factor can be also adopted. Below is a discussion of Eq. (2.1).

In [12][129], it is assumed that

$$\left\{ \begin{array}{l} \nu_{21} = \nu_{31} = \frac{\nu_0}{E_0} E_1 \\ \nu_{12} = \nu_{32} = \frac{\nu_0}{E_0} E_2 \\ \nu_{13} = \nu_{23} = \frac{\nu_0}{E_0} E_3 \end{array} \right. \quad (3.55)$$

where  $E_0$  and  $\nu_0$  are the initial Young's modulus and Poisson's ratio.

In the material model used in this dissertation, only diagonal terms such as  $\frac{1}{E_1}$  are reduced to represent damage. All off-diagonal terms such as  $-\frac{\nu_{21}}{E_1}$  are kept constant. From this, it can be derived that

$$\left\{ \begin{array}{l} v_{21} = v_{31} = v_0 \prod_{i=1}^n \frac{E_{1(i)}}{E'_{1(i)}} \\ v_{12} = v_{32} = v_0 \prod_{i=1}^n \frac{E_{2(i)}}{E'_{2(i)}} \\ v_{13} = v_{23} = v_0 \prod_{i=1}^n \frac{E_{3(i)}}{E'_{3(i)}} \end{array} \right. \quad (3.56)$$

where  $E'_{1(i)}$ ,  $E'_{2(i)}$ ,  $E'_{3(i)}$  are the principal direction Young's moduli of the current step  $i$  before updating in  $[C]^{'}_{(i)}$  and  $E_{1(i)}$ ,  $E_{2(i)}$ ,  $E_{3(i)}$  are the updated principal direction Young's moduli of the current step  $i$  in  $[C]^{''}_{(i)}$ .

It is assumed that the principal directions change gradually step-by-step in the rotating crack model, which means that the principal direction Young's moduli ( $E'_{1(i)}$ ,  $E'_{2(i)}$ ,  $E'_{3(i)}$ ) of the current step before updating are **approximately** the same as the principal direction Young's moduli ( $E_{1(i-1)}$ ,  $E_{2(i-1)}$ ,  $E_{3(i-1)}$ ) of the previous step after updating. These are evaluated to

$$\left\{ \begin{array}{l} v_{21(n)} = v_{31(n)} = v_0 \prod_{i=1}^n \frac{E_{1(i)}}{E'_{1(i)}} \approx v_0 \prod_{i=1}^n \frac{E_{1(i)}}{E_{1(i-1)}} = \frac{v_0}{E_0} E_{1(n)} \\ v_{12(n)} = v_{32(n)} = v_0 \prod_{i=1}^n \frac{E_{2(i)}}{E'_{2(i)}} \approx v_0 \prod_{i=1}^n \frac{E_{2(i)}}{E_{2(i-1)}} = \frac{v_0}{E_0} E_{2(n)} \\ v_{13(n)} = v_{23(n)} = v_0 \prod_{i=1}^n \frac{E_{3(i)}}{E'_{3(i)}} \approx v_0 \prod_{i=1}^n \frac{E_{3(i)}}{E_{3(i-1)}} = \frac{v_0}{E_0} E_{3(n)} \end{array} \right. \quad (3.57)$$

Poisson's ratios in the updated principal compliance matrix ( $C''[1,2]$ ,  $C''[1,3]$ ,  $C''[2,1]$ ,  $C''[2,3]$ ,  $C''[3,1]$  and  $C''[3,2]$ ) agree with calculations by Eq (3.55). The approximation may be less accurate for large crack rotations (i.e., large stiffness reductions). However, this needs to be further investigated. Eq (3.55) seems reasonable for the situation in which when a crack rotates 90 degrees, then  $v_{21}$  changes from a damage value to the initial value.

In the fixed smeared crack model, the fixed direction Young's moduli ( $E'_{n(i)}$ ,  $E'_{s(i)}$ ,  $E'_{t(i)}$ ) of the current step before updating in  $[C]^{'}_{(i)}$  are **always** the same as the fixed direction Young's moduli ( $E_{n(i-1)}$ ,  $E_{s(i-1)}$ ,  $E_{t(i-1)}$ ) of the previous step after updating in  $[C]^{''}_{(i-1)}$ . Therefore, Eq (3.55) is absolutely correct.

### 3.7. APPROXIMATION OF PRINCIPAL DIRECTION YOUNG'S MODULI

During an SLA computation, the values of  $\sigma_1, \sigma_2, \sigma_3$  are readily available for each integration point. However, the principal direction Young's moduli  $E_1, E_2, E_3$

need to be recomputed for the rotating crack in Section 3.6. This computation is expensive and needs to be performed for all integration points and for every SLA cycle. In this section, Eq. (3.55) is used to calculate an approximate principal direction stiffness to accelerate the procedure for selecting the critical element. However, the selection procedure can also be based on the accurate stiffness of principal directions computed by the rotation matrix in Section 3.6. Note that the Young's moduli of the critical element in principal directions are still computed by the rotation matrix in Section 3.6 after the critical element has been chosen.

The relation between the stiffness and strength follows from the stress-strain curve. Typically, stress-strain curves are determined in uniaxial experiments (Figure 3.11(a)).

During SLA, the three-dimensional stress-strain state of a material point has three principal directions, three principal stresses ( $\sigma_1, \sigma_2, \sigma_3$ ) and three principal strains ( $\varepsilon_1, \varepsilon_2, \varepsilon_3$ ). The largest principal stress and the corresponding strain govern tension failure. The point  $(\varepsilon_1, \sigma_1)$  can be plotted on the graph of the stress-strain curve (Figure 3.11(b)). In general, this point is not on the line of the reduced stiffness. This is due to the stresses in the other principal directions and the corresponding lateral contraction. Occasionally, the strain  $\varepsilon_1$  can even be negative, which forces the point  $(\varepsilon_1, \sigma_1)$  completely left of the curve.

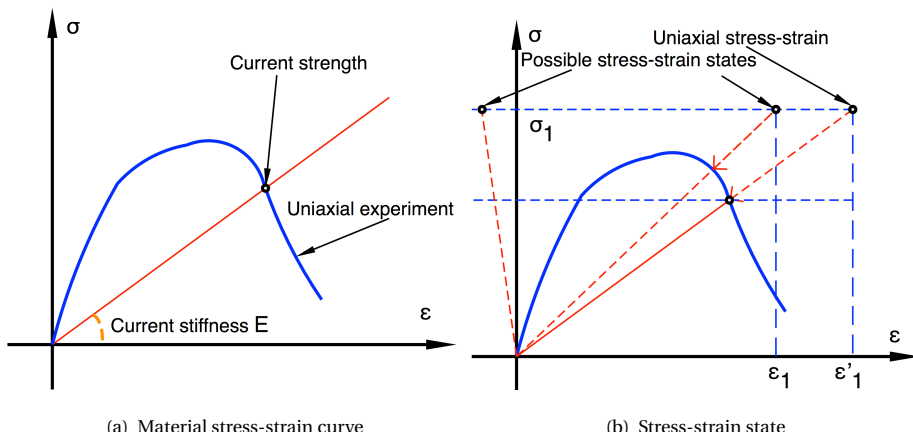


Figure 3.11: Material stiffness

In SLA, the reference load and associated stresses are scaled such that the fail-

ure criterion is fulfilled. Figure 3.11(b) shows that linearly scaling the stresses and strains does not produce a correct point on the damaged material curve. In some situations, the point scales to the origin, which is clearly unrealistic. If we do not know the current stiffness, we do not know the strength. If we do not know the strength, we cannot scale the load.

The solution is to remove the lateral contraction due to the stresses in the other principal directions. This changes the strain  $\epsilon_1$  into  $\epsilon'_1$ , and then the stress-strain point  $(\epsilon'_1, \sigma_1)$  is on the line of reduced stiffness (Figure 3.11(b)). This solution is not just a computational strategy; it is an important part of the description of material behaviour.

Hooke's law of an orthotropic material reads

$$\left\{ \begin{array}{l} \epsilon_1 = \frac{\sigma_1}{E_1} - \frac{\nu_{12}}{E_2} \sigma_2 - \frac{\nu_{13}}{E_3} \sigma_3 \\ \epsilon_2 = \frac{-\nu_{21}}{E_1} \sigma_1 + \frac{\sigma_2}{E_2} - \frac{\nu_{23}}{E_3} \sigma_3 \\ \epsilon_3 = \frac{-\nu_{31}}{E_1} \sigma_1 - \frac{\nu_{32}}{E_2} \sigma_2 + \frac{\sigma_3}{E_3} \end{array} \right. \quad (3.58)$$

The substitution of (3.55) in (3.58) gives

$$\left\{ \begin{array}{l} \epsilon_1 = \frac{\sigma_1}{E_1} - \frac{\nu_0}{E_0} \sigma_2 - \frac{\nu_0}{E_0} \sigma_3 \\ \epsilon_2 = \frac{-\nu_0}{E_0} \sigma_1 + \frac{\sigma_2}{E_2} - \frac{\nu_0}{E_0} \sigma_3 \\ \epsilon_3 = \frac{-\nu_0}{E_0} \sigma_1 - \frac{\nu_0}{E_0} \sigma_2 + \frac{\sigma_3}{E_3} \end{array} \right. \quad (3.59)$$

From (3.59), the stiffness is solved

$$\left\{ \begin{array}{l} E_1 = \frac{\sigma_1}{\epsilon_1 + \frac{\nu_0}{E_0} \sigma_2 + \frac{\nu_0}{E_0} \sigma_3} \\ E_2 = \frac{\sigma_2}{\epsilon_2 + \frac{\nu_0}{E_0} \sigma_1 + \frac{\nu_0}{E_0} \sigma_3} \\ E_3 = \frac{\sigma_3}{\epsilon_3 + \frac{\nu_0}{E_0} \sigma_1 + \frac{\nu_0}{E_0} \sigma_2} \end{array} \right. \quad (3.60)$$

It can be seen that Young's modulus in a certain direction depends not only on the stress and strain in the current direction but also on other directions as well as the initial ratio of Young's modulus and Poisson's ratio.

From Eq. (3.60),  $\epsilon'_1 = \frac{\sigma_1}{E_1}$  etc. are solved

$$\left\{ \begin{array}{l} \epsilon'_1 = \epsilon_1 + \frac{\nu_0}{E_0} \sigma_2 + \frac{\nu_0}{E_0} \sigma_3 \\ \epsilon'_2 = \epsilon_2 + \frac{\nu_0}{E_0} \sigma_1 + \frac{\nu_0}{E_0} \sigma_3 \\ \epsilon'_3 = \epsilon_3 + \frac{\nu_0}{E_0} \sigma_1 + \frac{\nu_0}{E_0} \sigma_2 \end{array} \right. \quad (3.61)$$

The uniaxial strains  $\epsilon'_1$  and  $\epsilon'_3$  are used to compute principal direction Young's moduli in Section 3.5.

### 3.8. DISCUSSION

The main advantage of SLA is its robustness; the algorithm is damage driven and via a sequence of critical events, it finds the correct load-displacement path. Disadvantages of SLA are the considerable computation time required, sensitivity to the size of stiffness decrements and difficulties with non-proportional loading.

Several improvements are presented in this chapter. Multiple failure criteria are available for SLA to consider the situation of tension, compression or shear. The orthotropic damage model is formulated based on the rotating smeared crack model. An improved saw-tooth model is proposed, which is governed by the stiffness reduction factor rather than the saw-tooth number.



# 4

## IMPROVEMENTS TO NON-PROPORTIONAL LOADING IN SLA

In static structural analysis, loads are often applied together (proportional loading). However, the load order can be important, for example first prestress on a concrete beam and subsequent removal of the formwork, which activates self-weight. Other examples are pushover loading of a masonry wall with permanent overburden and wind load after snow load on a roof structure. In general, non-proportional loading is a situation in which some loads are kept constant while others vary in time.

SLA has difficulties with non-proportional loading due to the total approach. In non-proportional SLA, the first strategy attempted was adding the extra stresses of the initial load into a proportional SLA scheme [12]. Instead, the applied single load  $F_{ref}$  in proportional SLA is replaced by a combination of the initial load  $F_{ini}$  and the current load  $F_{cur}$  in this chapter, which has been published in [132]. A major difference from the previous approach is that the initial stresses are recomputed for the damaged stiffness rather than the initial undamaged stiffness.

The algorithm of this chapter works well for the prestressed, simply supported, concrete-beam test in [12]. However, it failed to find a solution after certain SLA cycles when the prestress was increased from 1 MPa to 5 MPa and subsequently to 10 MPa. In addition, geometric non-linearity cannot be considered due to the total approach. Therefore, SLA is extended to an incremental approach in Chapter 5. Nevertheless, the algorithm of this chapter is promising because it is simple and relatively more robust than the conventional N-R method with standard arc-length control based on the tests. From a mathematical point of view, this algorithm can be perfected for non-proportional loading in SLA.

## 4

## 4.1. ALGORITHM PRINCIPLE

In proportional SLA, there is a single load that is the same in every analysis step. After the step, it is scaled by a factor  $\lambda$ , which is determined by the failure criterion for the most critical element. For example, the current load  $F_{cur} = \lambda F_{ref}$ , where  $F_{ref}$ , is a reference load. In non-proportional SLA, an extra initial load  $F_{ini}$  is applied simultaneously with  $F_{ref}$ . The total load is  $F_t = \lambda F_{ref} + F_{ini}$ . The target is to keep  $F_{ini}$  constant while  $F_{ref}$  is scaled. This can be written as  $F_t = \lambda(F_{ref} + F_{ini}/\lambda)$ . At the beginning of a load cycle,  $\lambda$  is unknown; therefore, it is estimated by  $v$  ( $\lambda$  of the previous cycle or 1 for the first cycle), which is consequently  $F_t = \lambda_1(F_{ref} + F_{ini}/v_1)$ . After one linear elastic analysis, a better estimate of  $v$  can be made  $v_2 = \lambda_1$ . It will be shown that the exact solution can be found in just two linear elastic analyses by an interpolation procedure such that  $v$  and  $\lambda$  become almost the same and the solution to a cycle is found.

Summarizing, in every load cycle the initial load is divided by a variable  $v$ , after which linear elastic analysis is performed and the total load is scaled by a factor  $\lambda$ . This procedure is repeated until at the end of each load cycle  $v = \lambda$ , such that the initial load remains constant.

## 4.2. PROPOSED NON-PROPORTIONAL LOADING PROCEDURE IN SLA

Consider a structure with two loads,  $F_{ini}$  and  $F_{cur}$ . The loads are applied one after the other. Load  $F_{ini}$  is applied first and kept constant while load  $F_{cur}$  is subse-

quently added and increased.

1. Apply loads  $F_{ini}/v_1$  and  $F_{ref}$  to the structure, replacing the previous loading.  $v_1$  is estimated, for example, by  $\lambda$  of the previous cycle or 1 for the first cycle (this is elaborated in section 4.3).
2. Perform linear elastic analysis.
3. Consider all elements and find the critical element and the load factor  $\lambda$  (this is elaborated in section 3.4, 3.5, 3.7).
4. Apply loads  $F_{ini}/v_2$  and  $F_{ref}$  to the structure, replacing the previous loading.  $v_2 = \lambda_1$  (this is elaborated in section 4.3).
5. Perform linear elastic analysis.
6. Consider all elements and find the largest stress. The load factor  $\lambda_2$  is basically failure stress over largest stress.
7. Compute the final  $\lambda$  of the load step.  $\lambda_3 = v_3 = \frac{-v_1\lambda_2 v_2 + \lambda_1\lambda_2 v_2 + \lambda_1 v_1 v_2 - \lambda_1 v_1 \lambda_2}{v_1\lambda_2 - \lambda_1 v_2}$  (this is elaborated in section 4.3).

4

Now the situation is that if we multiply the load by  $\lambda_3$ , then the structure is loaded such that the material just fails at a certain location and the first load is  $F_{ini}$  and the second load is  $\lambda_3 F_{ref}$ .

8. Reduce the stiffness and strength of the critical element based on the saw-tooth model (this is elaborated in section 3.6).
9. Scale output results by  $\lambda_3$ .
10. Restart at step 1 with the reduced stiffness and strength from current cycle.

### 4.3. CALCULATION OF INITIAL-LOAD FACTOR V

In every SLA computation step, there is a linear relation between the force magnitudes and relevant stresses and strains.

This can be written as

$$F = \lambda_1 \left( \frac{aF_{ini}}{v_1} + bF_{ref} \right) \quad (4.1)$$

where  $F$  is a cross-section force at some location of the structure and  $a$  and  $b$  represent the structure.  $F$  is equal to the local capacity so that the correct  $\lambda$  is applied. The equation can be rewritten.

$$\frac{1}{\lambda_1} = \frac{1}{F} \left( \frac{aF_{ini}}{\nu_1} + bF_{ref} \right) \quad (4.2)$$

where  $1/\lambda$  and  $1/\nu$  have a linear relation (Figure 4.1). Just two calculation steps are sufficient to solve  $\lambda$  and  $\nu$ .

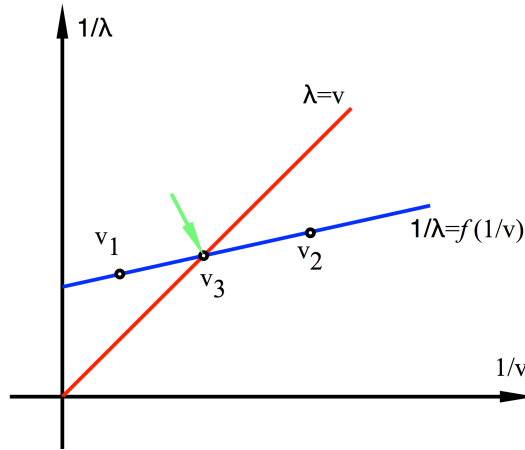


Figure 4.1: Function of initial-load factor  $\nu$  related to scaling factor  $\lambda$

The next step is similar, so

$$\frac{1}{\lambda_2} = \frac{1}{F} \left( \frac{aF_{ini}}{\nu_2} + bF_{ref} \right) \quad (4.3)$$

where  $a$ ,  $b$  and  $F$  are not changed since Young's moduli are not modified.  $F_{ini}$  remains the same during the scaling back step when

$$\lambda_3 = \nu_3 \quad (4.4)$$

Therefore,

$$\frac{1}{\lambda_3} = \frac{1}{F} \left( \frac{aF_{ini}}{\nu_3} + bF_{ref} \right) \quad (4.5)$$

From Eqs. (4.2), (4.3) and (4.5),  $\lambda_3$  and  $\nu_3$  can be solved.

$$\lambda_3 = \nu_3 = \frac{-\nu_1 \lambda_2 \nu_2 + \lambda_1 \lambda_2 \nu_2 + \lambda_1 \nu_1 \nu_2 - \lambda_1 \nu_1 \lambda_2}{\lambda_1 \nu_2 - \nu_1 \lambda_2} \quad (4.6)$$

If it happens that  $\lambda_2$  is almost equal to  $v_1$ , there is no need to sub-calculate  $\lambda_3$ . The condition for this is

$$\left| \frac{\lambda_2 - v_1}{v_1} \right| \ll 1\% \quad (4.7)$$

The equation can be simplified for special situations when all forces are applied at the same position and in the same direction.

$$\frac{1}{\lambda_1} = \frac{a}{F} \left( \frac{F_{ini}}{v_1} + F_{ref} \right) \quad (4.8)$$

where  $F$  is real total failure force for this step. Therefore, just one calculation step is needed to obtain the final  $\lambda$  and  $v$ .

4

$$\lambda_2 = v_2 = \frac{F_{ref} \lambda_1 v_1 + F_{ini} \lambda_1 - F_{ini} v_1}{F_{ref} v_1} \quad (4.9)$$

## 4.4. TEST CASE OF A SIMPLY SUPPORTED CONCRETE BEAM

An experiment by Hordijk [124] is used for testing, which is a simply supported concrete beam with two point loads at the top (Figure 4.2). The original specimen is a symmetric notched beam of total length 500 mm; span 450 mm; height 100 mm; thickness 50 mm and notch depth 10 mm. The distance between the loading points in the symmetric four-point loading scheme is 150 mm. However, the notch is removed and prestress on both ends of the beam is applied during analysis to test the non-proportional loading algorithm of SLA. This was also used in [12] [132]. The analysis is performed in ANSYS and ABAQUS. The concrete element is plane183, the size of which is 5 mm.

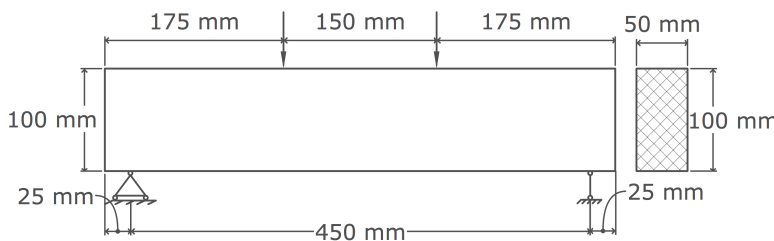


Figure 4.2: Test model dimensions

Three load cases are considered.

1. A vertical initial load D at the top. This is applied as two-point loads of 1 kN.

2. A horizontal initial load  $H$  at both ends of the beam. This is also applied as a stress of 1 MPa over the total area of the beam ends.
3. A vertical current load  $L$  at the top. This is applied in the same way as load  $D$ . The magnitude of this load is increased to failure and afterwards reduced.

Two load combinations are considered (Figure 4.3).

1. Initial load  $D$  plus current load  $L$  (both in the same direction at the same location) in Figure 4.3(a).
2. Initial load  $H$  and current load  $L$  (in different directions and at different locations) in Figure 4.3(b).

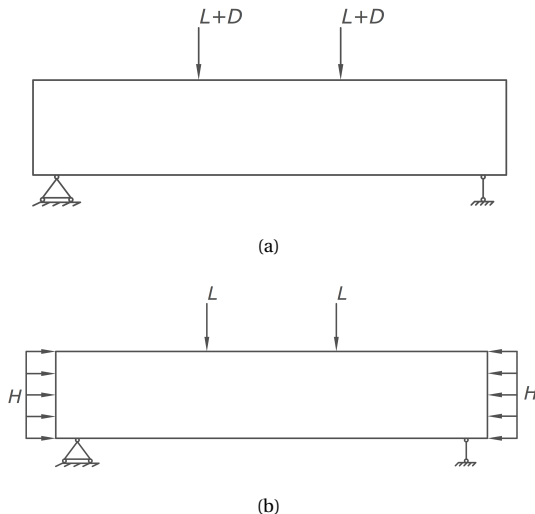


Figure 4.3: FEM model with load combinations

## 4.5. MATERIAL PROPERTIES AND FEM MODEL

This test considers softening for tension (Figure 4.4). The concrete properties are Young's modulus  $E = 32000$  MPa, Poisson's ratio  $\nu = 0.2$ , tensile strength  $f_t = 3$  MPa and fracture energy  $G_f = 0.06$  N/mm. The compressive behaviour is elastic. Eq. (4.10) [11] is used to determine ultimate strain  $\epsilon_u$  for different element sizes. Figure 4.4 shows the colour range of the maximum principal strain contours.

$$\epsilon_u = \frac{2G_f}{f_t h} \quad (4.10)$$

where the crack band width  $h$  is related to the element size. Eight-node plane-stress elements are used. The element size is 5 mm. For the square linear finite elements of the present example,  $h$  is suggested as being equal to the length of the size of the finite element. The plane element used in ABAQUS is CPS8R [145], which is an eight-node biquadratic plane-stress quadrilateral with reduced integration. The plane element used in ANSYS is PLANE183 [146]. It is a higher-order, 2-D, eight-node element. The integration point scheme for both element types is 2x2, however ANSYS averages the stress and strain of these four integration points as one element result in the post-processing. The stiffness reductions in SLA apply to the whole element. Therefore, the ultimate tensile strain of the ANSYS model is half that of the ABAQUS model.

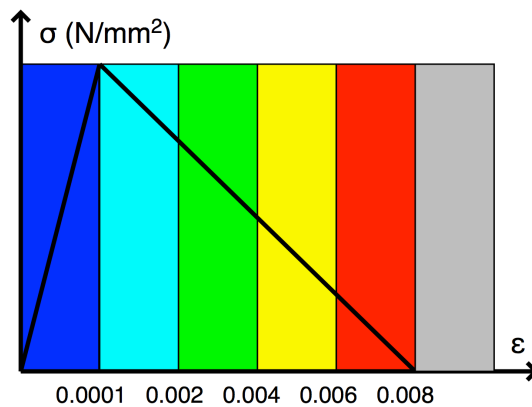


Figure 4.4: Tensile stress-strain curve and contour colour range for the concrete

Figure 4.5 shows the stiffness reductions when Young's modulus is sequentially reduced to 90% of the previous value.

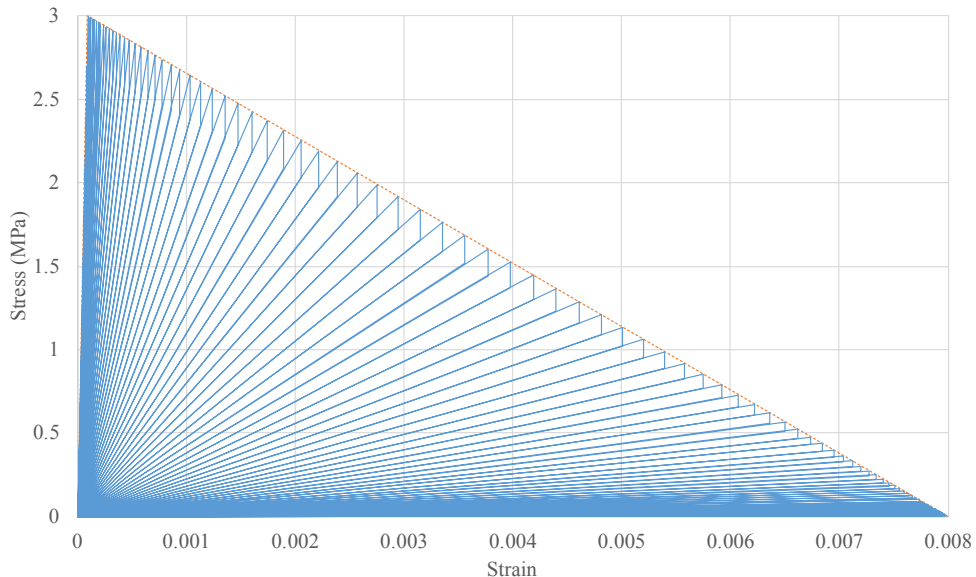


Figure 4.5: Sequentially reduced stiffness to 90% of the previous value

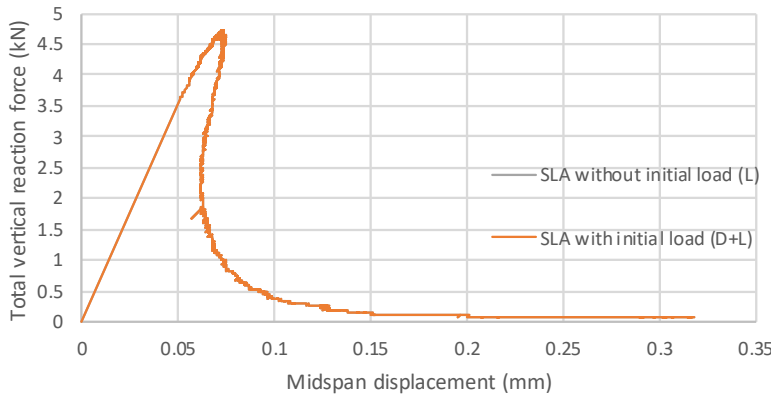
Analyses were performed by 1) standard N-R with arc length control in ABAQUS and 2) SLA in ANSYS [132]. The same material properties, element sizes (5 mm) and structural model were used in all analyses (Figure 4.4). In SLA and ISLA, the rotating smeared crack model was used. In N-R, the concrete damaged plasticity model was used to simulate concrete behaviour. The parameters inputted for this model are: dilation angle is 30°, eccentricity is 0.1,  $f_{b0}/f_{c0} = 1.16$ ,  $K = 0.667$ , and viscosity parameter is 0, which are default values [145].

## 4.6. ANALYSIS AND COMPARISON OF THE RESULTS

The two load combinations were analysed. For combination one, two SLA analyses with different loads were performed, and the results were compared. For the second combination, SLA and an arc-length control analysis were performed, and the results were compared.

Two analyses were performed. In the first analysis, the beam was loaded only by force  $L$  at the top, which was increased until collapse. In the second analysis, the beam was first loaded by force  $D = 1$  kN at the top. Subsequently, force  $L$  was added to  $D$  at the top.  $L$  was increased until collapse.

The total force-displacement curves are almost identical (Figure 4.6), and the maximum error of total load is less than 1%.



4

Figure 4.6: Initial load  $D$  and current load  $L$  were applied at the same position in the same direction (load combination one). The curves are on top of each other.

The horizontal pressure  $H$  at the end of the beam is 1 MPa. The resultant current load  $L$  is in the vertical direction, and the horizontal pressure  $H$  is in the horizontal direction. The SLA results fit well with arc-length control analysis results before the peak (Figure 4.7). The differences after the peak mainly result from different material models between SLA and arc-length control analysis as well as using average element results and the saw-tooth model's strength overshoot in SLA. After the peak, arc-length control analysis suffers divergence problems while SLA still remains robust. The prestress is "constant", ranging from 0.99 to 1.01 MPa (Figure 4.8). Further, the initial-load factors  $\nu$  vary together with the current load factors  $\lambda$ , with almost the same values (Figure 4.9). Compared with the no prestress result in Figure 4.6, the prestress improves the structural stiffness and its capacity. It can be observed that the displacement is reduced at the same reaction force before the peak, and the ultimate capacity increases from around 4.7 kN to 6.0 kN (Figure 4.10). This is caused by failure behaviour combined with bending and shear. In addition, prestress enhances the shear capacity.

In Figure 4.11, it can be seen that cracks are concentrated around the middle of the beam. The structure meets the maximum load when cracks extend to the middle height of the beam and one element's maximum principal strain goes to the green zone. The two cracks are almost symmetrical. However, after the peak, only

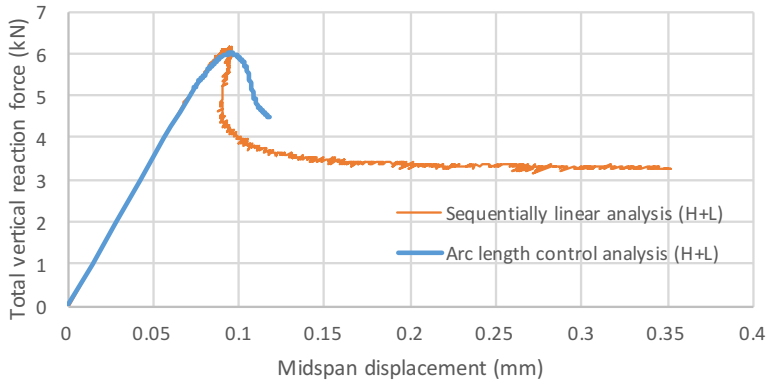


Figure 4.7: Load-displacement curves of load combination two

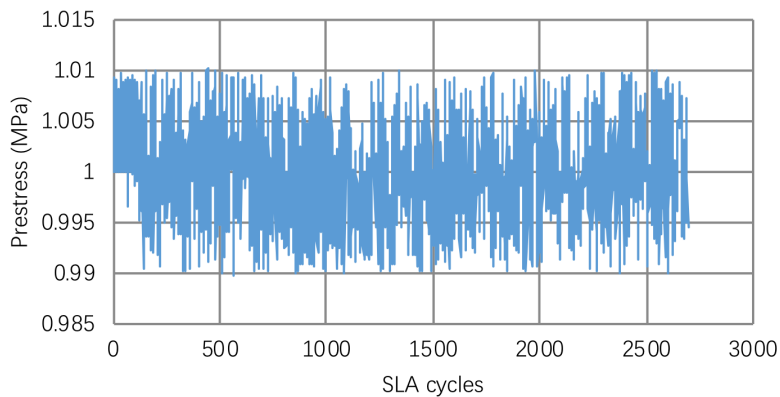


Figure 4.8: Prestress in the steps of SLA

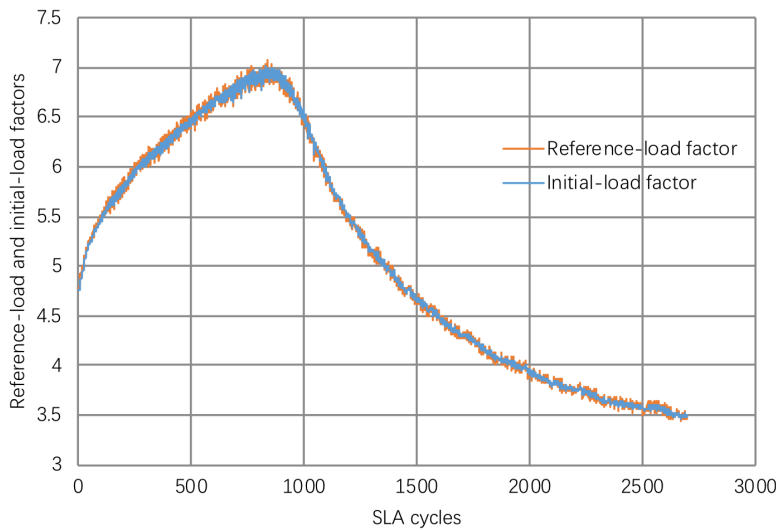


Figure 4.9: Constant-load factor  $\nu$  and live-load factor  $\lambda$  comparison. The curves overlap.

4

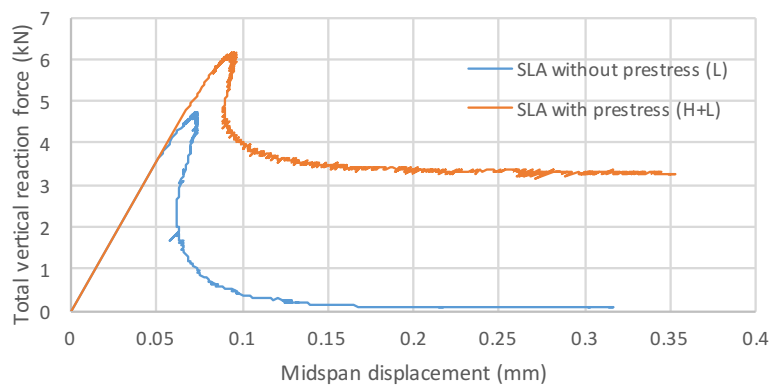
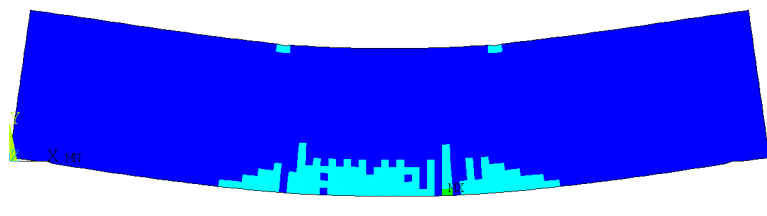
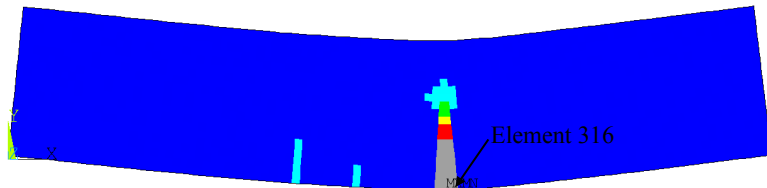


Figure 4.10: Prestress comparison for midspan point on concrete beam test

the right-hand cracks continue developing. A reaction force plateau occurs in Figure 4.7 when the bottom part of the crack meets the ultimate strain. The crack patterns align well with arc-length control results at the peak load (Figure 4.12). Nevertheless, the arc-length control cracks remain symmetrical after the peak while the SLA cracks localize at one side, which is more realistic compared with the experiment. This is because in reality, there is no absolutely symmetrical structure and structures always have imperfections. Eventually, cracks develop to the top of the beam, which prevents the structure from carrying more load. Moreover, there is no compressive damage during the whole loading procedure, which also demonstrates that the orthotropic model works well. The damages basically develop only in the horizontal direction (Table 4.1). The shear modulus is also reduced automatically due to the decrease of Young's modulus.



(a) Maximum principal strain at the peak

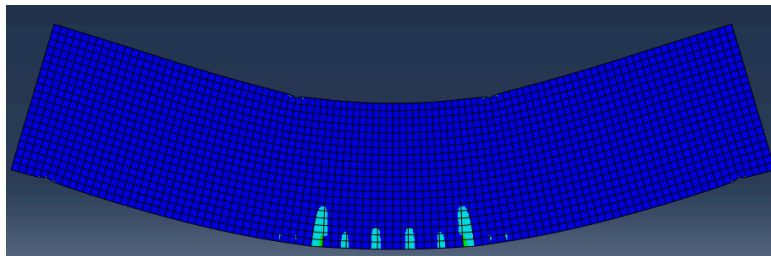


(b) Maximum principal strain after the peak

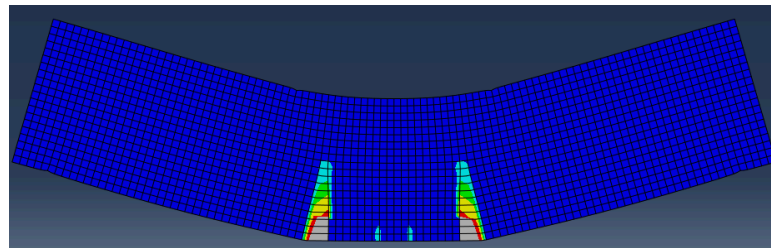
Figure 4.11: Maximum principal strain contour of SLA

Ex	Ey	Ez	Gxy
32000	32000	32000	13333.333
28800.001	32000	32000	13333.333
28851.541	31999.714	32000	13311.414
26018.092	31999.386	32000	13286.824
23467.793	31999.005	32000	13259.025
21166.375	31998.65	32000	13230.901
19094.763	31998.222	32000	13198.575
17224.998	31997.809	32000	13165.293
15537.75	31997.4	32000	13130.599
14019.009	31996.887	32000	13089.959
12648.471	31996.36	32000	13046.887
11411.927	31995.807	32000	13000.723
10296.483	31995.212	32000	12950.716
9290.454	31994.559	32000	12895.991
8383.255	31993.826	32000	12835.517
7565.312	31992.986	32000	12768.055
6826.449	31992.151	32000	12698.017
6160.586	31991.153	32000	12618.358
5559.447	31990.104	32000	12533.506
5016.936	31988.97	32000	12441.952
4526.734	31987.863	32000	12348.025
4084.211	31986.706	32000	12248.514
3684.041	31985.682	32000	12151.351
3322.575	31984.708	32000	12053.153
2996.529	31983.658	32000	11947.531
2703.5	31982.047	32000	11812.801

Table 4.1: Example of the stiffness reduction of element 316 marked in Figure 4.11



(a) Maximum principal strain at the peak



(b) Maximum principal strain after the peak

Figure 4.12: Maximum principal strain contour of the arc-length method

## 4.7. TEST CASE OF INCREASED PRESTRESS

This section employs the same FEM model as previous tests, but the applied prestress is increased from 1 MPa to 5 MPa and subsequently to 10 MPa.

When the prestress of the test case increases from 1 MPa to 5 MPa, at the beginning, the initial-load factor  $\nu$  can be adjusted to almost equal to the current load factor  $\lambda$ , as shown in Figure 4.13. However, after several cycles, the initial load factor  $\nu$  cannot be adjusted to equal the live load factor  $\lambda$ , as shown in Figure 4.14. It appears that the algorithm of non-proportional loading in SLA [132] as well as [12] is suitable only for weakly non-linear situations.

Similar results can be seen when the prestress is increased to 10 MPa. Compared with the prestress adjustment procedure before SLA fails to continue in Figure 4.15, the ratio between prestress factor  $\nu$  and live-load factor  $\lambda$  cannot meet 1 for SLA, as shown in Figure 4.16.

However, the proposed algorithm is still better than the N-R method with arc-length control. Figure 4.17 shows the force-displacement diagrams for 5 MPa prestress of N-R arc-length control and SLA. N-R arc-length control stops at a displace-

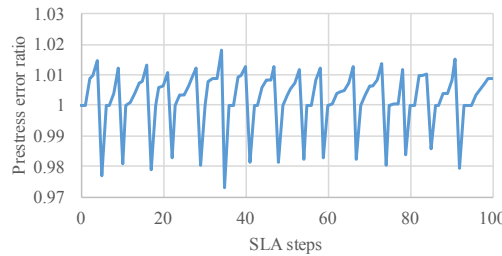


Figure 4.13: Prestress adjusting ratio  $\nu/\lambda$  for SLA analysis: The first 100 cycles are shown as an example of convergence to the correct value.

4

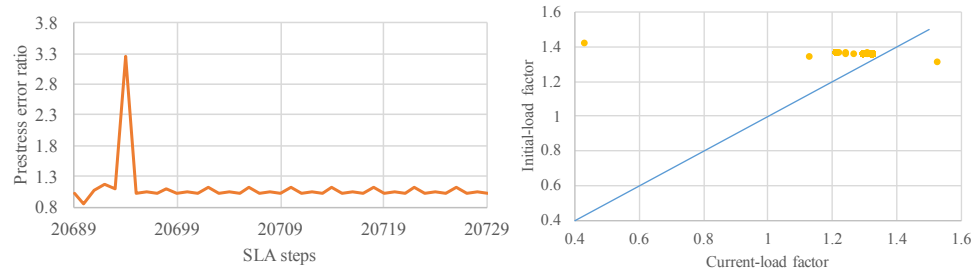


Figure 4.14: Prestress adjusting ratio  $\nu/\lambda$  for SLA analysis: 41 cycles are shown. All shown cycles fail to converge. (The peak has no particular meaning.)

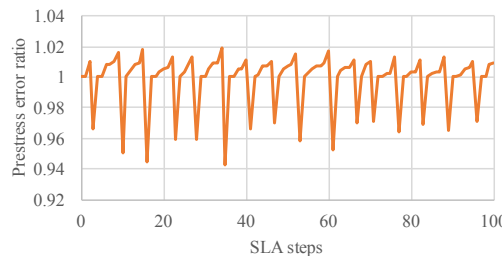


Figure 4.15: Prestress adjustment ratio  $\nu/\lambda$  for SLA analysis: The first 100 cycles are shown as an example of convergence to the correct value.

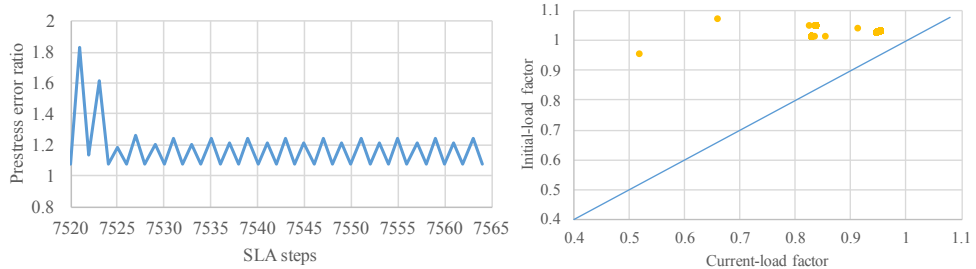


Figure 4.16: Prestress adjustment ratio  $v/\lambda$  for SLA analysis: 41 cycles are shown. All shown cycles fail to converge.(The peak has no particular meaning.)

4

ment of 1.1 mm while N-R arc length control can continue up to 1.8 mm. Figure 4.18 shows the reaction force-displacement diagrams for 10 MPa prestress of SLA and N-R arc-length control. They overlap in the beginning of the curves, but N-R arc length still diverges before SLA. Detailed results can be seen in Chapter 8.

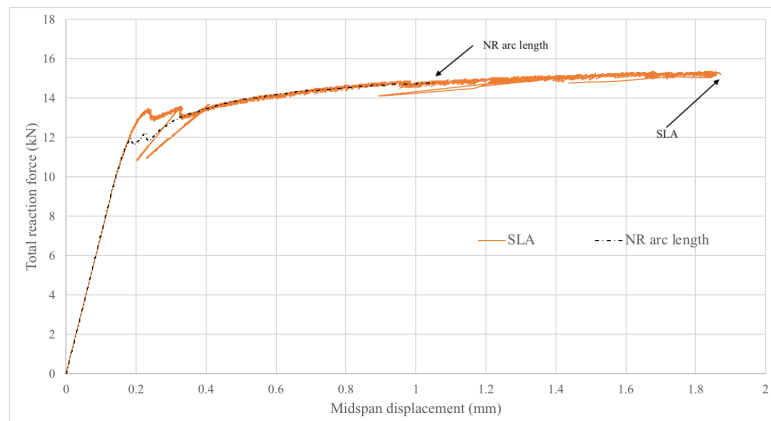


Figure 4.17: Reaction force-displacement diagrams for 5 MPa prestress test

## 4.8. DISCUSSION

This chapter focuses on non-proportional loading. The proposed algorithm for SLA of static non-proportional loading is simple, accurate, realistic and efficient. Since only an extra initial load is added to the original proportional loading SLA in [132], this algorithm can be easily applied to any element type (solid, plate, shell), failure criterion, load case (wind, snow, self-weight) or load combination. For non-

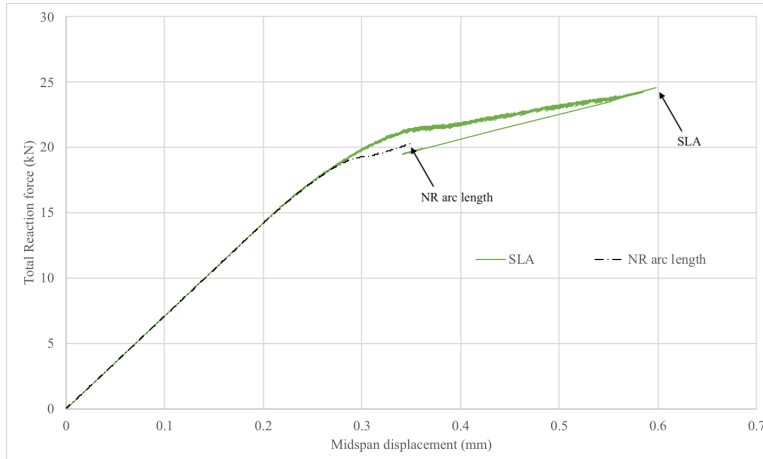


Figure 4.18: Reaction force-displacement diagram for 10 MPa prestress

proportional loading, each SLA cycle can be determined with just two linear analyses. It correctly predicts that just one crack will occur in an unreinforced beam while the N-R method needs a notch or imperfection at the correct location to prevent bifurcations and to trigger localization.

Compared with two strategies of non-proportional loading[12][132], the algorithm selects the critical integration point to which a damage increment is applied by extra stresses [9][12] or a varying initial-load factor [132]. In the proposed algorithm, a combination of the initial load and the current load is always applied on a structure, and a sequence of linear elastic analysis is performed with damaged secant stiffness. Therefore, the stresses of the initial load and the current load are recomputed from each damaged state. However, only the stresses of the current load are recomputed from each damaged state in the algorithm [12]. The stresses of the initial load are computed only from the initial undamaged state and then added into the expression of the stress state by the current load. One advantage of the proposed algorithm is that the stresses of the initial load are evaluated based on a correct damaged state for each cycle. Another advantage is that it is unnecessary to compute the expression of stress state for different element types and failure criteria. The scaling procedure of non-proportional loading is the same as that of proportional loading.

This proposed algorithm of non-proportional loading in SLA has some limitations, however. The initial load cannot be very large or should have little influence

on the critical element position due to the assumption that initial-load factor  $\nu$  and current load factor  $\lambda$  have a linear relationship, otherwise a positive initial-load factor, which should equal the current load factor, cannot be obtained. In addition, geometric non-linearity cannot be considered in this algorithm due to the total approach. Therefore, SLA is extended to an incremental approach in Chapter 5.

However, this algorithm is still suitable for weak non-linear problems that take more steps to render  $\nu$  equal to  $\lambda$ . For strong non-linear problems, the potentially improved solution is to simply estimate  $\nu$  by  $\lambda$  of the previous trial instead of calculating  $\nu$  via the interpolation procedure. Further research is needed.

# 5

## INCREMENTAL SEQUENTIALLY LINEAR ANALYSIS (ISLA)

In this chapter, a new algorithm is proposed that combines the advantages of the N-R method and SLA. The author proposes the algorithm be called **incremental sequentially linear analysis** (ISLA) [13][14]. The method is incremental; each increment begins and ends with an equilibrium state. The solution search path follows damage cycles sequentially with secant stiffness, tracing both damage history (explicit) and displacement history (implicit). The method is robust because all physical non-linearity is included in these cycles.

### 5.1. INTRODUCTION

The idea behind the proposed method is performing an incremental analysis with N-R iterations and linear elastic material behaviour with load or displacement control. As soon as the stress at some point is too large, the Young's modulus of the considered element is reduced, and the load is reduced or increased just to the level at which the stress is not too large.

In the proposed method, loads are directly applied onto the structure, which means the initial load  $F_{ini}$  and the current load  $F_{cur}$  are included instead of the ref-

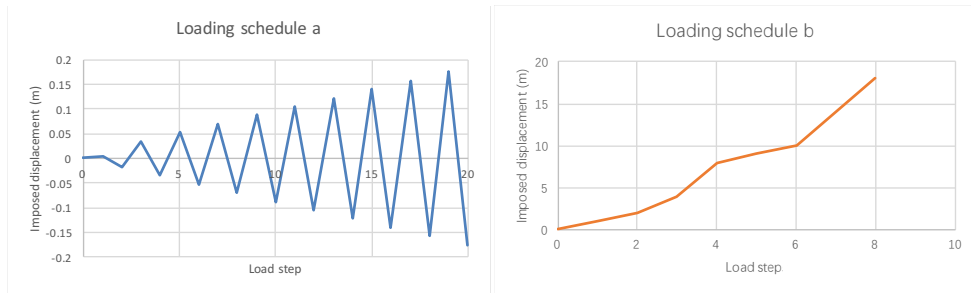


Figure 5.1: Loading schedule examples that can be applied in the new SLA

erence load  $F_{ref}$  in SLA. The loads can be defined in a loading schedule, for example hysteretic loading or monotonic loading (Figure 5.1).

## 5

Suppose that a structure is loaded by  $F_{ini}$  and  $F_{cur}$ , the first with an initial-load factor  $\lambda_{ini}$  and the second with a current load factor  $\lambda_{cur}$ . This is referred to as non-proportional loading. Here,  $\lambda_{cur}$  can be incremented (5.2 Load control) or first incremented and then automatically decremented (5.3 Load scaling control). In proportional loading, there is only  $\lambda_{cur}$  and no  $\lambda_{ini}$ .

Just as in SLA, a utilisation value is defined. The utilisation value is determined at the local level by the stress state and the failure surface of an element with elastic material properties. Utilisation values are computed for each element. A utilisation function  $\mu$  is defined as the largest utilisation value of all elements, which is a function of the load factors and the stiffness matrix  $K$  at the global level. The material is in equilibrium if

$$\mu(\lambda_{ini}, \lambda_{cur}, K) \leq 1 \quad (5.1)$$

which means that the stresses or strains of the critical element (i.e., the element that is the closest to the first or the next damage event) lie either on or within the failure surface.

An explicit application of the utilisation function is given in Chapter 6 for one element. A notched beam example with 9 elements which can be critical is shown in Chapter 7. The remainder of Chapter 5 is on the formulations and algorithms of ISLA.

## 5.2. LOAD CONTROL

For load control,  $\lambda_{ini}$  is fixed for all load steps and  $\lambda_{cur}$  is incremented. Note that  $\lambda_{cur}$  is fixed within a load step. The load factor  $\lambda_{cur}$  is applied to imposed forces or imposed displacements. Suppose that after load step  $n$ , the failure surface is reached somewhere.

$$\mu_n = \mu(\lambda_{ini}, \lambda_{cur}, K_n) = 1 \quad (5.2)$$

where the subscripts on  $\mu$  and  $K$  refer to a load step. For the next load step,  $\lambda_{cur}$  is increased to  $\lambda'_{cur}$ . If

$$\mu_{n+1}^1 = \mu(\lambda_{ini}, \lambda'_{cur}, K_{n+1}^0) > 1 \quad (5.3)$$

where  $K_{n+1}^0 = K_n$ . It is then restarted from  $\mu_n$ , which means that the displacements are reset to the values at the end of step  $n$ . Subsequently, the stiffness is reduced.

5

$$\mu_{n+1}^2 = \mu(\lambda_{ini}, \lambda'_{cur}, K_{n+1}^1) \quad (5.4)$$

where  $K_{n+1}^1$  means that the Young's modulus of the critical finite element is reduced in the stiffness matrix for this event, which is based on the rotating smeared crack with a constant stiffness reduction factor  $t^1$ . In this model, the Young's modulus in principal directions of the critical finite element is reduced. An event in which the stiffness is reduced is called a cycle. The superscripts on  $\mu$  and  $K$  refer to the cycle number within a load step.

The process is restarted from  $\mu_n$  and reduction of the stiffness matrix continues until

$$\mu_{n+1}^{m+1} = \mu(\lambda_{ini}, \lambda'_{cur}, K_{n+1}^m) \leq 1 \quad (5.5)$$

where  $K_{n+1}^m$  means the stiffness matrix is reduced  $m$  times for the critical element within a load step.

A routine with the name “Find  $\mu$ ” is defined in Figure 5.2. Figure 5.3 shows the program structure diagram for the imposed loading. The structure state refers to the displacements, velocities and accelerations of the nodes. The parameter  $r$  is defined as the material equilibrium convergence tolerance value, which indicates how close the stress of the critical element satisfies the constitutive law.

<sup>1</sup>Note that the value of the stiffness reduction factor is between 0 and 1. A large stiffness reduction factor value means a small stiffness reduction.

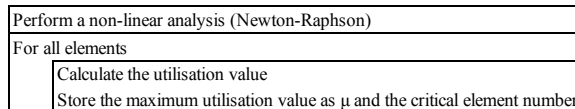


Figure 5.2: Program structure diagram for finding  $\mu$

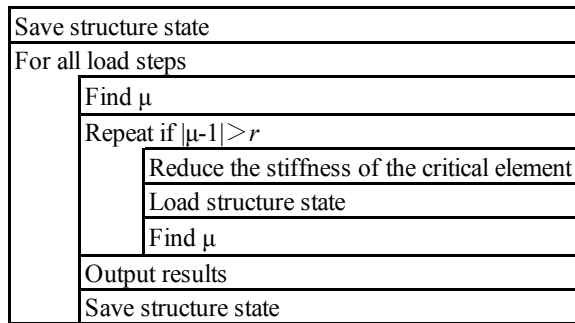


Figure 5.3: Program structure diagram for load control

Therefore, for load control of ISLA, the solution is to reduce the stiffness cycle-by-cycle when the load factors are fixed for each load step.

This algorithm has some drawbacks, however. For example, when the loading schedule is defined by force,  $\mu$  cannot become 1 simply by reducing the stiffness when a global peak in the load-displacement behaviour is presented. Therefore, a technique like arc-length control needs to be introduced so the peak can be passed and snap-throughs or snap-backs can be followed. In the following section, this technique is referred to as "load scaling control". However, an imposed displacement can be applied to avoid the need for such a control method for a number of problems.

### 5.3. LOAD SCALING CONTROL

For load scaling control,  $\lambda_{ini}$  is fixed and  $\lambda_{cur}$  is incremented or decremented depending on the capacity of the structure, which is based on  $\mu$ . Two control methods are introduced below for load scaling control. Chapter 6 shows how the load factors are scaled.

### 5.3.1. DAMAGE CONTROL METHOD

Suppose that after load step n the failure surface is reached somewhere.

$$\mu_n = \mu(\lambda_{ini}, \lambda_{cur}, K_n) = 1 \quad (5.6)$$

For the first cycle in the next load step, if

$$\mu_{n+1}^1 = \mu(\lambda_{ini}, \lambda_{cur}^1, K_{n+1}^0) > 1 \quad (5.7)$$

where  $\lambda_{cur}^1$  is an increased  $\lambda_{cur}$  and  $K_{n+1}^0 = K_n$  and the superscript on  $\lambda$  refers to the cycle number of a load step, the Young's modulus of the critical element is subsequently reduced and the process is restarted from  $\mu_n$

$$\mu_{n+1}^2 = \mu(\lambda_{ini}, \lambda_{cur}^1, K_{n+1}^1) \quad (5.8)$$

where  $K_{n+1}^1$  is the stiffness with reduced Young's modulus of the critical element.

If  $\mu$  is still larger than 1, then the process is again restarted from  $\mu_n$

$$\mu_{n+1}^3 = \mu(\lambda_{ini}, \lambda_{cur}^2, K_{n+1}^1) \quad (5.9)$$

where  $\lambda_2^2$  is a reduced  $\lambda_2^1$  based on a constant reduction  $q$  or a function  $q(\mu)$  ( $\lambda_2^2 = q\lambda_2^1$  or  $\lambda_2^2 = q(\mu)\lambda_2^1$ ). Parameter  $q$  is smaller than 1 but larger than  $\lambda_2/\lambda_2^1$  (e.g.,  $\lambda_2/\lambda_2^1$  is 0.9 and  $q$  is 0.95). Parameter  $q$  can be adjusted by a decreasing function  $q(\mu)$  where  $q(1) = 1$ .

If  $\mu$  is still larger than 1, then the process is repeated, restarting from  $\mu_n$  until

$$\mu_{n+1}^{m+1} = \mu(\lambda_{ini}, \lambda_{cur}^m, K_{n+1}^1) \leq 1 \quad (5.10)$$

where  $\lambda_{cur}^m$  means that  $\lambda_{cur}$  is adjusted  $m$  times, which is a reduced  $\lambda_{cur}^{m-1}$  based on a constant reduction  $q$  or a function  $q(\mu)$ .

Figure 5.4 shows the program structure diagram for the load scaling control.

In this thesis, this method is called the damage control method because Young's modulus of just the critical element is reduced once and remains unchanged during load factor adjustment iterations. As with SLA, only one element is damaged in each load step of the damage control method.

Therefore, to obtain softening behaviour by force loading in ISLA, the solution is to adjust load factors cycle-by-cycle when the stiffness is reduced only once at the beginning for each load step.

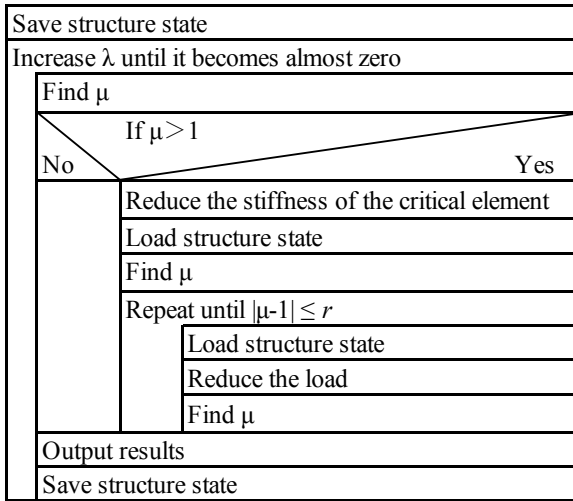


Figure 5.4: Program structure diagram of the damage control method for load scaling control

5

### 5.3.2. LOAD AND DAMAGE CONTROL METHOD

Compared with SLA, the damage control method has more calculation cycles since several extra cycles are necessary (interpolation procedure) for each stiffness reduction to reach an equilibrium state. To improve the efficiency of the damage control method, the stiffness is reduced rather than fixed during load factor adjustment iterations. Consequently, the total number of cycles still equals the number of stiffness reductions. In other words, the total number of cycles is not increased by the load factor scaling procedure.

To this end, equations (5.9) and (5.10) are adjusted. The stiffness matrix is reduced during iterations instead of being reduced only once and then fixed.

If  $\mu$  is larger than 1, then the process is restarted from  $\mu_n$

$$\mu_{n+1}^3 = \mu(\lambda_{ini}, \lambda_{cur}^2, K_{n+1}^2) \quad (5.11)$$

If  $\mu$  is still larger than 1, then the process is again restarted from  $\mu_n$

$$\mu_{n+1}^{m+1} = \mu(\lambda_{ini}, \lambda_{cur}^m, K_{n+1}^m) \leq 1 \quad (5.12)$$

where  $\lambda_2^m$  is a reduced  $\lambda_2^{m-1}$  based on a constant reduction  $q$  or a function  $q(\mu)$ . The program structure diagram is shown in Figure 5.5.

Therefore, to guarantee efficiency by the load scaling control in ISLA, the solution is to introduce a function for  $\lambda_{cur}$  and continue reducing the stiffness during

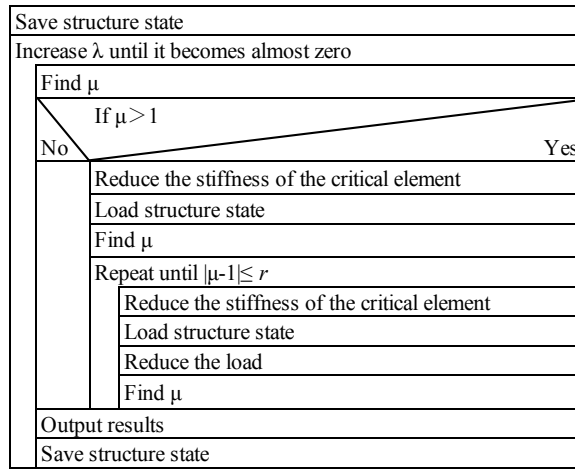


Figure 5.5: Program structure diagram of the load and damage control method for load scaling control

5

cycles.

To summarize, if the incremental load is prescribed in load steps, it is referred to as the load control method. Here, load can be both a prescribed force load increment or a prescribed displacement load increment. If the incremental load is scaled based on the reduced stiffness, it is referred to as the load and damage control method. The latter is especially suitable in case the problem cannot be handled in displacement control to obtain the post-peak behaviour. In addition, there is a third algorithm called the damage control method. Here, the stiffness is reduced only once in the first cycle no matter how many cycles the load step has. Since the stiffness remains unchanged after the first cycle, the scaling procedure follows a linear interpolation procedure to search for the suitable load factors. This is quite similar to SLA in that the algorithm reaches an equilibrium state for each damage step and the load factors are governed by the utilisation value. However, the difference is that in ISLA, each equilibrium state search starts from the equilibrium state of the previous “load step”, which indeed is the previous damage step, instead of restarting from the origin in the total scheme of SLA. However, in the load and damage control method, the stiffness continues to be reduced each cycle. Accordingly, the number of stiffness reductions is the same as the number of cycles in the load step.

## 5.4. UNIFIED FRAMEWORK

ISLA comprises the load control method and the load scaling control method as a combination of the damage control method and the load and damage control method, which depends on how many times the stiffness can be adjusted during cycles. For the load control method (Section 5.2) and the load and damage control method (Section 5.3.2), the stiffness can be reduced several times cycle-by-cycle in one load step. However, the stiffness can be reduced only once in one load step for the damage control method (Section 5.3.1). Actually, all methods can apply displacements or forces, which is shown in Section 5.5.

As a matter of fact, a unique framework can include all three algorithms by following the algorithm below:

5

1. Save the structure state (displacement of all nodes is initially zero).
2. Load the structure state.
3. Apply load increment to the structure. (For the load control method, the load increment is based on the loading schedule. For the damage control method, the initial-load increment can be the unity load and is thus determined by the utilisation value similar to SLA. For the load and damage control method, the load increment can be prescribed based on a loading schedule at the beginning and then scaled especially for the post-peak.)
4. Perform an N-R analysis (the two involved procedures are explained in Section 5.5).
5. Consider all elements and calculate  $\mu$ .
6. Store  $\mu_{max}$ , the maximum  $\mu$  and the critical element number.
7. If  $\mu_{max}$  is smaller than 1, **save** the structure state and go to step 2 with the **next** load step.
8. For the load control method or load and damage control method, reduce the stiffness of the critical element. For the damage control method, the stiffness remains unchanged when it has already been reduced in this load step, otherwise the stiffness of the critical element is reduced.

9. For the load control method, go to step 2 with the **same** load increment as for this load step. For the load scaling control method, go to step 2 with a prescribed or a scaled load increment for this load step based on the utilisation value.

Follow this loop until all load steps are applied or the stiffness of the structure is extremely small.

Steps 2 to 9 comprise one cycle. The differences between these three algorithms are the way the load increment is applied in Step 3 and the way the next equilibrium state is reached with the procedure in Step 8 (stiffness changes) and Step 9 (load changes).

## 5.5. COMPUTATION PROCESS

In this section, the algorithms are illustrated by studying the incremental process. Figure 5.6 shows the restart procedure<sup>2</sup> of the implicit algorithm. It is important to save and load the structure state. Only when  $|\mu - 1|$  is smaller than  $r$  will the structure state be saved and overwritten. Consequently, the analysis is restarted with the structure state of the last cycle of the previous load step. Without the restart command, the algorithm would continue with the structure state of the previous cycle, which would be incorrect. This restart procedure ensures that the calculation of each load step is based on the correct structure state and stiffness.

5

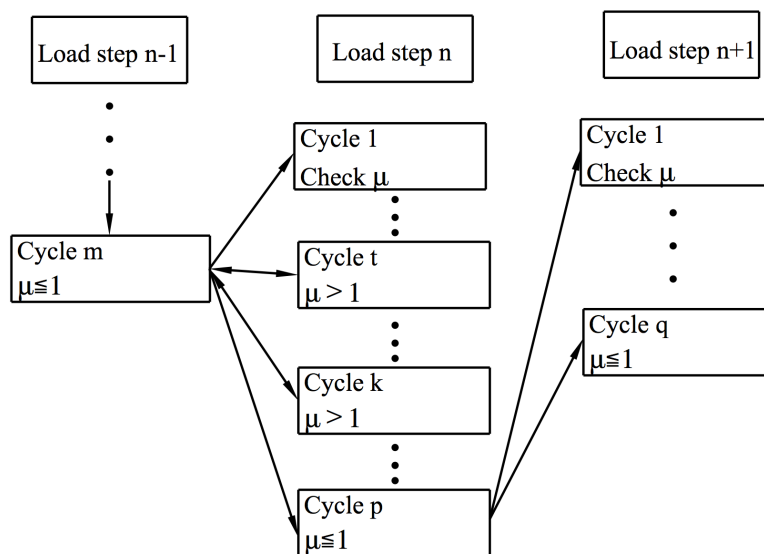


Figure 5.6: Restart procedure of the algorithm

Eq. (5.13) shows how the displacement history is saved and updated incrementally.

$$\bar{u}' = u + \Delta u'$$

$$F' = F + \Delta F(K, K') + K'(\Delta u' - \Delta u(K, K')) \quad (5.13)$$

Below is the interpretation of this equation with displacement states.  $F$  and  $F'$  are the internal force of the current and the next equilibrium state.  $\Delta u'$  is the incremental displacement between these two equilibrium states, which means that it is

<sup>2</sup>ANSYS restart cannot reuse the factorized stiffness matrix, which causes low efficiency of the stiffness regeneration.

an incremental procedure.  $\Delta F(K, K')$  and  $\Delta u(K, K')$  are the varying force and displacement caused by the stiffness change (a function of the previous stiffness and the new stiffness), which is an N-R procedure to reach a new equilibrium state due to the stiffness change. Figure 5.7 shows how the N-R procedure works. From Load step n-1 to Load step n, either displacements or forces can be applied. The green lines are the possible  $\Delta F$  and  $\Delta u$  determined by different load types, so the green dots are the possible temporary states before a new equilibrium state is reached.  $K'(\Delta u' - \Delta u(K, K'))$  is the extra force resulting from the load factor change (either displacements or forces), which is an N-R procedure with a constant positive secant stiffness. Accordingly, the procedure follows the pink line to reach the new equilibrium state (from the red dot to the pink dot) in Figure 5.7. The N-R procedure with a constant positive stiffness ensures the robustness of the computation. Meanwhile, the N-R procedure with the stiffness change, but without any load increment, is also essential and significant. Actually, the N-R procedure with a constant positive secant stiffness cannot find the solution without the stiffness change, especially for the softening behaviour. In other words,  $\Delta F$  and  $\Delta u$  make it possible to always use a constant positive stiffness to search for a new equilibrium state, even for softening behaviour.

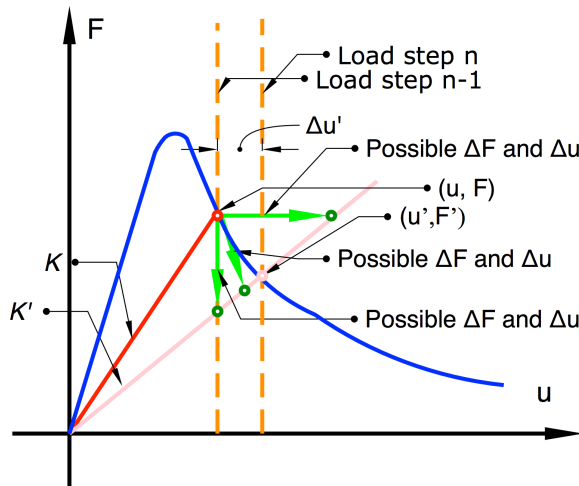


Figure 5.7: Generic searching path of the Newton-Raphson procedure in this algorithm with the displacement states for Load step n-1 and n

Figure 5.8 illustrates the search paths of the imposed loading of force control

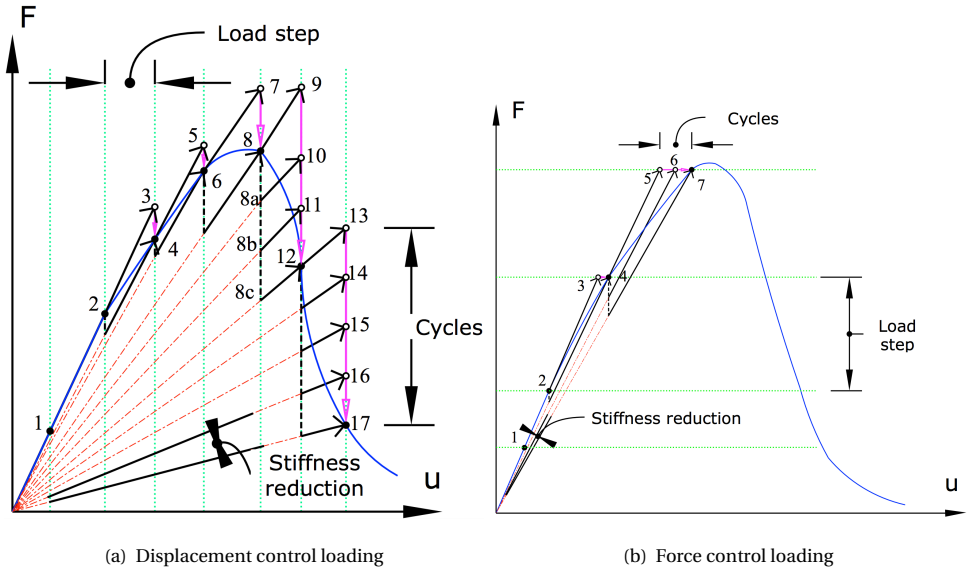


Figure 5.8: Searching path for load control

and displacement control separately.  $F$  and  $U$  represent the force vector and displacement vector. The blue line is the target curve. The green dotted lines present the load steps. The red dashed lines present the current stiffness, which has been reduced from the previous value based on the stiffness reduction. The solid black arrow lines are the procedure paths for each cycle. The pink solid arrow lines are the output paths for all the cycles in one load step. The solid dots are the equilibrium states, and the open dots are the temporary trial states. It should be noted that the paths of the dashed black lines result from internal force change along with stiffness reduction. The N-R procedure was performed to update the internal force based on the current displacements and the reduced stiffness. When an equilibrium state is reached, a load increment is applied for the next load step. If  $\mu$  is smaller than 1, the next load increment is applied (Step 1 → 2 → 3 in Figure 5.8(a)). Otherwise, the procedure restarts from the structure state of the previous load step, which means that the displacements are reset to the values of the previous load step. Below, two procedures of one cycle are described:

- Firstly, the secant stiffness of the critical element of the previous cycle is reduced by the defined stiffness reduction factor, which is the same as for SLA. It

is noted that the damage procedure is irreversible, which means that all stiffness reductions of the previous cycles are repeated before the current cycle in this load step. Due to these stiffness reduction procedures, the internal forces are updated based on the displacements of the previous load step and the algorithm reaches a temporary equilibrium state, which is automatically calculated by the non-linear implicit scheme with N-R iterations. Eq. (5.14) is adopted to update a temporary equilibrium state for force control loading while Eq. (5.15) is employed for displacement control loading. One N-R iteration is enough for a geometrically linear analysis, but geometrical non-linearity may require several iterations.

$$K' \Delta u = F_{ext} - F_{int} \quad (5.14)$$

$$K' \Delta u = -F_{int} \quad (5.15)$$

where  $\Delta u$  is an increment displacement,  $K'$  is the reduced stiffness,  $F_{int}$  is the updated internal forces due to the reduced stiffness and  $F_{ext}$  is the external forces for force control loading.

- Secondly, the incremental load is applied, and a linear analysis is performed for the current load step.

For instance, an equilibrium state begins at Step 8 and ends at Step 12 (a load step). A new load increment is applied at Step 9. Subsequently, the stiffness is reduced sequentially from Step 10 to Step 12 (cycles). The search path of this load step is Step 8 → 9 → 8 → 8a → 10 → 8 → 8b → 11 → 8 → 8c → 12.

Figure 5.9 shows the algorithm path of the damage control method and the load and damage control method for applying a force load.

Figure 5.10 shows a step-by-step example of the load control method with imposed displacement for either proportional loading or non-proportional loading from load step n-1 to load step n. The solid red line represents the correct stiffness for a certain equilibrium state while the dashed line stands for the estimated stiffness for the imbalance state. The orange dashed line is defined as a load step. The solid green arrow line denotes the actual calculation procedure while the dashed arrow line demotes the nominal outputting procedure. When  $|\mu - 1| > r$  for load step n, the stiffness is reduced. Meanwhile, the procedure is restarted from load step n-1.

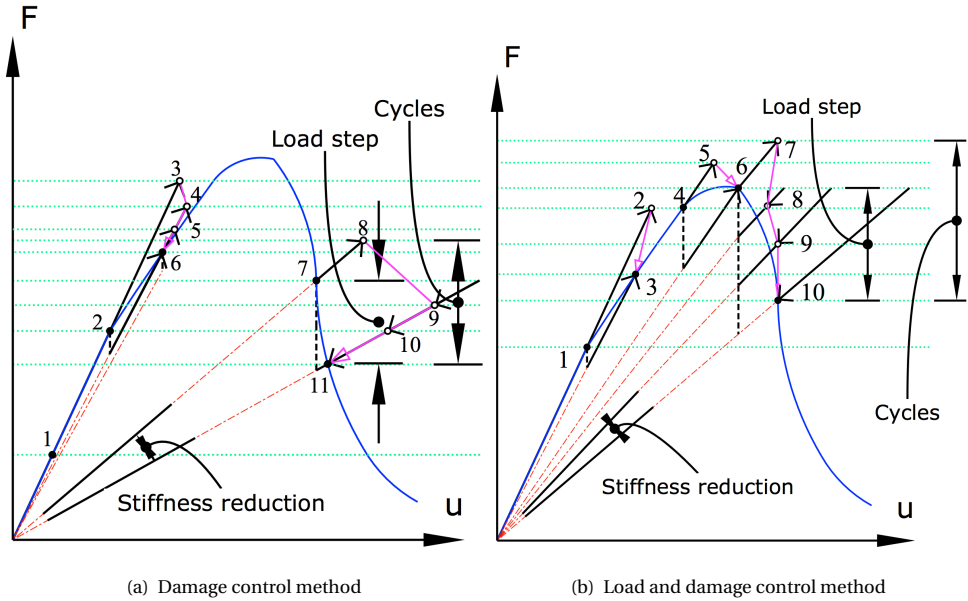


Figure 5.9: Search path of arc-length control

This procedure continues until the proper stiffness has been found when  $|\mu - 1| \leq r$ .

Due to linear analysis with reduced stiffness, the post-procedure for result scaling is allowed when  $\mu$  is larger than 1. Therefore, snap-back behaviour can still be obtained for imposed displacement control loading. Figure 5.11 shows the scaling procedure when  $\mu$  is larger than 1. The pink line indicates the scaling procedure. However, it supports only proportional loading because of the post-procedure, otherwise the initial load is also scaled with the current load for non-proportional loading.

The load and damage control method involves a similar procedure as the load control method shown in Figure 5.12. The major disparity is that the force as well as the stiffness needs to be scaled to make  $\mu \leq 1$ . The dashed orange line represents the load scaling procedure. Since the procedure is controlled by the load scaling control method, snap-back behaviour can be obtained without the post-procedure of result scaling whether it involves proportional loading or non-proportional loading.

In the damage control method, "event-by-event" [11] damage cycles can be followed and represent the case that only one element is damaged once for each load

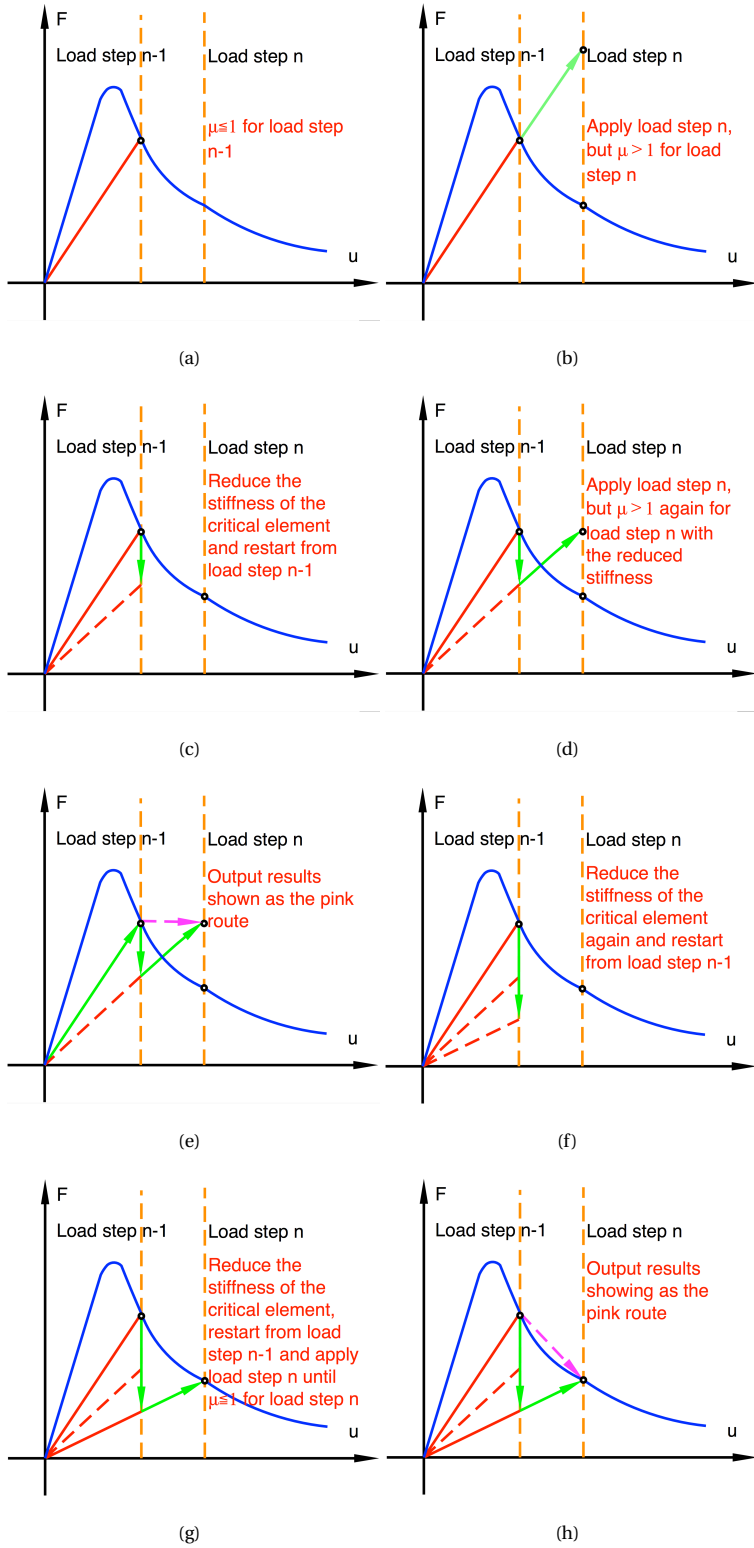


Figure 5.10: A step-by-step example for the load control method with imposed displacement

5

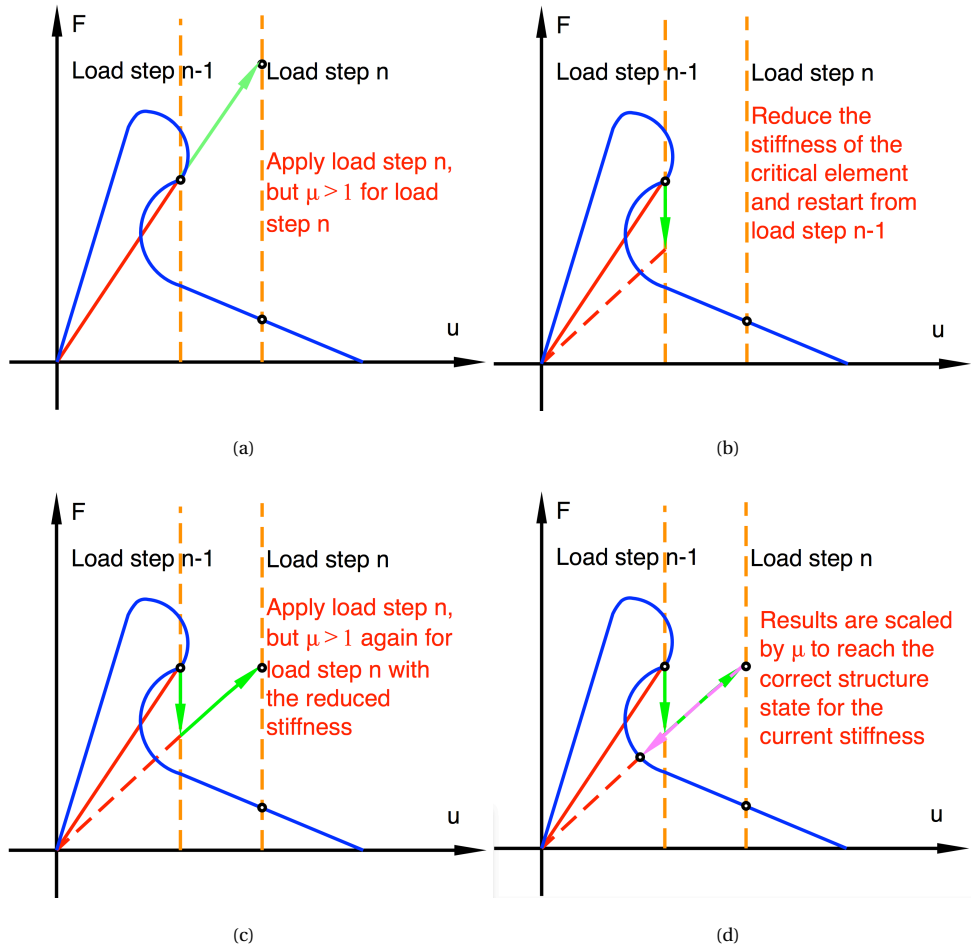


Figure 5.11: Scaling procedure of the load control method for proportional imposed displacement loading to obtain snap-back behaviour

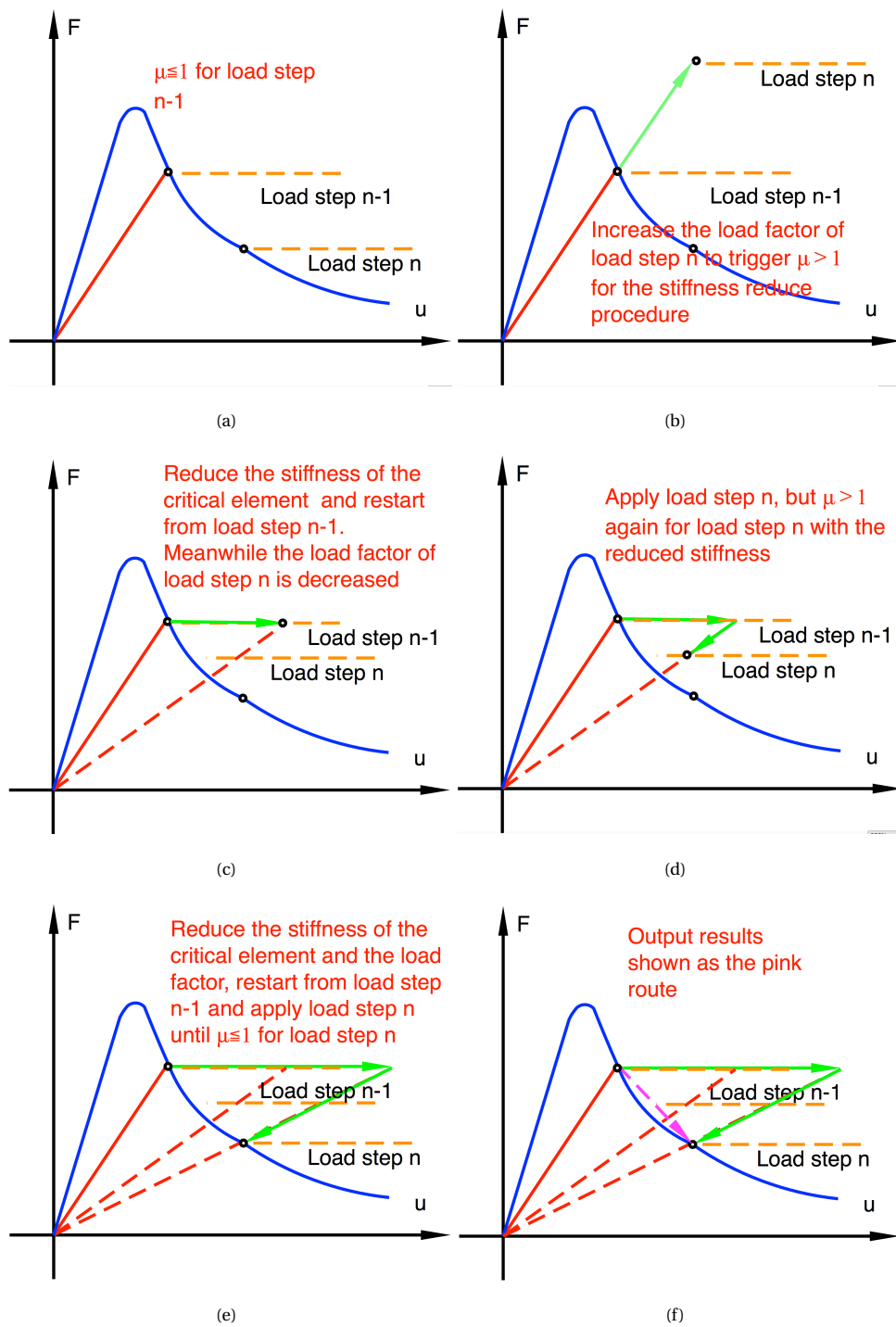


Figure 5.12: A step-by-step example of the load and damage control method with force loading

step. The damage control method is more accurate but also more time-consuming. Figure 5.13 shows the damage control method with force loading. Actually, the damage control method can also be used for the displacement loading shown in Figure 5.14.

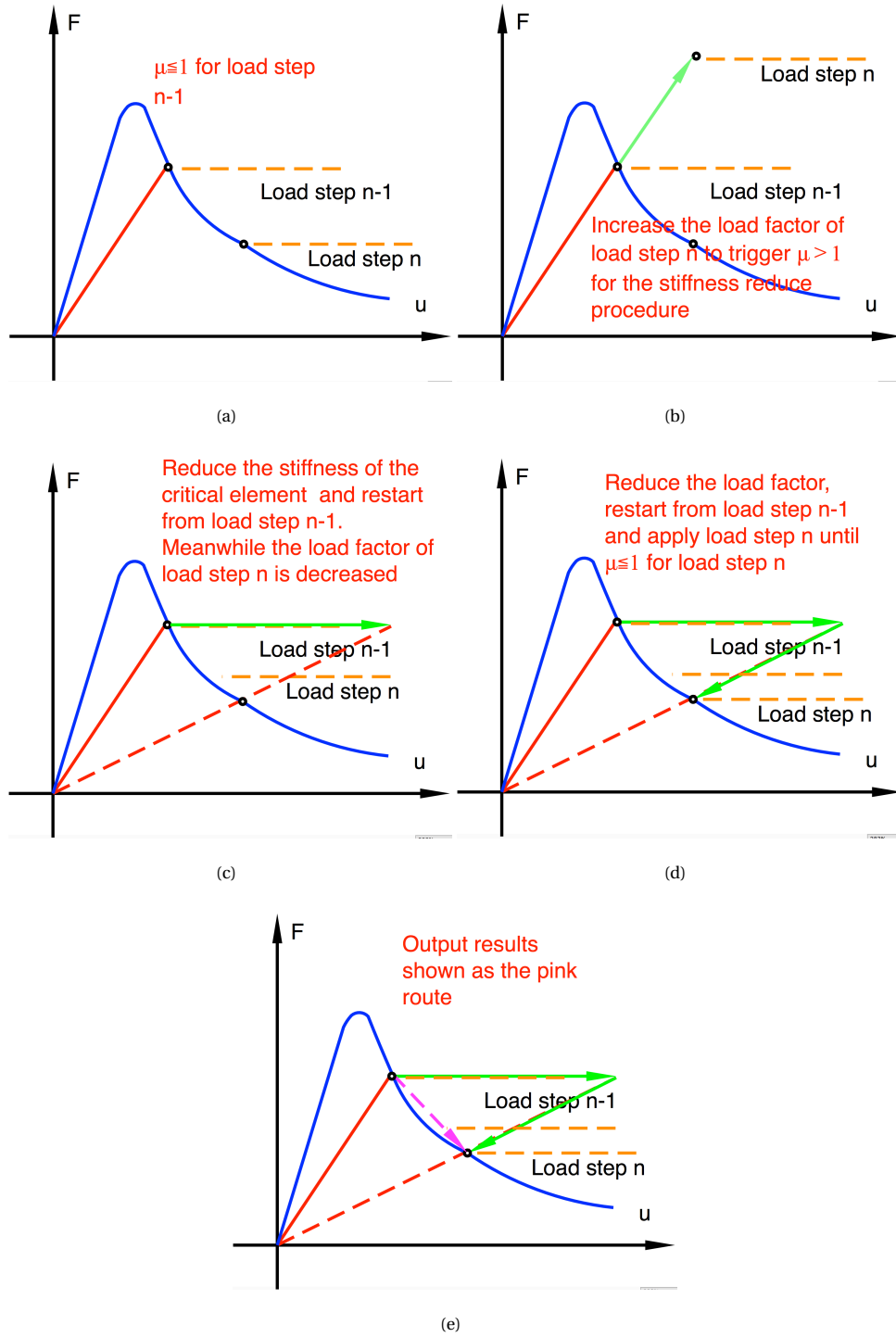


Figure 5.13: A step-by-step example of the damage control method with force loading

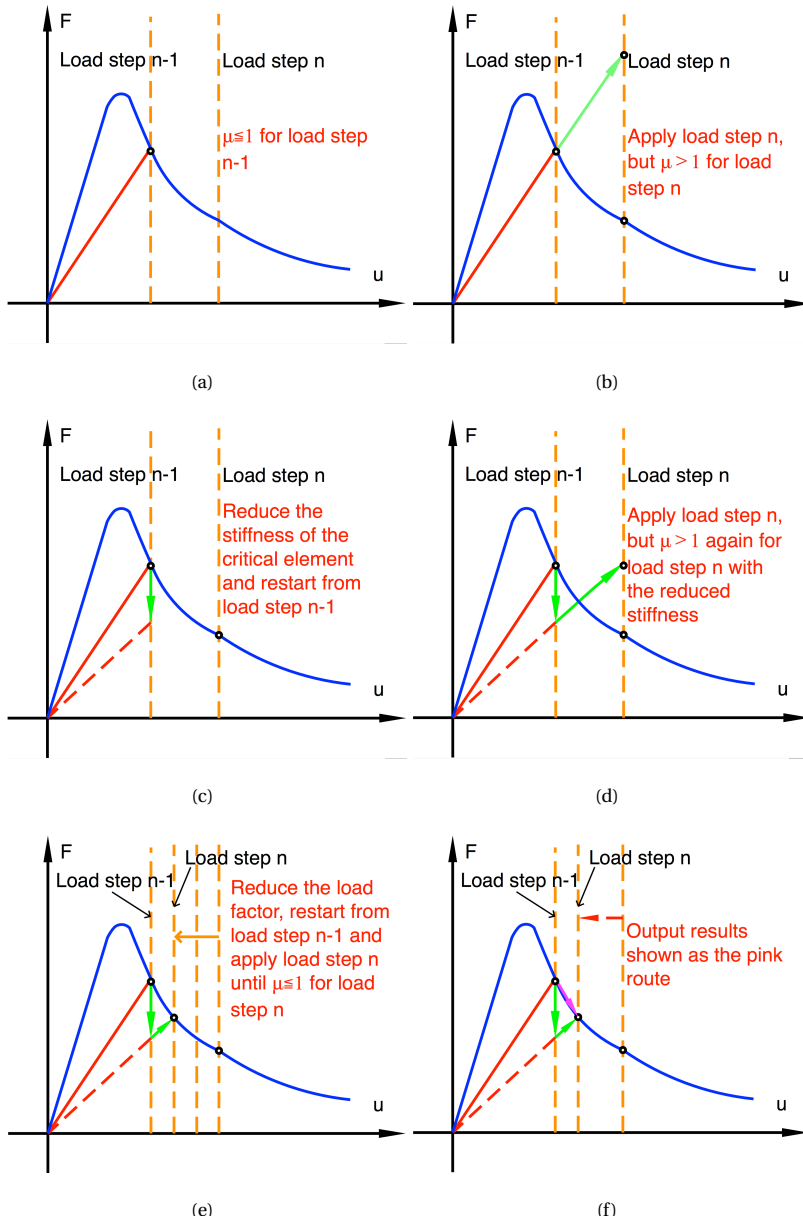


Figure 5.14: A step-by-step example of the damage control method with displacement loading

## 5.6. COMPARISON OF SLA AND ISLA

Sequentially linear analysis (SLA) and incremental sequentially linear analysis (ISLA) have several features in common. Young's modulus of the material around a critical integration point is reduced. The critical integration point is defined as the point with the largest utilisation factor. The load is adjusted to make the largest utilisation factor equal to one. In other words, all integration points pass the utilisation factor check.

On the other hand, there are differences between SLA and ISLA, which are shown in Table 5.1.

Table 5.1: Differences between SLA and ISLA

SLA		ISLA
proportional loading	non-proportional loading [8]	
unit load is mapped back linearly	load factor is solved in 3 cycles	load factor is incremented or decremented
	displacements are not saved	displacements are saved
one linear elastic analysis in each load step	several linear elastic analyses in each load step	several nonlinear analyses in each load step

## 5.7. DISCUSSION

The new algorithm extends SLA to classical non-linear implicit analysis with N-R iterations. The name we propose for this solution method is incremental sequentially linear analysis (ISLA): the words “sequentially” and “linear” refer to the established sequentially linear analysis from which the method is derived; the word incremental refers to the incremental procedure, which is new compared to SLA that uses a total approach.

The proposed method is highly robust, similar to SLA. The solution search path follows damage cycles sequentially with secant stiffness, which is based on physical parameters (damage history and displacement history) instead of numerical parameters. The equilibrium state is updated based on stiffness reductions of critical elements and load increments. Damage is also correctly introduced to the structure at the corresponding displacements. The algorithm does not switch between methods and thus does not depend on the values of switch parameters. The method is an incremental procedure and can be easily extended to geometrically non-linear analysis and transient analysis, as demonstrated later.

Indeed, an implicit scheme is chosen in this thesis (N-R iterations). However, an explicit scheme can also be used in the algorithm. The main difference in an explicit scheme is that the algorithm with an explicit scheme continues searching from the current state, which may not be an equilibrium state, to update incremental displacements, rather than restarting from the previous equilibrium state, as with the implicit scheme.

The following are important definitions for ISLA. The new algorithm has two types of calculation steps: load steps and cycles. The load steps follow a loading schedule or a scheme of scaled loads. A cycle is a step in which the stiffness is reduced. The structure state is the displacements, velocities and accelerations of the nodes. Parameter  $r$  is defined as the equilibrium convergence tolerance value. The equilibrium state is defined as the stresses or strains of the critical element equal to or smaller than the failure surface at the local level, which is a function of the stiffness and load factors at the global level. The main procedure is to start at an equilibrium state, damage the stiffness and reach a new equilibrium state until all load steps are applied.

In the load control method, each load step can contain one increase or decrease of the load and several reductions of Young's modulus of various elements. In the damage control method, each load step can contain one reduction of Young's modulus and several changes of the load. In the load and damage control method, each load step can contain several changes of the load and several reductions of Young's modulus of various elements. Table 5.2 outlines the differences of these methods.

Table 5.2: Changes in load and Young's modulus within one load step

ISLA	Load	Young's modulus
Load control method	Once increased or decreased (prescribed loading)	One or more critical elements and several reductions
Damage control method	Once increased and several changes (scaled loading)	One critical element and one reduction
Load and damage control method	Once increased and several changes (scaled loading)	One or more critical elements and several reductions

For imposed displacement loads, it is recommended that the load control method be used. For force loads, this method can also be used, but the post-peak response cannot be obtained. The damage control method and the load and damage control method can be used to determine the post-peak behaviour and snap-back

behaviour of structures. The load and damage control method is much faster than the damage cycle method. It is also robust and provides the same results. Based on efficiency, the load control method and the load and damage control method are suggested for large structures.

In addition, the load control method and the load scaling control method are recommended for a total approach such as SLA for non-proportional loading. Compared with SLA in Chapter 3, the load applied to a structure is the actual load instead of a reference load. Hereby, it is not necessary to scale the results by  $\lambda$ . Indeed,  $\lambda$  in SLA describes both the structural capacity and the material utilisation while  $\lambda$  in ISLA describes the structural capacity and  $\mu$  describes the material utilisation. With the introduction of this new constraint  $\mu$  into SLA, the equilibrium is determined by the utilisation function  $\mu$  rather than a unit load with the load factor  $\lambda$  in standard SLA. Compared with the non-proportional loading algorithm in Chapter 4, the main advantage of the load scaling control method is that the solution search direction is certain, which makes  $\mu$  equal to or smaller than 1. When the load factor continues to be reduced based on  $\mu$ , this target can always be achieved for the problems mentioned in Chapter 4.



# 6

## ELABORATION OF LOAD SCALING CONTROL IN ISLA

Structures can be loaded by imposed forces and imposed displacements. Each is multiplied by a load factor  $\lambda$ , which is increased in small steps and, after the peak load, is reduced in small steps. The reduction steps should be such that further damage occurs, otherwise it would be just unloading. In traditional non-linear analysis, a technique called arc-length control is used to determine the correct reduction steps. In ISLA, it is not convenient to use arc length, so another method has been developed to obtain the same effect. We refer to this as load scaling control.

The aim of this chapter is to elaborate load scaling control for ISLA to obtain the after-peak behaviour of structures loaded by forces or displacements. Load scaling control should make the load meet the current structure capacity, such that the utilisation function  $\mu$  is almost 1 (based on the material equilibrium convergence tolerance value  $r$  in Chapter 5).

Two types of control methods are elaborated and validated based on the damage control method and the load and damage method and demonstrated in several applications. In the damage control method, the stiffness is reduced in one cycle and the load is subsequently reduced in several cycles. Here, load scaling control

is similar to an extrapolation procedure with fixed stiffness. In the load and damage control method, the load is scaled, and the stiffness is reduced simultaneously. Therefore, the utilisation function  $\mu$  is determined by both the stiffness  $K$  and the load factor  $\lambda$ . It can be expected that the utilisation function is not smooth in  $\lambda$  due to the ongoing stiffness reduction, which excludes all common root-finding algorithms. Therefore, a new root-finding strategy is proposed that scales the load factor  $\lambda$  by a decreasing function until  $\mu$  is almost 1.

In this chapter, first, the root-finding strategy in the damage control method is explained (Section 6.1). Second, the root-finding strategy in the load and damage control method is explained for one load step and one element (Section 6.2). For the latter method, a parameter study is performed (Section 6.3). In Section 6.4, the two methods are tested for several load steps and one element. In the last section 6.5, the parameters are optimized to improve accuracy and efficiency.

## 6

### 6.1. DAMAGE CONTROL METHOD

In the damage control method, the stiffness is reduced once and afterwards remains fixed. When the stiffness is fixed, the situation can be regarded as linear or weakly non-linear. Therefore, the relationship between the load factor and the utilisation function can be solved by an extrapolation procedure (in fact, it is the first step of the N-R method using the secant for finding roots). Equations 5.7 to 5.10 can be written as

$$\mu_{n+1}^1 = C_0 \quad (6.1)$$

$$\mu_{n+1}^2 = C_0 + C_1 (\Delta E) + C_2 \lambda_{cur}^1 \quad (6.2)$$

$$\mu_{n+1}^3 = C_0 + C_1 (\Delta E) + C_2 \lambda_{cur}^2 \quad (6.3)$$

where  $C_0$  represents the value of  $\mu$  with a new load factor of Load step  $n + 1$ ,  $\Delta E$  is the stiffness reduction,  $C_1$  represents a non-linear function of  $\Delta E$  and  $\mu$ , and  $C_2 \lambda$  represents a linear relation of  $\lambda$  and  $\mu$  when the stiffness is fixed. The superscripts on  $\mu$  and  $\lambda$  refer to the cycle number within a load step. The value of the utilisation function  $\mu$  should be 1, therefore,

$$1 = \mu_{n+1}^4 = C_0 + C_1 (\Delta E) + C_2 \lambda_{cur}^3 \quad (6.4)$$

From which  $\lambda_{cur}^3$  can be solved.

$$\lambda_{cur}^3 = \lambda_{cur}^1 + (\lambda_{cur}^2 - \lambda_{cur}^1) \frac{1 - \mu_{n+1}^2}{\mu_{n+1}^3 - \mu_{n+1}^2} \quad (6.5)$$

The load factor  $\lambda_{cur}^2$  can be any value close to but different from  $\lambda_{cur}^1$ . The algorithm uses less iterations if  $\lambda_{cur}^2$  is defined as  $\lambda_{cur}^1$  over  $\mu_{n+1}^2$ . Therefore,

$$\lambda_{cur}^3 = \lambda_{cur}^1 \frac{(2\mu_{n+1}^2 - 1 - \mu_{n+1}^2 \mu_{n+1}^3)}{\mu_{n+1}^2 (\mu_{n+1}^3 - \mu_{n+1}^2)} \quad (6.6)$$

Equation (6.6) in fact scales the load to the level at which the most loaded element is loaded just up to its strength, which is typical for SLA as well.

Similar to SLA, the equilibrium state of proportional loading can be reached by scaling  $\lambda_{cur}^2$  due to the way  $\lambda_{cur}^2$  is defined. On the other hand,  $\lambda_{cur}^3$  is needed to obtain the equilibrium state for non-proportional loading.

Moreover, a strongly non-linear situation can also be supported by introducing iterations of Equation (6.6). Hereby, Parameter  $p$  is defined as an adjusted value that varies depending on  $\mu$  to render  $|\mu - 1|$  smaller than  $r$ . Actually,  $p$  is smaller than 1 when  $\mu$  is larger than 1, and vice versa.

$$\lambda_{cur}^m = \lambda_{cur}^1 \frac{(2\mu_{n+1}^2 - 1 - \mu_{n+1}^2 \mu_{n+1}^3)}{\mu_{n+1}^2 (\mu_{n+1}^3 - \mu_{n+1}^2)} p^{m-3} \quad (6.7)$$

where  $m$  is current number of cycles. After several loops,  $\mu$  can be almost 1. In addition, the stiffness reduction factor should be set close to 1 for accuracy. Figure 6.1 shows the program structure diagram for the damage control method with load scaling control.

6

## 6.2. LOAD AND DAMAGE CONTROL METHOD

This section explains how the load factor is reduced within a load step in the load and damage control method, the algorithm of which is shown in Figure 5.9. The principle is to reduce the load factor and the stiffness simultaneously until the stress of the critical element becomes equal to the strength of this element. Two simple load reduction functions are selected, so the load can descend cycle-by-cycle. One is a linear function:

$$\lambda_{cur}^m = \lambda_{cur}^1 (n' - m) / n' \quad (6.8)$$

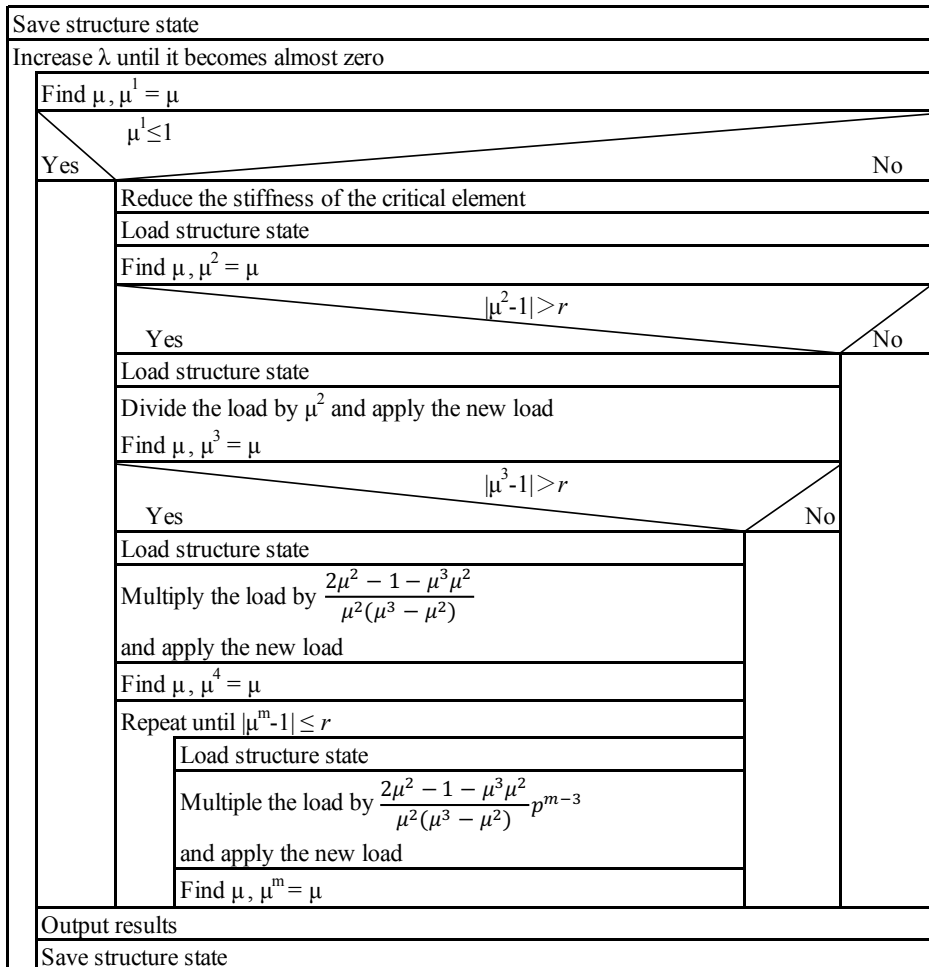


Figure 6.1: Program structure diagram of load scaling control for the damage control method

where  $m$  represents the cycle number and  $n'$  is maximum number of cycles. The other is an exponential function:

$$\lambda_{cur}^m = \lambda_{cur}^1 q^{m-1} \quad (6.9)$$

where  $q$  is the load reduction factor, which should be smaller than 1.

Figure 6.2 shows the stress-strain curve of the saw-tooth model for concrete with linear softening of 1.43 MPa tensile strength and 0.002 ultimate strain. The strength can be described in cycles rather than strain. Below is the function of the strength for a certain cycle in a certain load step.

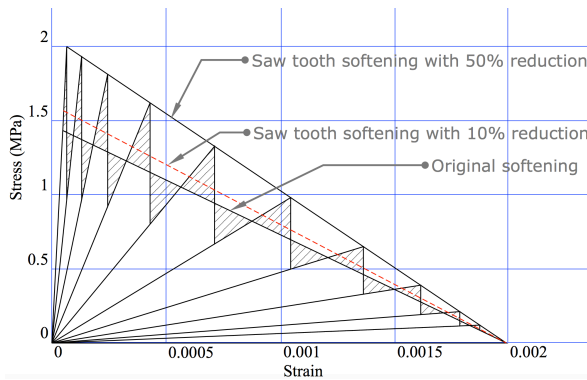


Figure 6.2: Stress-strain curve of the saw-tooth model

6

$$f(m) = \frac{f_t \epsilon_u E t^m t^{m'}}{\left(\epsilon_u - \frac{f_t}{E}\right) E t^m t^{m'} + f_t} \quad (6.10)$$

where  $E$  is Young's modulus,  $f_t$  is the tensile strength, and  $\epsilon_u$  is the ultimate strain for linear softening.  $E t^{m'}$  is the initial stiffness for a certain load step. The initial value for  $m'$  is 0 for the undamaged state. The decreasing rate of strength depends on the stiffness reduction factor  $t$ . This function is derived from a linear softening diagram as in Figure 6.2.

For the load to meet the capacity, the decreasing rate of the load factor has to be larger than that of the stiffness. The rates depend on the values of  $n$ ,  $q$  in the decreasing function and the stiffness reduction factor  $t$ .

A one element example has been studied (concrete with linear softening of 1.43 MPa tensile strength and 0.002 ultimate strain). The initial stiffness reduction factor

**6**

$t$  is 0.95,  $n$  is 100 and  $q$  is 0.95. Only one load step is considered, and there is no damage beforehand. The initial stresses vary due to different load factors. These two functions have been checked for robustness of three initial stresses. Figure 6.3 (Eq. (6.8)) and Figure 6.4 (Eq. (6.9)) show how the capacity and load decrease in cycles, which are represented by the strength and stress of the critical element. The solid line (Eq. (6.10)) represents the strength, which becomes lower due to the stiffness reduction. The strength drops to almost 0 MPa around Cycle 150. The other lines show the decreasing stress caused by the load reduction procedure with different initial stresses. An equilibrium state is reached when the curves of strength and stress meet at an intersection. For the first function (Figure 6.3), the stress can reach strength after several cycles, even though it is set very high via a loading schedule. A similar result can be obtained for the second function in Figure 6.4. From these figures, it can be concluded that both the linear and exponential functions can provide equilibrium states regardless of how large the initial-load factor is, which is a prerequisite for robustness of the method. Nevertheless, the values of  $n$  and  $q$  must be chosen correctly. In addition, it can be seen that the exponential function requires fewer cycles than the linear function.

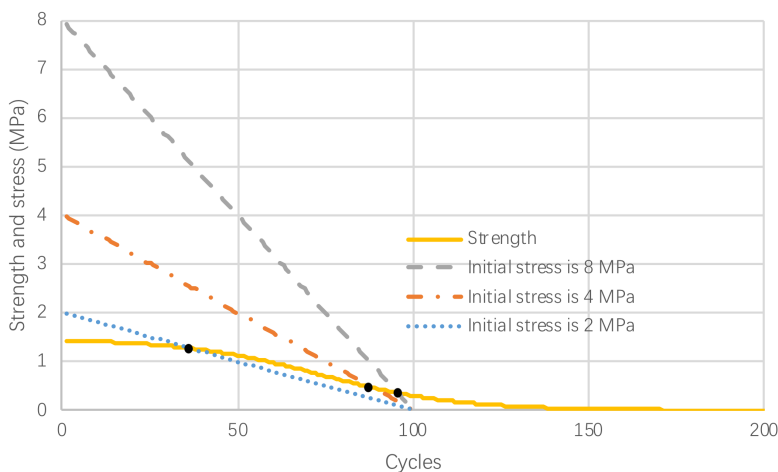


Figure 6.3: Strength function (Eq. (6.10)) and stress due to the linear load function (Eq. (6.8)) for different initial stresses

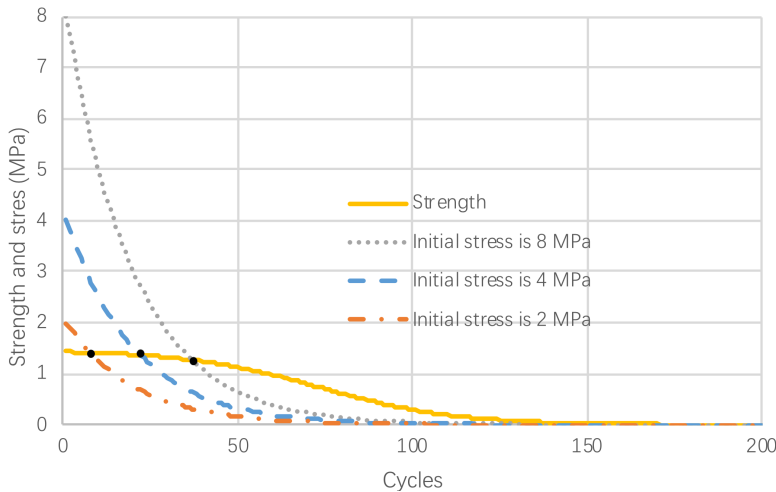


Figure 6.4: Strength function (Eq. (6.10)) and stress due to the exponential function (Eq. (6.9)) for different initial stresses

## 6.3. PARAMETER DETERMINATION FOR LOAD AND DAMAGE CONTROL

In this section, a sensitivity study is performed for the stiffness reduction factor  $t$ , the linear function parameter  $n$  and the exponential function parameter  $q$  to provide suggestions for the parameter values. Only one load step and one critical element are considered, and there is no initial damage.

### 6.3.1. STIFFNESS REDUCTION FACTOR STUDY

In this subsection, Eq. (6.10) is studied. Figure 6.5 shows how the tensile strength changes in cycles when the stiffness reduction factor  $t$  is set to 0.5, 0.9 and 0.95. It can be seen that the strength drops to almost zero around 50, 100 and 150, respectively. In Figure 6.6, the cycle strength curve changes when the beginning stiffness of a certain load step decreases from the undamaged state to certain levels when  $t$  is 0.95. The beginning point of the strength curve shifts to right gradually, along with the stiffness reduction. In other words, the initial strength for a certain load step is the final damaged strength of the previous load step. It can be seen that the strength decreases increasingly faster when the beginning stiffness of a certain load step decreases. Therefore,  $n$ ,  $q$  and  $t$  should be optimized based on stiffness

reduction levels.

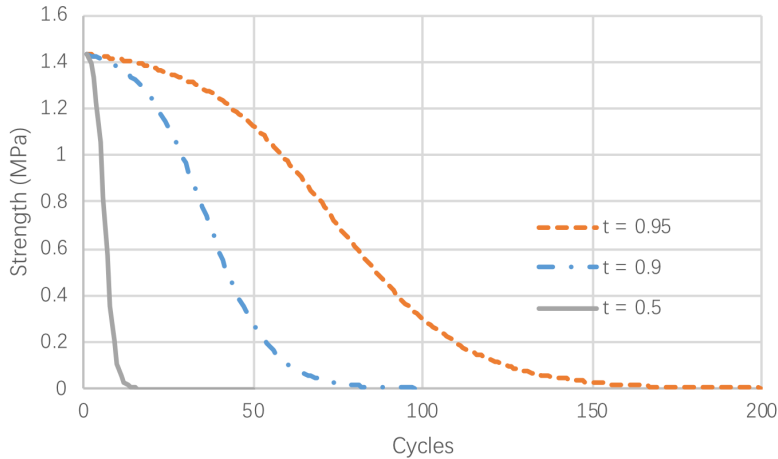


Figure 6.5: Cycle strength curves Eq. (6.10) for different stiffness reduction factors

## 6

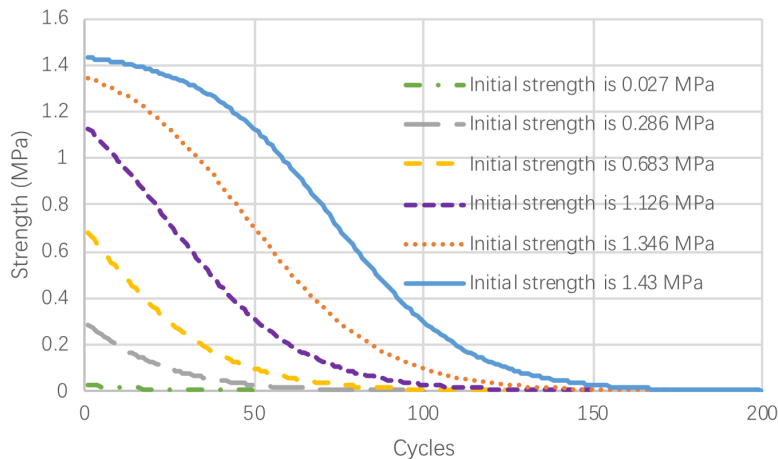


Figure 6.6: Cycle strength curves Eq. (6.10) for different initial stiffnesses

### 6.3.2. LINEAR FUNCTION PARAMETER STUDY

The decreasing rate of the linear function Eq. (6.8) is determined by  $n$ , as shown in Figure 6.7, when  $n'$  is 50, 100 and 200. The initial load factor is set to the value that makes element stress equal to 2 MPa.

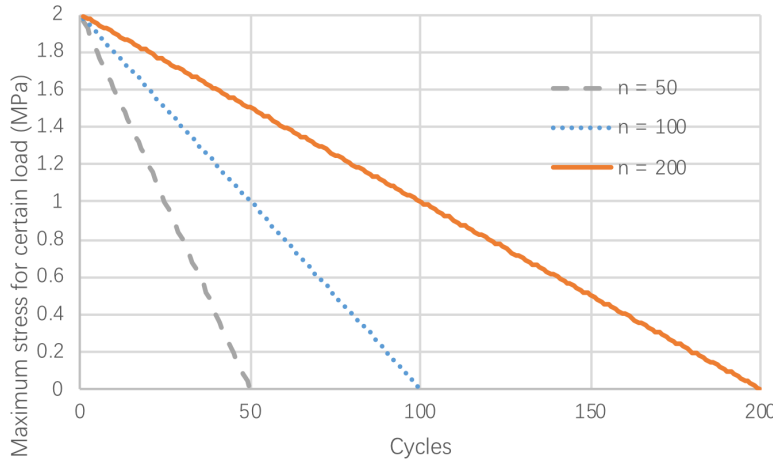


Figure 6.7: Cycle-stress curves for different maximum numbers of cycles  $n$  (linear function Eq. (6.8))

The second-order derivation of Eq. (6.10) is written below.

$$\frac{d^2}{dm^2} f(m) = \frac{-Eln(t)^2\epsilon_u f_t^2(Et^{2m}\epsilon_u - t^m f_t - t^{2m} f_t t)}{(Et^m\epsilon_u - t^m f_t + f_t)^3} \quad (6.11)$$

The initial suggested number for  $n'$  is the value when  $\frac{d^2}{dx^2} f(m)$  is zero. For instance,  $n'$  is 5, 35 and 72 when  $t$  is 0.5, 0.9 and 0.95, respectively. Accounting for accuracy, the minimum stiffness reduction factor  $t$  is 0.75 when  $n'$  is 13 to ensure the maximum number of cycles greater than 10, otherwise the structure is unloaded too much. For an extreme situation, the maximum value  $n$  can be 369 if  $t$  is set to 0.99, which nevertheless involves costly calculations in terms of time. Actually,  $n'$  needs to be reduced when the beginning stiffness for the certain step becomes increasingly smaller. If the calculation efficiency is compromised, using a smaller stiffness reduction factor  $t$  when the value of the utilisation function  $\mu$  is lower than a certain number has a better effect on improving accuracy than adjusting the maximum number of cycles  $n$ .

6

### 6.3.3. EXPONENTIAL FUNCTION PARAMETER STUDY

The decreasing rate of the exponential function Eq. (6.9) is determined by the stiffness reduction factor  $q$ , as shown in Figure 6.8, when  $q$  is 0.9, 0.95 and 0.98. According to Figure 6.8, it takes roughly 50, 100 and 200 cycles for the load to drop to almost zero, respectively. The load needs to decrease faster than the capacity;

therefore, the cycle number when the load is almost zero needs to be smaller than when the capacity is almost zero. Consequently, the suggested default number for  $q$  is 0.95 when  $t=0.9$  while it is 0.98 when  $t=0.95$ . Similarly,  $q$  also needs to be reduced when the beginning stiffness for a certain load step becomes increasingly smaller.

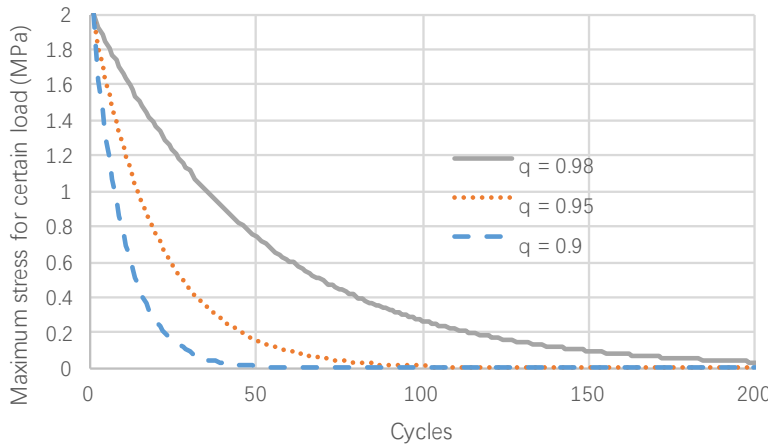


Figure 6.8: Cycle-stress curves for different load reduction factors  $q$  (the exponential function Eq. (6.9))

## 6.4. SINGLE ELEMENT UNIAXIAL TENSILE TEST FOR A LOAD-SCHEDULING

In this section, the damage control method and the load and damage control method with the linear load reduction function and exponential load reduction function are investigated for a single element uniaxial tensile test with a loading schedule rather than one load step as in the previous sections. One beam element with length of 3 m and a cross-section of  $0.00784 \text{ m}^2$  is considered. One node is fixed while a point load is applied at the other node in the beam direction, as in Figure 6.9. The loading schedule for load steps is monotonic loading, and the initial load is 11 kN in Figure 6.10, which determines the load factor of the first cycle of each load step. After the first cycle, the load factor is scaled cycle-by-cycle. Concrete properties with linear softening are selected for testing. Young's modulus is 30000 MPa, and Poisson's ratio is 0.2. The tensile strength is 1.43 MPa, and the ultimate strain is 0.002. Compressive behaviour is elastic, and the stiffness reduction factor is 0.9.



Figure 6.9: FEM model of the tensile test

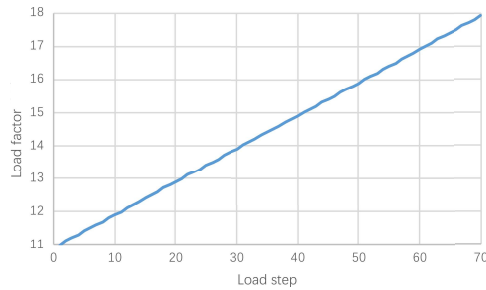


Figure 6.10: Loading schedule of the tensile test

#### 6.4.1. DAMAGE CONTROL METHOD TEST

Only one cycle of load scaling is necessary since proportional static analysis is used. To test the second load scaling procedure, non-proportional loading is introduced by first applying a constant force (10 kN). It can be seen that both results align well with the material properties in Figure 6.11. The maximum stress and strain are both 1.4165 MPa and 0.002. There is slightly lower stress than the tensile strength due to Poisson's ratio. According to Table 6.1 and 6.2, non-proportional loading takes one additional cycle to achieve a utilisation value of 1. Due to the constant force applied first, the load-step factor curve for non-proportional loading shifts vertically down from that for proportional loading in Figure 6.12.

Table 6.1: Utilisation values along with load steps and cycles for proportional loading

Load step	1	2	3	3	4	4	5	5	6	6
Cycle	1	1	1	2	1	2	1	2	1	2
Utilisation value	0.991	1	1.009	1	1.026	1	1.045	1	1.069	1
Load step	7	7	8	8	9	9	10	10	11	11
Cycle	1	2	1	2	1	2	1	2	1	2
Utilisation value	1.098	1	1.133	1	1.178	1	1.236	1	1.31	1
Load step	12	12	13	13	14	14	15	15	16	16
Cycle	1	2	1	2	1	2	1	2	1	2
Utilisation value	1.406	1	1.533	1	1.701	1	1.922	1	2.218	1
Load step	17	17	18	18	19	19	20	20	21	21
Cycle	1	2	1	2	1	2	1	2	1	2
Utilisation value	2.611	1	3.137	1	3.84	1	4.782	1	6.045	1
Load step	22	22	23	23	24	24	25	25	26	26
Cycle	1	2	1	2	1	2	1	2	1	2
Utilisation value	7.738	1	10.009	1	13.057	1	17.148	1	22.638	1

6

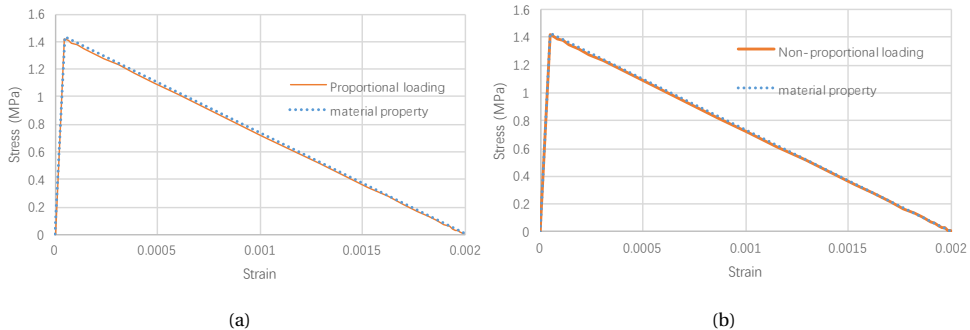


Figure 6.11: Stress-strain curves for proportional loading and non-proportional loading. Both overlap with the material property

#### 6.4.2. LOAD AND DAMAGE CONTROL

##### LINEAR LOAD REDUCTION FUNCTION TEST

Two extreme situations in which the stiffness reduction factors are 0.75 at the lowest and 0.99 (close to 1) are added to the test, as well as a default value of 0.9. The maximum number of cycles  $n'$  for 0.99 is 100, which is sufficiently accurate with a maximum allowance of 369.  $n'$  is 35 when  $t$  is 0.9, while  $n'$  is 13 when  $t$  is 0.75. The stress-strain curve is nearly the same as the material property when the reduction factor is 0.99 (Figure 6.13). For both situations, when  $t$  is 0.9 and 0.75, there are some

Table 6.2: Utilisation values along with load steps and cycles for non-proportional loading

Load step	1	1	1	2	2	2	3	3	3	4	4	4
Cycle	1	2	3	1	2	3	1	2	3	1	2	3
Utilisation value	1.891	1.424	1	1.915	1.434	1	1.944	1.445	1	1.98	1.46	1
Load step	5	5	5	6	6	7	7	7	8	8	8	8
Cycle	1	2	3	1	2	3	1	2	3	1	2	3
Utilisation value	2.025	1.479	1	2.083	1.504	1	2.157	1.536	1	2.253	1.578	1
Load step	9	9	9	10	10	10	11	11	11	12	12	12
Cycle	1	2	3	1	2	3	1	2	3	1	2	3
Utilisation value	2.38	1.633	1	2.546	1.706	1	2.765	1.802	1	3.055	1.93	1
Load step	13	13	13	14	14	14	15	15	15	16	16	16
Cycle	1	2	3	1	2	3	1	2	3	1	2	3
Utilisation value	3.442	2.1	1	3.956	2.326	1	4.642	2.626	1	5.558	3.026	1
Load step	17	17	17	18	18	18	19	19	19	20	20	20
Cycle	1	2	3	1	2	3	1	2	3	1	2	3
Utilisation value	6.781	3.558	1	8.416	4.267	1	10.602	5.211	1	13.527	6.47	1

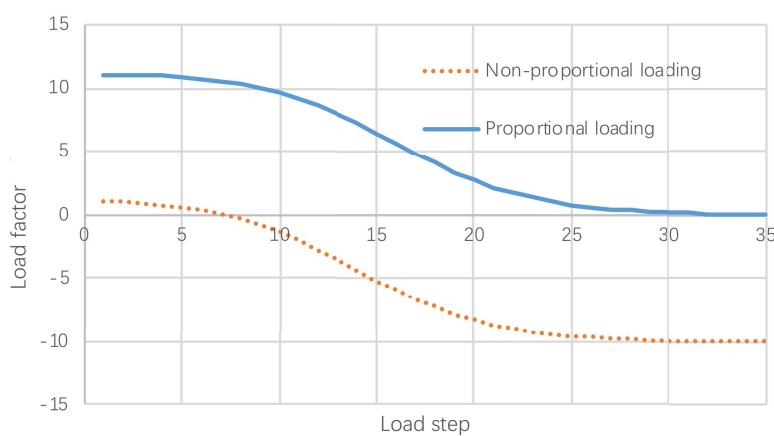


Figure 6.12: Scaled load factor comparison for proportional and non-proportional loading

errors, especially when the stiffness is very small, as in Figure 6.14 and 6.15. A visible error occurs just after the peak when  $t$  is 0.75. This is because  $\mu$  is not exactly 1 for each load step. Table 6.3 provides an example that shows the exact unit check value when the stiffness reduction factor is 0.9. However, due to proportional static analysis, a post-scaling procedure of results is allowed. In this case, the errors are nearly gone in Figure 6.14 and 6.15. After several tests, apart from directly increasing the stiffness reduction factor to almost 1, no clear clues are found in regard to improving the accuracy by only defining the suitable maximum number of cycles  $n'$  for each load step. This is especially tricky because the maximum number is not constant and needs to be reduced when the beginning stiffness of the load steps is being reduced.

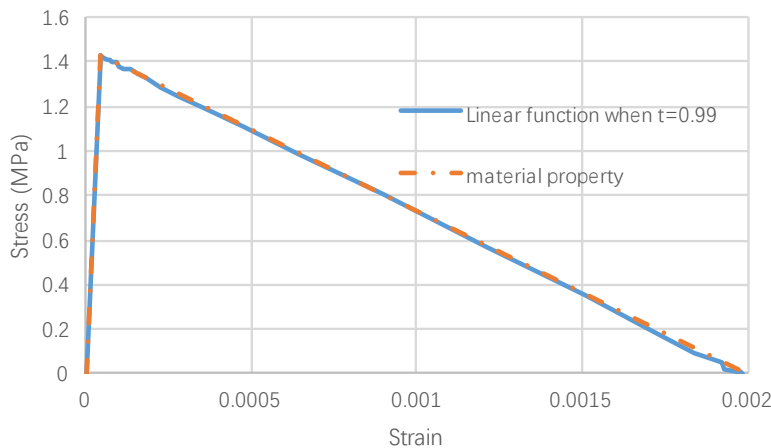


Figure 6.13: Stress-strain curves for linear function Eq. (6.8) when the stiffness reduction factor is 0.99

Table 6.3: Utilisation values for linear function Eq. (6.8) when the stiffness reduction factor is 0.9

Load step	1	2	3	4	5	6	7	8	9	10	11	12
Utilisation value	0.991	1	0.982	0.994	0.98	0.997	0.991	0.998	0.995	0.961	0.881	0.992
Load step	13	14	15	16	17	18	19	20	21	22	23	24
Utilisation value	0.889	0.895	0.899	0.901	0.902	0.903	0.903	0.903	0.903	0.903	0.903	0.903
Load step	25	26	27	28	29	30	31	32	33	34	35	36
Utilisation value	0.903	0.903	0.903	0.903	0.903	0.903	0.903	0.903	0.903	0.903	0.903	0.903

The accuracy can be improved by increasing the stiffness reduction factor when the unit check number becomes smaller than a certain value, such as 1.05. In this case, the stiffness reduction factor would be set to 0.995 when the utilisation

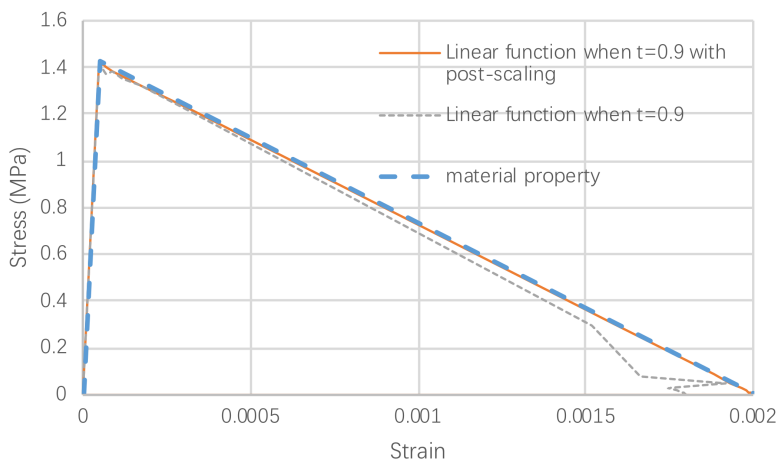


Figure 6.14: Stress-strain curves for linear function Eq. (6.8) when the stiffness reduction factor is 0.9 with and without post-scaling

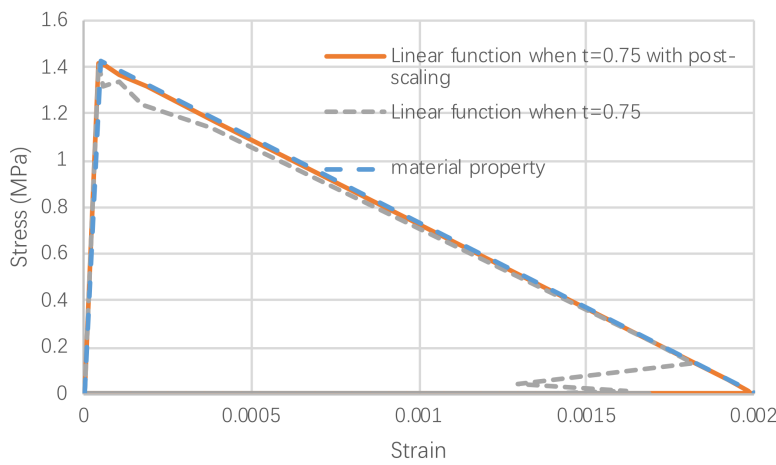


Figure 6.15: Stress-strain curves for linear function Eq. (6.8) when the stiffness reduction factor is 0.75 with and without post-scaling

value is lower than 1.05. Figure 6.16 shows the accuracy is improved by this procedure. The effort is noticeable when the stiffness is small, which nevertheless costs more cycles.

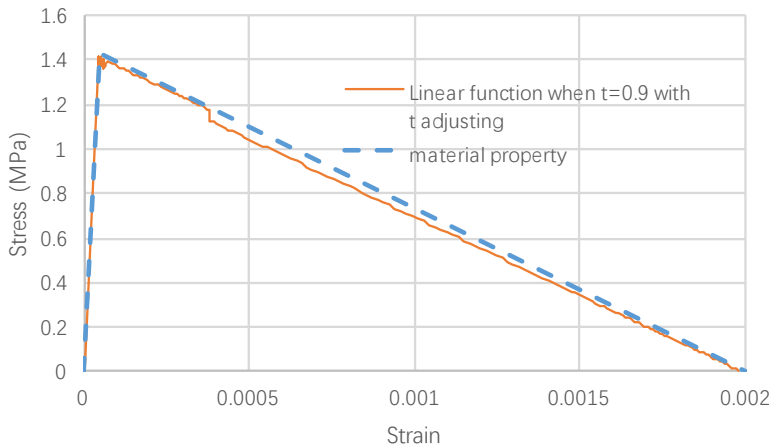


Figure 6.16: Stress-strain curves for linear function Eq. (6.8) with a stiffness reduction factor that is initially 0.9 and 0.995 when then unit check value is lower than 1.05

6

#### EXPONENTIAL LOAD REDUCTION FUNCTION TEST

Since the stiffness reduction factor is 0.9, the exponential load reduction function factor is 0.95. The curve in Figure 6.17 shows good alignment with the material properties. To be more exact, the utilisation value for each load step is 0.977, which is the constant and has a smaller error, rather than a fluctuating and larger error from the linear load reduction function. Speaking of efficiency, the exponential load reduction function costs more cycles than the linear one when the beginning stiffness of a certain load step is high (Load step 3). However, the same number of cycles remains afterwards, while the cycle number for the linear load reduction function is augmented, as well as errors (Load step 21).

Table 6.4: Utilisation value change in cycles for different functions for Load step 3

Cycle	1	2	3	4	5	6	7	8
Linear function	1.009	0.982						
Exponent function	1.009	1.016	1.008	1.2	1.14	1.083	1.029	0.977

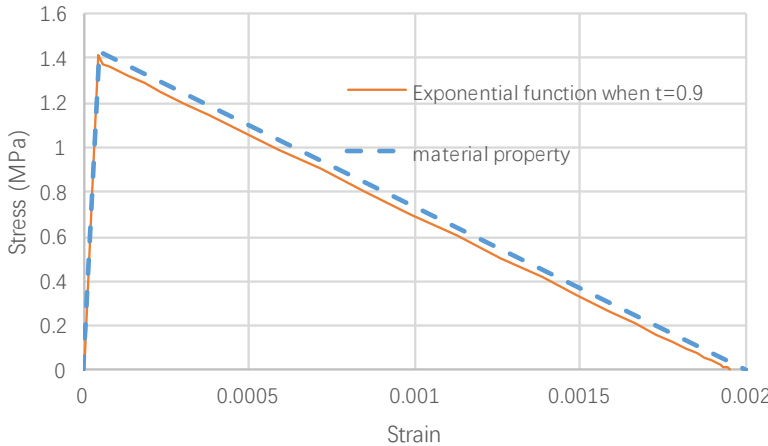


Figure 6.17: Stress-strain curves for exponential function Eq. (6.9) when the stiffness reduction factor is 0.9

Table 6.5: Utilisation value change in cycles for different functions for Load step 21

Cycle	1	2	3	4	5	6	7	8	9	10	11	12	13	14	15
Linear function	5.064	1.231	1.26	1.287	1.31	1.328	1.339	1.342	1.334	1.312	1.275	1.217	1.136	1.025	0.881
Exponent function	6.045	7.679	1.77	1.2	1.14	1.083	1.029	0.977							

6

## 6.5. OPTIMIZATION

This section focuses on the optimization of load scaling control. Since the utilisation value  $\mu$  represents the relationship between the structure capacity and loads, an optimized scheme is proposed based on  $\mu$  to ensure accuracy and efficiency.

In general, when  $\mu$  is larger than a value such as 2, the load factor is multiplied by a function related to  $\mu$ , such as  $1.2/\mu$ , for both methods. This situation means that the applied load is too large compared with the current capacity of the structure. Actually, it is recommended that an initial-load factor amplitude like  $\lambda_2^{n+1} = 1.1\lambda_2^n$  is applied to the load increment for a load step rather than following a loading schedule.

For stiffness reduction, the residual stiffness is set to improve the efficiency, which can be 0.1% of the initial stiffness or the ratio of the residual stress and the ultimate strain. Subsequently, the stiffness can be reduced by a large stiffness reduction factor or directly set as an extremely small value, which can be determined by the ratio of the residual stress and the strain related to the crack band and the maximum crack width.

As for the damage control method, only an initial load factor amplitude  $e$  larger than 1 and a stiffness reduction factor  $t$  smaller than 1 are necessary for optimization since load scaling control is based on an extrapolation procedure. Figure 6.18 shows the optimized scheme for the damage control method, in which  $x$  and  $j$  control  $e$  and  $t$  separately. Indeed  $e$  and  $t$  are supposed to be reduced by  $x$  and  $j$  separately when  $\mu$  increases to a certain value like  $a$ .

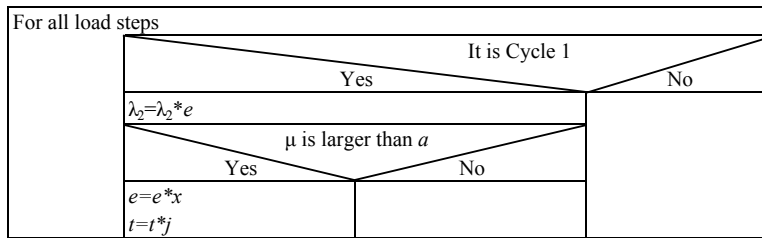


Figure 6.18: Optimized load scaling control for the damage control method

6

For the load and damage control method, the exponential load reduction function is adopted based on test results from the previous section. It can be seen that the exponential load reduction function is more robust and accurate than the linear load reduction function although it is less efficient than the linear load reduction function when the stiffness is nearly unchanged. Apart from the initial load factor amplitude  $e$  and stiffness reduction factor  $t$ , the load scaling control procedure should also be optimized. Figure 6.19 shows the optimization scheme for the load and damage control method. Four variables smaller than 1 ( $f$ ,  $g$ ,  $h$  and  $i$ ) are introduced to replace  $q$  in the exponential function (6.9), which depends on  $\mu$ . Actually,  $q$  needs to be increasingly closer to 1 when  $u$  becomes increasingly closer to 1, which is determined by the boundaries  $b$ ,  $c$  and  $d$ . However,  $q$  cannot be extremely close to 1 because the decrease rate for load factors must be greater than the decrease rate for stiffness, otherwise  $\mu$  would be always larger than 1. In addition, these four variables should also be decreased by  $y$  (smaller than 1) when  $\mu$  of the initial load factor is larger than  $a$ .

Moreover, a similar scheme can also be introduced to increase the load factor when  $\mu$  is smaller than a certain value, for instance 0.9, to prevent a situation in which the load factor is reduced too much.

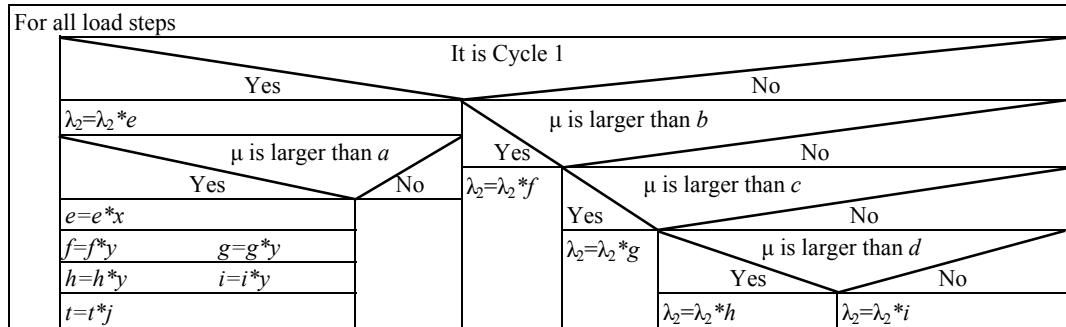


Figure 6.19: Optimized load scaling control for the load and damage control method

## 6.6. DISCUSSION

In this chapter, load scaling control is elaborated for ISLA. Consequently, the after-peak behaviour can be obtained by force control loading. ISLA with the load scaling control method has the possibility of being robust for quasi-brittle materials with force control loading. In addition, load scaling control can be also employed with displacement control loading.

For the damage control method, an extrapolation procedure is employed. This strategy is accurate but requires extra cycles for one stiffness reduction.

For the load and damage control method, the exponential load reduction function Eq. (6.9) is adopted rather than the linear load reduction function Eq. (6.8) due to the balance of efficiency and accuracy. An optimized scheme is implemented based on values of the utilisation function. This load and damage control method is robust and does not increase computation costs because the total number of cycles equals the number of times the stiffness is reduced for all damaged elements. However, its accuracy and efficiency need to be improved. In addition, the accuracy of the linear load reduction function can be improved by lowering the stiffness reduction factor when the utilisation value is smaller than a certain number. For further research, it is recommended that the linear load reduction function and exponential load reduction function be combined based on stiffness reduction to improve the accuracy and efficiency.



# 7

## VALIDATION OF ISLA FOR PROPORTIONAL LOADING

To validate ISLA [13][14] and compare the different methods in the approach, an experiment [124] is used for testing, which involves a simply supported concrete beam with a notch in the middle (Figure 7.1).

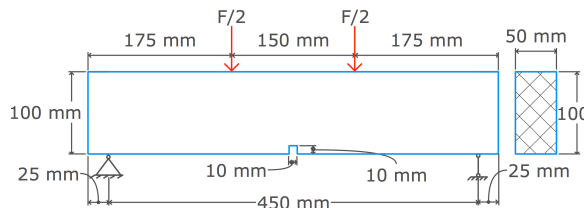


Figure 7.1: Test model of notched beam

For the load control method, a four-point loading scheme is applied in two ways as prescribed displacements and prescribed forces. For the damage control method and the load and damage control method, scaled forces are applied by the load scaling control method.

## 7.1. MATERIAL PROPERTIES AND FEM MODEL

The example considers softening for tension (Figure 7.2). The concrete properties are  $E=32000$  MPa, Poisson's ratio  $\nu=0.2$ , tensile strength  $f_t=3$  MPa and fracture energy  $G_f=0.06$  N/mm. The compressive behaviour is elastic. Eq. (7.1) is used to determine the ultimate strain  $\varepsilon_u$  of the tensile strain-softening diagram, as a function of the crack band width. Figure 7.2 shows the colour range of the horizontal tensile strain contours.

$$\varepsilon_u = \frac{2G_f}{f_t h} \quad (7.1)$$

where the crack band width  $h$  is related to the element size. Four-node plane-stress elements are used. The element size is 10 mm<sup>1</sup>. For the square linear finite elements of the present example,  $h$  is suggested to be equal to the length of the size of the finite element.

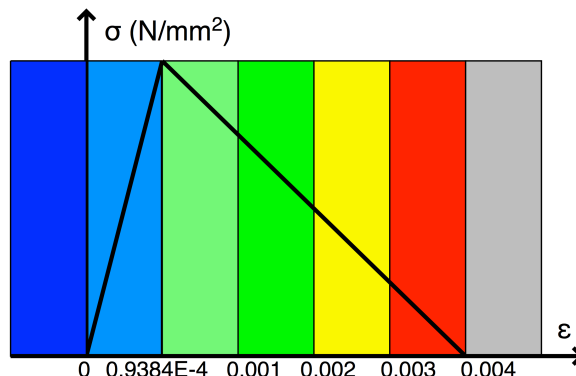


Figure 7.2: Tensile stress-strain curve and contour colour range for concrete

Figure 7.3 shows the stiffness reduction when Young's modulus is sequentially reduced to 90% of the previous value. The default residual stiffness is set as 0.1% of

<sup>1</sup>In all beam analyses, the element size is 5 mm except for the analysis in this chapter, where it is 10 mm. The explanation for this is as follows. The 10-mm elements with one integration point match the 10-mm notch. As a consequence, the damage is distributed over the width of the notch and can be interpreted to occur in the middle of this width. This situation is symmetrical with respect to the stress trajectories. The symmetrical crack pattern can be well understood. In addition, ISLA is programmed on ANSYS, in which the material properties can be changed at the element level instead of the integration point. Therefore, to investigate the stress-strain behaviour of the integration point, the quadratic elements with four integration points used in other chapters are replaced by the linear elements with one integration point. However, a 5-mm mesh produces essentially the same results as quadratic elements.

the initial stiffness, compared with 0.001% of the initial stiffness. Subsequently, the stiffness is set as 0.12 MPa, the corresponding crack width of which is 10 mm.

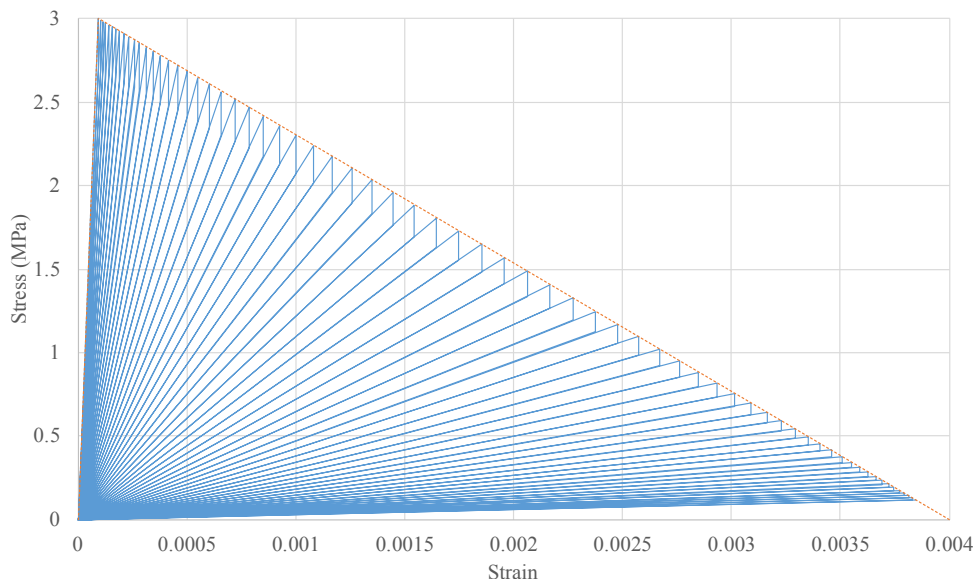


Figure 7.3: Sequentially reduced stiffness to 90% of the previous value

7

Just one integration point is used in the elements above the notch while the other elements have four integration points. Only the elements above the notch can be damaged, and others are kept elastic. Figure 7.4 identifies nine elements above the notch. For Elements 1, 3, 6 and 8, detailed results are shown.

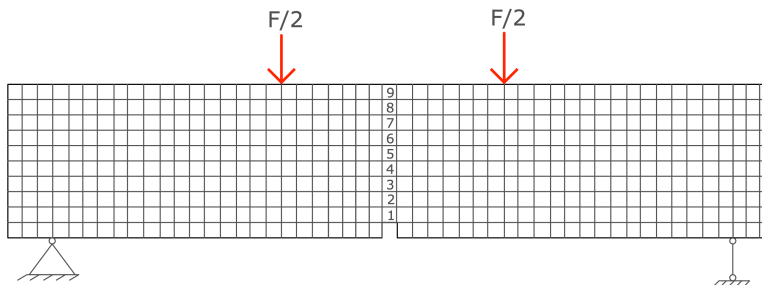
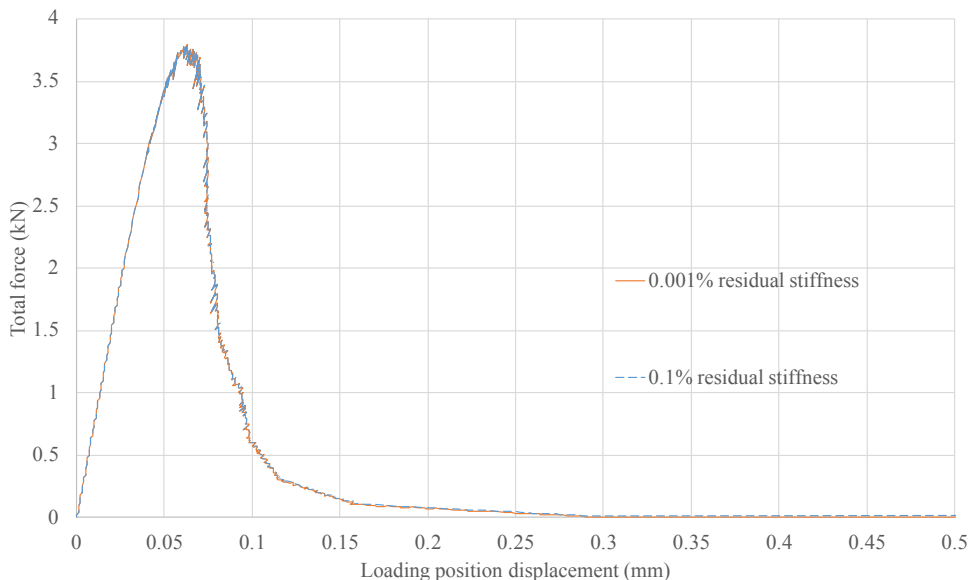


Figure 7.4: Finite element mesh and element numbers ahead of the notch

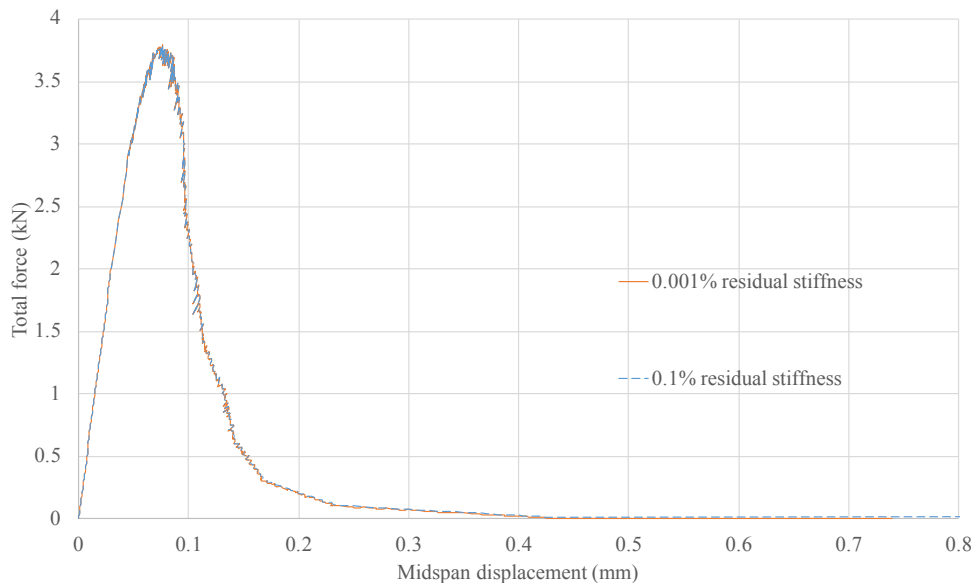
## 7.2. DAMAGE CONTROL FOR THE SCALED FORCE TEST

In this section, a scaled force loading test is performed by the damage control method, as elaborated in Figure 5.13, to trace post-peak behaviour. Two-point loads are applied, as shown in Figure 7.1. Results are outputted until the loading position displacement is 0.5 mm. The stiffness reduction factor is 0.9, and residual stiffness is compared to 0.1% and 0.001% of the initial stiffness.

Figure 7.5 shows the force-displacement diagrams of the damage control for the loading position and midspan separately with different residual stiffnesses. It can be seen that the two diagrams overlap each other, indicating good accuracy for both residual stiffnesses. However, the total number of cycles dramatically increases from 1,605 for 0.1% residual stiffness to 4,146 for 0.001% residual stiffness. The number of cycles is three for all load steps. For non-proportional loading, the number of cycles for all load steps increases to four. There is no error for the utilisation function, so the diagram of the damage control is used to compare this with other methods in terms of accuracy.



(a) Displacements selected from the loading position



(b) Displacements selected from the bottom of the beam midspan

Figure 7.5: Load-displacement diagrams of damage control with different residual stiffnesses

### 7.3. LOAD CONTROL FOR THE IMPOSED DISPLACEMENT TEST

In this section, an imposed displacement loading test is performed by the load control method, as elaborated in Figure 5.10. Two-point loads are applied, as shown in Figure 7.1. Figure 7.6 indicates the step size of imposed displacements.

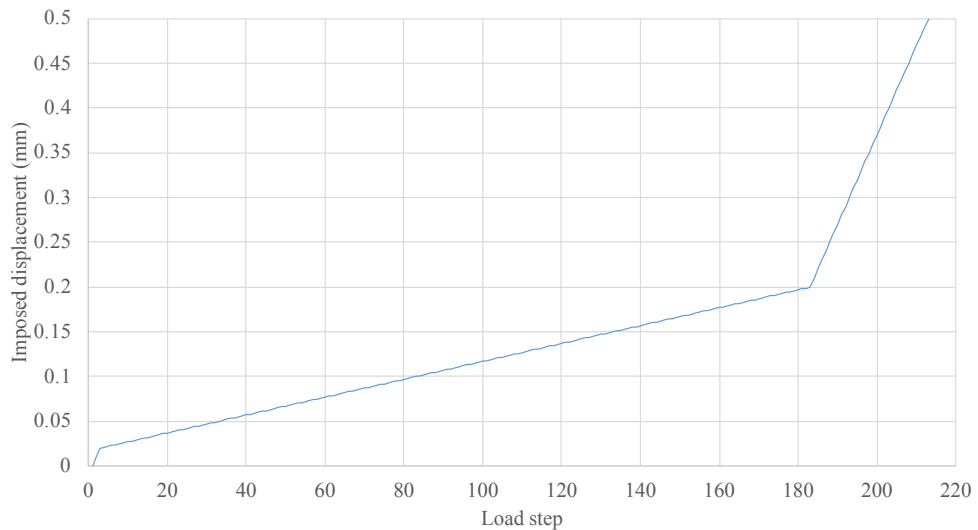


Figure 7.6: Loading schedule with imposed displacement load steps of 0.01(2), 0.001(180) and 0.01(30) mm

Figure 7.7 shows the force-displacement diagrams obtained from 212 load steps for the damage control method and load control method (midspan and loading position separately). It can be seen that the two diagrams overlap each other, indicating good accuracy for both methods. The only difference is that the damage control method has traced snap-backs while the displacement from the load control method increases monotonically. The selected steps are indicated for post-processing. When the displacement increment is amplified by magnitudes of 2 and 5, Figure 7.8 shows the comparison of different load increments in the load control method. It can be seen that the objectivity of load increments is achieved in for load control.

Figure 7.9 shows the deformation and damage for six values of the displacement load. It can be observed that the crack starts at the notch and slowly grows upwards. The horizontal tensile strain contour shows the damage process.

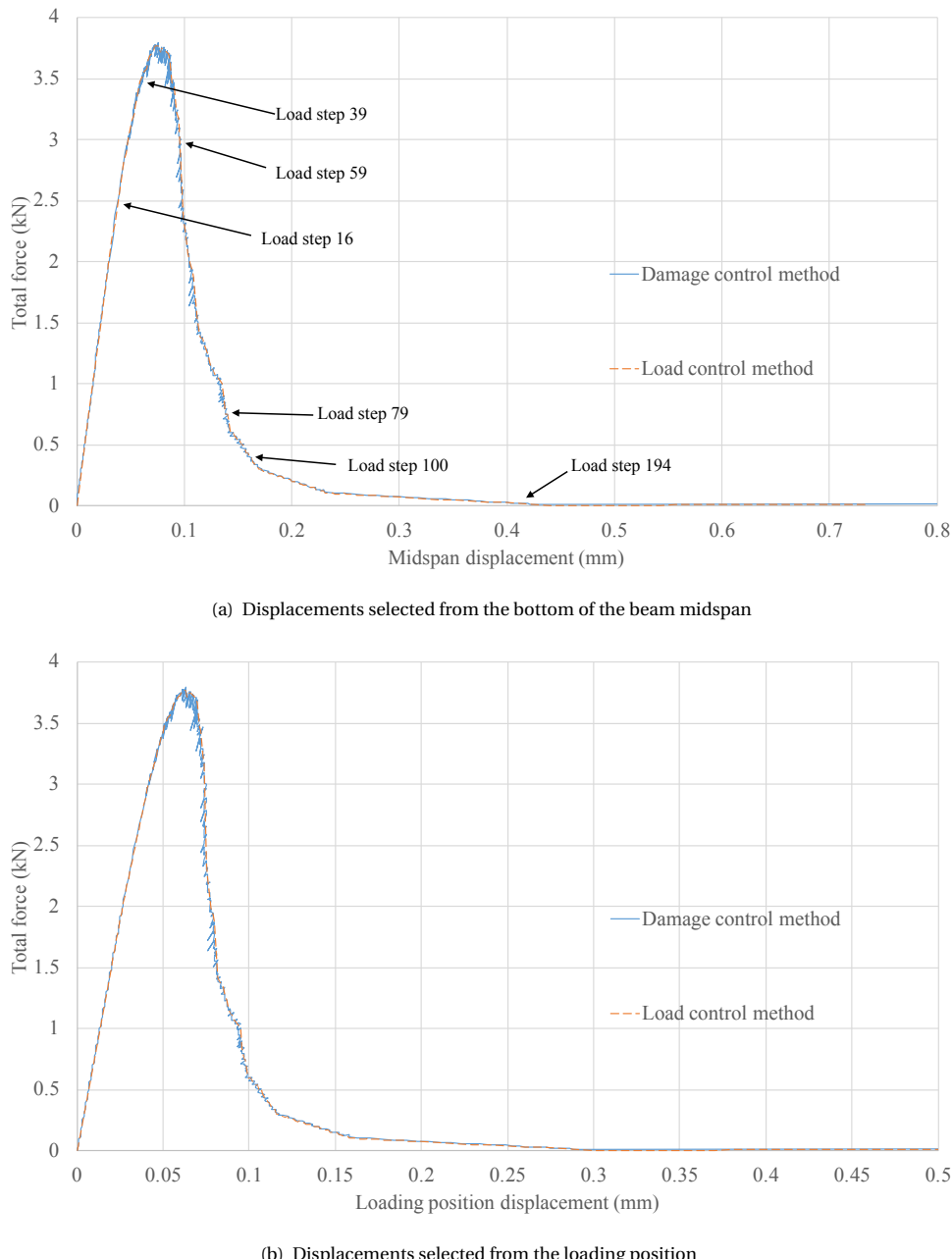
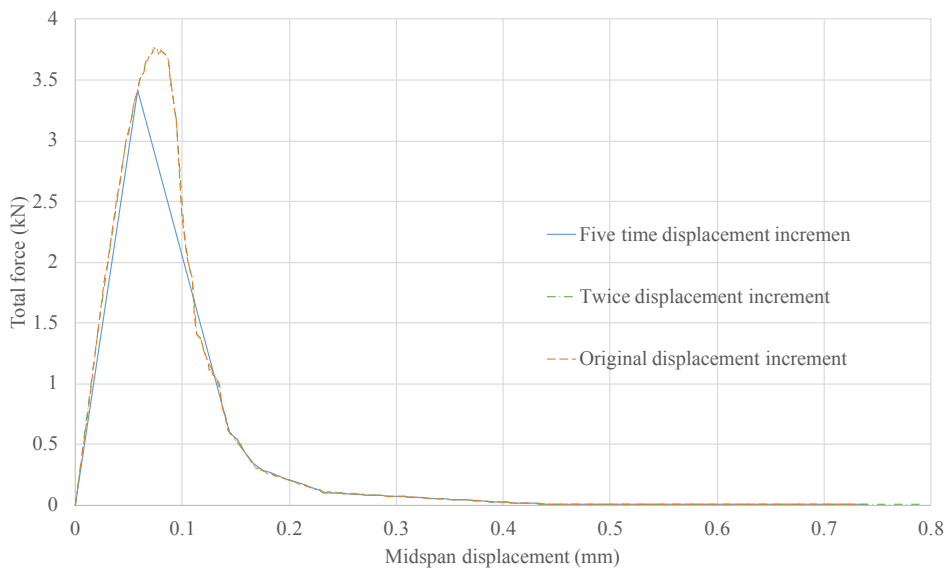
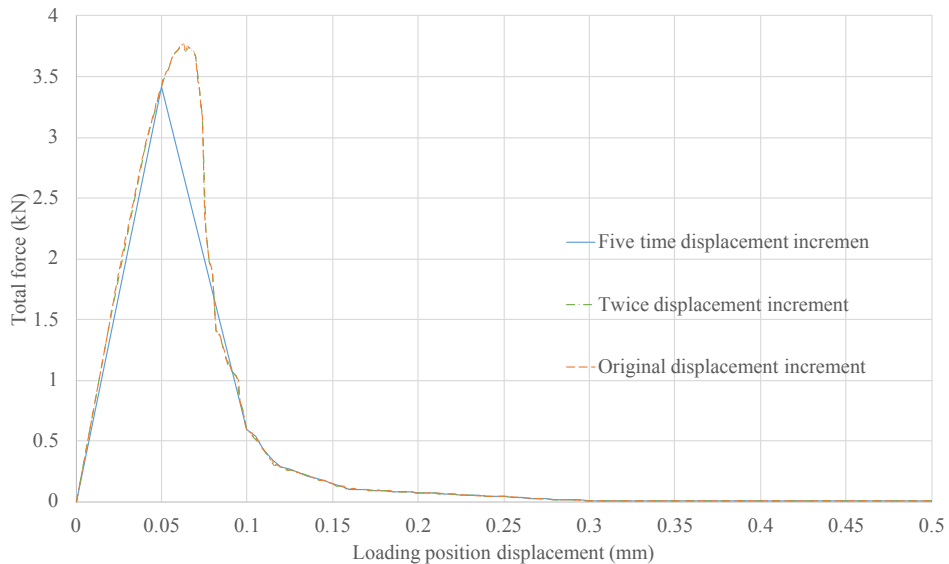


Figure 7.7: Load-displacement diagrams of the notched beam test for the load control and the damage control methods: (a) total force versus midspan displacement and (b) total force versus loading position displacement



(a) Displacements selected from the bottom of the beam midspan



(b) Displacements selected from the loading position

Figure 7.8: Load-displacement diagrams of the notched beam test for different displacement increments in the load control method

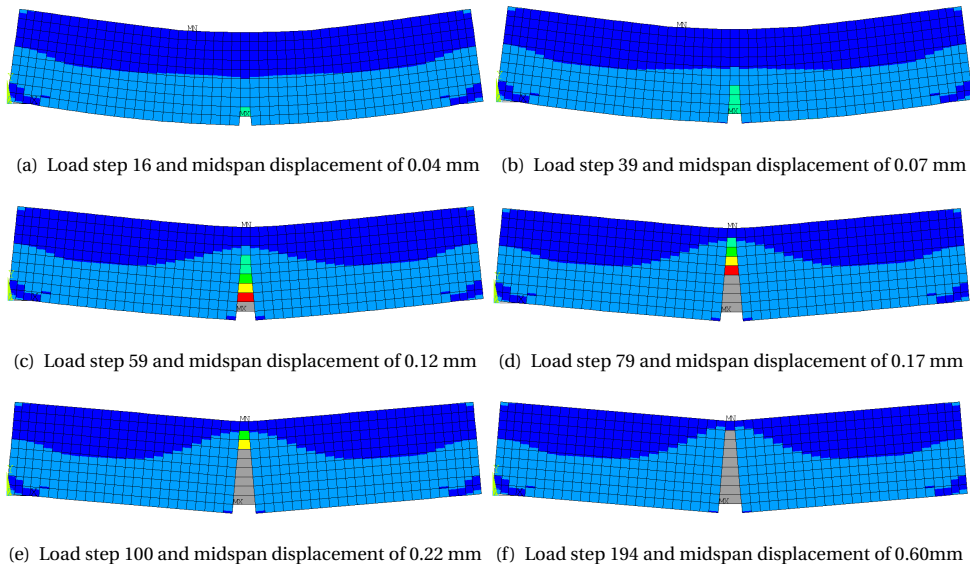


Figure 7.9: Horizontal tensile strains (x-direction, strain contour) for six positions marked in Figure 7.7 (imposed force loading)

Figure 7.10 shows the principal tensile stress-strain results for element 1. The blue dots show the principal stress and principal strain in the element integration point for all 212 load steps. Strains larger than 0.005 are not displayed. The red line is the defined envelope of the material tensile stress-strain curve. The dots are sometimes below the curve because the crack grows in small jumps, which causes local unloading. If the load steps and stiffness reductions were infinitely small, then all the blue dots would be exactly on the red curve. In real tests, the cracks also grow in small jumps, but this is related to material inhomogeneity instead of step size of computational stiffness. The boxes labelled a to d are zoomed-in in Figures 7.11 to 7.14.

Figures 7.11 to 7.14 shows the development of cycles in the four load steps (indicated by a to d) on the stress-strain curve in Figure 7.10. The figure shows how the present algorithm works by going from one equilibrium state to another cycle-by-cycle. Figure 7.14 shows the stress redistribution procedure and the difference between a stiffness reduction in element 1 and a stiffness reduction in another element or multiple other elements. When element 1 is the critical element, the stiff-

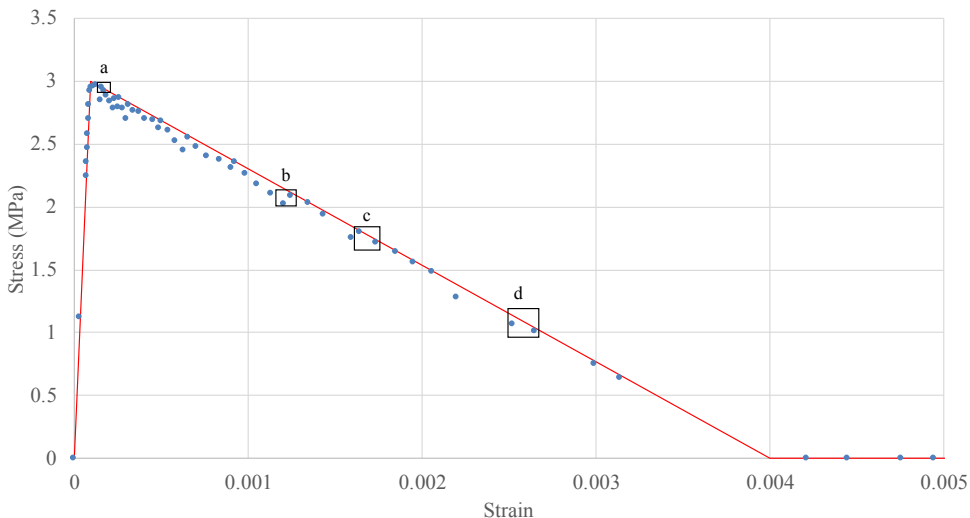


Figure 7.10: Principal tensile stress versus principal tensile strain of element 1 for the load control method with imposed displacement loading

7

ness of element 1 is reduced and its stress decreases. When another element is critical, the stiffness of element 1 remains constant and its stress increases. This can be observed in Figure 7.11 (one reduction), Figure 7.13 (one reduction) and Figure 7.14 (three reductions), while Figure 7.12 shows no reduction for element 1. In a similar way, the results of elements 3, 6 and 8 are shown in Figures 7.15 to 7.17, respectively. Note that when the damaged element is not critical in current cycle, the stress and strain of this element are below the target softening curve due to the failure criterion that the critical element is on the target softening curve.

Figure 7.18 shows the stress and strain situations of the considered elements at the six load steps marked in Figure 7.10. It can be observed that the damage progresses correctly and sequentially along the material curve. These figures are consistent with the crack strain patterns in Figure 7.9.

Figure 7.19 shows the number of cycles for all load steps, the total of which is 749. It can be seen that Load step 59 has the maximum number of cycles (71). This load step corresponds to a significant redistribution and crack growth just beyond the peak. The critical element number fluctuates from 1 to 6, as shown in Figure 7.20, for Load step 59. Element 1 remains critical in most cycles (19), followed by Element 6 (14). Figure 7.21 shows errors of the utilisation function for all load steps

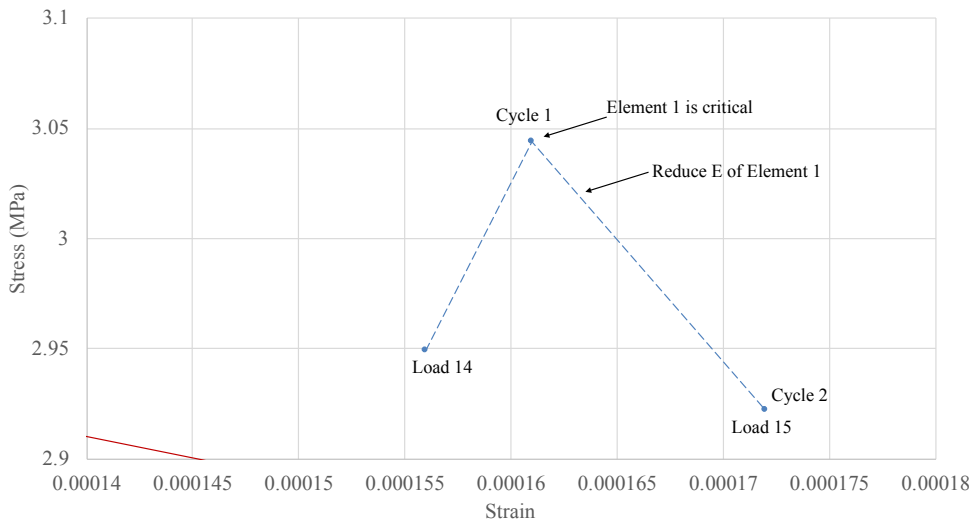


Figure 7.11: Enlargement of area a in Figure 7.10 (two cycles in Load step 15)

7

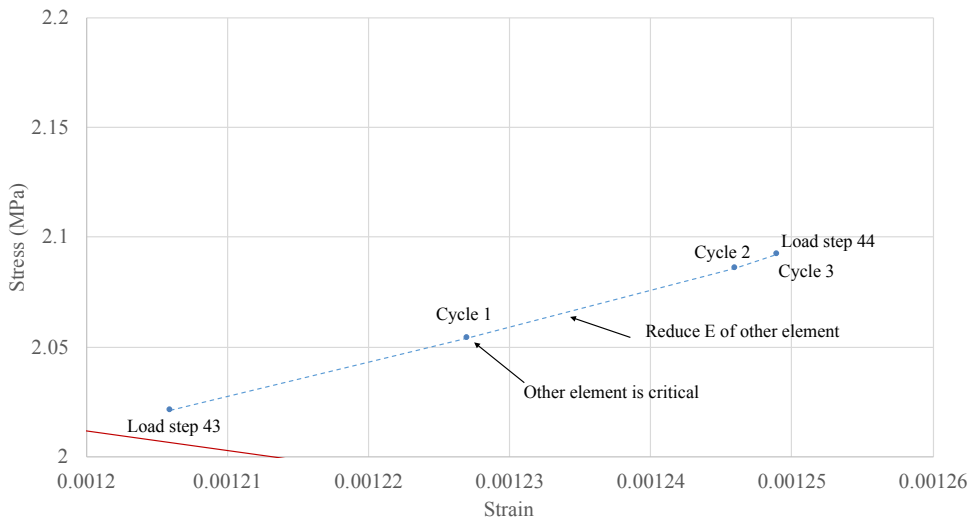


Figure 7.12: Enlargement of area b in Figure 7.10 (three cycles in Load step 44)

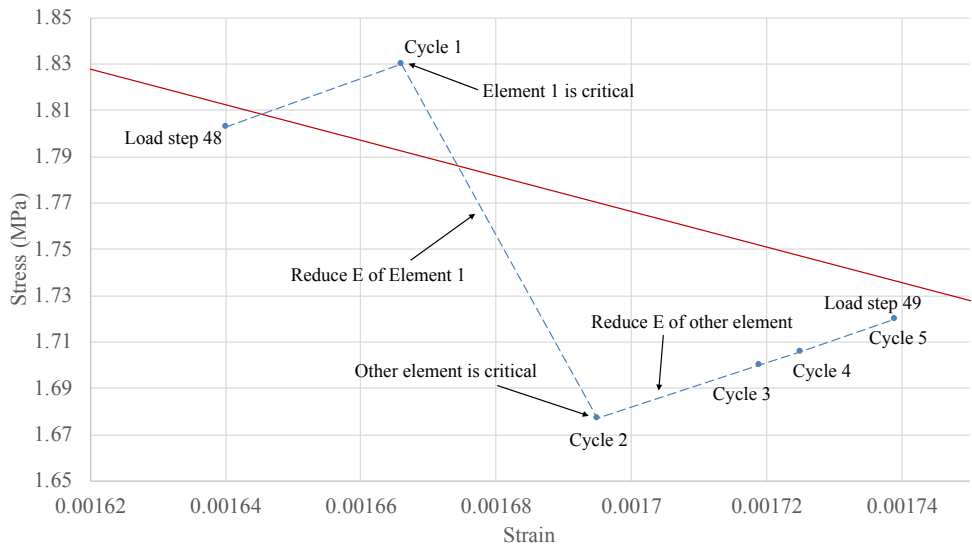


Figure 7.13: Enlargement of area c in Figure 7.10 (five cycles in Load step 49)

7

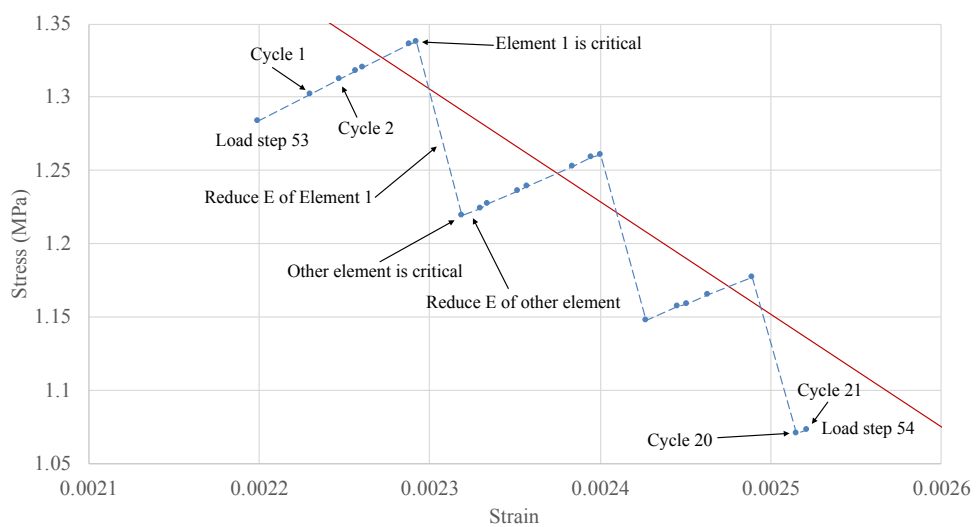


Figure 7.14: Enlargement of area d in Figure 7.10 (21 cycles in Load step 54)

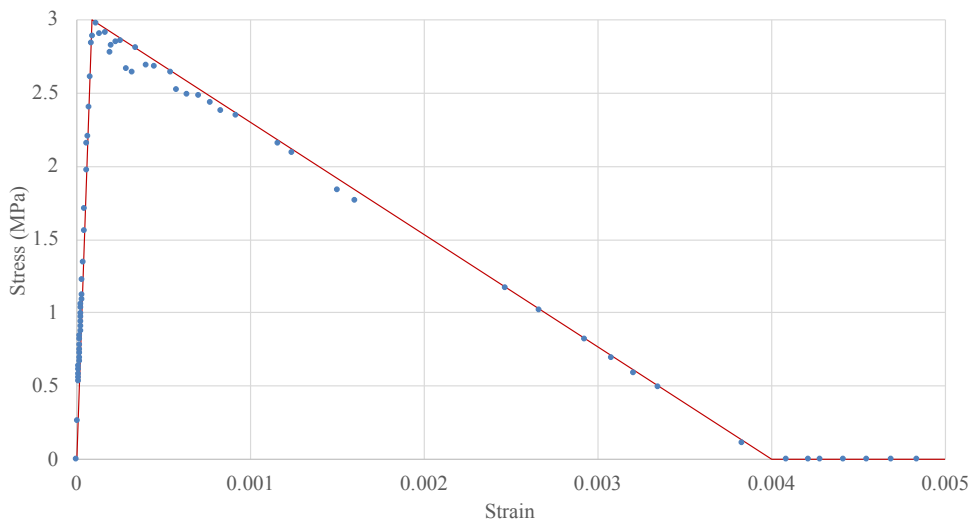


Figure 7.15: Principal tensile stress versus principal tensile strain of element 3 for the load control method with imposed displacement loading

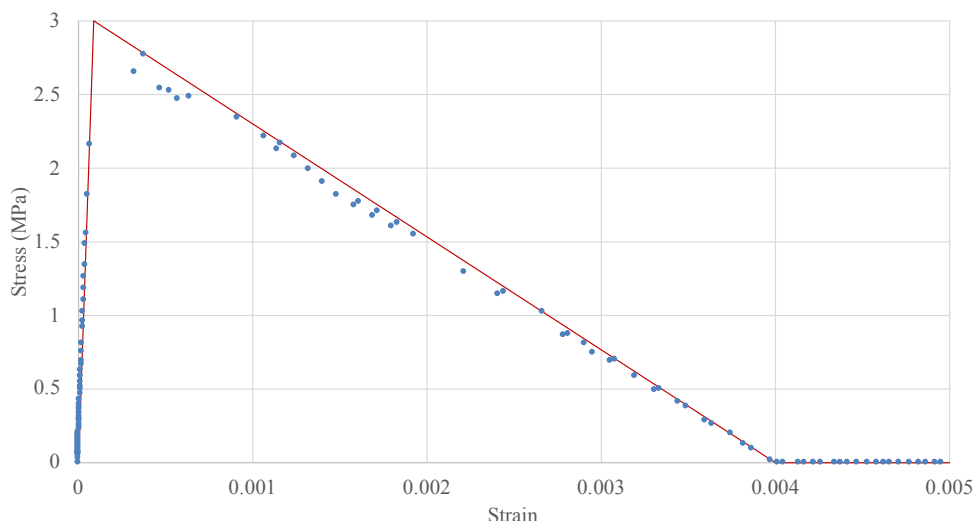


Figure 7.16: Principal tensile stress versus principal tensile strain of element 6 for the load control method with imposed displacement loading

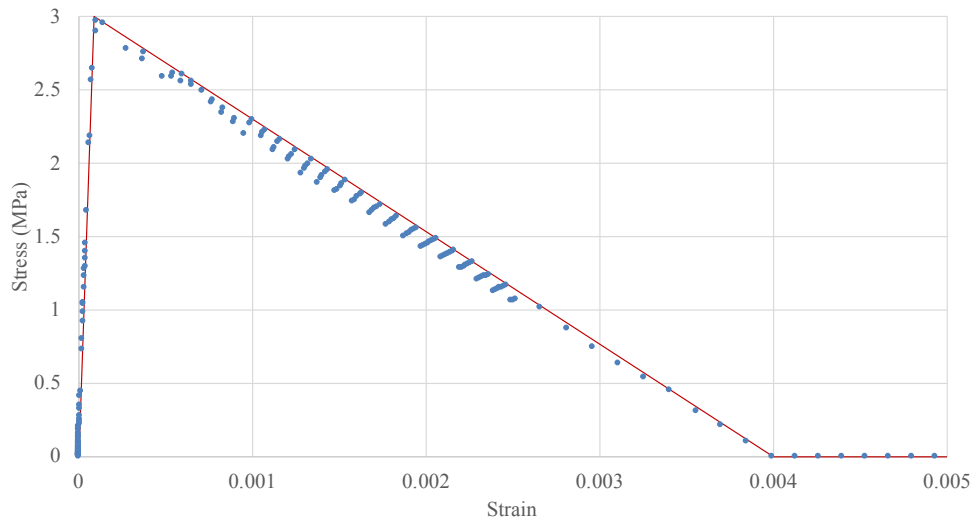
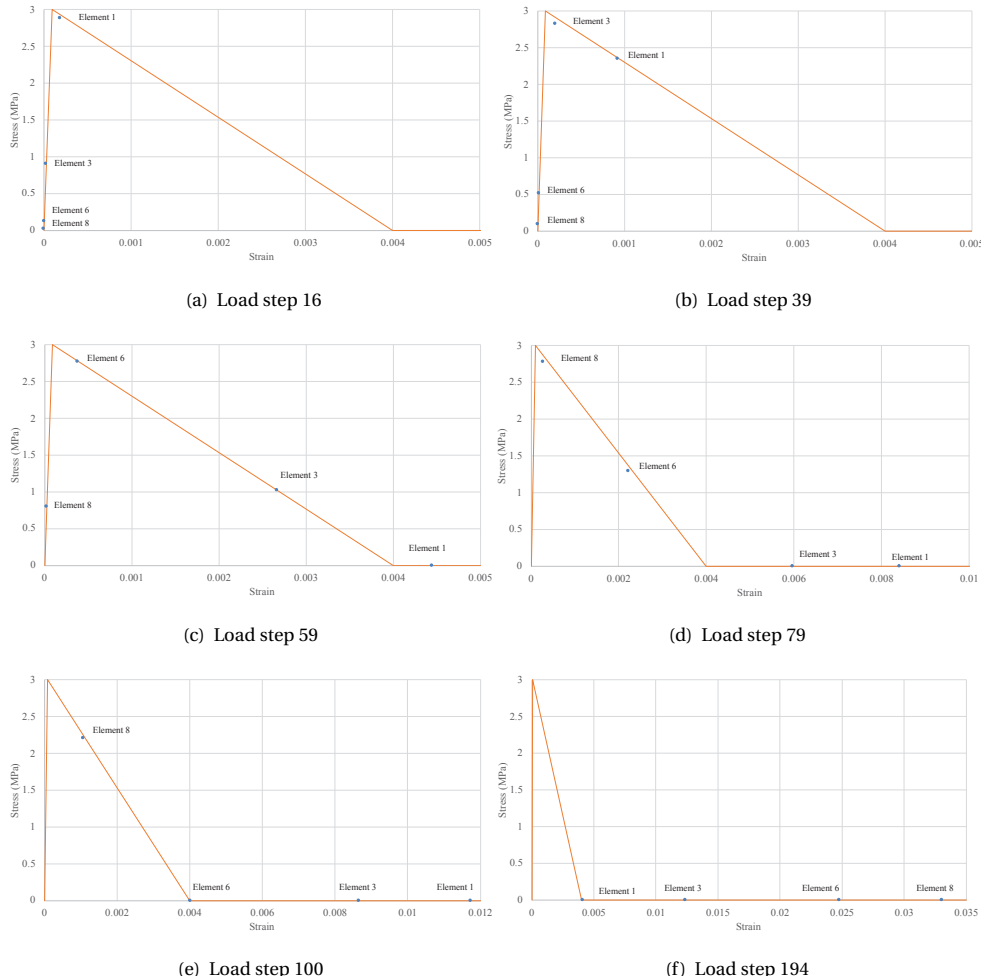


Figure 7.17: Principal tensile stress versus principal tensile strain of element 8 for the load control method with imposed displacement loading

7

of the load control method due to the utilisation function being not exactly 1, but smaller than 1. The maximum error is 3.80%. However, the displacement-force diagrams of the load control method and damage control method overlap each other in Figure 7.7. This is because the load steps adjacent to the load steps with relatively large errors of the utilisation function have small errors, which immediately corrects the error. Figure 7.22 shows the displacement (midspan and loading position) versus total reaction force curve, including results of all cycles, for Load step 59. The reaction force continues to decrease while the midspan displacement increases in Figure 7.22(a) and the displacement at the loading position remains the same.



7

Figure 7.18: Results for four elements and six different load steps, indicated as the position along the material stress-strain curve

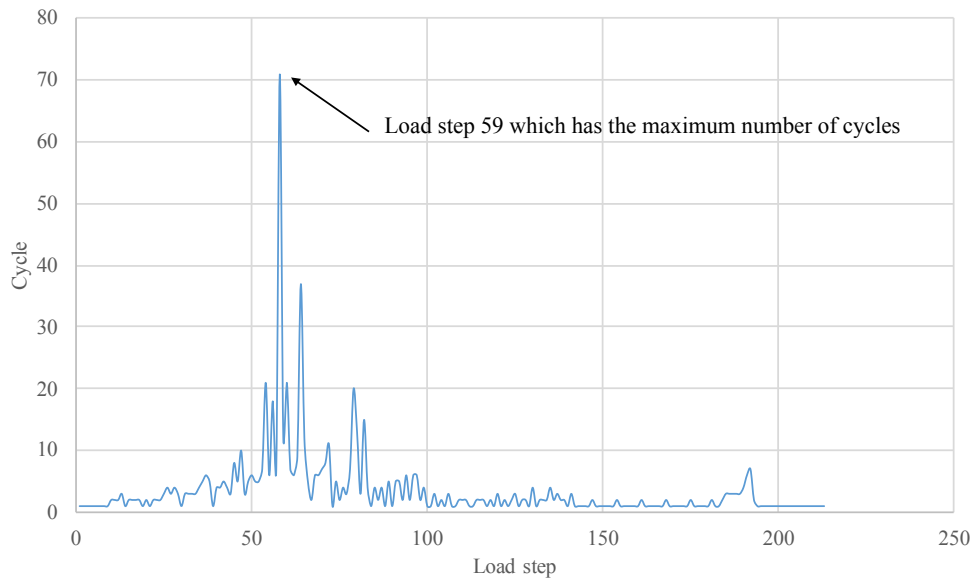


Figure 7.19: Number of cycles of all load steps for the load control method (imposed displacement loading)

7

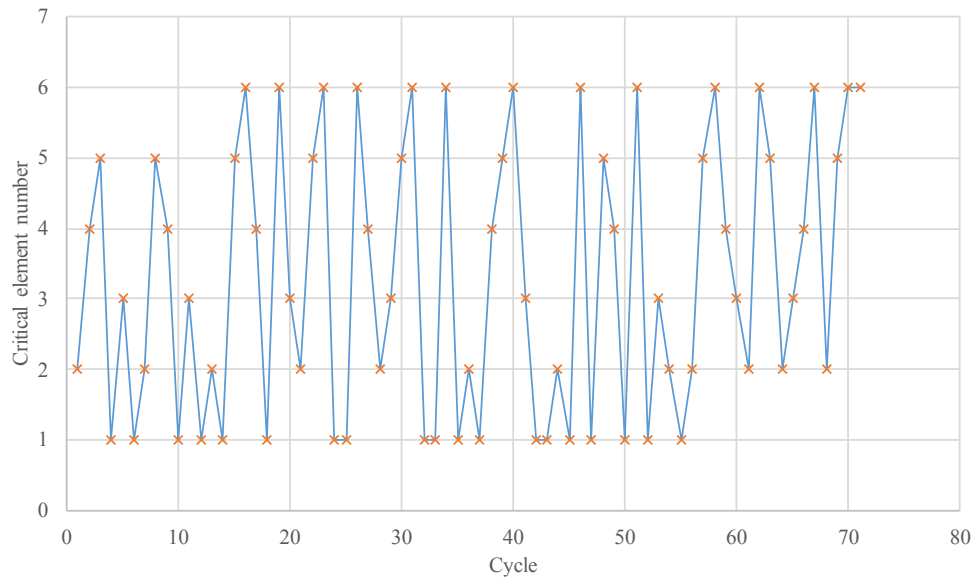


Figure 7.20: Critical element number of all cycles in Load step 59 (i.e., the load step that required most cycles as indicated in Figure 7.19 (imposed displacement loading))

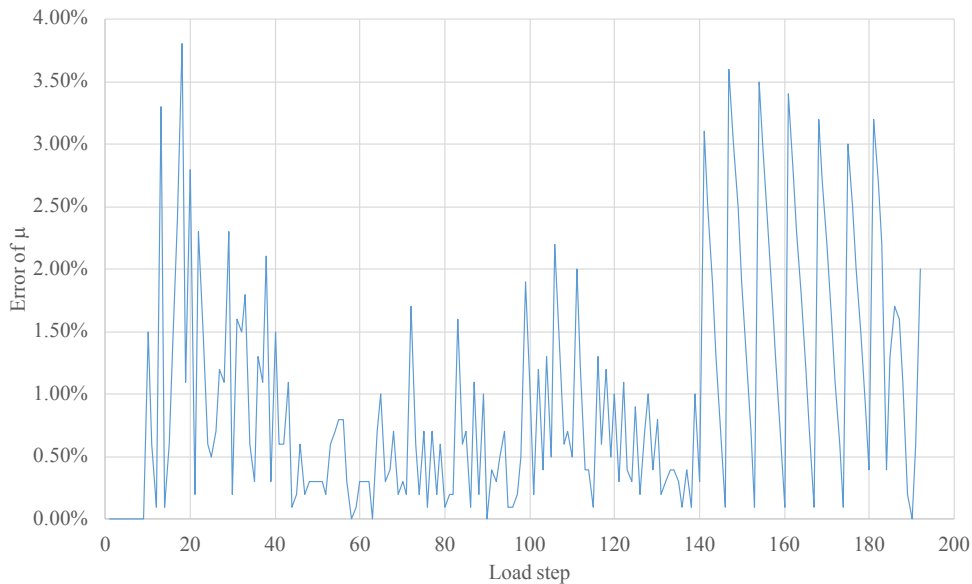


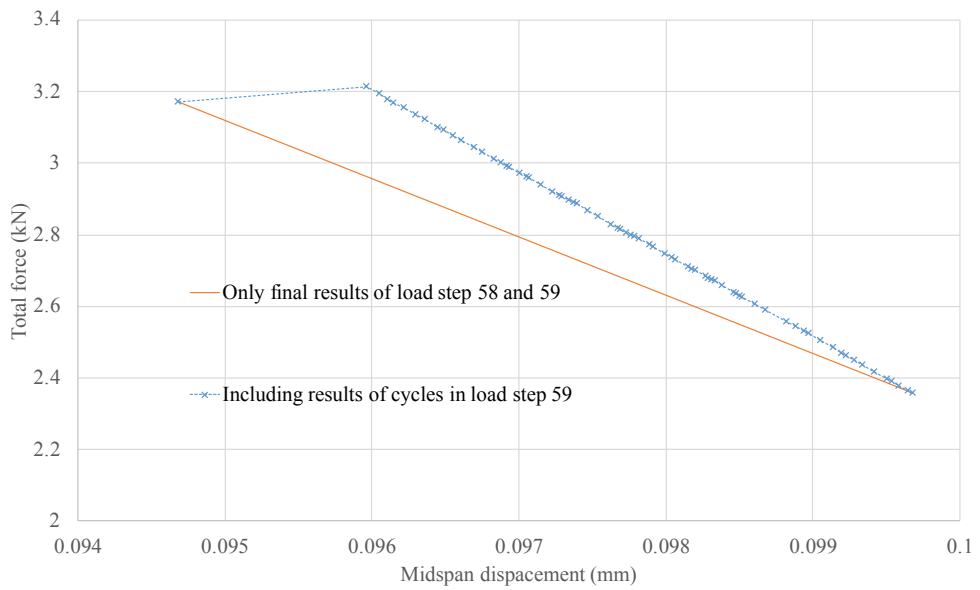
Figure 7.21: Errors of the utilisation function for all load steps of the Load control method when the stiffness reduction factor is 0.9 (imposed displacement loading)

## 7.4. LOAD CONTROL FOR THE IMPOSED FORCE TEST

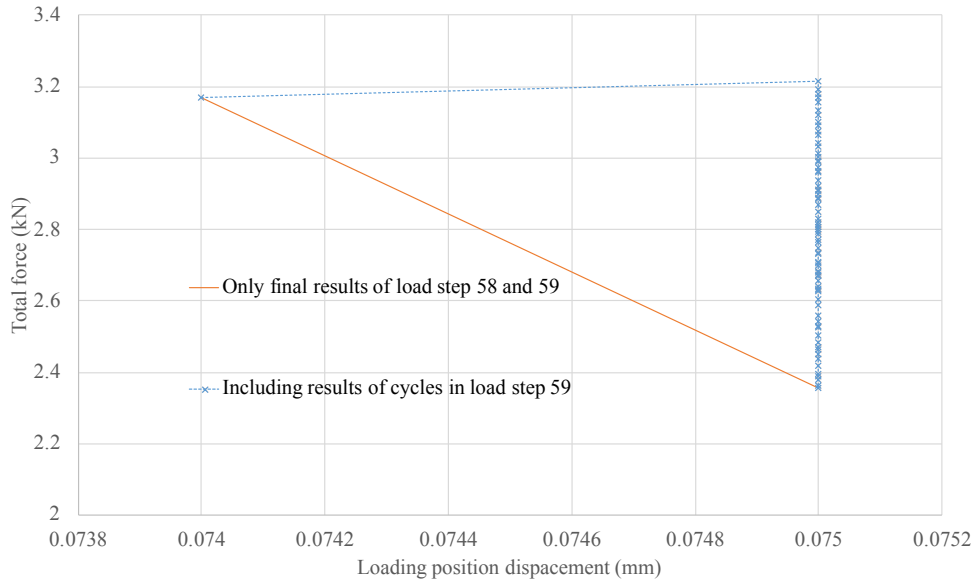
7

An imposed force loading test is also performed for the same model. Two-point loads are applied, as shown in Figure 7.1. Imposed forces have been applied in 300 total steps of the fixed step size (0.02 kN). The elements selected for output are the same as those for imposed displacement loading.

Figure 7.23 shows the midspan displacement-total force diagrams for the imposed displacement loading (previous section) and the imposed force loading. The selected steps for post-processing are indicated. It can be seen that the two curves overlap each other before the peak, but the curve of force control loading stops at Load step 191 as there is no solution for a load higher than 3.8 kN. Because the load and damage control method is not used, post-peak behaviour cannot be traced. Figure 7.24 shows the cycle number of all load steps. The final Load step 190 has the maximum number of cycles (14). Figure 7.25 shows how the critical element number changes from cycle to cycle in Load step 190. Figure 7.26 shows how this algorithm reaches a new equilibrium state ( $\mu \approx 1$ ) during cycles at the peak. The midspan displacement remains constant and then decreases periodically while the



(a) Total force versus midspan displacement



(b) Total force versus loading position displacement

Figure 7.22: Total force-displacement diagrams for Load step 59 only: (a) force versus midspan displacement and (b) force versus loading position displacement (imposed displacement loading)

total reaction force is kept the same.

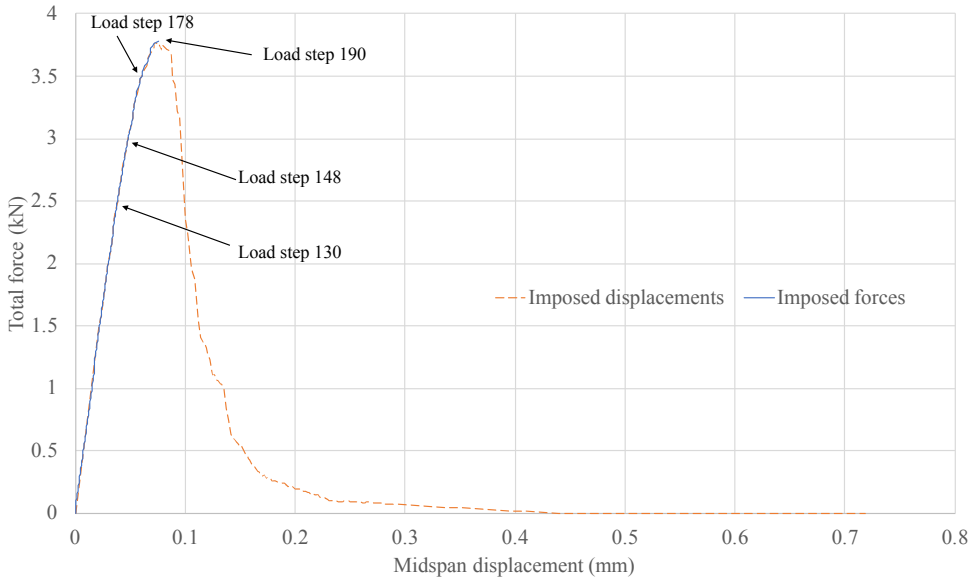


Figure 7.23: Comparison of displacement-reaction force diagrams for imposed displacement loading and imposed force loading

Figure 7.27 shows the deformation and damage for four values of the load. It is observed that the crack starts at the notch and slowly grows upwards. Only four elements are damaged. The displacement-total force diagram reaches the peak at the moment when the strain of the first element goes into the dark green zone and the fourth element is damaged, as shown in Figure 7.27(d).

Figures 7.28 to 7.30 show stress-strain results, which are similar to those of displacement control loading.

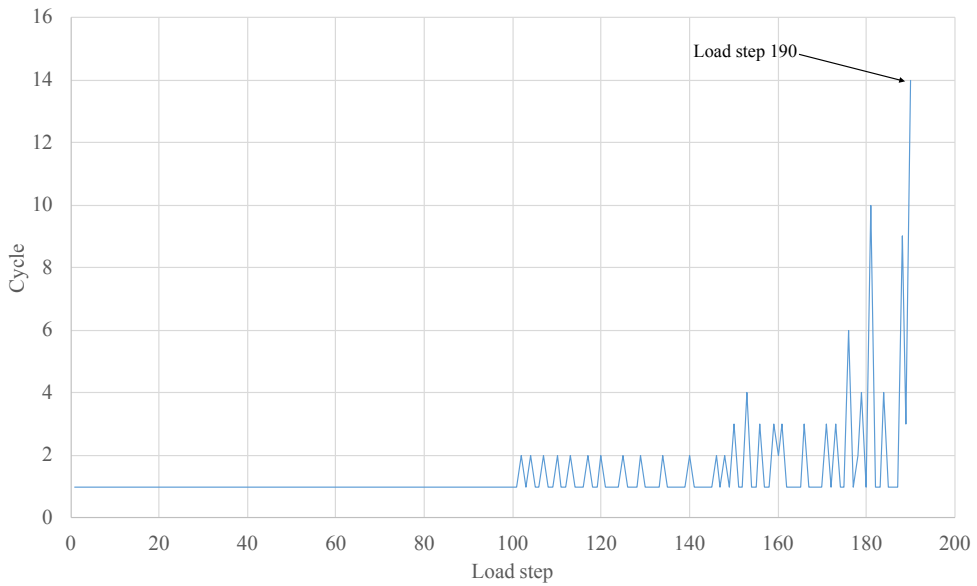


Figure 7.24: Number of cycles of all load steps for the load control method (imposed force loading)

7

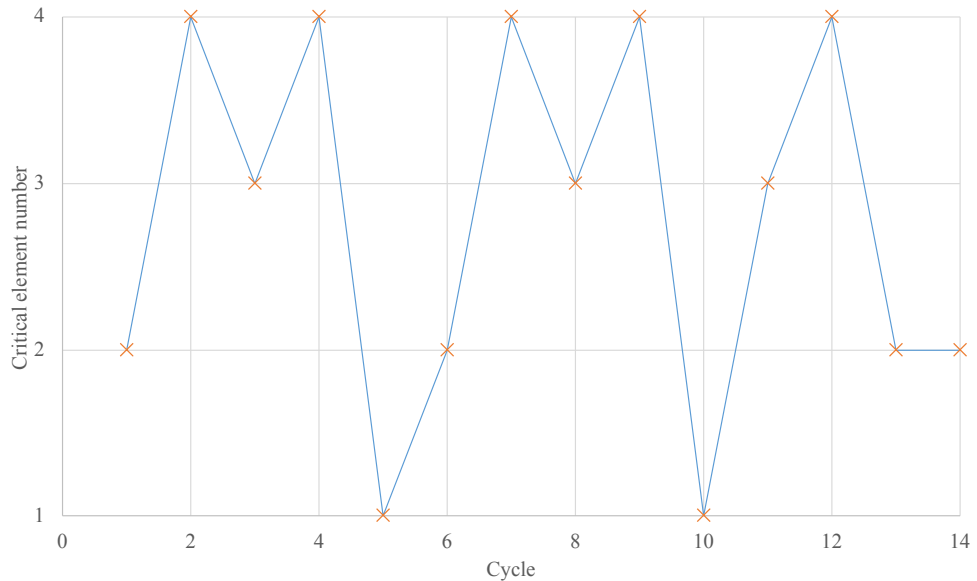


Figure 7.25: Critical element number of every cycle in Load step 190 (imposed force loading)

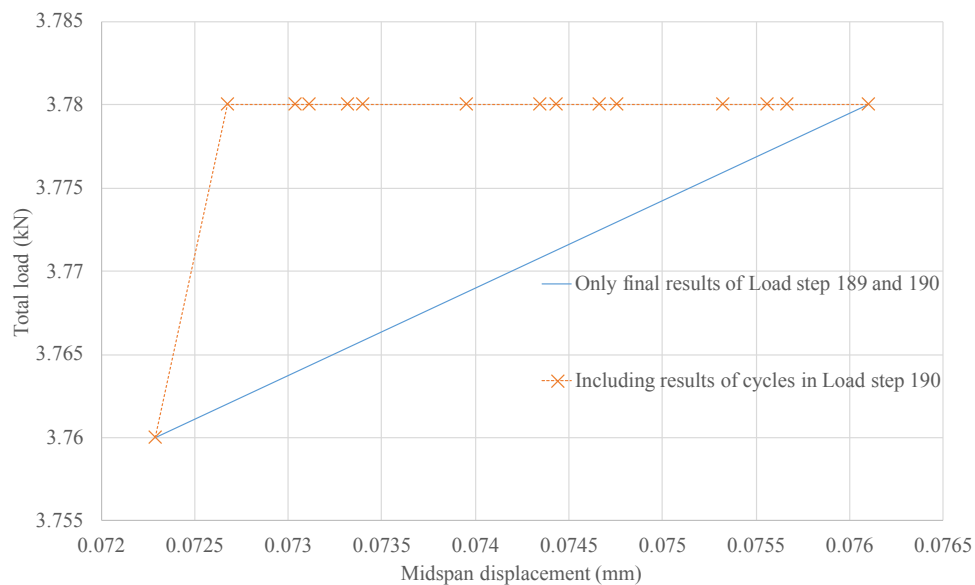


Figure 7.26: Enlargement of the peak in Figure 7.23 (imposed force loading)

7

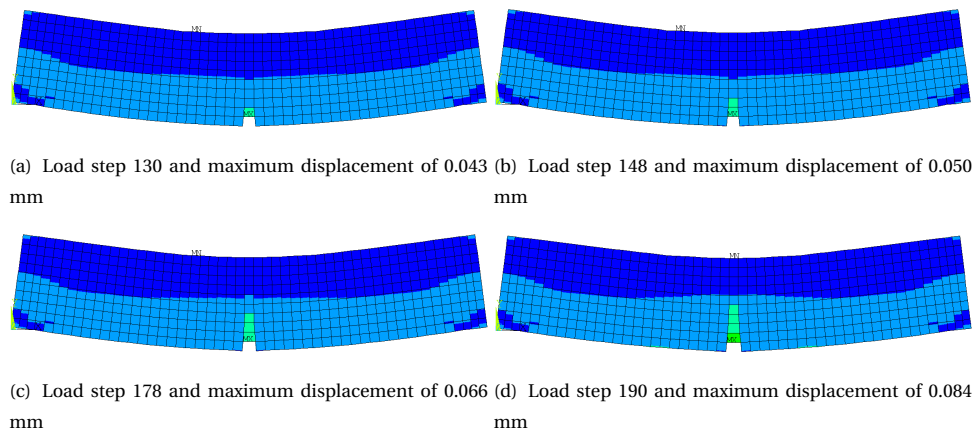


Figure 7.27: Horizontal tensile strain contour for different load steps marked in Figure 7.23 (imposed force loading)

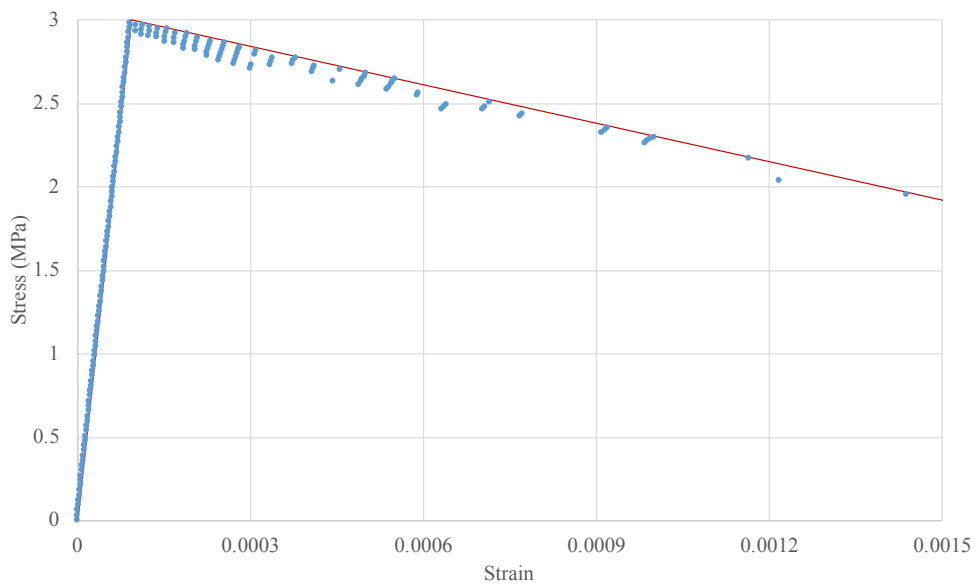


Figure 7.28: Principal tensile stress versus principal tensile strain of element 1 for the load control method with imposed force loading

7

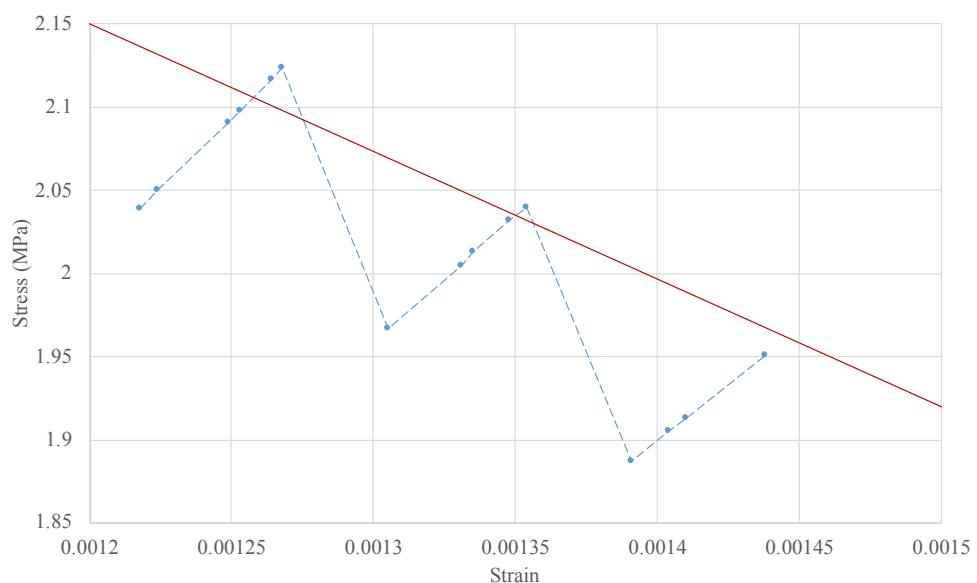


Figure 7.29: Enlargement of area a in Figure 7.28

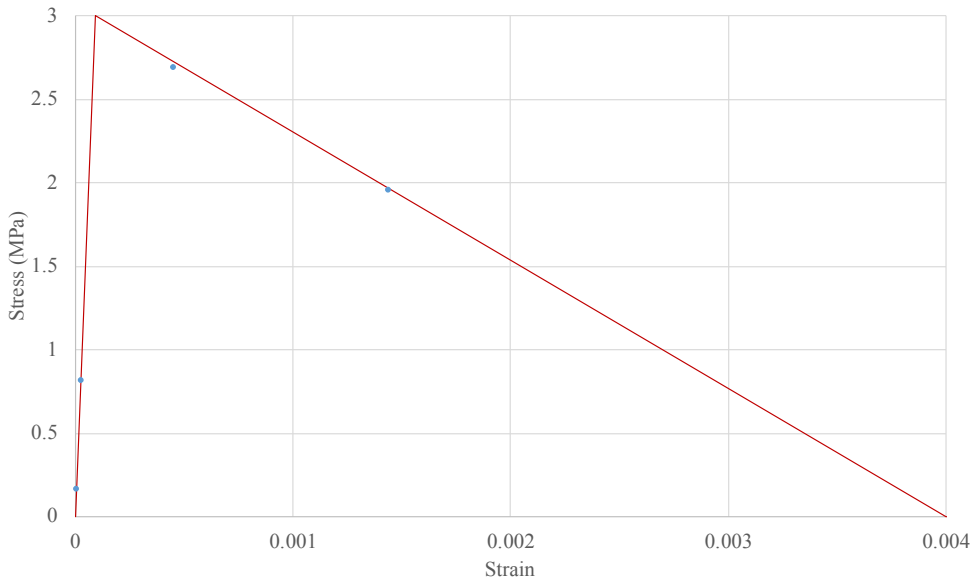


Figure 7.30: Results for four elements in Load step 190, indicated as the position along the material stress-strain curve

## 7.5. LOAD AND DAMAGE CONTROL FOR THE SCALED FORCE TEST

In Section 7.3, an imposed displacement loading is applied, which enables tracing all pre-peak and post-peak behaviour. In the previous section, an imposed force loading test was applied. This load control method cannot pass the peak. In this section, a scaled force loading test is performed for the same model by the load and damage control method, as elaborated in Figure 5.12, to trace the post-peak behaviour. Again, two-point loads are applied, as shown in Figure 7.1. Results are outputted until the loading position displacement is 0.5 mm, which is equal to the last situation for imposed displacement loading (Figure 7.6). The default stiffness reduction factor is still 0.9, which is compared with a value of 0.5. The initial value of the load scaling factor is 1.1 and continues to be reduced.

Figure 7.31 shows force-displacement diagrams for the loading position and midspan separately for the load and damage control method with load scaling control and compares the results with results of the load control method with imposed displacement loading and the damage control method. It can be seen that these diagrams overlap each other, indicating good accuracy for all methods. Figure

7.32 shows the number of cycles for all load steps of the load and damage control method. It can be seen that Load step 88 has the maximum number of cycles (22). This load step corresponds to the moment when the total reaction force drops to zero and the midspan displacement is 0.427 mm. The corresponding crack pattern is shown in Figure 7.33. It can be observed that the x direction strain of element 8 goes to the red zone while elements 1 to 7 are fully damaged. The exponent function used in the load and damage method is not efficient when the load is close to zero.

The total number of all cycles of all load steps is 614 for the load and damage control method and 749 for the load control method. This is because for several load steps, there was no damage to any element in the load control method. Figure 7.34 shows errors of the utilisation function for all load steps of the load and damage control method, the maximum of which is 4.30%. However, these errors have little influence on the displacement-force diagram. The reason for this is explained in Section 7.3.

However, when the stiffness reduction factor decreases from 0.9 to 0.5, large differences can be observed in the displacement-force diagrams for stiffness reduction factors of 0.9 and 0.5 as shown in Figure 7.37. Figure 7.35 and Figure 7.36 show the number of cycles and the error of the utilisation function for every load step of the load and damage control method. Although the maximum number and the total number of cycles drop to 13 and 88 compared to 2 and 614, the maximum error of the utilisation function increases from 4.30% to 18.00%. The stiffness reduction factor cannot be small, such as 0.5, otherwise there are not enough saw teeth to ensure accuracy. The solution is to add extra saw teeth below the residual stiffness or to choose a larger stiffness reduction factor to improve accuracy. However, the objectivity of the stiffness reduction is still achieved in the load and damage control for this coarse stiffness reduction factor.

At the global level, in the previous section (Figure 7.22), the results of cycles are shown when the reaction force decreased from 3.17 kN in Load step 58 to 2.356 kN in Load step 59 for the load control method. In this section, the force-displacement diagrams from Load step 42 to Load step 52 marked in Figure 7.31 are selected for the load and damage control method, as shown in Figure 7.38, for the same period as the load control method. In general (Figure 7.38(a)), displacement increases from 0.093 mm to 0.098 mm and the total reaction force decreases from 3.18 kN to

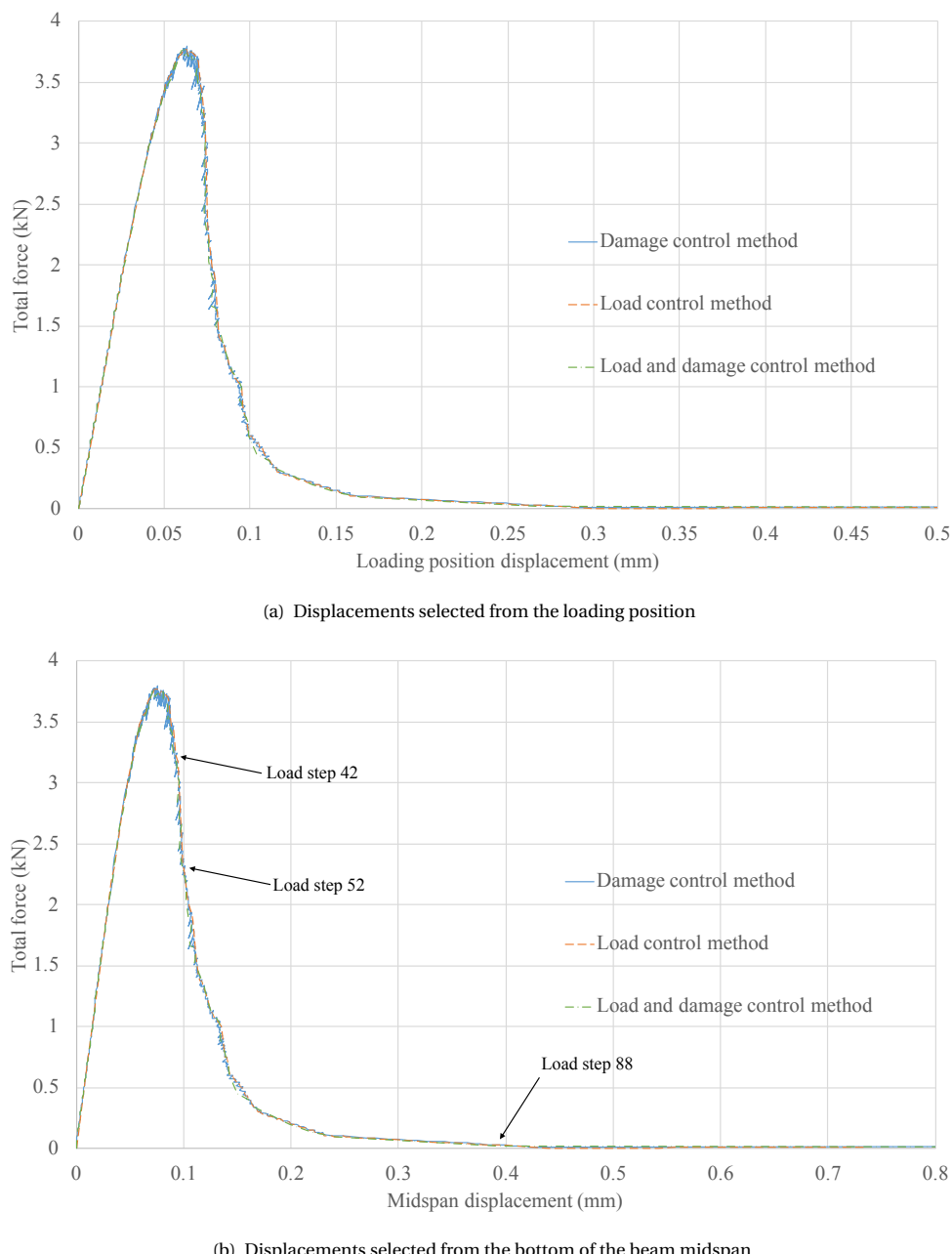


Figure 7.31: Load-displacement diagrams of the notched beam test for the load control and the load and damage control

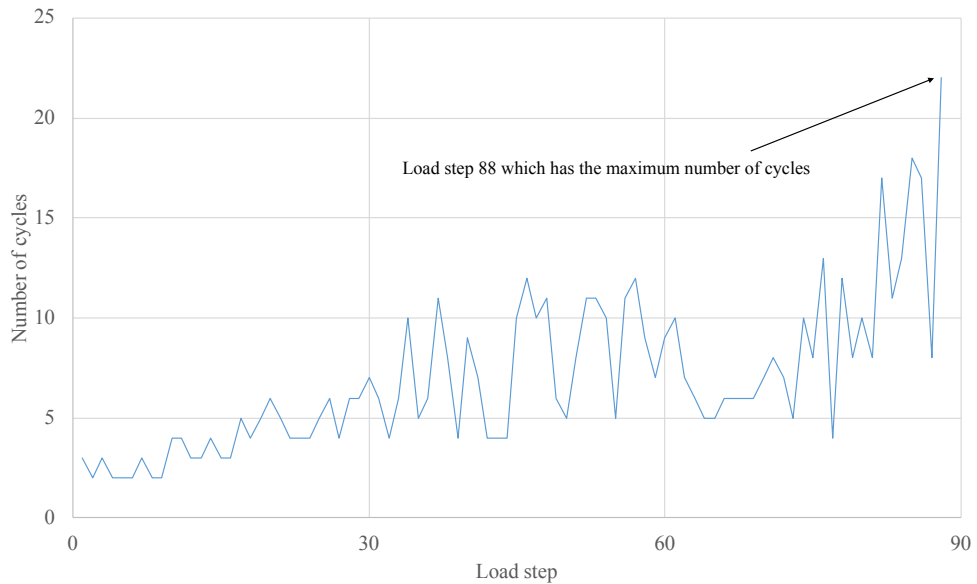


Figure 7.32: Number of cycles for all load steps of the load and damage control when the stiffness reduction factor is 0.9

7

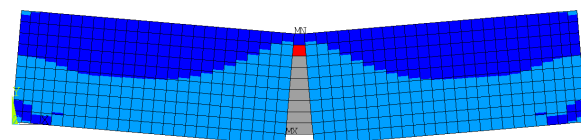


Figure 7.33: Horizontal tensile strain contour of Load step 82 marked in Figure 7.31 (Load and damage control method)

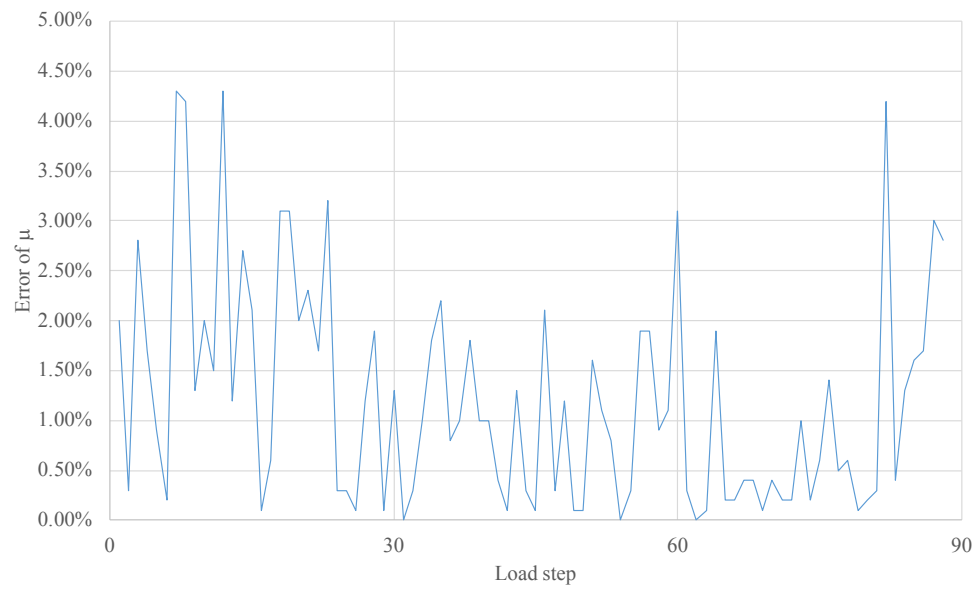


Figure 7.34: Errors of the utilisation function for all load steps of the load and damage control method when the stiffness reduction factor is 0.9

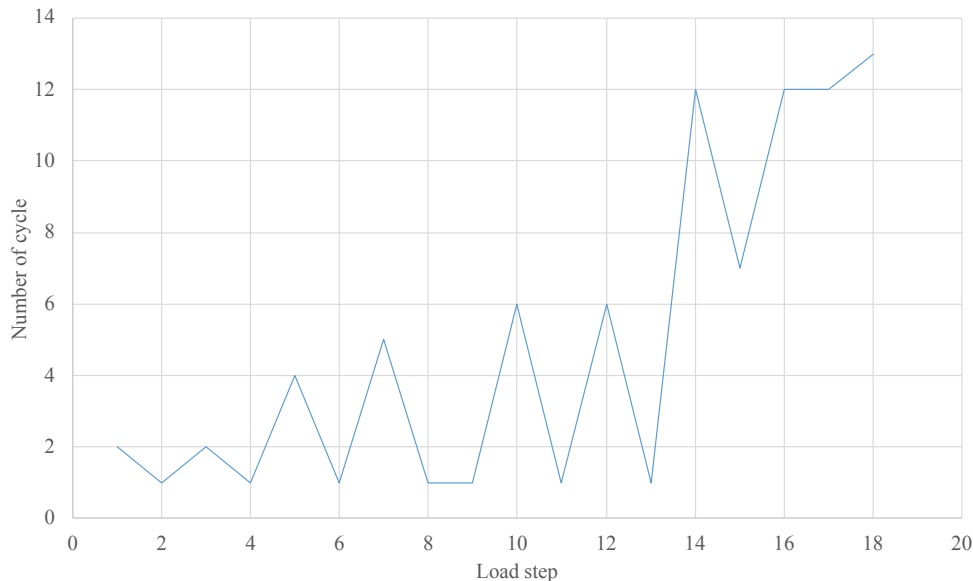


Figure 7.35: Number of cycles for all load steps of the load and damage control method when the stiffness reduction factor is 0.5

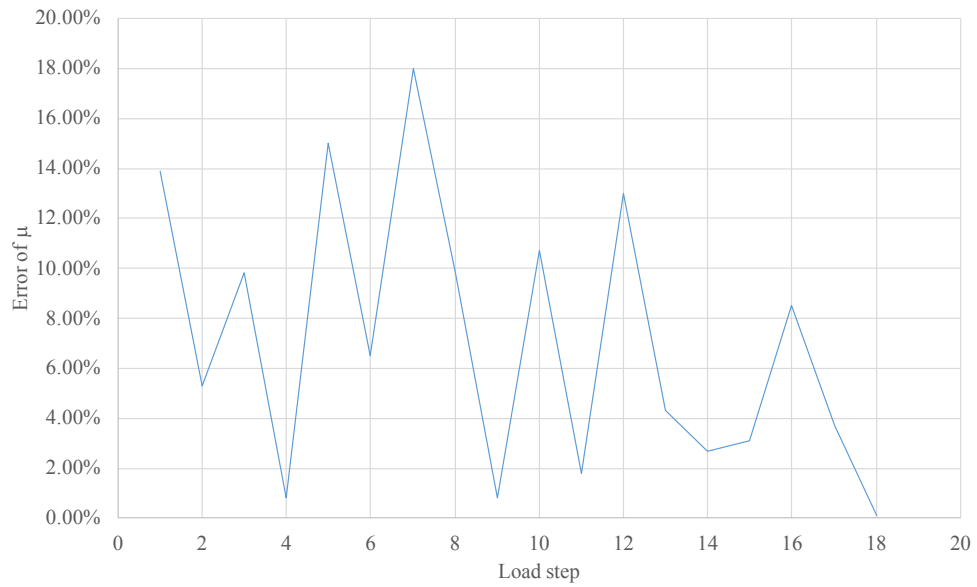


Figure 7.36: Errors of the utilisation function for all load steps of the load and damage control method when the stiffness reduction factor is 0.5

7

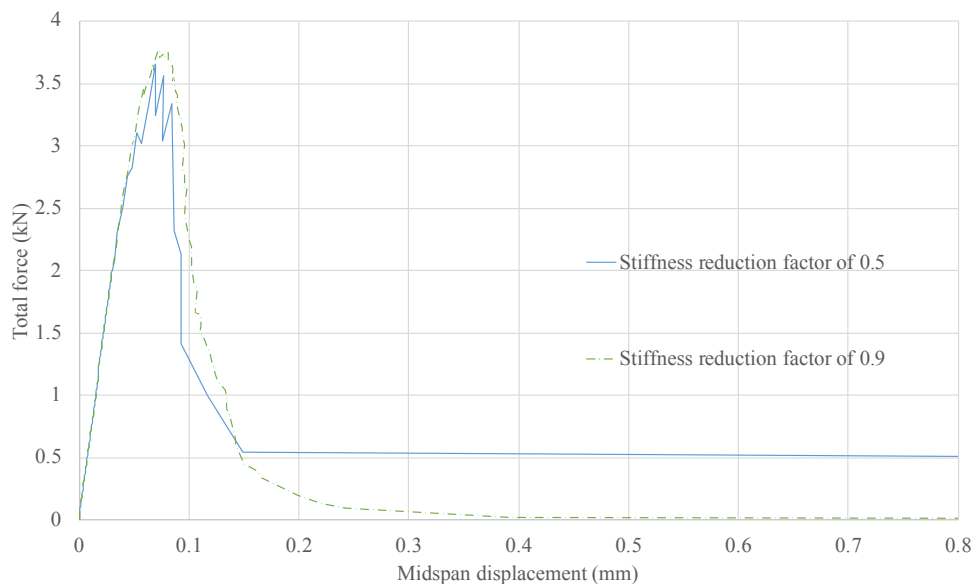
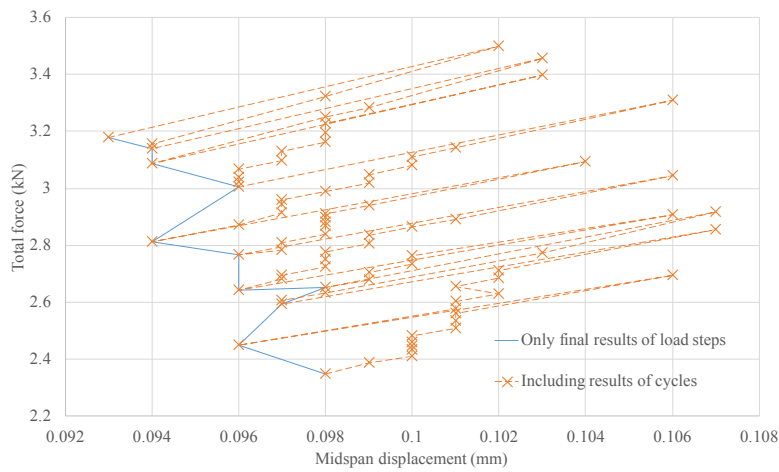


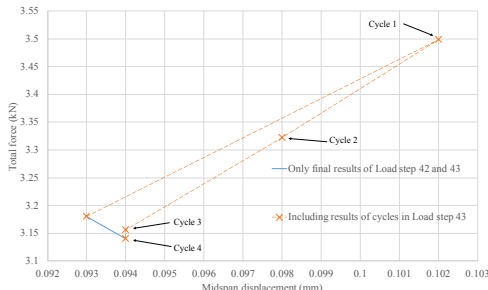
Figure 7.37: Comparison of displacement-force diagrams for different stiffness reduction factors

2.35 kN. Snap-backs are traced in Figure 7.38(c) while the displacement increases in Figure 7.38(b) and remains unchanged in Figure 7.38(d). In all figures, the load increases in the first cycle and then continually decreases until the utilisation function is smaller than 1, whereas the stiffness is reduced continuously.

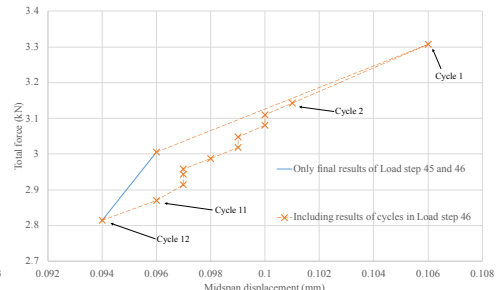
At the local level, Figure 7.39 shows the stress-strain results for element 1. The blue dots show the principal stress and principal strain in the element integration point. Strains greater than 0.005 are not displayed. The orange line is the defined envelope of the material tensile stress-strain curve. It can be seen that almost all the blue dots are on or below the orange line. Figure 7.40 shows the stress-strain results, including all cycles from load step 42 to 52. When element 1 is critical, its stiffness is reduced, which causes a faster decrease of stress than of strain, for example in Figure 7.41 from Load step 45 to 46. The strain increases even when the stress decreases in Figure 7.42. Otherwise, the stress and strain are scaled at the same rate as the secant stiffness when element 1 is not critical in all figures.



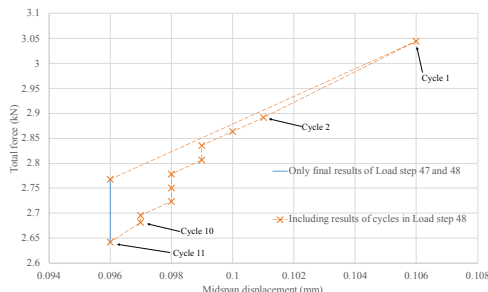
(a) From load step 42 to 52



(b) From load step 42 to 43



(c) From load step 45 to 46



(d) From load step 47 to 48

Figure 7.38: Force-displacement diagrams, including results of cycles

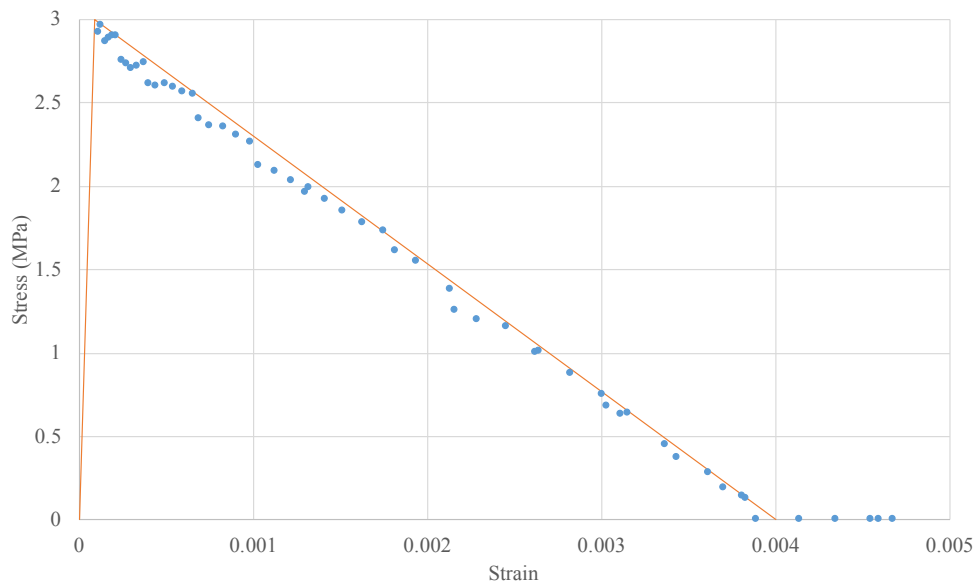


Figure 7.39: Principal tensile stress versus principal tensile strain of element 1 for the load and damage control method

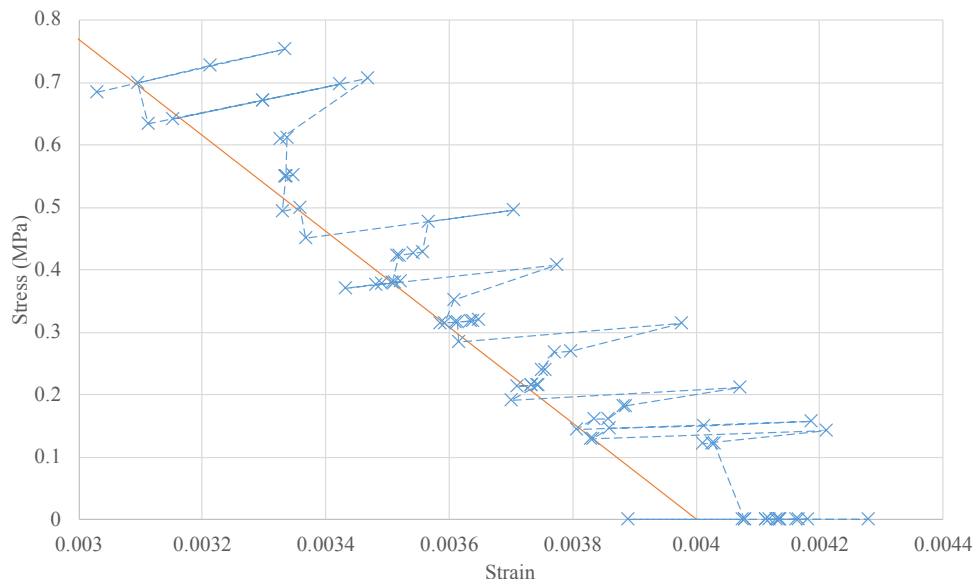


Figure 7.40: Principal tensile stress versus principal tensile strain, including all cycles from Load steps 42 to 52 for element 1

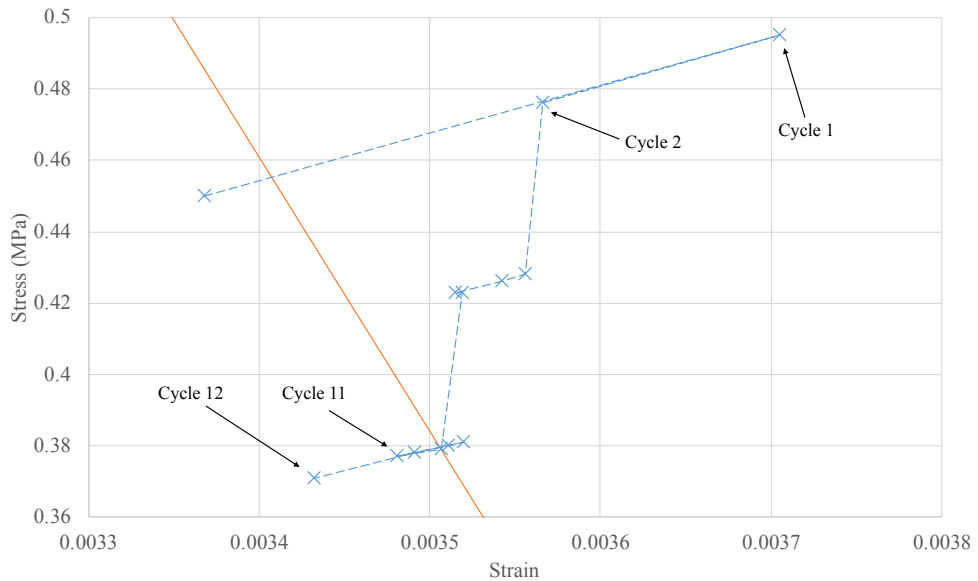


Figure 7.41: Principal tensile stress versus principal tensile strain, including all cycles from Load steps 45 to 46 for element 1

7

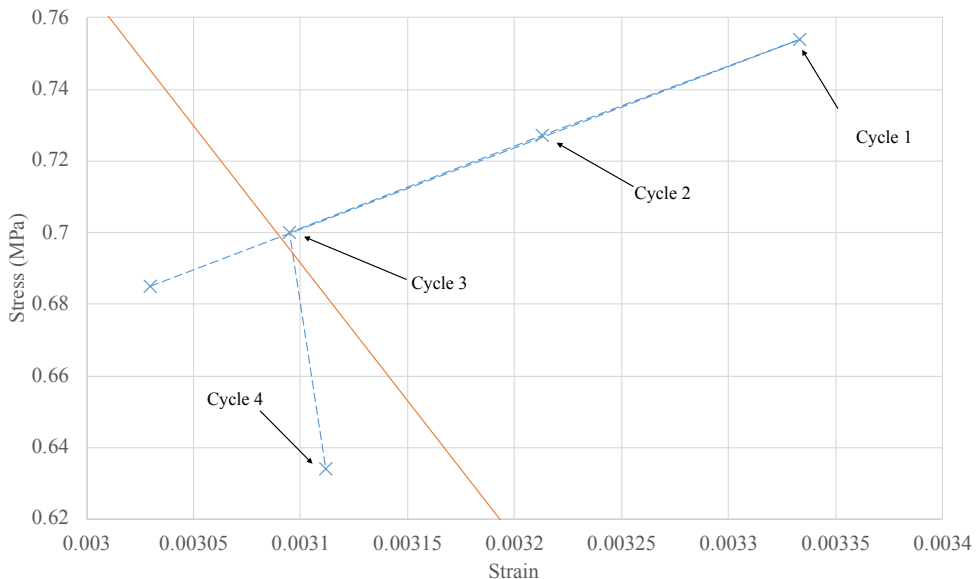


Figure 7.42: Principal tensile stress versus principal tensile strain, including all cycles from Load steps 42 to 43 for element 1

## 7.6. LOAD CONTROL FOR SNAP-BACK BEHAVIOUR TEST

To test the load control method and obtain snap-back behaviour for the proportional imposed displacement loading, as elaborated in Figure 5.11, the tensile strength is doubled while the ultimate strain is halved. Consequently, the fracture energy remains identical, as shown in Figure 7.43. Meanwhile, the notch is removed while only monotonic loading is applied, as shown in Figure 7.44. All elements were permitted to undergo damage. Otherwise, the displacement-force diagram does not exhibit snap-back behaviour. The loading schedule consists of 14 displacement steps of 0.01 mm each.

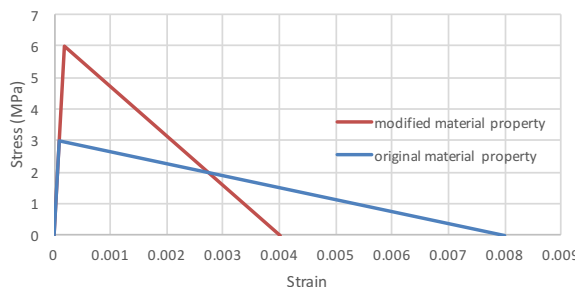


Figure 7.43: Original softening behaviour versus modified softening behaviour

7

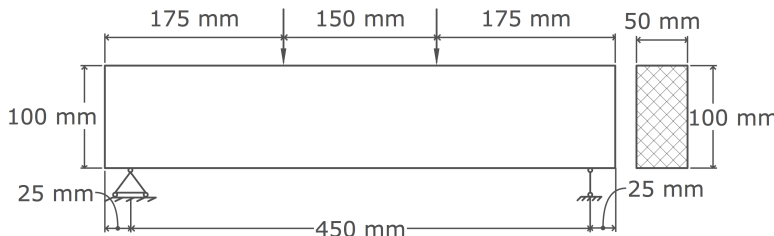
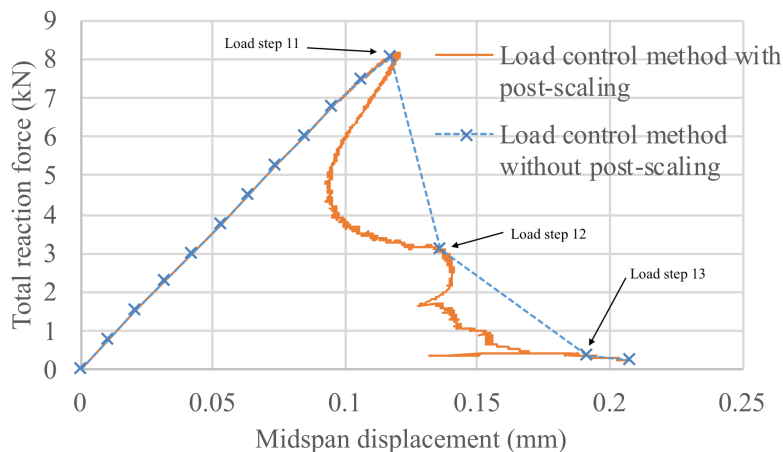


Figure 7.44: Modified model without notch for snap-back behaviour test

Figure 7.45 shows the load-displacement diagrams for the modified material properties with and without the post-scaling procedure in the load control method. Due to the implicit method, the load step can still be very large without losing accuracy. The post-scaling procedure in the load control method can still obtain snap-back behaviour from Load step 11 to Load step 12 for proportional imposed displacement loading. Figure 7.46 indicates the principal tensile strain contour from

Load steps 11 to 13, with failure behaviour changes from distribution to localization shown in Figure 7.46(a) and 7.46(b). The localized crack continues to propagate after the capacity peak. This phenomenon is realistic because there is no purely symmetrical structure without imperfections. The structure becomes unstable and begins to rotate seriously at Load step 13 because of the large stiffness distinction between the left and right of the structure caused by the cracks on the left. As a matter of fact, the material under the loading point is damaged shown in Figure 7.46(c).



7

Figure 7.45: Displacement-reaction force curves for the modified material property with and without the scaling procedure in the load control method

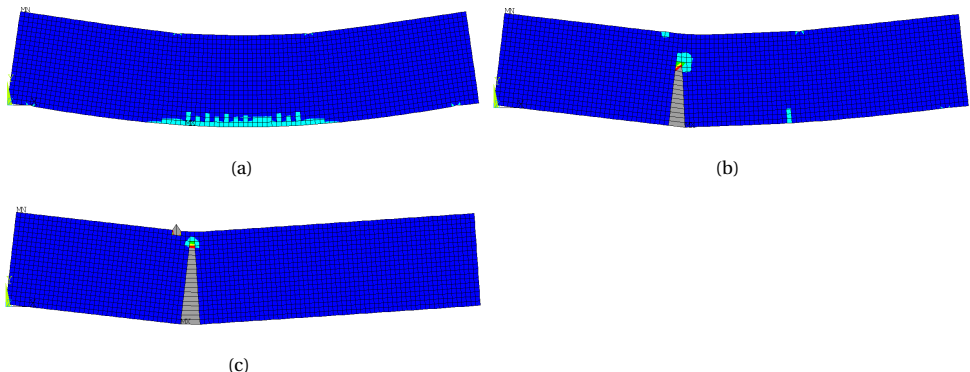


Figure 7.46: Principal tensile strain contour for the last three load steps

## 7.7. DISCUSSION

The principle, algorithms and search paths of ISLA are shown and demonstrated in this chapter. This method is incremental; each increment begins and ends with an equilibrium state. The solution search path follows displacement history and damage cycles sequentially with secant stiffness rather than being guided by numerical parameters. The effectiveness of the scheme with cycles is illustrated in detail for a number of typical prescribed load steps for the load control method and scaled load steps for the load scaling control method. Plots of the number of cycles per load step, element criticality and stress-strain jumps illustrate the search path. The stiffness is reduced in all methods (load control method, damage control method, and load and damage control method), whereas the load is prescribed in the load control method but scaled in the damage control method and the load and damage control method. When the stiffness is reduced, the stress is reduced at the local level, and the total force is reduced at the global level. Strain and displacement can increase or decrease based on the load. For the damage control method and load and damage control method, scaling control is conducted with fixed positive secant stiffness for an incremental load such that the stress and strain at the local level and total force and displacement at the global level are scaled with the secant stiffness. For the example considered, the method is highly robust, as with SLA.

Three methods are compared in this chapter, namely the load control method, damage control method, and load and damage control method. The load control method is suitable for imposed displacement loading. Post-peak behaviour cannot be traced by the load control method for imposed force loading. For the load scaling control method, the damage control method is accurate but time-consuming, while the load and damage control method balances accuracy and efficiency. Although the load and damage control method has some errors, which result in underestimation for certain load steps, in the next load step, the structure can be reloaded to states with a utilisation function closer to 1. Locally, the stress and strain may deviate from the target softening curve due to the failure criterion that the critical element is on the target softening curve, which means other damaged but not critical elements are below the curve. Globally, there is little underestimation of the displacement-force response. The displacement-force curves of the damage control method and the load and damage control method overlap with each other. There-

fore, it is recommended to optimize the stiffness reduction and load scaling factors in the load and damage control method rather than to use the damage control method, which requires almost triple the number of cycles as the load and damage control method for proportional loading and four times the number for non-proportional loading. When the stiffness reduction factor is enlarged, the total number of cycles increases.

In addition, for proportional imposed displacement loading, snap-back behaviour still can be obtained by a post-scaling procedure. However, for non-proportional loading, force loading is essential to obtain snap-back behaviour.

# 8

## VALIDATION OF ISLA FOR NON-PROPORTIONAL LOADING

Chapter 4 shows that it is challenging to analyse non-proportional loading by SLA. On the other hand, non-proportional loading can be naturally analysed by ISLA [13] without modifications because it is an incremental approach. The example in this chapter focuses on the robustness of this method for non-proportional loading [13]. To this end, the notched beam mentioned in Chapter 4 is re-used and subjected to the combination of a horizontal prestress  $P$  at both ends of the beam and a vertical load  $L$  at the top, as illustrated in Figure 8.1. The geometry and properties are adapted from Hordijk's experiment [124].  $P$  is applied as a stress of 1, 5 or 10 MPa over the total area of the beam ends instead of only 1 MPa as previously done [12] [132]. Here, the prestress is varied from low to high to illustrate aspects of non-proportional loading.  $L$  is applied as two-point loads up to and beyond the peak. The analyses are performed by 1) standard N-R with force control in ABAQUS, 2) standard N-R with arc-length control in ABAQUS, 3) SLA in ANSYS [132] and 4) ISLA in ANSYS. The same material properties, element sizes (5 mm) and structural model are used in all analyses (Section 4.5). The algorithm from Chapter 4 is used for non-proportional loading in SLA. All the material properties, the colour range of

the maximum principal strain contours, geometry dimensions and FEM model are the same as in Section 4.5.

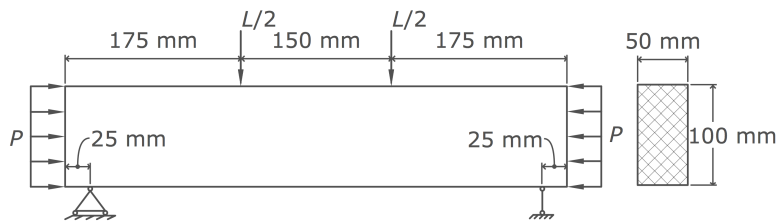


Figure 8.1: Test model dimension and load combination

## 8.1. COMPARISON FOR LOW PRESTRESS

First, a relatively low prestress of 1 MPa is used for comparison between the load and damage control method of ISLA and SLA, which is the same as the original FEM model [12] to introduce non-proportional loading in SLA. Figure 8.2 shows ISLA and SLA deliver almost the same force-displacement diagram. Moreover, for both methods, one crack is localized and propagates to the top of the beam, as shown in Figures 8.4 and 8.3. Actually, the plateau of the curve extends to more than 10 mm (not shown). Neither method has a divergence issue.

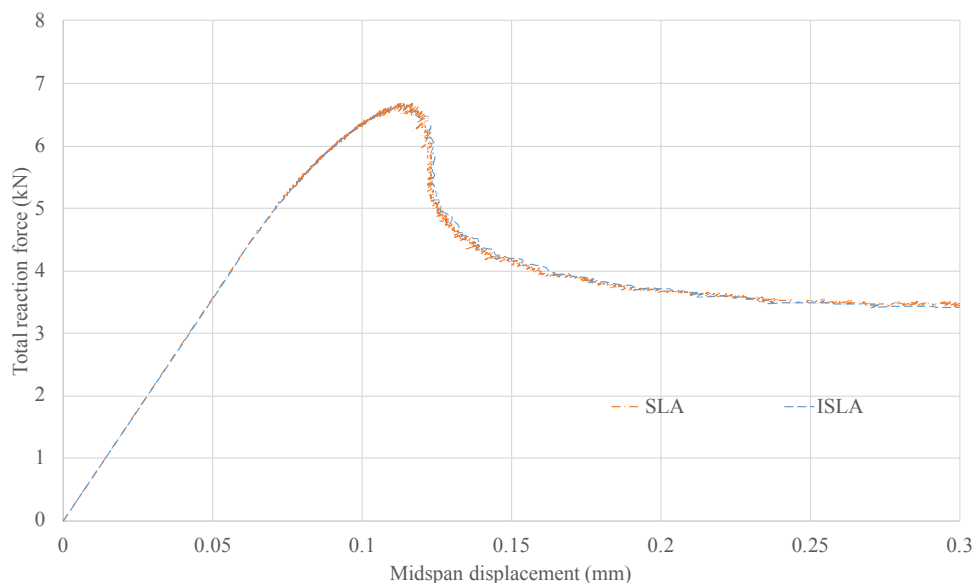


Figure 8.2: Reaction force-displacement diagrams for 1 MPa prestress

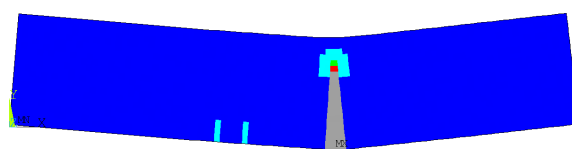


Figure 8.3: Maximum principal strain contour when the midspan displacement is 0.3 mm by SLA for 1 MPa prestress

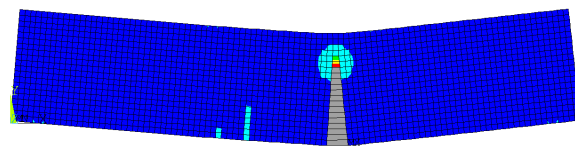


Figure 8.4: Maximum principal strain contour when the midspan displacement is 0.3 mm by ISLA for 1 MPa prestress

## 8.2. COMPARISON FOR MEDIUM PRESTRESS

Figure 8.5 shows the force-displacement diagrams for 5 MPa prestress of SLA, ISLA, N-R and N-R arc-length control with marked deviation points of SLA, N-R and N-R arc-length control. The SLA analysis stops at a displacement of 1.8 mm while ISLA can continue up to 2.2 mm and further. The cracks have already propagated to the top of the beam at the displacement of 2.2 mm in ISLA. Hence, ISLA results beyond this point are not shown. The diagram of SLA is quite similar, but the N-R method fails earlier. The reason that the SLA algorithm stops at 1.8 mm displacement is explained in Section 4.7.

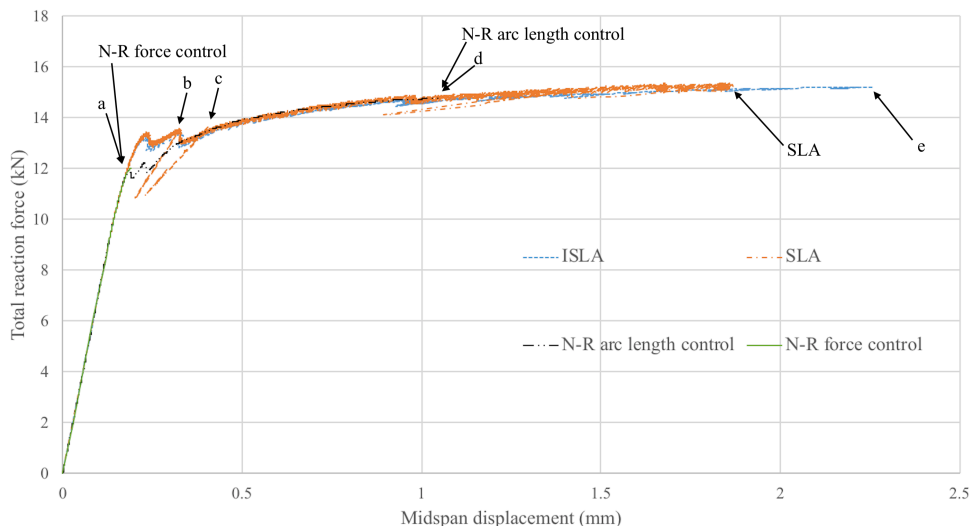


Figure 8.5: Reaction force-displacement diagrams for the 5 MPa prestress test

Figure 8.6 shows the crack propagation calculated by ISLA at five stages, which are marked in Figure 8.5. Initially, symmetrical ductile cracks occur at the bottom of the beam, and the maximum principal strain of two symmetrical critical ele-

ments goes into the green zone in Figure 8.6(a). At this moment, the displacement-reaction force diagram meets the end point of the initial slope. Afterwards, the right critical crack propagates much faster than the left crack until the displacement-reaction force diagram reaches the first peak shown in Figure 8.6(b). Subsequently, the displacement-reaction force diagram drops slightly and then rises to a second peak when the left critical crack catches up with the right one in Figure 8.6(c). Then, the development of the left critical crack surpasses the right one in Figure 8.6(d). Finally, the main cracks bifurcate, with branch cracks forming and extending to the top of the beam in Figure 8.6(e). There is no further damage due to the elastic compressive capacity. Similar crack propagation is obtained by SLA, for which the final crack pattern is shown in Figure 8.7. The spacing of cracks is governed by the positions of the critical elements, which have the largest ratio of the maximum principal stress versus strength in a cycle. Initially, multiple elements can be critical, and cracks start in a distributed manner. Eventually, however, only two dominant cracks survive while other elements are unloaded. An advantage of SLA and ISLA are their ability to handle bifurcations properly. For a four-point loaded beam, two dominant cracks are beneath the loading positions.

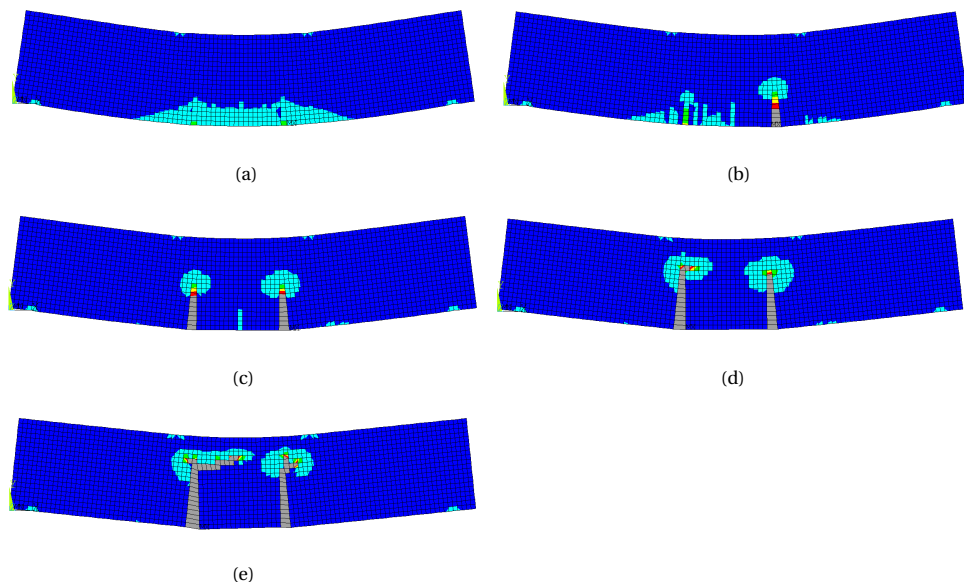


Figure 8.6: Maximum principal strain contours of crack propagation by ISLA for the 5 MPa prestress test

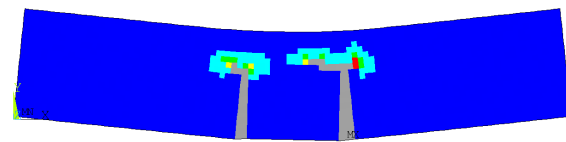


Figure 8.7: Maximum principal strain contour of final crack pattern by SLA for the 5 MPa prestress test

Figure 8.5 shows that the reaction force-displacement diagrams of N-R analysis reach only the end point of the initial slope although the structure shows overall hardening behaviour. The value of the initial slope is the same as with SLA and ISLA. The N-R crack pattern is also similar to SLA and ISLA, but there are fewer cracks (Figure 8.8).

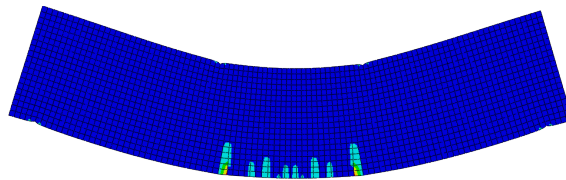


Figure 8.8: Maximum principal strain contour of final crack pattern by N-R force control analysis for the 5 MPa pre-stress test

8

Only extremely small load steps ( $10^{-7}$  at the end) with N-R arc-length control can find the hardening part of the reaction force-displacement diagram shown in Figure 8.5. The first peak is lower than in SLA and ISLA, but they align well after the second peak. After this, they both have a similar hardening slope. As shown in Figure 8.9, the ultimate crack pattern is similar to that of ISLA and SLA while there are fewer cracks at the end point of the initial slope and at the first peak, which results in lower capacity than SLA and ISLA.

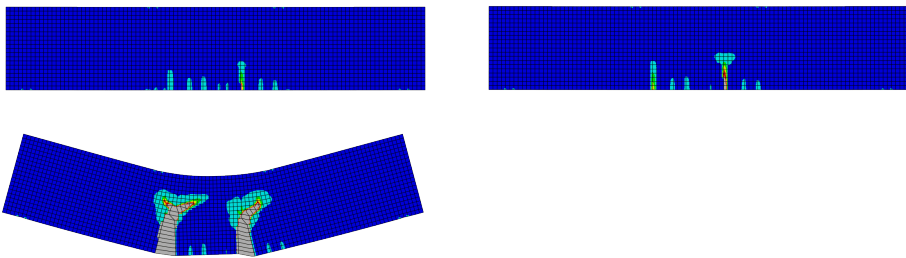


Figure 8.9: Maximum principal strain contours of crack propagation by N-R arc-length control analysis for the 5 MPa prestress test

### 8.3. COMPARISON FOR HIGH PRESTRESS

Figure 8.10 shows the reaction force-displacement diagrams for 10 MPa pre-stress of SLA, ISLA, N-R and N-R arc length control with marked deviation points of SLA, N-R and N-R arc length control. They overlap in the beginning of the curves. SLA fails to continue earlier than the 5 MPa prestress test and does not reach the final hardening slope. N-R arc length control diverges before N-R force control.

Figures 8.11 and 8.12 show the crack patterns for ISLA and SLA, the positions of which are marked in Figure 8.10. In SLA, the numerical procedure stops at the stage of two major symmetrical cracks. ISLA continues and also shows the formation of branch cracks. The main difference in terms of crack development in the 5 MPa pre-stress test is that two dominant cracks simultaneously. This is caused by the higher prestress having a greater effect on preventing cracks from propagating to the top of the beam.

The reaction force-displacement diagram of the Newton-Raphson method with force control is in a good agreement with SLA and ISLA from the initial slope to the final hardening slope (Figure 8.10). The hardening behaviour can be obtained without arc-length control. Figure 8.13 also shows symmetrical crack development in N-R force control until the branch crack moment whereas ISLA has random branch cracks.

Figure 8.14 shows the number of cycles of each load step in ISLA. For the 5 MPa prestress test, the total number of cycles in ISLA is 13,047 while the number in SLA before divergence is 20,688. The total number of increments for N-R arc-length control is 258,958. A very small arc length has to be employed to reach convergence,

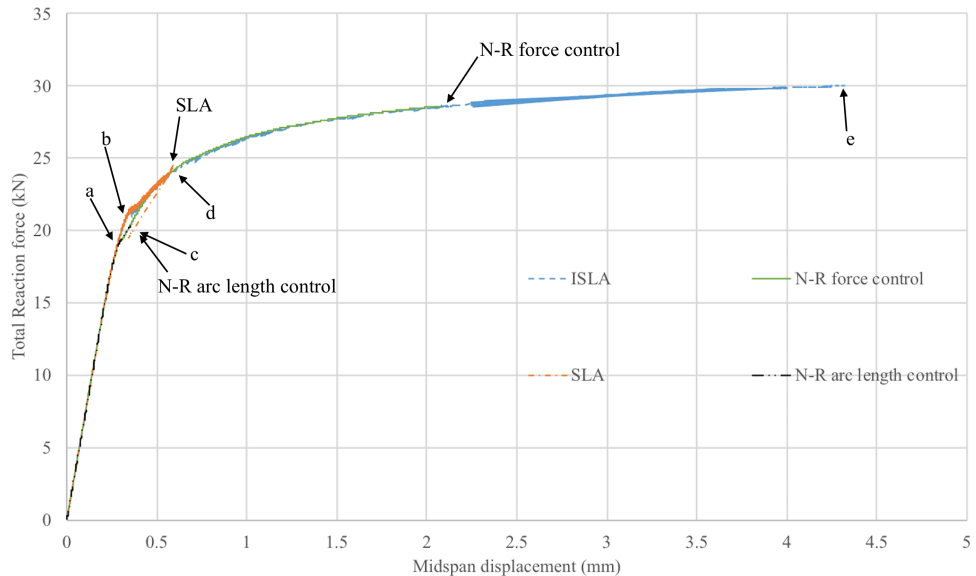


Figure 8.10: Reaction force-displacement diagram for 10 MPa prestress

8

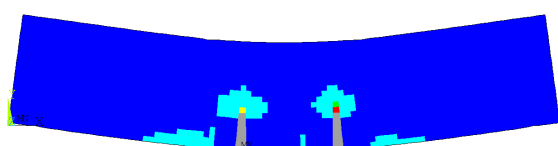


Figure 8.11: Maximum principal strain contour of the final crack pattern by SLA for the 10 MPa prestress test

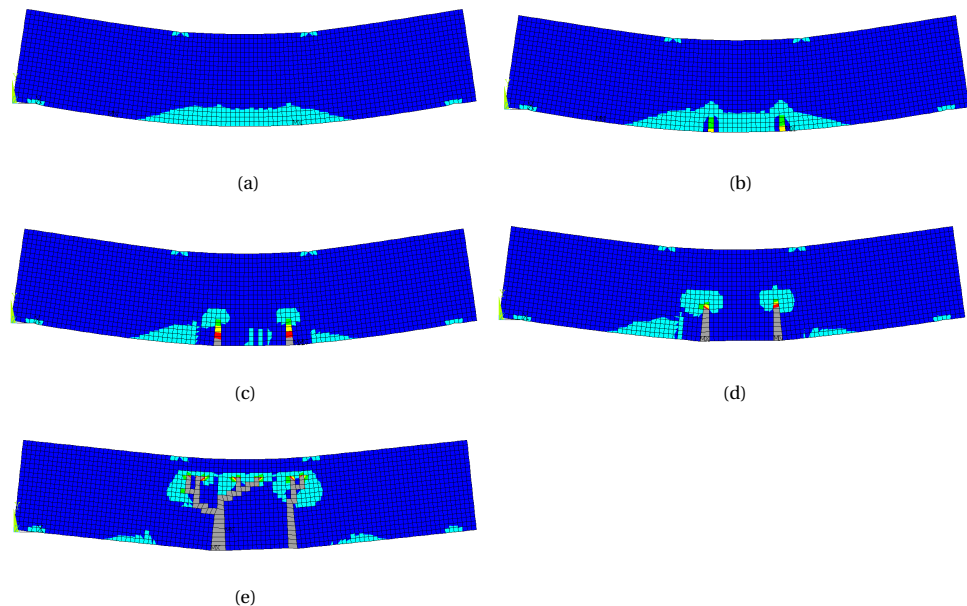


Figure 8.12: Maximum principal strain contours of the crack propagation by ISLA for the 10 MPa prestress test

8

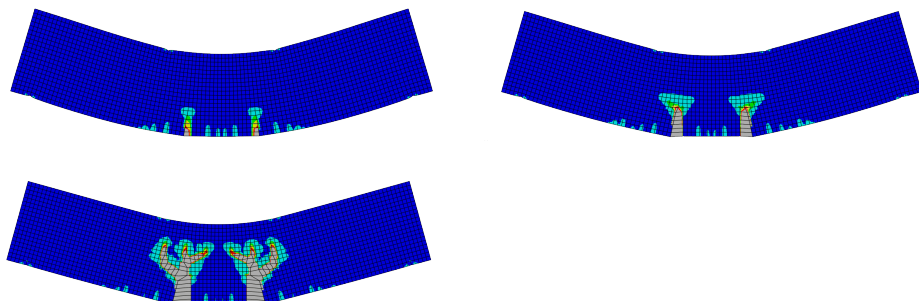


Figure 8.13: Maximum principal strain contours of the crack propagation by N-R force control analysis for the 10 MPa prestress test

with each increment having several iterations. The maximum number of cycles of a load step in ISLA is 23. For the 10 MPa prestress test, the total number of cycles in ISLA is 18,936 while the number in SLA before divergence is 7,519. The total number of cycles in SLA for the 10 MPa prestress test is smaller than the number in ISLA because SLA diverges very early. The maximum number of cycles of a load step in ISLA is 21. From these numbers, it is clear that ISLA requires the lowest number of computation steps. Nevertheless, it is recommended to further improve the efficiency of ISLA by reducing the number of cycles.

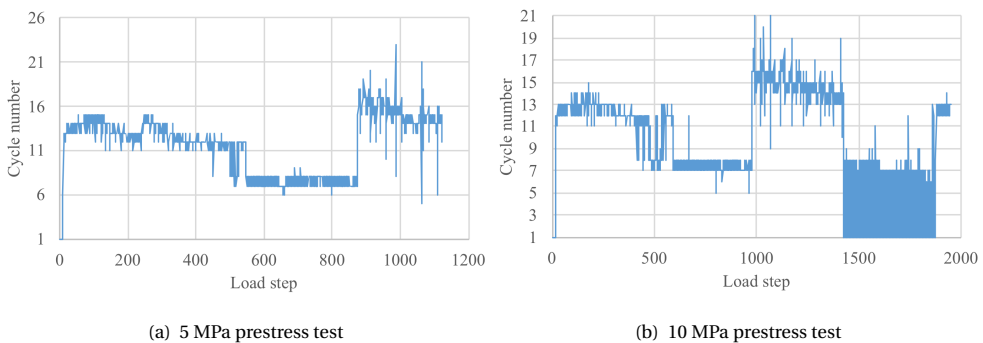


Figure 8.14: Numbers of cycles of each load step in ISLA

The strength limit of the beams can be calculated by hand from equilibrium due to the linear elastic compression zone. The limit strength is

$$F = \frac{1}{2} P \frac{h - d}{a} \quad (8.1)$$

where  $P$  is the prestress force (uniformly applied),  $h$  is the beam depth,  $d$  is the element size and  $a$  is the horizontal distance between a load and a support reaction. The computational results comply with this hand calculation.

## 8.4. DISCUSSION

The results show that ISLA is more robust than SLA and N-R arc-length control. Non-proportional loading can be analysed without modifications in ISLA due to the incremental approach. The principle, algorithms and search paths demonstrated for proportional loading in Chapter 7 are the same as those for non-proportional loading in ISLA. There is no restriction on the load definition; load cases can be

applied and removed simultaneously or separately. Non-proportional SLA as proposed in Chapter 4 does not converge for medium and high prestresses on the specimens analysed in this chapter. ISLA, on the other hand, does converge.

The bending cracks in the specimens branch into multiple cracks. For accurate computation of the crack branches, the N-R method with arc-length control requires a very small step size and a great deal of computation time. ISLA also requires significant computation time but is still faster than the N-R method with arc-length control. However, the number of cycles required for ISLA needs to be reduced to improve its efficiency. There are certainly opportunities for this.

Large prestress values prevent softening of the force-displacement relation while the stress-strain relation does soften. The cracks of SLA and ISLA grow one after the other intermittently, whereas the cracks grow simultaneously in the non-linear N-R method with arc-length control. The point at which the bending cracks branch into multiple cracks is higher for 5 MPa prestress than for 10 MPa prestress. For even higher prestress values, the crack branching starts directly at crack initiation. On the other hand, for low prestress values like 1 MPa, this point is higher than the beam height, which results in no branch cracks and a softening force-displacement curve.



# 9

## EXTENSION OF ISLA TO GEOMETRICAL NON-LINEARITY

In Chapter 5 and 6, the algorithm of ISLA is explained. In Chapter 8, the algorithm is demonstrated on the physical non-linear behaviour of plain concrete. In this chapter, geometrically non-linearity is extended to ISLA. Often, in many concrete and masonry structures, the geometrical non-linearity is relatively small and can be analysed robustly by kinematic descriptions (total Lagrangian, updated Lagrangian and corotational) with N-R iterations. However, the physical non-linearity is large and can be robustly analysed by ISLA.

The implementation principle is to consider geometric non-linearity by the kinematic descriptions while physical non-linearity is considered in damage cycles with reduced secant stiffness. ISLA is an incremental procedure and thus geometric non-linearity can be naturally included in ISLA. When geometric non-linearity is considered, the B matrix (the strain-displacement relation) and geometric non-linear matrix (which is related to the 2nd Piola-Kirchhoff stress) are updated in each increment by the kinematic descriptions [110]. Only the material matrix is updated by ISLA.

## 9.1. INDIRECT DISPLACEMENT CONTROL IN LOAD AND DAMAGE CONTROL

In standard arc-length control [113][114][116] the arc parameter works properly for problems related to geometric non-linearities but often fails due to material instability, which leads to localized failure process zones [118][119][120]. The solution is to select only the DOFs involved in the failure process instead of all DOFs [118][119][15]. A new constraint has been developed based on the energy release rate and does not need to predict and select the DOFs related to the localized failure process zones [120].

Similar to arc-length control, indirect displacement control is introduced in the load and damage control method to avoid or pass localized failure process zones. If the current load is a concentrated nodal force, the solution is to apply imposed displacement with the load control method to replace the nodal force with the load and damage control method. However, if varying forces are applied to multiple nodes (e.g., in case of pressure or other forms of distributed loadings), direct displacement control is impossible. To this end, the concept of a control point in the load and damage control method is defined for indirect displacement control to avoid or pass localized failure process zones.

A control point is a selected node at a critical position (e.g., midspan of a simply supported beam or plate). It is assumed that the displacement of the control point is always increasing. Therefore, the control point is loaded by imposed displacement, which can be defined by a loading schedule or a function such as  $u_n = u_{n-1} + \Delta u$ , where  $\Delta u$  is an incremental displacement, instead of a force. The unbalance nodal force factor  $\lambda_r$  of the control point is defined as the difference of the nodal force between the control point loaded by the imposed displacement and the node loaded by the current load, the factor of which is  $\lambda_2$ .  $\lambda_r$  of the control point can be obtained after a cycle. The current load factor  $\lambda_2$  is adjusted according to the unbalanced force ( $\lambda_2^m = \lambda_2^{m-1} - \lambda_r^{m-1}$ ). This procedure is repeated until  $\lambda_r$  is smaller than a tolerance value  $r_r$  and then the next incremental imposed displacement is applied. Figure 9.1 shows the algorithm for indirect displacement control in the load and damage control.

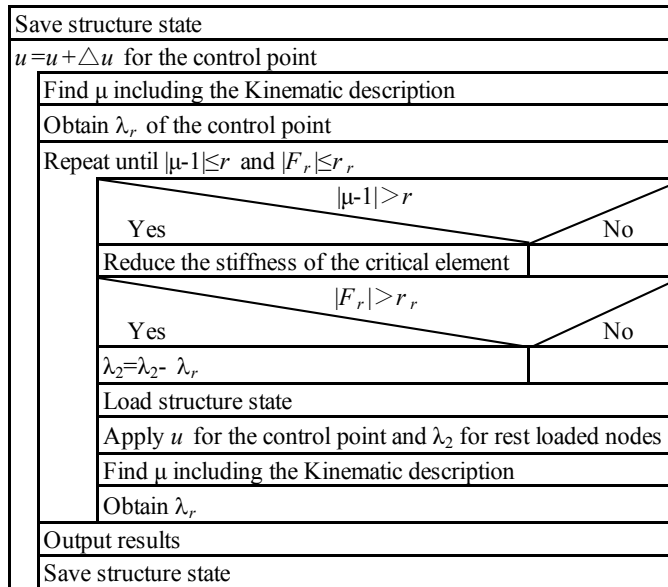


Figure 9.1: Program structure diagram of indirect displacement control of the control point in the load and damage control method

## 9.2. MASONRY WALL OUT-OF-PLANE BENDING TEST

### 9.2.1. MODELLING APPROACH

A test [147][148] was performed at TU Delft on a wall (1.4 metres long and 2.75 metres high), loaded out-of-plane. This specimen was a single-wythe wall constructed of calcium silicate units (214 mm x 71 mm x 102 mm). The masonry properties were  $E=3500$  MPa, Poisson's ratio  $\nu = 0.21$ , tensile strength  $f_t = 0.15$  MPa and fracture energy  $G_f = 0.015$  N/mm. The compressive behaviour was elastic. The wall was subjected to a constant overburden load of 0.2 MPa and subsequently subjected to a uniform face pressure load via airbags. The wall was fully clamped at its base. For the top boundary, the horizontal in-plane and out-of-plane translations were fixed, as well as all rotations, but the top boundary was free to displace vertically. The two side supports are free. Figure 9.2 shows the experiment setup used for the out-of-plane test. At phase one, a -30 kN line load corresponding to 0.2 MPa overburden was applied at the top beam in the Y direction. Then, at phase two, lateral pressure was applied to the whole wall.

The analyses were performed by 1) geometrically linear and physically non-

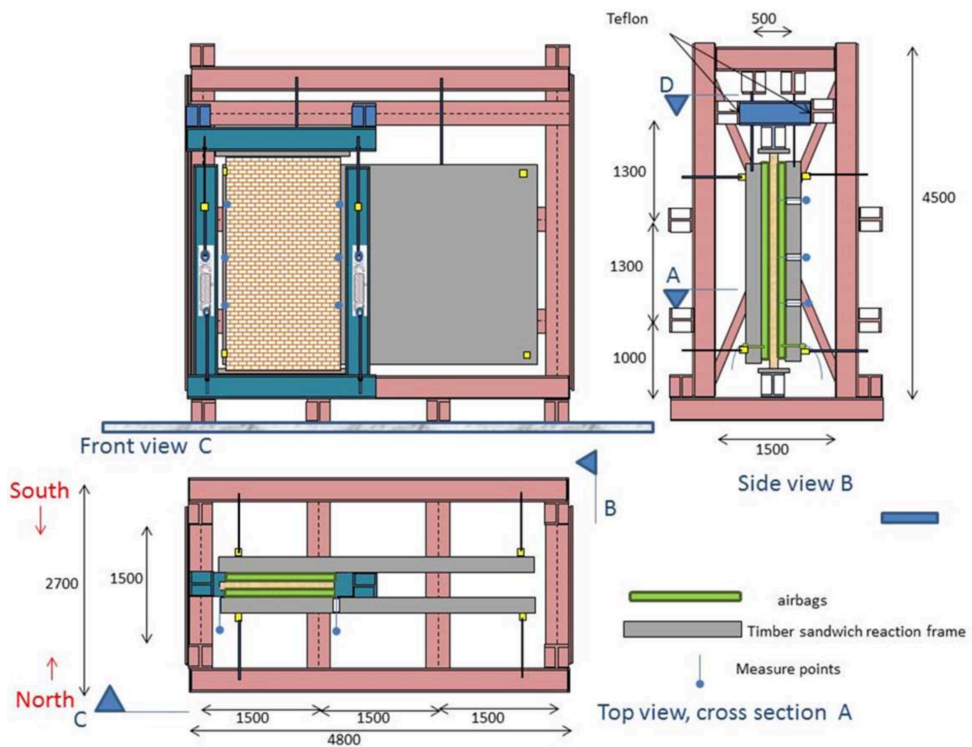


Figure 9.2: Scheme of the test setup used for the out-of-plane test

linear N-R analysis with arc-length control [113] in ABAQUS, 2) geometrically and physically non-linear N-R analysis with arc-length control in ABAQUS, 3) geometrically linear and physically non-linear SLA in ANSYS and 4) geometrically and physically non-linear ISLA in ANSYS. In ISLA, the control point was the central node of the wall and the stiffness reduction factor was 0.75.

The same material properties, element sizes (0.1m x 0.1m) and structural model were used in all analyses. Masonry is modelled by eight-node quadrilateral shell elements, which have nine integration points in the thickness direction<sup>1</sup>. The FEM model is shown in Figure 9.3. The top and bottom layer of the wall are marked. Figure 9.4 shows the colour range of the principal tensile strain contours.

The aim is to validate ISLA with geometrically non-linearity by gaining the out-of-plane mechanism of masonry walls and characterizing the post-peak behaviour after the first crack.

---

<sup>1</sup>ANSYS can only update the material properties at the element level. Nine layers of shell elements with section offset were used in ISLA

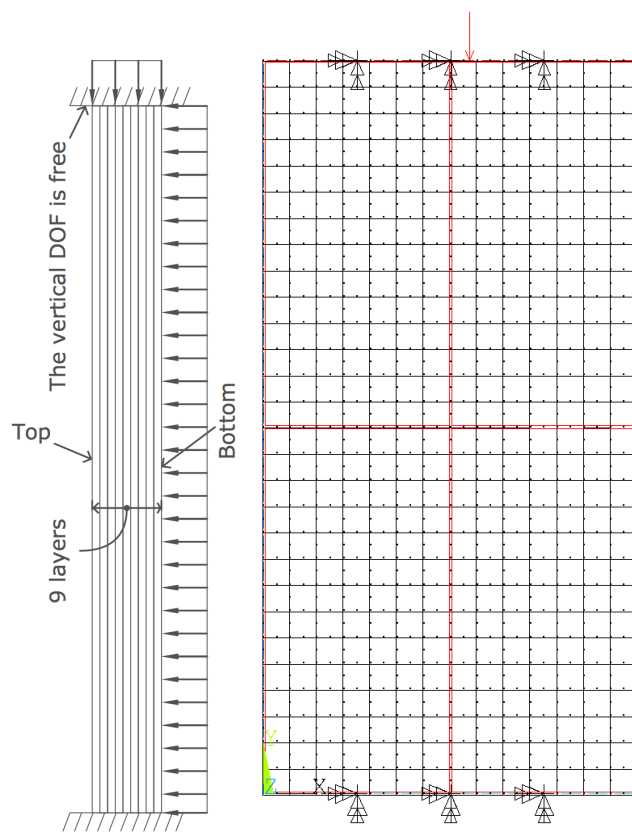


Figure 9.3: FEM model

9

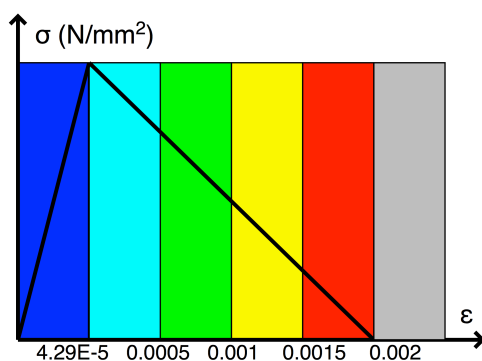


Figure 9.4: Contour colour range

### 9.2.2. TEST RESULTS

Figure 9.5 shows the total lateral force versus midspan displacement diagram for ISLA with geometrical non-linearity. The total lateral load meets the peak 10 kN at 2.6 mm, and the peak plateau remains stable until the displacement is 5.6 mm. Then, the total load drops below 8 kN when the midspan displacement increases to 9 mm. Subsequently, the total load becomes almost zero when the ultimate displacement is approximately 100 mm (98 mm). Figures 9.6 and 9.7 show maximum principal strain contours from the peak until the displacement meets at around 100 mm, the positions of which are marked in Figure 9.5 for ISLA. The total force is at the peak when maximum principal strain at both edges reaches the ultimate strain in Figure 9.6(a) and cracks occur at the midspan of the wall in Figure 9.6(b). Afterwards, the damage is localized in one row of elements in Figure 9.6(e). The plateau was stable until the midspan crack extended from the edges to the middle of the wall in Figure 9.6(h). This was followed by the moment that the maximum principal strain of one row of elements reached ultimate tensile strain while other rows of elements unloaded, as in Figure 9.7(b). Figure 9.7(e) depicts the maximum principal strains of the elements, which are not located at the midspan unloading, from the value marked in green to the value marked in light blue. Figure 9.7(i) shows the crack patterns in the thickness direction when the total lateral force is almost zero. Meanwhile, the crack patterns at the edges of the wall are similar to those shown in Figure 9.6(a) during the damage procedure from Figure 9.6(b) to Figure 9.7(i). The major distinction is that more layers of the elements are damaged, the maximum principal strains of which reach ultimate tensile strain.

Figure 9.8 shows the utilisation values and the unbalanced load factors of the control point of cycles for the load steps at positions e and f. It can be seen that an equilibrium state is not reached until the utilisation value  $\mu$  is smaller than 1 and the unbalanced force factor  $\lambda_r$  of the control point is smaller than 1. For the load step at position e,  $\mu$  is 0.971 and  $\lambda_r$  is 0.184 when an equilibrium state is reached at cycle 13. For the load step at position f,  $\mu$  is 0.995 and  $\lambda_r$  is 0.009 when an equilibrium state is reached at cycle 6.

Figure 9.9 shows midspan displacement versus total lateral force diagrams for ISLA, SLA and the N-R method with arc-length control. The deviation points of N-R and SLA are marked in Figure 9.9. It can be observed that the peak capacities agree

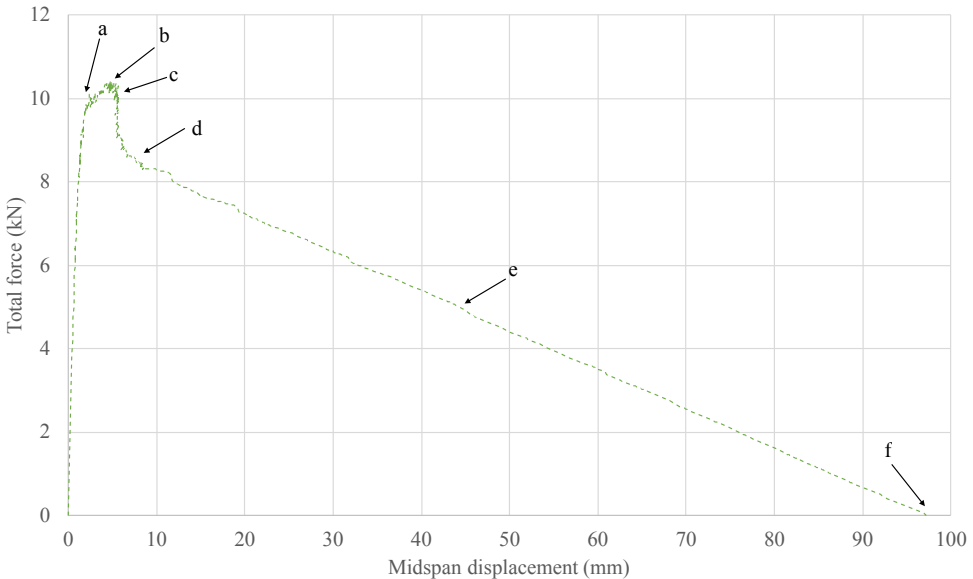
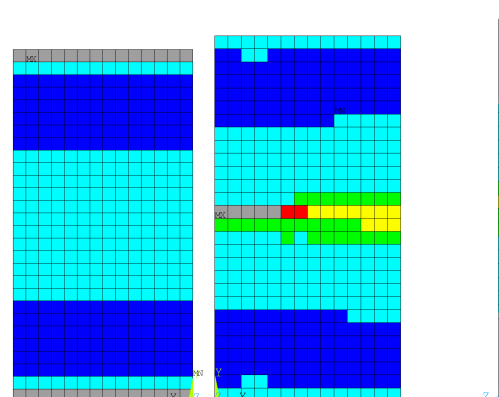
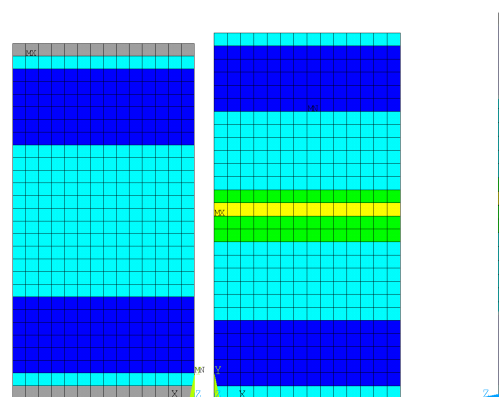
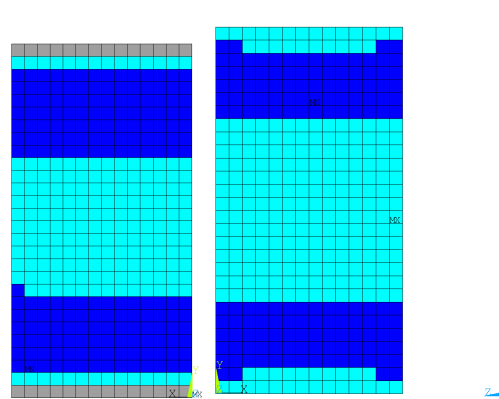


Figure 9.5: Total lateral force versus midspan displacement curve for ISLA with geometrical non-linearity

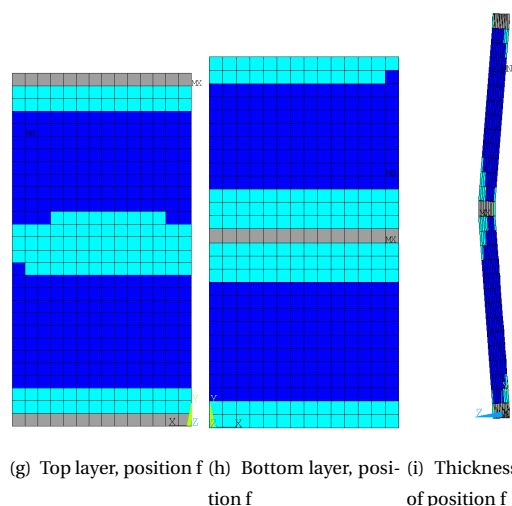
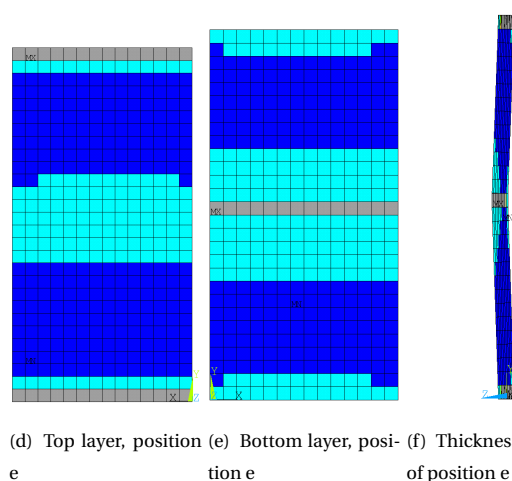
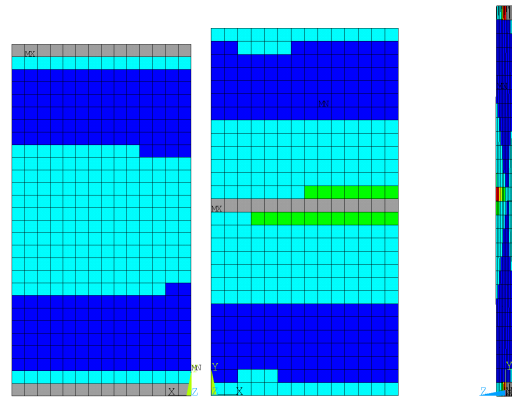
well for these four analyses. However, the post-peak behaviour is different. The geometrically linear analyses from both SLA and the N-R method show a plateau and slight hardening behaviour. They do not exhibit post-peak softening. This confirms that geometrical non-linearity is essential for this problem. Geometrically non-linearity governs post-peak softening behaviour. ISLA can trace the total load to position f when it becomes almost zero and midspan displacement is approximately 100 mm. However, the N-R method with arc-length control [113] diverges close to position e when the midspan displacement is roughly 50 mm. This divergence is related to the localized failure process zones, which are shown later. Possible solutions for arc-length control [113] are to select only the DOFs involved in the failure process [118][119][15] or a new constraint based on the energy release rate[120].

Figure 9.10 shows the crack patterns at the edges and midspan by the N-R method with geometrical non-linearity, the positions of which are marked in Figure 9.9. The edge and midspan cracks are reliable when the capacity meets the peak shown in Figures 9.10(a) and 9.10(b). Figures 9.10(c) and 9.10(d) depict midspan crack development after the peak, showing a discontinuous contour of several elements. The geometrical and physical non-linearity cause localized failure process



9

Figure 9.6: Damage procedure shown by maximum principal strain contour from position a to position c by ISLA with geometrical non-linearity



9

Figure 9.7: Damage procedure shown by maximum principal strain contour from position d to position f by ISLA with geometrical non-linearity

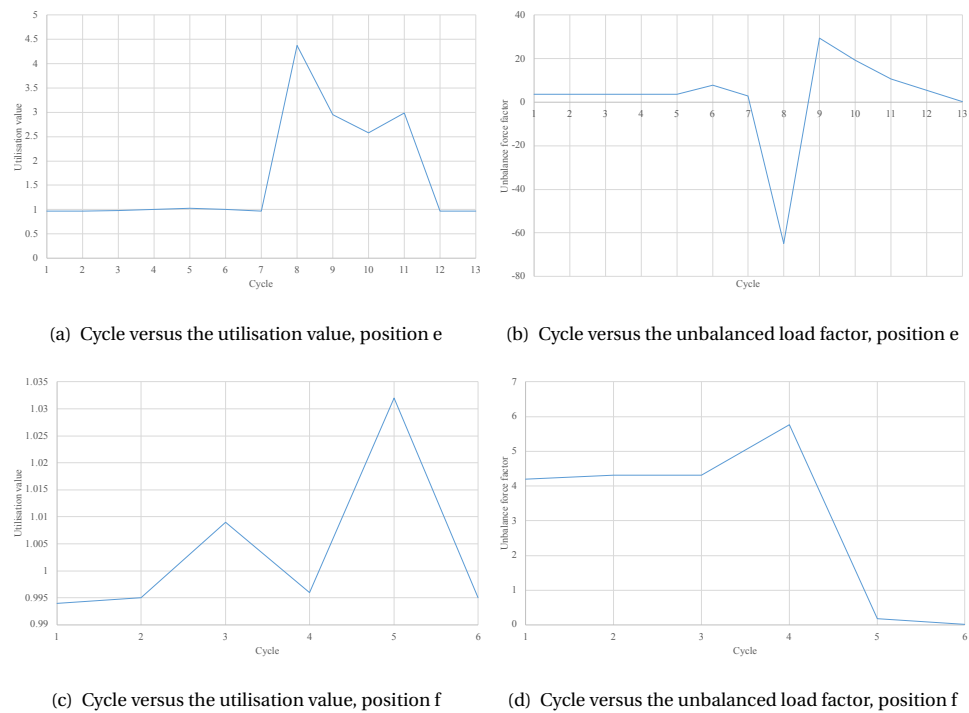


Figure 9.8: Cycle versus the utilisation value and the unbalanced load factor of the control point

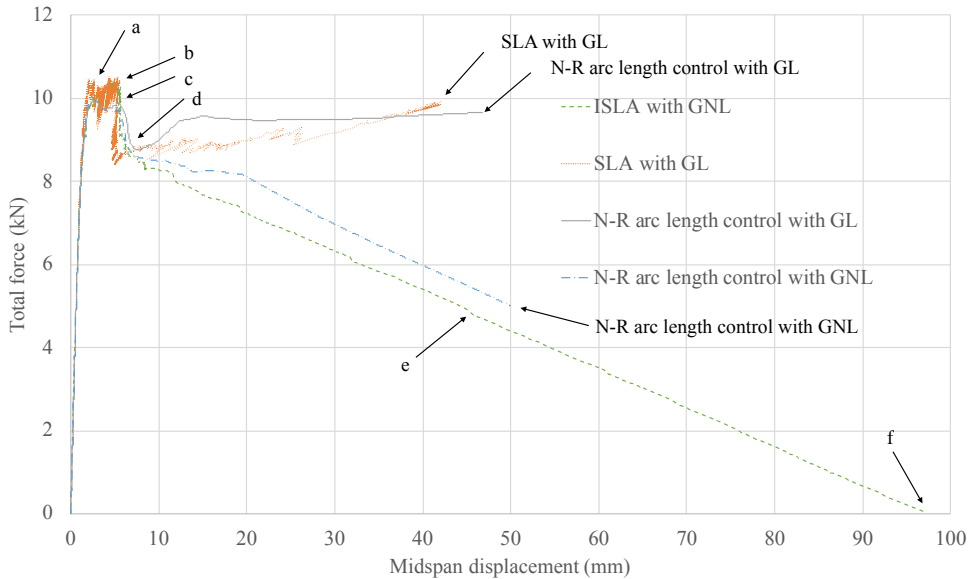


Figure 9.9: Midspan displacement-force curves for comparison of ISLA, SLA and the N-R method with arc-length control

zones, which is an unrealistic equilibrium state. The damage procedure thus cannot be traced properly.

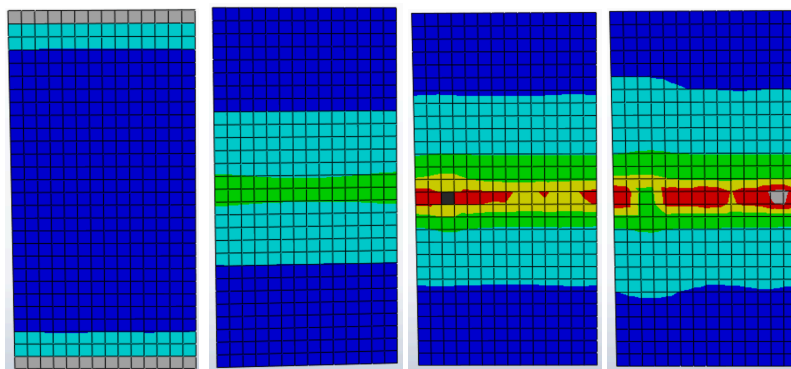
Figure 9.11 shows the maximum principal strain contour when the total reaction force drops to around 8 kN from SLA, the positions of which are marked in Figure 9.9. The crack patterns are similar to those from ISLA. However, SLA exhibits hardening behaviour after this due to the lack of geometrical non-linearity in the current version of SLA.

## 9

### 9.3. DISCUSSION

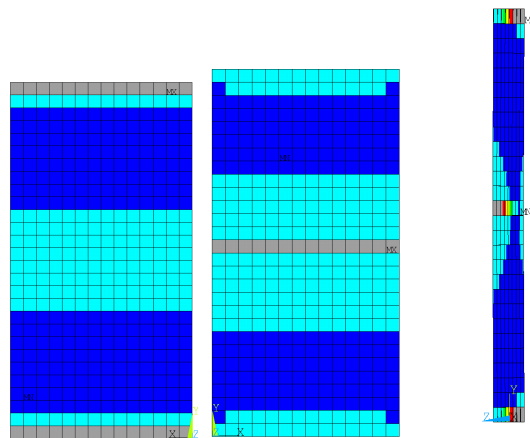
ISLA exhibits robustness and accuracy when geometrical non-linearity is considered. The displacement-force diagram can extend to the load step when the total load is zero. Crack propagation has been correctly and smoothly traced. In the wall out-of-plane test, geometrical non-linearity influences not only structure deformation but also ductility (post-peak behaviours).

Indirect displacement control of the control point is introduced to the load and damage control method in ISLA to avoid or pass the localized failure process zones



(a) Top layer, position b (b) Bottom layer, position b (c) Bottom layer, position c (d) Bottom layer, position between position c and d

Figure 9.10: Damage procedure at the edges and midspan by the N-R method with geometrical non-linearity



(a) Top layer, position d (b) Bottom layer, position d (c) Thickness direction of position d

Figure 9.11: Maximum principal strain at the edges and midspan and in the thickness direction at the beginning point of the hardening part (position d) by SLA

caused by geometrical and physical non-linearity. Without indirect displacement control, ISLA cannot trace the post-peak softening behaviour. Although the control point is selected at the critical position of the wall, the control point can be any loaded node since the nodal forces of all loaded nodes are adjusted based on the control point, which has a similar advantage as the improved arc-length control [120]. In Chapter 11, the control point is selected at the loading position, which is not a critical position.

The standard arc length [113][114][116] diverges due to localized failure process zones. The possible solutions are to select only the DOFs involved in the failure process [118][119][15] or a new constraint based on the energy release rate[120].

# 10

## EXTENSION OF ISLA TO TRANSIENT ANALYSIS

In this chapter, ISLA is extended to transient analysis. ISLA is an incremental procedure; therefore, transient non-linearity can be naturally included in it. The implementation principle considers transient non-linearity by the Newmark time integration scheme while physically non-linearity is considered in damage cycles with reduced secant stiffness. The damage control method for static analysis (Chapter 5) is modified and used for transient analysis.

ISLA is validated for concrete in a multiple degree of freedom system. The material model of ISLA is the saw-tooth model, which follows the reduced secant stiffness for unloading globally or locally.

### 10.1. IMPLEMENTATION

The Newmark time integration scheme and the N-R method can be used for implicit non-linear transient analysis as implemented in ANSYS. Eq. (10.8) is used to solve increment displacements [110].

$$\hat{K}^t = K^t + c_0 M \quad (10.1)$$

$$\hat{f} = f_e^{t+\Delta t} + M(c_1 \dot{u}^t + c_2 \ddot{u}^t) - f_i^t \quad (10.2)$$

$$\hat{K} u_1^{\Delta t} = \hat{f} \quad (10.3)$$

$$\ddot{u}_i^{t+\Delta t} = c_0 u^{\Delta t} - c_1 \dot{u}^t - c_2 \ddot{u}^t \quad (10.4)$$

$$\hat{K}_i^{t+\Delta t} = K^{t+\Delta t} + c_0 M \quad (10.5)$$

$$r_i^{t+\Delta t} = f_e^{t+\Delta t} + M \ddot{u}^{t+\Delta t} - f_i^{t+\Delta t} \quad (10.6)$$

$$\hat{K}_i^{t+\Delta t} d u_{i+1}^{\Delta t} = r_i^{t+\Delta t} \quad (10.7)$$

$$u_{i+1}^{\Delta t} = u_i^{\Delta t} + d u_{i+1}^{\Delta t} \quad (10.8)$$

where the coefficients are given by

$$c_0 = \frac{1}{\beta \Delta t^2}, \quad c_1 = \frac{1}{\beta \Delta t}, \quad c_2 = \frac{1}{2\beta} - 1 \quad (10.9)$$

and  $K$  is the non-linear material stiffness matrix. The matrix  $\hat{K}$  and  $\hat{f}$  are called the dynamic stiffness matrix and the effective load vector. It can be concluded that the transient effect can be naturally implemented in ISLA since the change of the material stiffness matrix  $K$  in ISLA has no influence on the extra component  $c_0 M$  in the dynamic stiffness matrix and the effective load vector  $\hat{f}$ .

In ISLA, the acceleration and internal force vector are updated in the Newmark time integration scheme and the N-R method while the non-linear material stiffness matrix is linearised by the saw-tooth model. The details of ISLA are elaborated in Chapter 5. In this dissertation, the N-R method is used as part of ISLA as well as independently of ISLA. In the remainder of this chapter, the term N-R method refers to the independent method that has been used to check ISLA. The main difference between ISLA and the N-R method is the computation of the incremental displacement  $\Delta t$ . In the N-R method,  $\Delta t$  is computed by multiple  $d u^{\Delta t}$  in Eq. (10.8) with the updated  $K$  (positive or negative). In ISLA,  $\Delta t$  is computed with one  $d u^{\Delta t}$  with the fixed reduced  $K$  (always positive). Due to the fact that transient analysis is sensitive to stiffness change, ISLA should follow both load steps (the relationship between time and acceleration) and damage cycles (stiffness reduction). That is to say, the proposed method needs to reach a dynamic "equilibrium" state [110] for each stiffness reduction in a cycle, which is the principle of the damage control method, while the stiffness continued to be reduced in the load control method and the load and damage control method. Meanwhile, the equilibrium state should

also be reached for each load step defined by the load schedule. A modified damage control method is introduced based on the version for static analysis, which has two main distinctions. One is that time is adjusted along with the scaled acceleration during cycles since the load is time-dependent in transient analysis. The other is each a load schedule is added. Equilibrium states are searched for after every stiffness reduction. This search is repeated until the load factor reaches the value of the current load step. Subsequently, the next load step is applied.

Suppose that after a load (acceleration) step  $n$ , somewhere the failure surface is reached. The second  $\lambda, n$  and  $m$  below represent the current load factor, the load step and the cycle number, respectively.

$$\mu_n = \mu(\lambda_{ini}, \lambda_n, K_n) = 1 \quad (10.10)$$

For the first cycle in the next load step, if

$$\mu_{n+1}^1 = \mu(\lambda_{ini}, \lambda_{n+1}^0, K_{n+1}^0) > 1 \quad (10.11)$$

where  $\lambda_{n+1}^0$  is an updated  $\lambda_n$  based on the loading schedule,  $K_{n+1}^0 = K_n$ , and the superscript on  $\lambda$  refers to the cycle number of a load step, subsequently reducing the Young's modulus of the critical element and restarting from  $\mu_n$

$$\mu_{n+1}^2 = \mu(\lambda_{ini}, \lambda_{n+1}^1, K_{n+1}^1) \quad (10.12)$$

where  $K_{n+1}^1$  is the stiffness with reduced Young's modulus of the critical element.

If  $\mu$  is still larger than 1, then the procedure is again restarted from  $\mu_n$

$$\mu_{n+1}^3 = \mu(\lambda_{ini}, \lambda_{n+1}^2, K_{n+1}^1) \quad (10.13)$$

where  $\lambda_{n+1}^2$  is a reduced  $\lambda_{n+1}^1$ .

If  $\mu$  is still larger than 1, then the procedure is repeated, restarting from  $\mu_n$  until

$$\mu_{n+1}^{m'+1} = \mu(\lambda_{ini}, \lambda_{n+1}^{m'}, K_{n+1}^1) \leq 1 \quad (10.14)$$

where  $\lambda_{n+1}^{m'}$  means that  $\lambda_{cur}$  is adjusted  $m'$  times, which is a scaled  $\lambda_{n+1}^{m'-1}$ .

The above procedure is continued with the dynamic "equilibrium"  $\mu_{n+1}^{m'+1}, \lambda_{n+1}^0$  from the loading schedule and the reduced stiffness  $K_{n+1}^1$

$$\mu_{n+1}^{m'+2} = \mu(\lambda_{ini}, \lambda_{n+1}^0, K_{n+1}^1) \quad (10.15)$$

$$\mu_{n+1}^{m''+1} = \mu(\lambda_{ini}, \lambda_{n+1}^{m''}, K_{n+1}^2) \leq 1 \quad (10.16)$$

This loop is followed with  $K_{n+1}^2, K_{n+1}^3, K_{n+1}^4 \dots$  until

$$\mu_{n+1}^m = \mu(\lambda_{ini}, \lambda_{n+1}^0, K_{n+1}^w) \leq 1 \quad (10.17)$$

where  $w$  means the stiffness is reduced  $w$  times.

Figure 10.1 shows the program structure diagram of the modified damage control method for transient analysis in ISLA. There are  $m$  cycles for Load step  $n$ . The load step will not be updated from  $n$  to  $(n + 1)$  until the scaled  $\lambda_n^m$  is equal to  $\lambda_n$ . During  $m$  cycles,  $w$  dynamic "equilibrium" are reached based on  $\mu$  and the corresponding reduced stiffness. In this algorithm, the incremental time  $t$  is adjusted by Eq. (10.18).

$$t_n^m = \frac{\lambda_n^m - \lambda_{n-1}}{\lambda_n - \lambda_{n-1}} \Delta t \quad (10.18)$$

where  $\Delta t$  is the defined time increment of a load step.

Due to the transient effects, the factor  $\lambda$  cannot be scaled only by the extrapolation procedure as shown in Figure 6.1, which is based on the assumption that  $\lambda$  and  $\mu$  have a linear or a weakly non-linear relationship. Therefore, it is recommended that  $\lambda$  is scaled by the extrapolation procedure in the first ten cycles and that  $\lambda$  is then scaled by the bisection method (Eq. (10.19)). Note that  $\lambda_n^m$  cannot be smaller than  $\lambda_{n-1}$ , otherwise the time increment becomes negative. Therefore, the extrapolation procedure is replaced by the bisection method when  $\lambda_n^m$  is smaller than  $\lambda_{n-1}$  even though  $m$  is smaller than 10.

$$\lambda_n^m = \frac{\lambda_u + \lambda_l}{2} \quad (10.19)$$

where  $\lambda_u$  is the upper boundary of  $\lambda$  and  $\lambda_l$  is the lower boundary of  $\lambda$ . The initial value of  $\lambda_u$  is  $\lambda_n$  while that of  $\lambda_l$  is  $\lambda_{n-1}$ .  $\lambda_u$  is updated by  $\lambda_n^m$  when  $\mu$  is larger than 1.  $\lambda_l$  is updated by  $\lambda_n^m$  when  $\mu$  is smaller than 1.

The default tolerance  $r$  is 0.1%. Note that the utilisation value  $\mu$  cannot be 1 for the certain stiffness  $K$  due to the transient effect. When  $m$  is larger than 9 and  $\mu$  is smaller than 1.001, an equilibrium is assumed to be reached since extra damage can be introduced into the system with a constant stiffness reduction factor <sup>1</sup>.

<sup>1</sup>Note that the value of the stiffness reduction factor is between 0 and 1. A large stiffness reduction factor value means a small stiffness reduction.

When  $m$  is larger than 20, the algorithm restarts from the previous equilibrium state and searches for the next equilibrium state of  $K'$  in which the stiffness of the critical element is reduced. The reason why an equilibrium cannot be found is that if a structure snaps back, the load needs to be reduced, which leads to a time decrement. For a static analysis, damage control method can always find an equilibrium state for the certain stiffness when  $\mu$  is exactly 1 (Chapter 7).

The strategies mentioned above guarantee computational robustness mathematically. In general, a dynamic "equilibrium" can be reached with the extrapolation procedure within 10 iterations if no extra damage is introduced by the constant stiffness reduction factor.

Comparing the modified damage control method in ISLA and the N-R method, the stiffness is based on  $du^{\Delta t}$  in the N-R method whereas the time and the acceleration are scaled based on the fixed and reduced stiffness with a constant stiffness reduction factor in the modified damage control method.

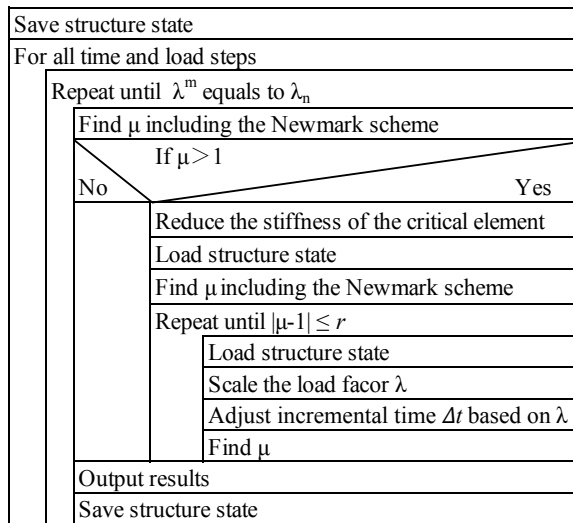


Figure 10.1: Program structure diagram of the modified damage control method for transient analysis in ISLA

## 10.2. FEM MODEL AND MATERIAL PROPERTIES

A multiple DOF system was used to test the algorithm. Four beam elements were considered with 6 m length in total and a square-section (the section data was 0.2 X 0.2) in Figure 10.2. The left node of Element 1 was subjected to an acceleration in the horizontal direction. Concrete properties with linear softening were considered to validate the robustness and the accuracy for brittle materials. Young's modulus is 30000 MPa, and Poisson's ratio is 0. The tensile strength is 1.43 MPa, and the ultimate strain is 0.002. Compressive behaviour is elastic. The values of point masses and acceleration were exaggerated to ensure the material would yield. The loading schedule consists of 50 load steps of  $0.3 \text{ m/s}^2$  and the time of every load step is 0.02 s. There are four-point masses of 8000 kg. The selected stiffness reduction factors are 0.95 and 0.99. The tolerance value of ISLA is 0.1%.



Figure 10.2: FEM model of the multiple degree of freedom system with element number

## 10.3. TEST RESULTS

Figure 10.3 shows time versus strain of element 1 before cracking. It can be seen that only one wave vibration occurred before the concrete softens. A similar phenomenon can be seen for the displacement result at the global level, as shown in Figure 10.4. The inertia force of the acceleration is large enough for the transient effect, otherwise when the acceleration load is halved, multiple wave vibrations can be observed when the concrete is still elastic, as shown in Figure 10.5.

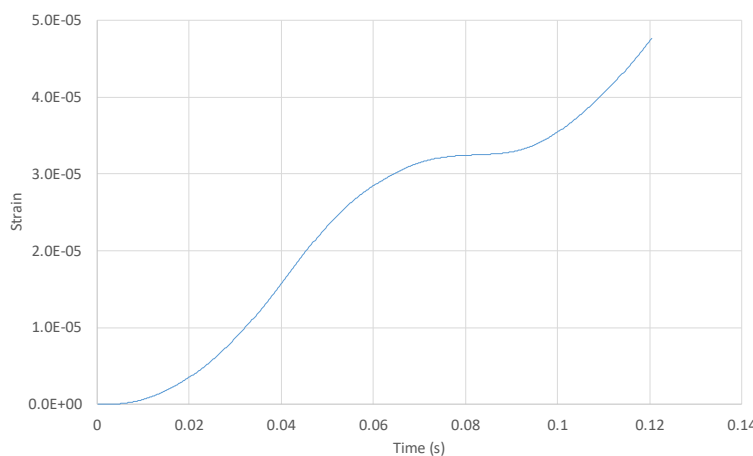


Figure 10.3: Time versus strain of element 1 for the N-R method

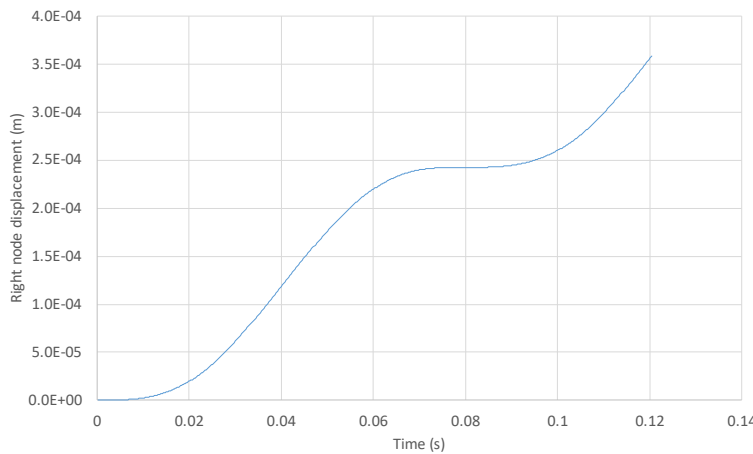


Figure 10.4: Time versus right node displacement of element 4 for the N-R method

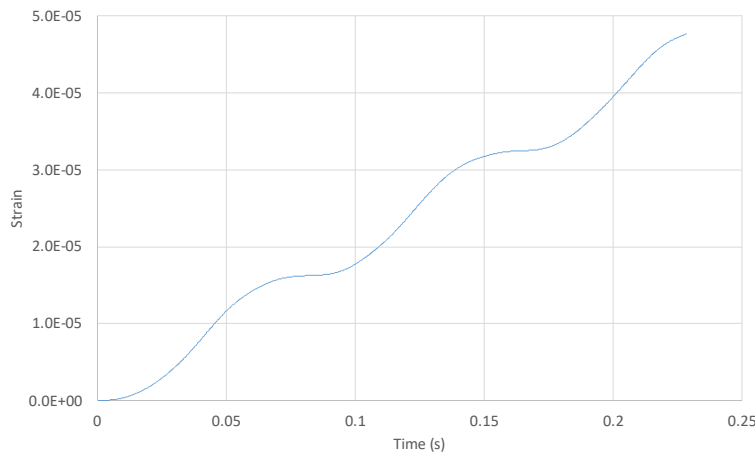


Figure 10.5: Time versus strain of element 1 for the N-R method when the acceleration is halved

Figure 10.6 shows time versus top node displacement for N-R and ISLA, and it can be seen that they overlap each other. However, not visible in Figure 12.6 is that the small stiffness reduction factor results in extra damage. Figure 10.7 shows the relative differences of ISLA compared with the N-R method for different stiffness reduction factors. The maximum value of the relative difference is 7.01% for the stiffness reduction factor of 0.95 while it is 1.27% for the stiffness reduction factor of 0.99. The starting moments of the difference are related to crack initiation (0.14 s and 0.16 s for the stiffness reduction factors of 0.95 and 0.99, respectively). For both stiffness reduction factors, the difference increases to the peak at 0.2 s and then continues to decrease.

Figure 10.8 shows time versus stress of different elements for the N-R method and ISLA. Damage is localized in Element 1. When Element 1 begins to soften, other elements unload rather than become damaged. After the stress of Element 1 drops to zero, stresses of other elements fluctuate. ISLA aligns well with the N-R method for all elements when the stiffness reduction factor is 0.99, in Figure 10.8 (a). However, the stiffness reduction factor of 0.95 causes slightly lower stress, especially when the damage is initialized for Element 1 in Figure 10.8 (b). Similarly, the time-strain curves of Element 1 for the N-R method and ISLA overlap each other in Figure 10.9 (a). However, the difference from the stiffness reduction factor of 0.95 can be observed when the curves are zoomed-in until 0.24 s, at which point the strain of

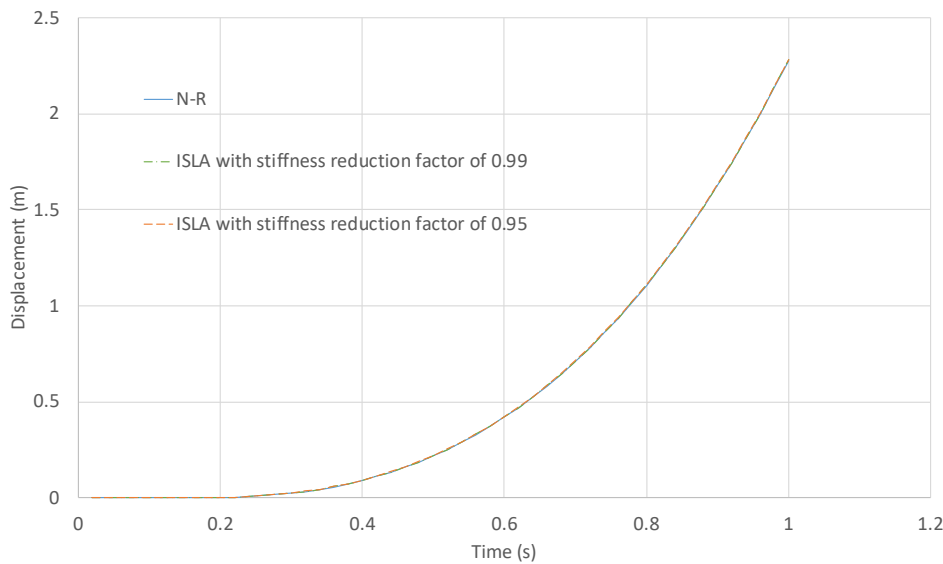


Figure 10.6: Time versus right node displacement of element 4 for the N-R method and the modified damage control method

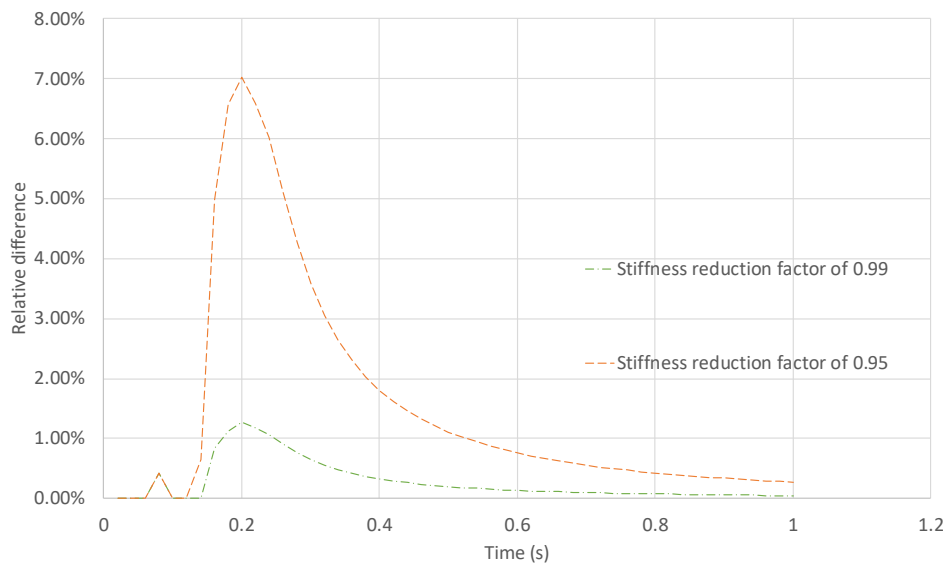
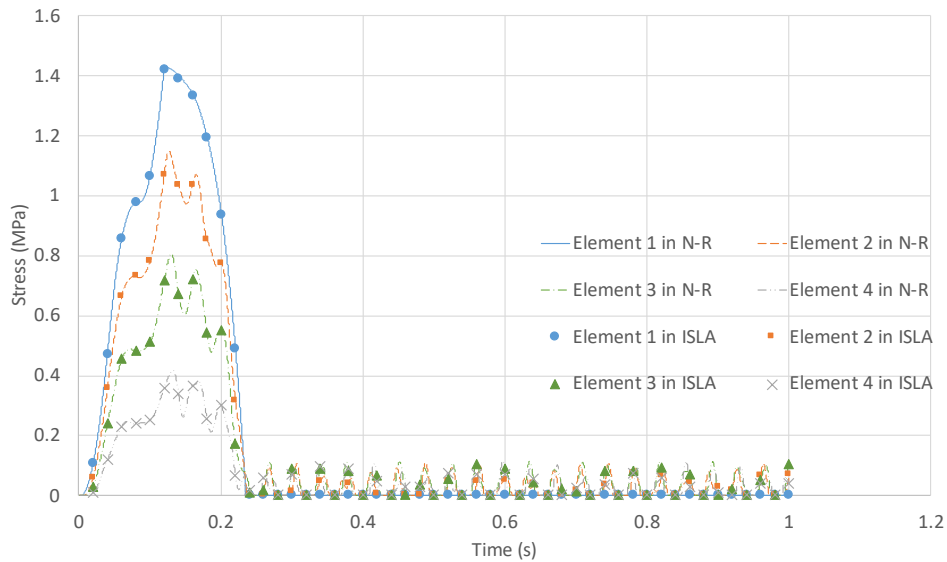
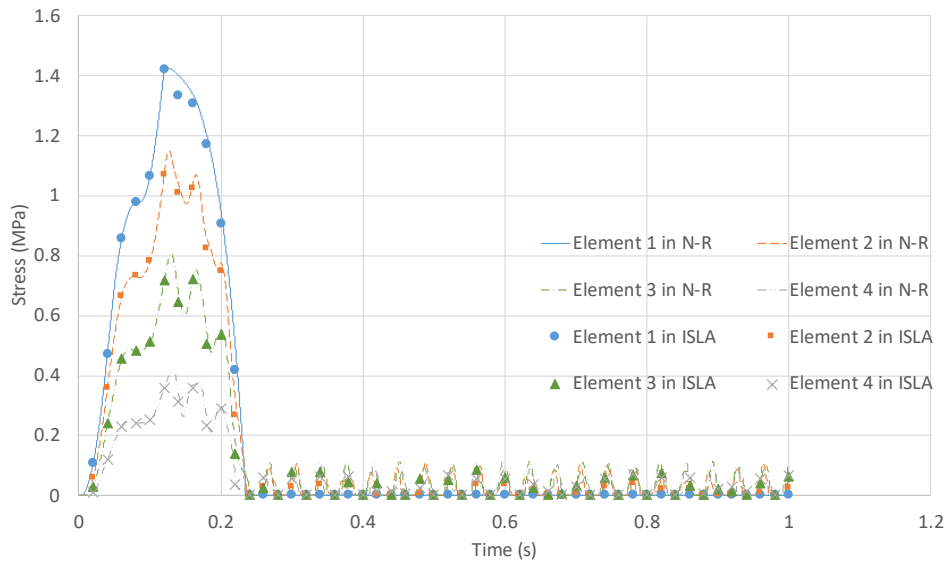


Figure 10.7: Relative difference of right node displacement of element 4 between the N-R method and the modified damage control with different stiffness reduction factors

Element 1 just exceeds the ultimate strain, as shown in Figure 10.9 (b). Figure 10.10 shows the relative differences of strain between the N-R method and ISLA with different stiffness reduction factors. The maximum value of the relative difference is 8.59% at 0.18 s for the stiffness reduction factor of 0.95 while it is 1.76% at 0.16 s for the stiffness reduction factor of 0.99. For both stiffness reduction factors, the difference does not accumulate monotonically with the acceleration increase. The larger differences result from extra damage from the stiffness reduction factor of 0.95. The extra damage is especially serious when the stiffness changes abruptly. This is why the moment when the material begins to soften has relatively larger errors. The extra damage can be quantified as the error of the utilisation value  $\mu$  in ISLA, as shown in Figure 10.11. The error is defined as the relative difference between  $\mu$  and 1. The error starts when the damage is initialized for Element 1 at 0.14 s for both stiffness reduction factors. The maximum error for the stiffness reduction factor of 0.99 is 0.9% while that for the stiffness reduction factor of 0.95 is 4.8%. Note that there is no error of  $\mu$  in the damage control method for static analysis in Chapter 7. Figure 10.12 shows time versus number of stiffness reductions. The stiffness reduction factor of 0.99 needs five times the number needed for 0.95 for each time increment. A large stiffness reduction factor such as 0.99 is unnecessary and not efficient when strain reaches the ultimate strain. Figure 10.13 shows stiffness reduction versus number of cycles for different stiffness reduction factors. When the number of cycles is 10, it indicates that the utilisation value is smaller than 0.999, the extra damage of which may influence the computational accuracy. The number of cycles does not exceed 10, which means a dynamic "equilibrium" (the utilisation value is not larger than 1) is reached for each stiffness reduction by the extrapolation or interpolation procedure. Due to the non-linearity caused by the transient effect, more than three cycles are needed to reach a dynamic "equilibrium".



(a) Stiffness reduction factor of 0.99



(b) Stiffness reduction factor of 0.95

Figure 10.8: Time versus stress for different stiffness reduction factors

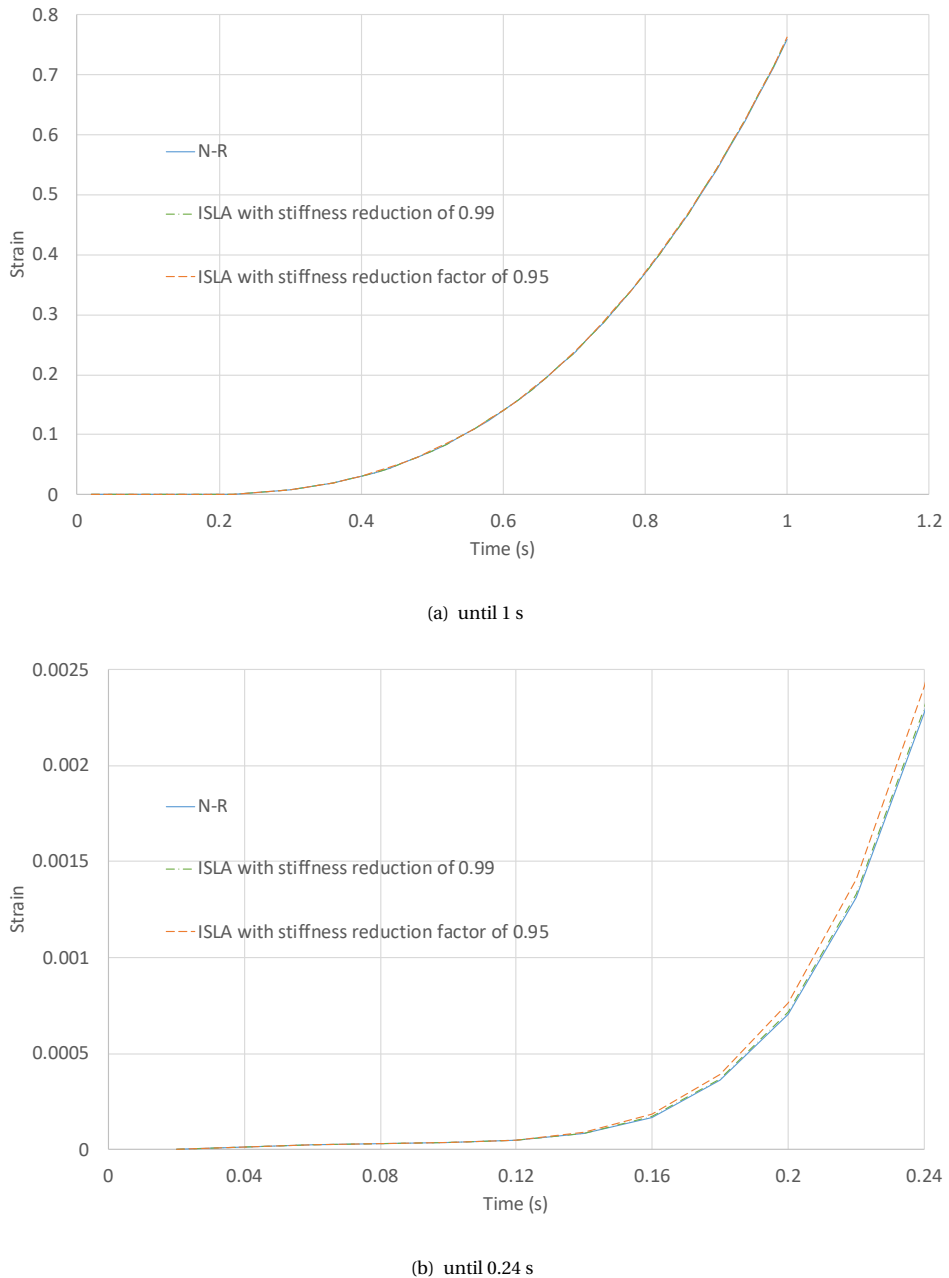


Figure 10.9: Time versus strain of Element 1 for different stiffness reduction factors

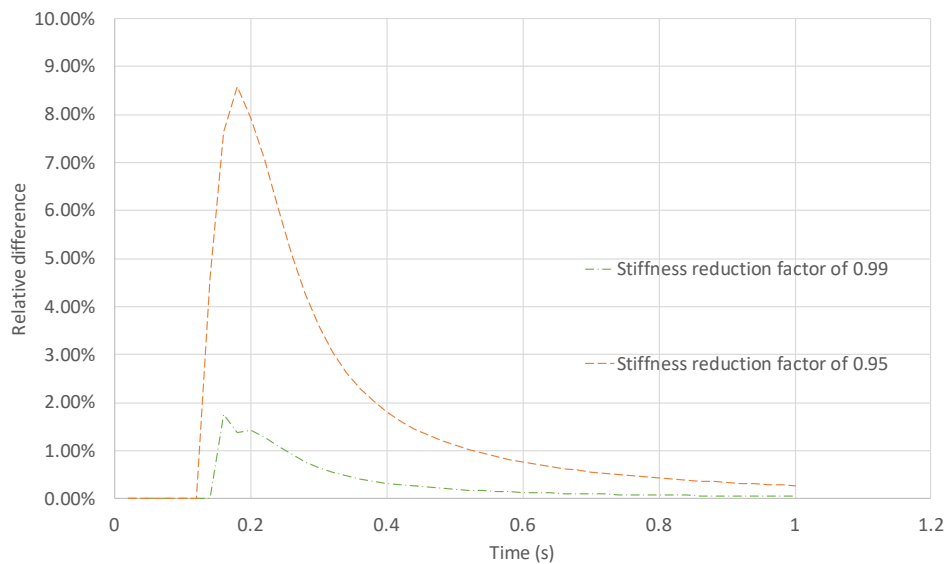


Figure 10.10: Relative strain difference of Element 1 between the N-R method and ISLA with different stiffness reduction factors

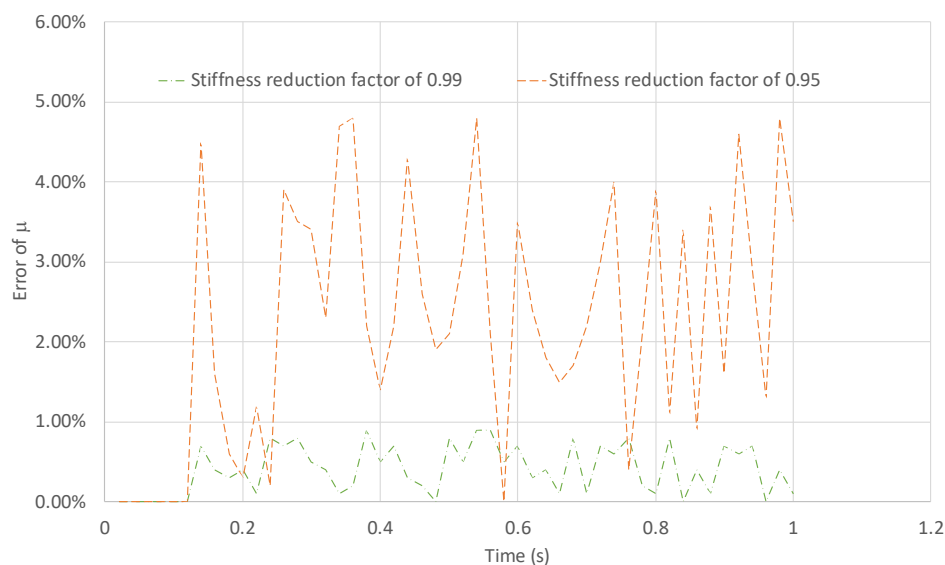


Figure 10.11: Utilisation value error versus time in ISLA for different stiffness reduction factors

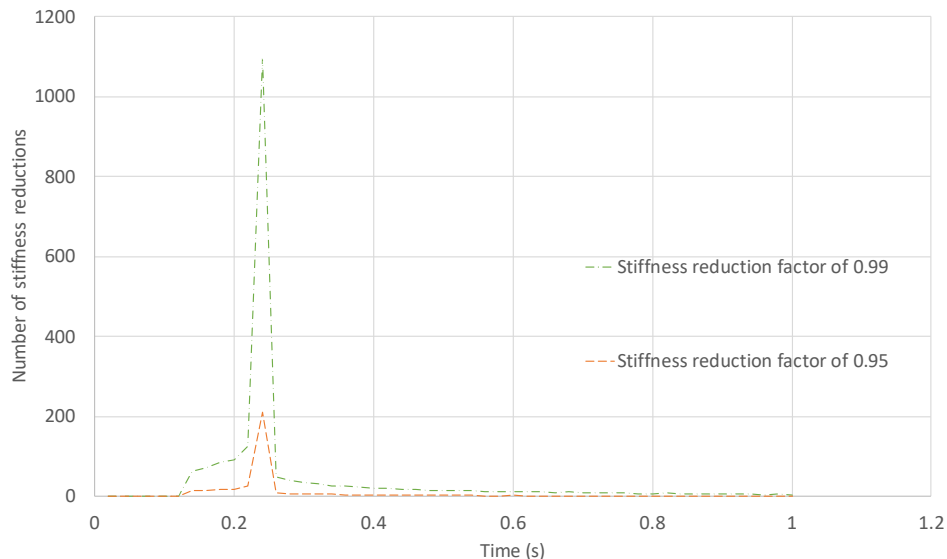


Figure 10.12: Number of stiffness reductions versus time for different stiffness reduction factors

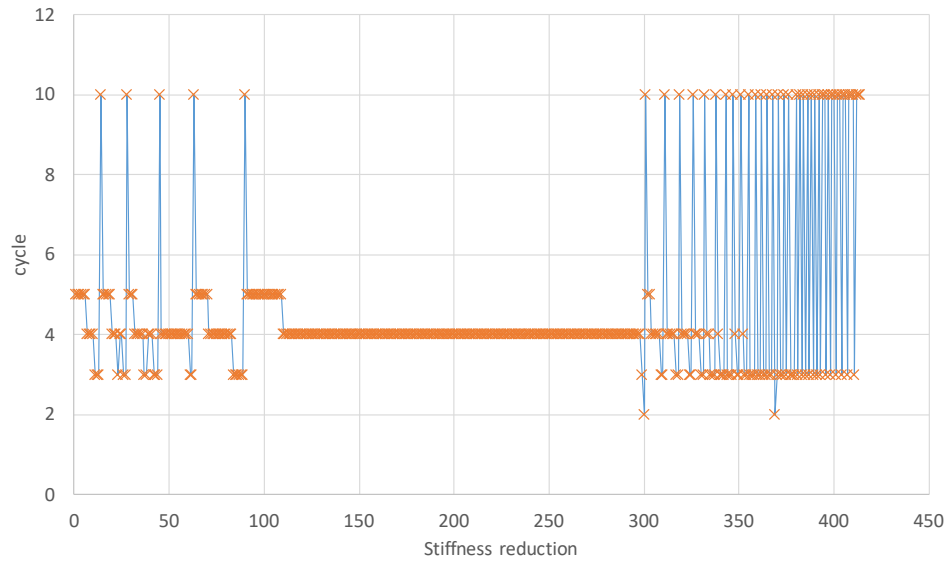
## 10.4. DISCUSSION

In this chapter, ISLA is extended to transient analysis. The transiently loaded bar example shows that the analysis is robust due to the saw-tooth model for brittle materials.

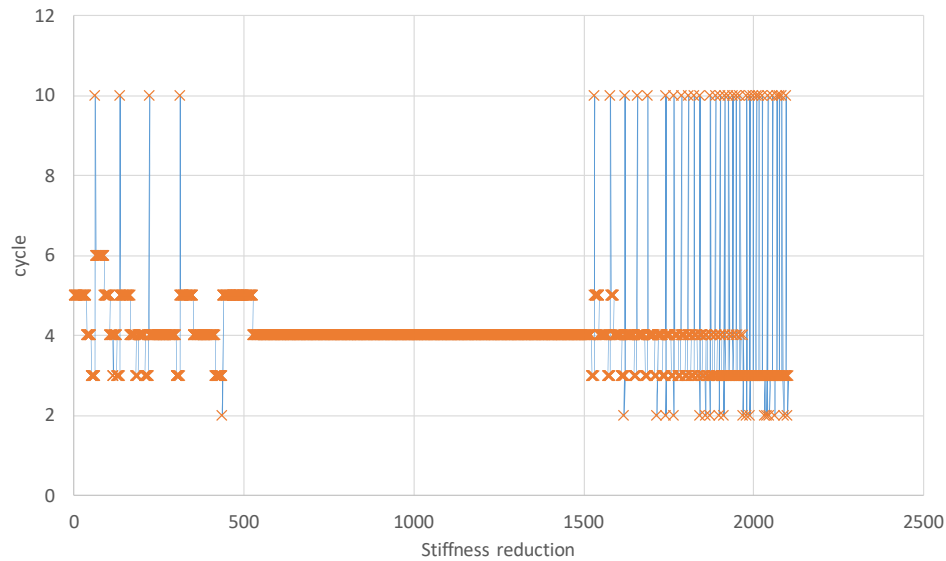
The analysis is also accurate provided that the stiffness reduction factor <sup>2</sup> is large. It is hypothesized that the latter is caused by the concrete material model, which includes a dramatic change in tangent stiffness at crack initiation. Extra damage can be introduced by a small constant stiffness reduction factor and exaggerated by the transient effect. In this transient analysis, relatively small stiffness reductions cause too much damage, which results in errors in the utilisation values. Such errors do not occur in the damage control method for static analysis (see Chapter 7). In future development, a varying stiffness reduction factor may overcome this problem. A large stiffness reduction factor may be used when the damage is initialized; a small stiffness reduction factor may be used when the ultimate strain is reached.

ISLA and the N-R method have different ways of updating the stiffness. Updat-

<sup>2</sup>Note that the value of the stiffness reduction factor is between 0 and 1. A large stiffness reduction factor value means a small stiffness reduction.



(a) Stiffness reduction factor of 0.95



(b) Stiffness reduction factor of 0.99

Figure 10.13: Stiffness reduction versus number of cycles for different stiffness reduction factors

ing the stiffness in ISLA is based on the damage history with secant stiffness while in N-R, it is based on the displacement history with tangent stiffness. The N-R method employs the current stiffness at the end of the current iteration for the next iteration while SLA and ISLA use the damaged stiffness, which is based on the saw-tooth model, at the end of the current cycle for the next cycle. The passive and proactive updating procedure results in the fact that SLA and ISLA have relatively smaller stiffnesses for the same displacements after one iteration. Furthermore, extra damage may be introduced when a small stiffness reduction factor is used, which can cause different equilibrium states to be found. In addition, the stress and strain are re-distributed due to the stiffness reduction before applying the load increment of the next load step in ISLA whereas they are not split in N-R, which may lead to different equilibrium states. Apart from that, in SLA and ISLA, critical elements are chosen cycle-by-cycle, which means that for each cycle, only one critical element is chosen, whereas in the N-R method, the stiffnesses of multiple elements is updated simultaneously. Moreover, due to the failure criterion of SLA and ISLA that the stress-strain state of the critical element is on the material curve, the stress-strain states of other damaged elements are below the curve. Over all, SLA and ISLA have more flexible results than the exact solution while N-R has stiffer results than the exact solution. However, it is undetermined which method has a higher capacity because SLA and ISLA have smaller stiffnesses, for which the saw-tooth model is introduced, but stress and strain redistribution causes more elements to carry the load. These stiffness differences may cause large effects in transient analysis. As a result, ISLA and the N-R method may obtain different equilibrium states.

Although reinforced concrete is not studied in this chapter, it is expected that this material can also be analysed by transient ISLA. The saw-tooth model for brittle materials follows the secant stiffness for unloading, whereas the plastic material model for reinforcement follows the initial stiffness for unloading. Even when the acceleration increases monotonically at a global level, damaged elements may still unload at a local level. When the saw-tooth model is used for ductile materials, the incorrect unloading path may cause an unrealistic response. ISLA can be extended to search for a non-secant unloading path (see Appendix B). However, the implementation may cause divergences of ISLA due to the non-linearity of the plastic material model [83]. Consequently, this has not yet been solved.

# 11

## APPLICATION OF ISLA AT THE STRUCTURAL LEVEL

In this chapter, ISLA is validated at the structural level, including the aspect of non-proportional loading. Two structural examples tested in the laboratory are selected, a masonry facade settlement test and a full-scale masonry house pushover test.

### 11.1. MASONRY FAÇADE SUBJECTED TO DEAD LOAD AND SETTLEMENT

Due to underground construction, existing buildings may suffer settlement damage. A laboratory test was carried out on a scaled masonry facade subjected to tunnel-induced settlement [149]. SLA was used to simulate this experiment [134][131]. However, it was necessary to make compromises due to the non-proportional loading. The problem is that the initial dead load cannot be kept on the structure with a factor 1.0 when scaling the settlement load. To partially solve this, the settlement load scaled as well as the combination of settlement load and dead load were scaled [134][131]. This, however, resulted in only 20% dead load on

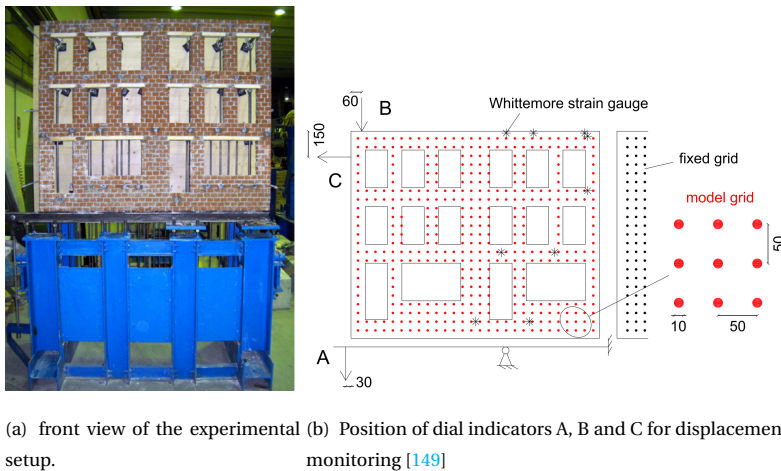
the structure, which is unrealistic. In addition, it was not possible to determine the ultimate capacity of the settlement load by SLA. In general, the initial load cannot be fully applied [9][12] and difficulties are encountered in SLA in determining the initial-load factor [132] when the initial load and the current load can both damage a structure. On the other hand, ISLA can compute this case well. The objective of this chapter is not only to show the robustness of ISLA but also to compare the load control method and the load and damage control method as well as the orthotropic damage model and the isotropic damage model at the structural level.

### 11.1.1. MODELLING APPROACH

The experimental setup is shown in Figure 11.1(a). Positions A, B and C are selected for monitoring in Figure 11.1(b). The facade is scaled to 1/10 of the real dimensions. The quantities involved in the experiment follow the equations of the dimensional analysis [150]. The aim of the experiment is to keep the material strength and the stress conditions as close as possible to the prototype ones. To reproduce the real stresses, the material-specific weight of the model should be 10 times larger than that of the prototype material. Therefore, several point loads are applied before settlement loading. Figure 11.2 depicts the geometry and the positions of the initial point loads and the settlement load. The dimensions and force values are shown in Table 11.1. The settlement load is applied by vertical displacement of 0.5(23) mm at the left support of a steel beam. The steel beam is 60 mm deep and has 50-mm-wide flanges. The flanges as well as the web have a thickness of 5 mm. The facade was built on a base interface layer with a thickness of 5 mm. Table 11.2 shows the material properties. Beam elements are used for the wood lintels and the steel beam. Plane-stress elements are used for masonry, which are higher-order 2-D, eight-node elements. The integration point scheme is 2x2. The finite element size is 10.5 mm x 13.3 mm, and the crack band width was estimated as the square root of the element area, 11.8 mm.

For ISLA analyses, the stiffness reduction factor was taken as 0.25. Figure 11.3 shows the corresponding saw-tooth model, and Figure 11.4 shows the colour range for the principal tensile strain contours used for post-processing. The incremental displacement is 0.01 mm for each load step for the load control method. The results of the load control method are compared with those of the load and damage control

method. Both an orthotropic damage model (the rotating smeared crack model) and an isotropic damage model were used in the computations.



(a) front view of the experimental setup.  
 (b) Position of dial indicators A, B and C for displacement monitoring [149]

Figure 11.1: The experiment model, Whittemore strain gauges for crack width monitoring and grid of markers for photogrammetric measurements (dimensions in mm)

Dimension	Value (mm)	Force	Value (N)	Force	Value (N)
$l_1$	84	$F_1$	230	$F_6$	469
$l_2$	126	$F_2$	296	$F_7$	195
$h_1$	106	$F_3$	319	$F_8$	498
$h_2$	218	$F_4$	392	$F_9$	304
$h_3$	108	$F_5$	358	$F_{10}$	467

Table 11.1: Model's geometrical dimension and applied load values

### 11.1.2. TEST RESULTS FOR THE LOAD CONTROL METHOD

Figures 11.5 and 11.6 show the vertical displacement of B and horizontal displacement of C, respectively, related to the prescribed displacement at A, and compare the load control method and the experiment. The numerical results align well with those of the experiment. The load control method jumps over snap-backs robustly due to the saw-tooth model. Both displacements of B and C have linear relationships with A. The increasing rate of the vertical displacement at B is slightly smaller than 1 while the horizontal displacement at C is slightly larger than 1, compared to the prescribed vertical displacement at A. In addition, the vertical displace-

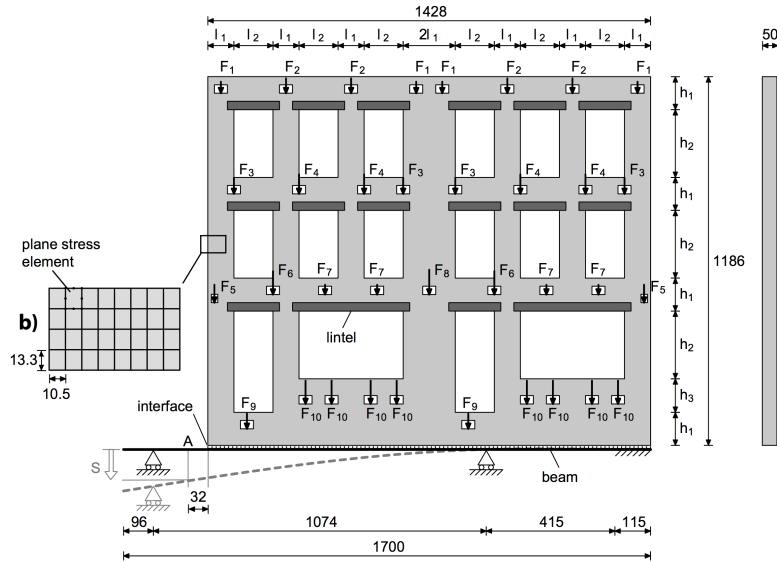


Figure 11.2: Geometric dimension of the scaled masonry facade (dimensions in mm). The thickness of the facade, lintels and interface is 50 mm [134]

Material	Parameter	Value
Masonry	Young's modulus	$E = 3 \times 10^9 \text{ N/m}^2$
	Density	$\rho = 1.9 \times 10^3 \text{ kg/m}^3$
	Poisson's ratio	$\nu = 0.2$
	Tensile strength	$f_t = 0.1 \times 10^6 \text{ N/m}^2$
	Fracture energy	$G_f = 10 \text{ N/m}$
Lintel wood	Young's modulus	$E_w = 11 \times 10^9 \text{ N/m}^2$
	Density	$\rho_w = 0.5 \times 10^3 \text{ kg/m}^3$
	Poisson's ratio	$\nu_w = 0.15$
Beam steel	Young's modulus	$E_s = 2.1 \times 10^{11} \text{ N/m}^2$
	Density	$\rho_s = 7.5 \times 10^3 \text{ kg/m}^3$
	Poisson's ratio	$\nu_s = 0.3$
Base interface	Normal stiffness	$k_n = 0.7 \times 10^9 \text{ N/m}^3$
	Tangent stiffness	$k_t = 1 \text{ N/m}^3$
	Tensile strength	$f_{t,b} = 0 \text{ N/m}^2$

Table 11.2: Material parameters for the numerical model

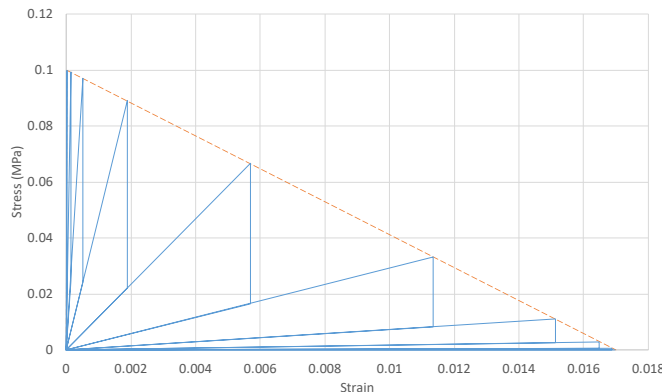


Figure 11.3: Saw-tooth model for the settlement test

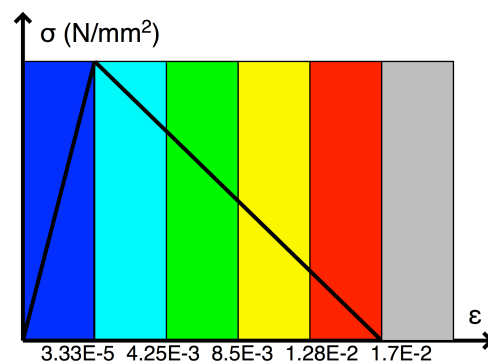


Figure 11.4: Contour colour range for the settlement test

ment of A from the experiment is 11.5 mm. In ISLA, the maximum vertical displacement of A is approximately 20 mm (20.675 mm) when the structure cannot carry the initial point loads. On the other hand, in the case of SLA [131], the vertical displacement of A reaches only 2 mm when the factor of the initial load cannot be 1.

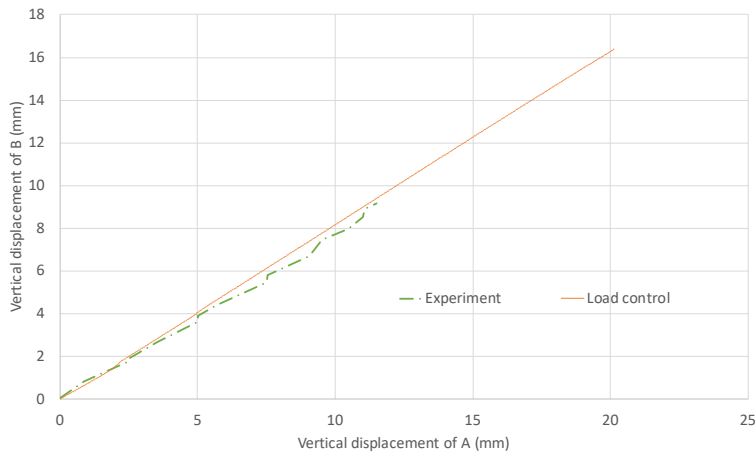


Figure 11.5: The relationship between the vertical displacement of A and B for the experiment and the load control method

Figure 11.7 shows the experimental crack pattern when the vertical displacement of A is 10 mm. The numbered cracks are selected and named for post-processing. Figure 11.8 shows the crack propagation first after the initial loads and then for the vertical displacement of A at 2.5 mm, 5 mm, 7.5 mm, 10 mm and 15 mm, respectively. The point loads result in initial damage without the settlement load. This initial load potentially caused divergence when searching for a suitable  $\nu$  for non-proportional loading of SLA in Chapter 4 because the point load and the settlement load both govern the damage process. ISLA does not have such problems due to the incremental approach. Figure 11.9 shows the result of the load control method for the ultimate displacement of A. Apart from the cracks marked according to the experiment, additional cracks are marked in Figure 11.9. Speaking of crack propagation, cracks are localized initially at Crack 1, then at Crack 2 and, finally, at Crack 3, which are major cracks. In contrast, Cracks 4 to 8 are relatively small. When the displacement of A increases above 10 mm, Cracks 9 and 10 can be observed. Figure 11.10 shows the crack propagation of different positions. Cracks 1 and 2 open at

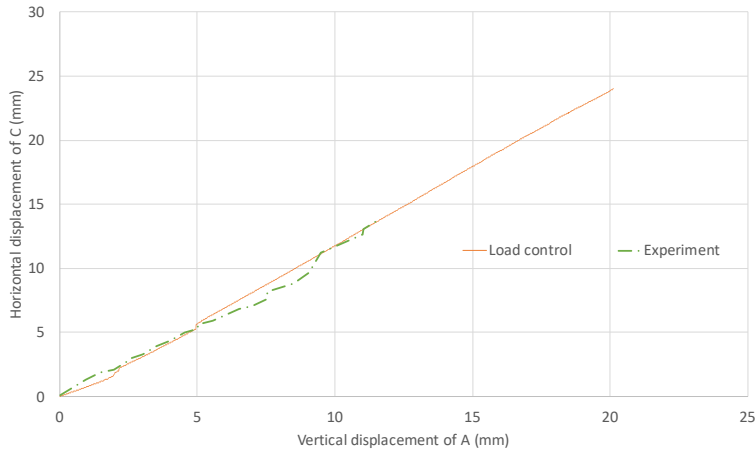


Figure 11.6: The relationship between the vertical displacement of A and the horizontal displacement of C for the experiment and the load control method

displacement of 2 mm while Cracks 3 and 4 open at displacement of 5 mm. Crack 9 starts to open at displacement of 9 mm. Unloading and crack closure can be observed for Crack 8. It can also be observed that the behaviour of Crack 2 is different from that in the experiment results due to the mesh-directional bias. Crack 2 tends to follow the mesh lines of the straight rectangular mesh and does not jump to the free surface of the window. The vertical initial load may influence the cracks to expand vertically and not jump to the free surface of the window. Moreover, the disconnections between the lintels and masonry are ignored, which may affect details of crack propagation. In addition, the extra damage is introduced to the rectangular element at the corner of the opening when the stiffness is updated at the element level. Triangle elements may solve this issue. This aspect of mesh-directional bias has not been studied here, but improvements can be achieved [151][152][153]. Apart from this aspect, the ISLA load control method is able to capture cracking behaviour and non-proportional loading in a reasonable manner. The initial load can be kept at 1.0. On the other hand, SLA can trace crack propagation only until 2 mm when the factor of the initial load cannot be 1 [131].

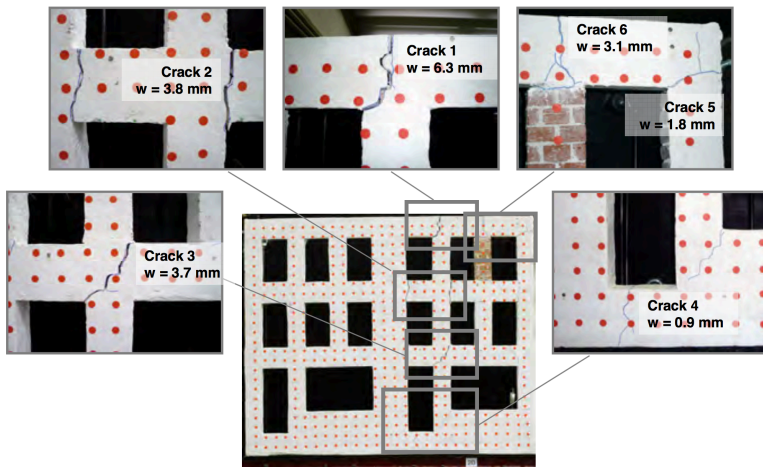


Figure 11.7: Crack patterns of the experiment when the displacement of A is 10 mm

### 11.1.3. TEST RESULTS FOR THE LOAD AND DAMAGE CONTROL METHOD

For displacement history, the load control method jumps over snap-backs while the load and damage control method follows snap-backs. For the stiffness damage history, both methods trace the whole damage process, including snap-backs.

Compared with the load control method, the load and damage control method has similar crack patterns. Figure 11.11 shows the results of the two methods for the ultimate displacement of A. Snap-back behaviour can be seen from the curves of the load and damage control method in Figures 11.12 and 11.13. These snap-backs can also be deduced from Figure 11.14, which shows the load step versus displacement of Position A. Four positions are marked for post-processing. The snap-backs are related to explosive crack propagation, especially when cracks are initialized at new positions. Figure 11.15 shows the development of the maximum crack width with increasing vertical displacement. It can be seen that cracks develop dramatically at certain vertical displacements of A, for example the stage at 4.92 mm. Figure 11.16 shows two snap-back moments for which the displacement decreases to zero, the positions of which are marked in Figure 11.14. Moreover, it can be seen in Figure 11.17 that cracks continue developing, especially at the left part of the facade when the displacement of A reaches the ultimate value at stage d.

Although the displacement history of snap-backs cannot be followed by the

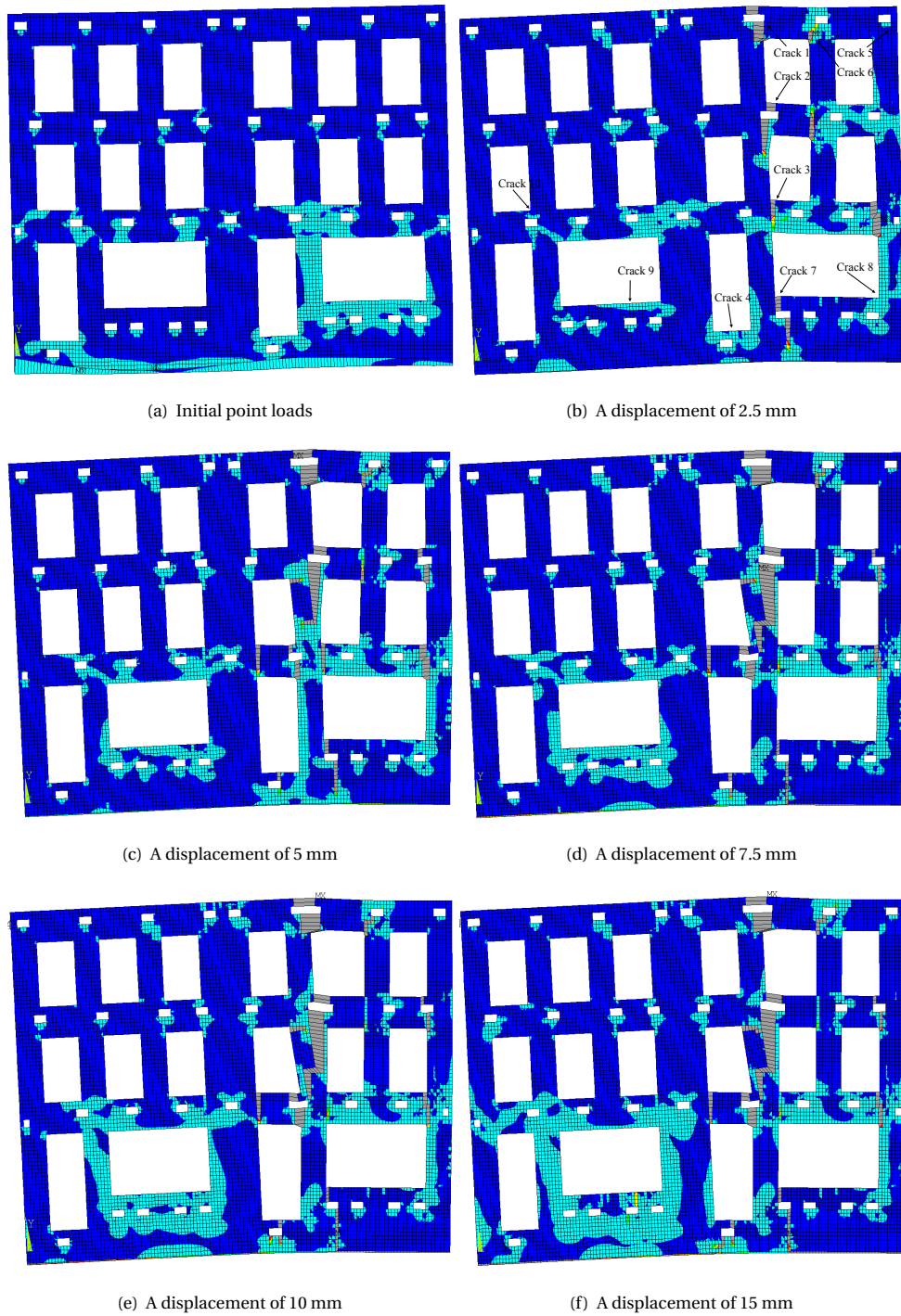


Figure 11.8: The maximum principal strain contours with different vertical displacements of A for the load control

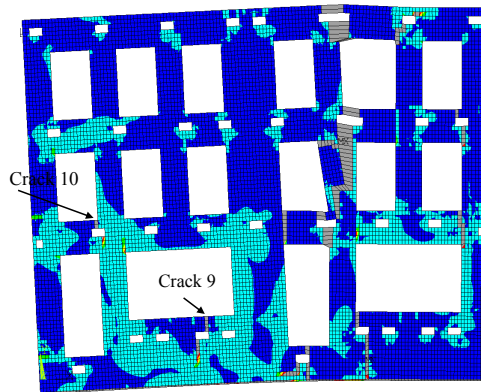


Figure 11.9: Maximum principal strain contours of the load control method when the displacement of A is the ultimate displacement of 20 mm

load control method, the fluctuation of utilisation values during cycles illustrates the snap-back phenomenon. The utilisation value reaches 1 after a long search process. For instance, Figure 11.18 shows the utilisation value fluctuation during cycles when the vertical displacement of A jumps from 4.92 mm to 4.93 mm, the peak of which indicates the maximum snap-back moment and the corresponding displacement.

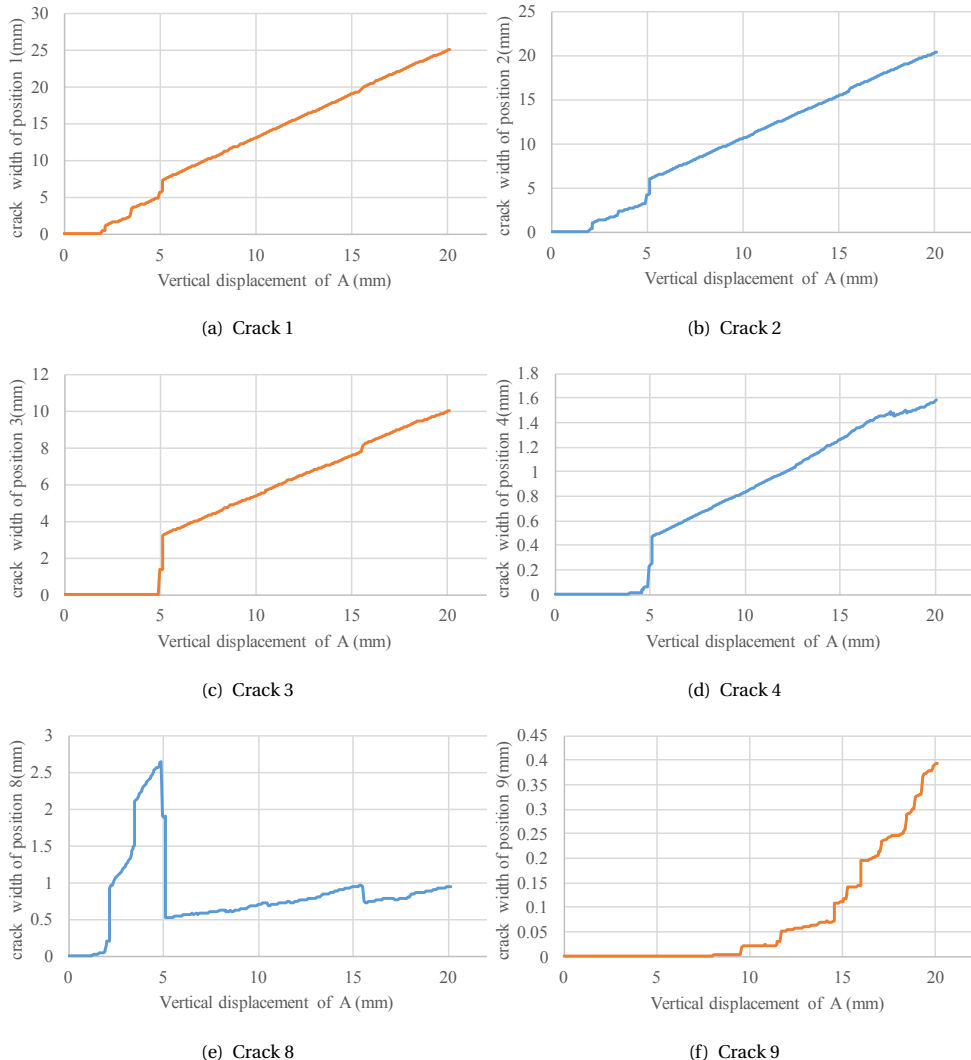


Figure 11.10: Crack propagation at different positions along with the displacement of A for the load control method

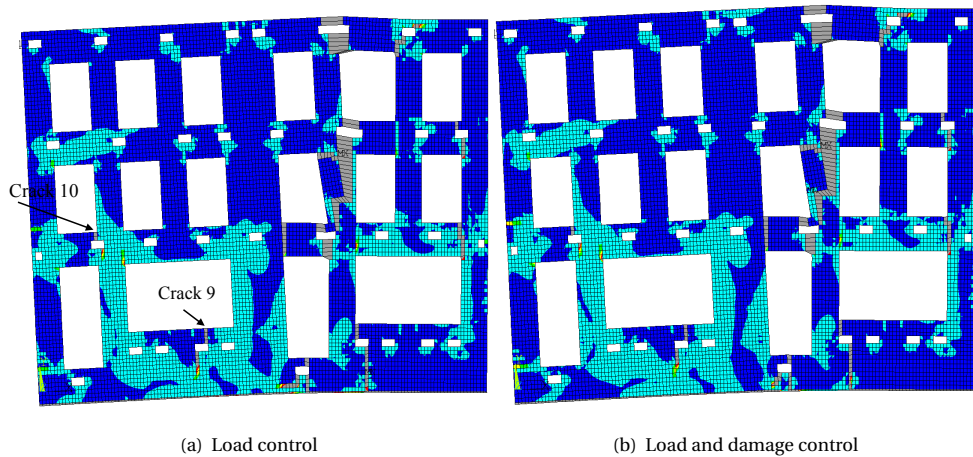


Figure 11.11: The maximum principal strain contours of the load control method and the load and damage control method when the displacement of A is the ultimate displacement of 20 mm

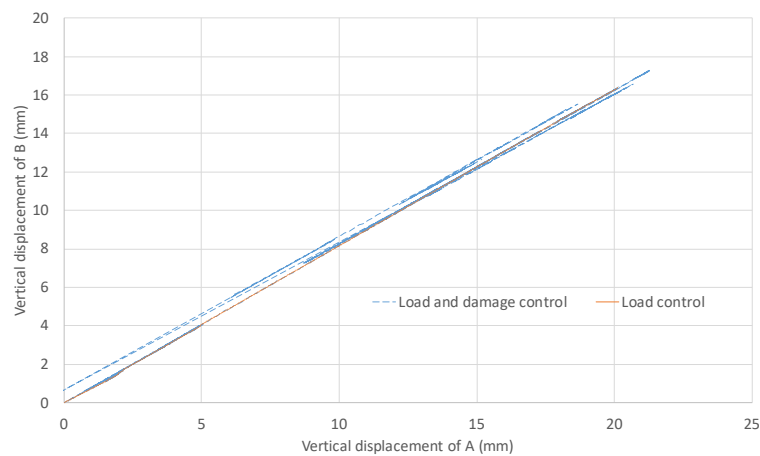


Figure 11.12: The relationship between the vertical displacement of A and B for the load control method and the load and damage control method

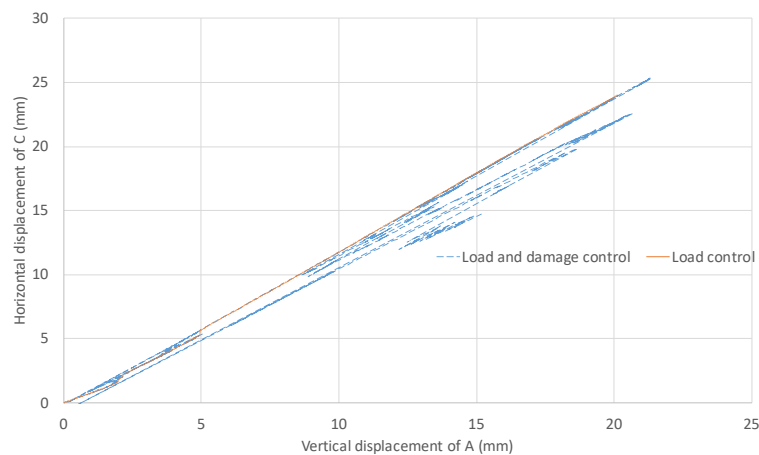


Figure 11.13: The relationship between the vertical displacement of A and the horizontal displacement of C for the load control method and the load and damage control method

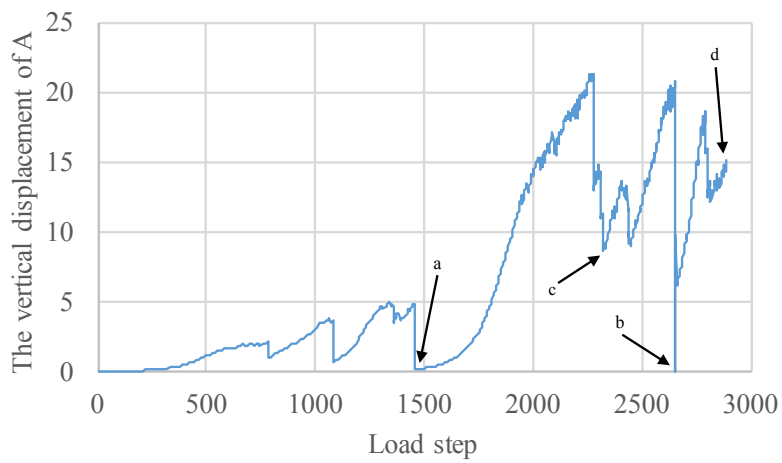


Figure 11.14: The relationship between load steps and the vertical displacement of A for the load and damage control method

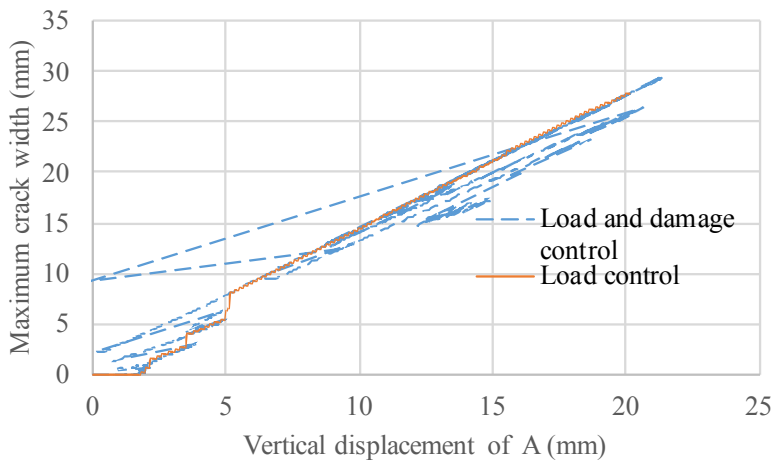


Figure 11.15: The relationship between the vertical displacement of A and the maximum crack width

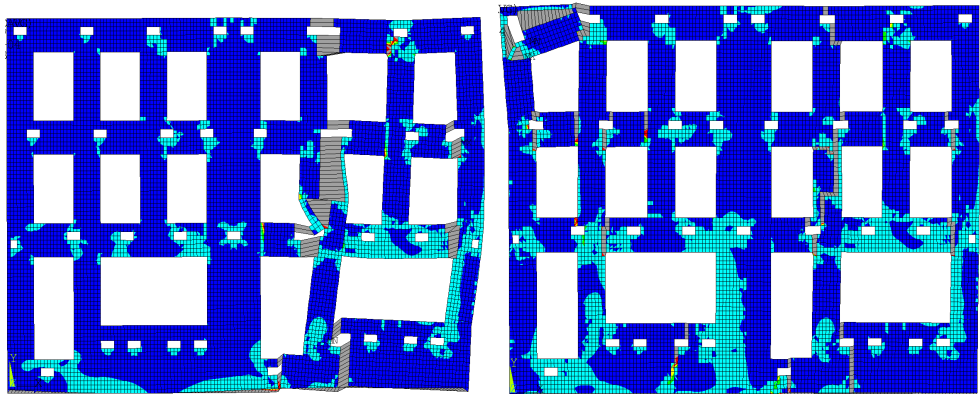
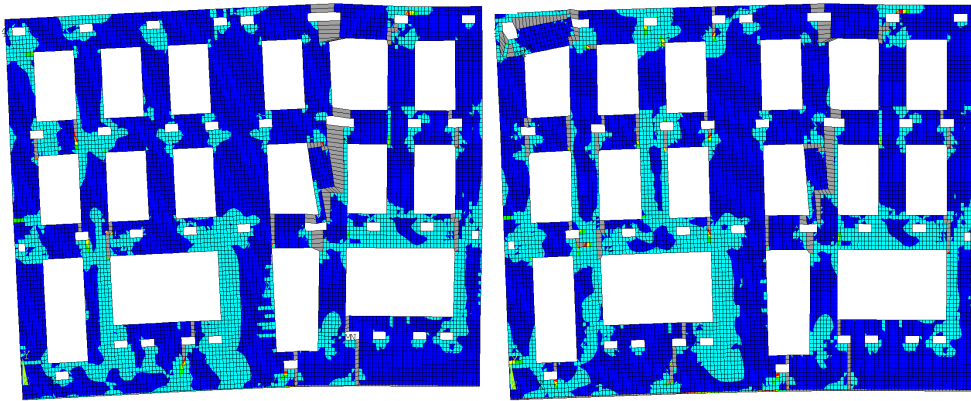


Figure 11.16: The maximum principal strain contour when the displacement of A is zero for the load and damage control method



(a) Position c marked in Figure 11.14

(b) Position d marked in Figure 11.14

Figure 11.17: The maximum principal strain contours after the moment when the displacement of A is the ultimate displacement for the load and damage control method

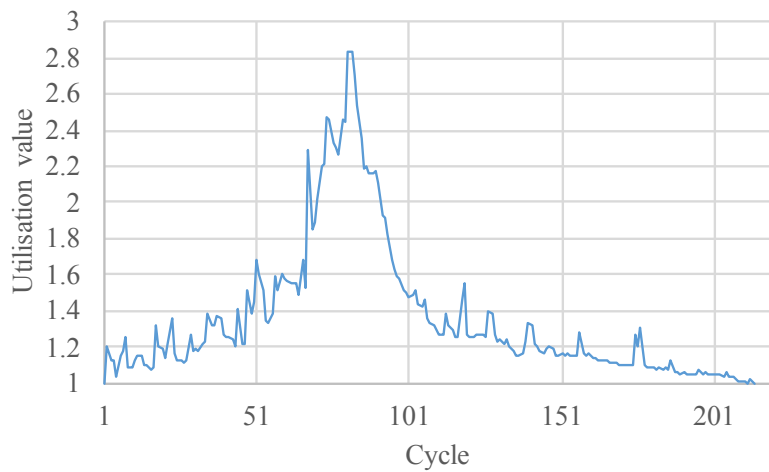


Figure 11.18: The utilisation value of cycles for the load step when the vertical displacement of A jumps from 4.92 mm to 4.93 mm. The load control method starts with a utilisation value of 1 and ends with a utilisation value of 1. Equilibrium is found in 214 cycles.

### 11.1.4. COMPARISON OF ORTHOTROPIC AND ISOTROPIC DAMAGE MODELS

The analyses of the previous section were re-performed with the isotropic damage model instead of the orthotropic damage model. Here, the structure cannot carry the settlement load when the vertical displacement of A is only 1.7 mm for the load control method and the load and damage control method. Figure 11.19 shows utilisation values of cycles for the last load step for the load control method. No equilibrium state can be reached for this load step. Figure 11.20 shows how the facade loses the capacity to carry the initial vertical load cycle-by-cycle. Actually, the facade cannot carry the vertical load when the settlement load is decreased to zero by the load and damage control method in Figure 11.21. The reason for this premature collapse is that parts in the right side of the wall are tensioned and perpendicularly compressed. When the masonry cracks in tension, it also fails in compression due to the isotropic damage model.

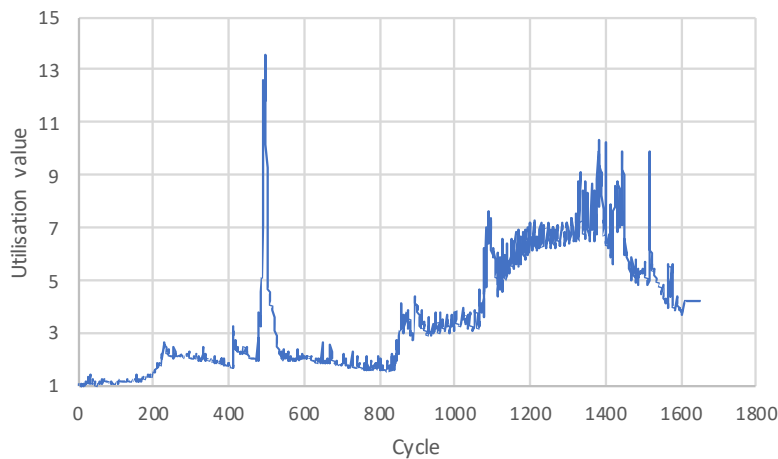


Figure 11.19: The utilisation values of cycles for the last load step of the load control method with the isotropic damage model (The utilisation value presents material equilibrium state. When  $\mu = 1$ , it is an equilibrium state.)

Consequently, this illustrates the capacity to resist non-proportional loads and the details of the constitutive model. The orthotropic damage model, which is more realistic, has the capacity for compression or tension along with crack direction when a crack is fully developed.

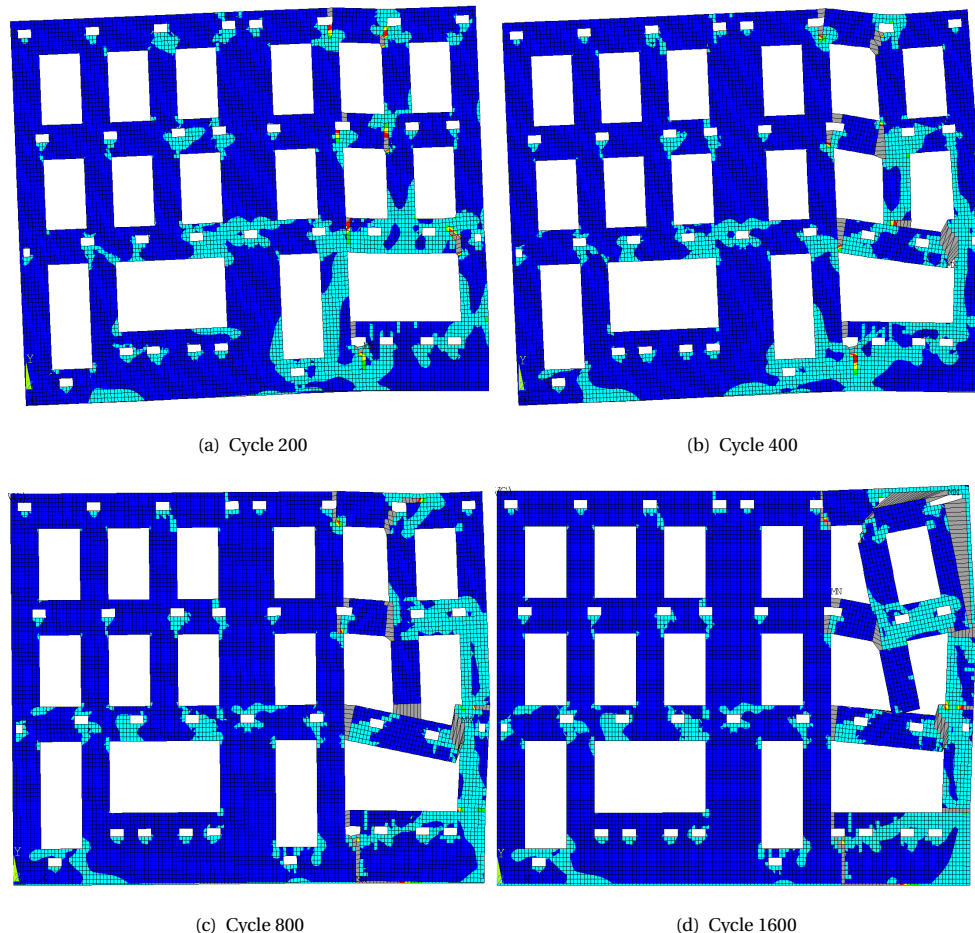


Figure 11.20: The maximum principal strain contours of the results of cycles of the last load step, which cannot reach an equilibrium state. ( $\mu$  is larger than 1) for the load control method with the isotropic damage model

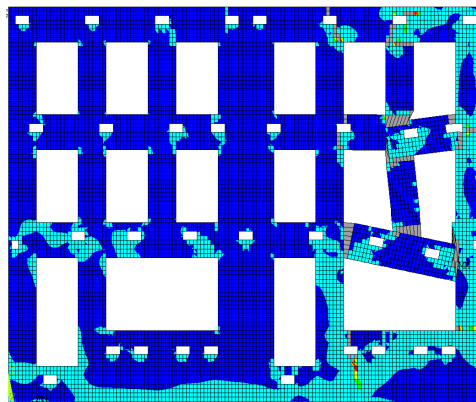


Figure 11.21: The maximum principal strain contour of the cycle of the last load step for the load and damage control method with the isotropic damage model when the displacement of A drops to zero and cannot reach an equilibrium state.

## 11.2. MASONRY HOUSE SUBJECTED TO DEAD LOAD AND PUSHOVER

Buildings in the Netherlands were not designed for earthquake loading because earthquakes did not occur until some 15 years ago. The reason for recent earthquakes is the extraction of natural gas from deep, porous rock layers. Gas has been extracted for approximately the last 50 years, and the gas fields are partially empty, so the porous rock layers sometimes partially collapse. This causes earthquakes up to Magnitude 3.2 on the Richter scale, with the possibility for higher magnitudes in the future, which buildings have not been designed to withstand. Consequently, large engineering efforts have been made in regard to the following subjects: predicting future earthquake magnitudes, predicting the strength and ductility of traditional building types, and developing retrofitting methods.

A two-storey assemblage, calcium silicate, brick masonry building with concrete floors was tested in the Stevin Lab (TU Delft) on behalf of NAM, with a view to validating models for assessing the seismic capacity of Groningen houses [154]. A quasi-static cyclic pushover test was performed using a steel reaction frame to apply the load at the floor levels.

### 11.2.1. MODELLING APPROACH

A sketch of the test setup is shown in Figure 11.22. The facades of the specimen as shown in Figure 11.23 have a length of 5.4 m and a depth of 5 m. The total height of the specimen is 5.4 m. The south and north facades, which are identical, are represented by only two piers, which are connected to the transversal walls. Two pier sizes were selected: on the western side, the wide piers P1 and P3 have a width of 1.1 m, while on the eastern side, the narrow piers P2 and P4 have a width of 0.6 m. The thickness of the masonry is 100 mm while that of the concrete floors is 165 mm. Small calcium silicate brick units with dimensions of 210x71x100 mm were used. A running bond pattern was adopted, allowing for the interlocking of the bricks at the corners of the transversal walls and the piers. The masonry properties are  $E=2710$  MPa, Poisson's ratio  $\nu=0.2$ , tensile strength  $f_t = 0.14$  MPa and tensile fracture energy  $G_f = 0.01$  N/mm. The elastic modulus of the masonry is taken as the average value in the directions perpendicular and parallel to the bed joints. The tensile strength is taken as the minimum value of out-of-plane masonry flexural strength perpendicular and parallel to the bed joint. The compressive strength  $f_c$  is taken as -5.84 MPa. Linear softening is considered for tension while softening is not considered for compression (i.e., ideal elastic-plastic behaviour in compression is assumed). The concrete properties are elastic with  $E=38000$  MPa and Poisson's ratio  $\nu=0.2$ .

At the first-storey level, the floor is connected horizontally to the piers by anchors 6 mm in diameter, which are cast in the floor and masoned in the piers. The narrow piers are connected by three anchors and the wide piers by five anchors. These anchors are commonly used as horizontal buckling or wind load support of piers, and they are not designed to withstand any vertical load. At the second-storey level, the floor is laid on both the loadbearing transversal walls and the piers. The boundary condition and connections are simplified in the FEM model. Half the specimen is considered, making use of symmetry. The specimen is hinged at the ground floor. The transversal walls are clamped to the piers. The first floor is hinged to the transversal walls and connected horizontally to the piers. The second storey is hinged to the transversal walls and the piers.

A quasi-static cyclic pushover test was performed in the lab. The masonry structure was loaded by four actuators (Figure 11.22b), two per each floor, positioned at approximatively 1.1 m inwards from the facades. A displacement was im-

posed at the second storey while the force ratio was kept as 1:1 at the two floor levels ( $F_1 + F_3 = F_2 + F_4$ ). To impose a constant ratio between the forces at the two floor levels, the forces in the actuators No. 1 and 3 at the second storey were mechanically coupled to the forces at the first storey level ( $F_1 = F_3$ ,  $F_2 = F_4$ ). In the FEM model, monotonic pushover was applied with the indirect displacement control loading (Chapter 9).

For ISLA, the element size is taken as 200 mm x 200 mm, and the stiffness reduction factor is taken as 0.25. The crack band width is assumed to be 200 mm. The corresponding saw-tooth model is shown in Figure 11.24. Masonry is modelled by eight-node quadrilateral shell elements, which have three layers in the thickness direction for the transversal walls and one layer in the thickness direction for the piers<sup>1</sup>.

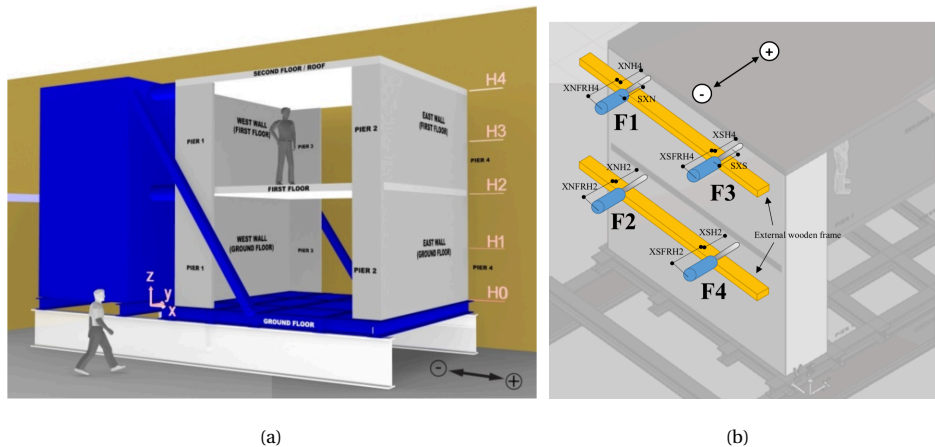


Figure 11.22: Test setup

### 11.2.2. TEST RESULTS

Figure 11.25 compares the results of ISLA and the experiment in terms of total shear force versus displacement at the second storey. The positions from a to h are marked for post-processing. ISLA traces the whole diagram robustly, the displacement of which is more than the ultimate value of the experiment. The part of

<sup>1</sup>The current ISLA implementation in ANSYS can only update the material properties at the element level instead of the integration point level. Layers of shell elements with section offset are used in ISLA

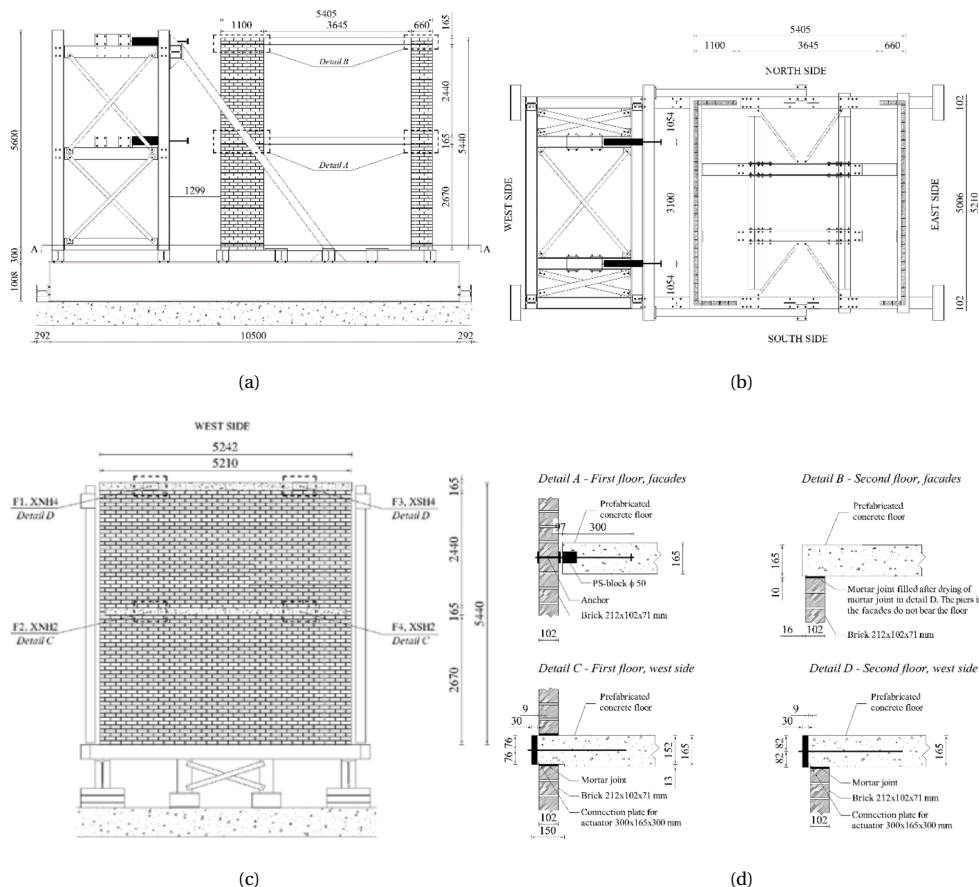


Figure 11.23: Test specimen: (a) Front view (southern side); (b) Top view of ground floor in section A-A; (c) Side view (western side); (d) Construction details.

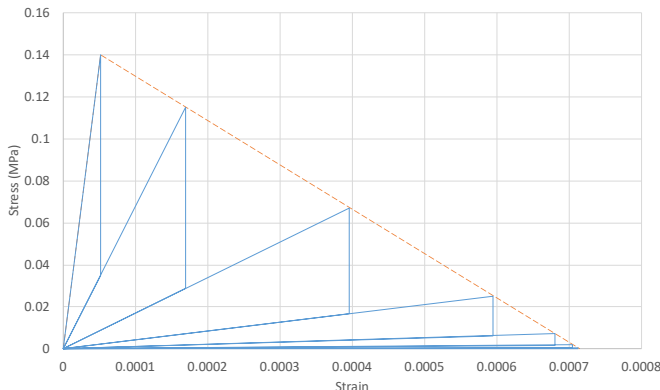


Figure 11.24: Saw-tooth model for the pushover test

the curve for displacements larger than 100 mm is not shown in Figure 11.25. ISLA successfully jumps over snap-backs. The jump-overs cause explosive crack propagation, the damage of which is reflected as the number of cycles in Figure 11.26. There are 2,223 cycles when ISLA jumps over from e to f at the displacement of 41 mm. It can be seen that the peak and the initial slope of ISLA are smaller than those of the experiment, due to two reasons. Firstly, the boundary condition and the connections are considered as hinges instead of initially clamped connections with non-linear springs or non-linear interface elements, which causes the FEM model to be more flexible than the specimen. Secondly, the material properties are taken to be relatively conservative. The tensile strength is taken as the minimum value of out-of-plane masonry flexural strength perpendicular and parallel to the bed joint. The fracture energy can be larger. The residual shear force of ISLA is larger than that of the experiment quantitative, which may be due to different loading conditions (monotonic loading for ISLA and cyclic loading for the experiment). The damage from loading in the other direction (cyclic loading) is not considered in ISLA. A more realistic FEM model and material properties can be calibrated for a better quantitative alignment between ISLA and the experiment. The main goal here is to demonstrate that ISLA, in a qualitative sense, is able to produce post-peak behaviour, including the drops reflecting brittle processes, and that the initial dead load can be kept on the structure while the second load is incremented.

Figures 11.27 and 11.28 show the main damage and crack pattern for the ex-

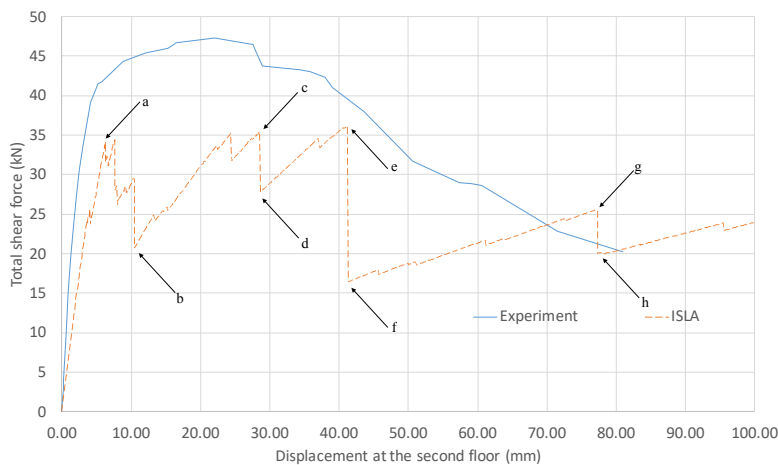


Figure 11.25: Total shear force versus displacement at the second storey for ISLA and the experiment

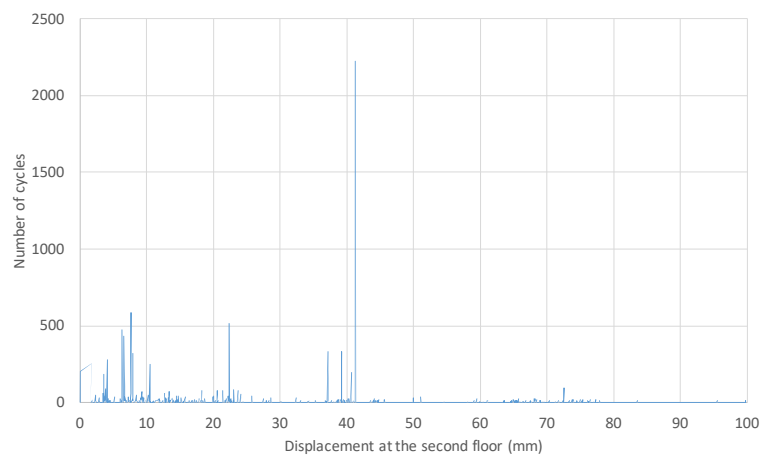


Figure 11.26: Number of cycles versus displacement at the second storey for ISLA

periment. The failure mechanism is mainly governed by the in-plane damage of the piers at the ground floor. Figure 11.29 shows the crack pattern from position a to position h, as marked in Figure 11.25. In the analysis, the flange effect was not included [155], and the running bond allows a strong connection between the piers and the transversal walls. As a result, in the experiment, cracks propagate among the almost whole area of the transversal walls while in the analysis, cracks are localized at the edges adjacent to the piers. Except for this, the crack pattern for ISLA is realistic compared with that of the experiment. The rocking of piers is successfully localized in the ISLA analysis, the diagonal crack of which governs the failure mechanism. The cracks are initialized at the bottom and top of piers when the capacity reaches the peak capacity in Figure 11.29(a). Afterwards, ISLA successfully jumps over snap-backs, including four pairs ((a & b, c & d, e & f, g & h)). The snap-backs are caused by the diagonal crack on the wide pier at the ground floor. The capacity drops sharply when the wide pier is split by the diagonal crack in Figure 11.29(f). Meanwhile, the cracks propagate dramatically at the bottom of the narrow pier and the top of the wide pier. Finally, the edge of the transversal wall is pushed out by the wide pier at the corner of the first storey in Figure 11.29(h). Figure 11.30 shows the crack pattern in the x, y, z global coordinate system, instead of the principal direction, as depicted in Figure 11.29(h), in the global coordinate. It can be seen that the failure mechanism is governed by the in-plane vertical or diagonal cracking of the wide pier.

The utilisation values of all load steps are determined by the tension component instead of the compression component for this case. The compression crush can be indirectly regarded as tension splitting in the other direction.



Figure 11.27: Main damage in the wide piers at the ground floor for the experiment

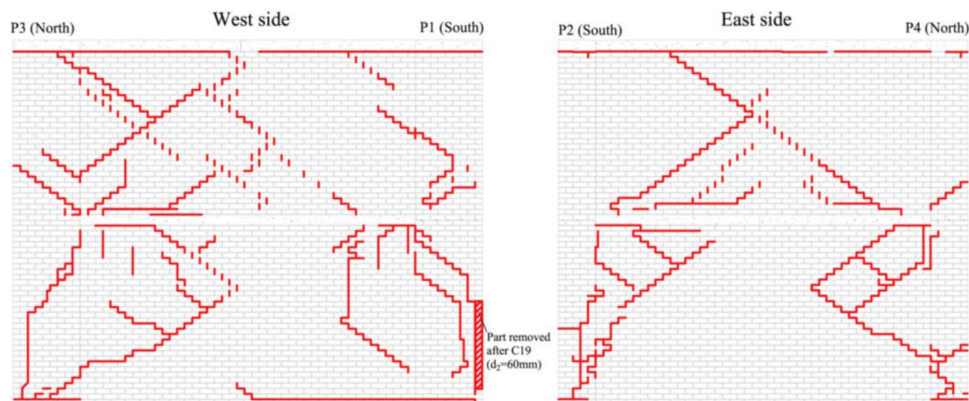


Figure 11.28: Crack pattern for the experiment

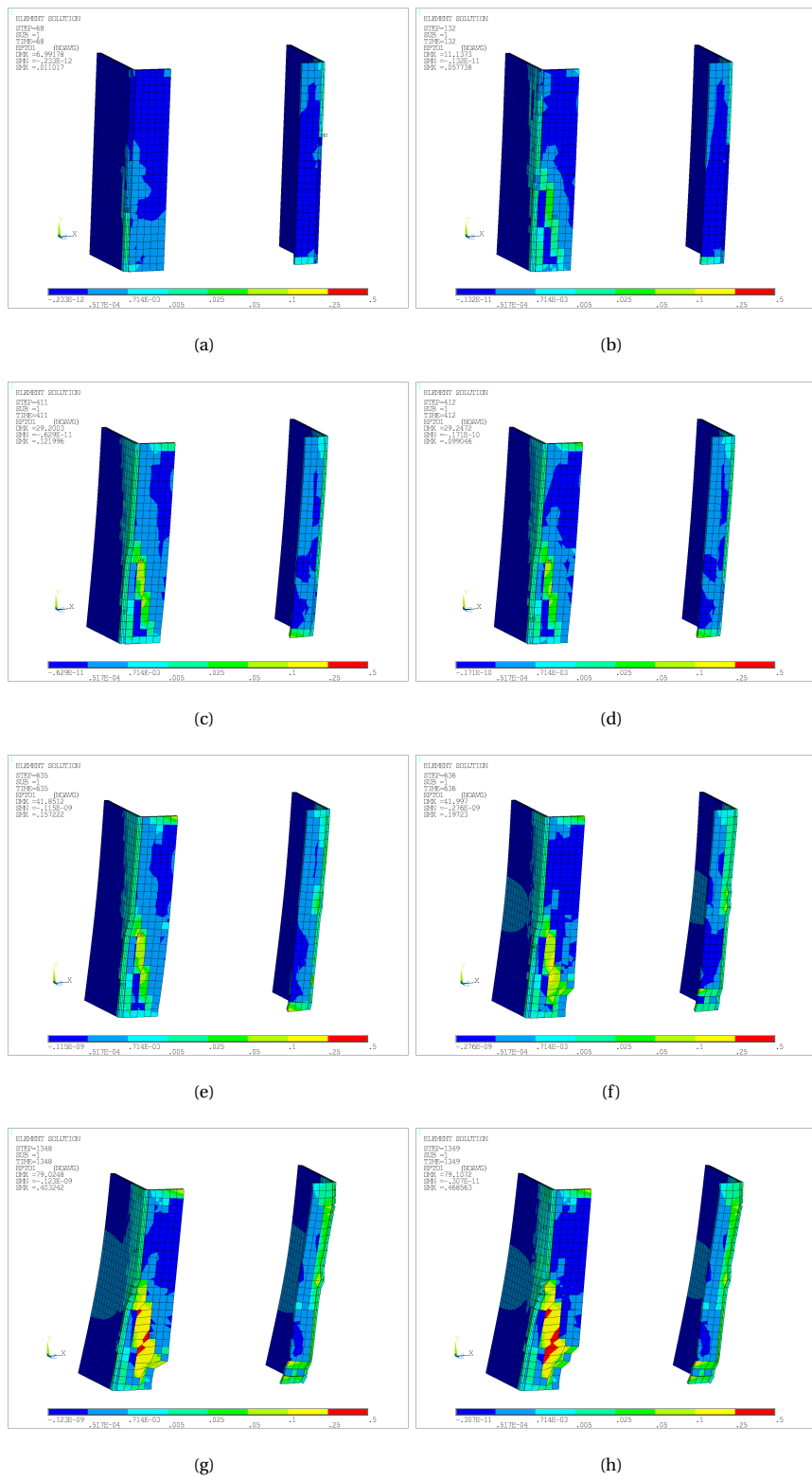


Figure 11.29: Maximum principal strain contours for ISLA from position a to position h marked in Figure 11.25

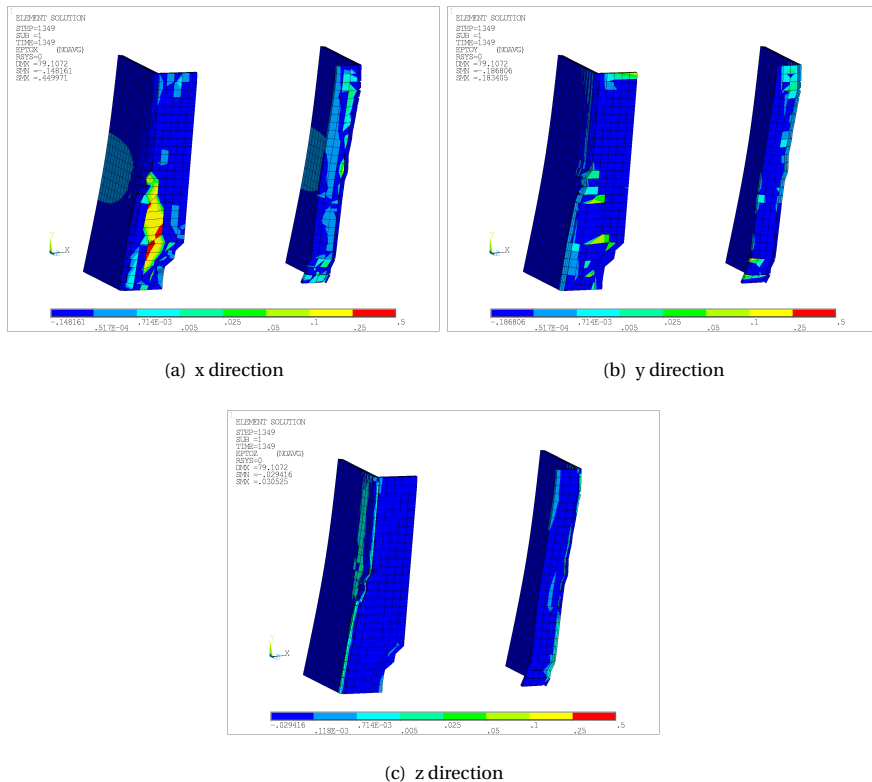


Figure 11.30: Global strain contours for Figure 11.29(h)

## 11.3. DISCUSSION

### 11.3.1. MASONRY FAÇADE SUBJECTED TO DEAD LOAD AND SETTLEMENT

For the non-proportionally loaded masonry facade, ISLA is more robust than SLA. The load-displacement diagram of ISLA can be continued much further than that of SLA. The initial load can be always kept at 1.0 in ISLA due to the incremental approach. The challenge from non-proportional loading in tests is that the initial load causes damage. The damage can be fully considered during the whole process with ISLA, while the initial load cannot be fully applied in SLA[9][12] and difficulties may be experienced with SLA in determining the initial-load factor in [132] when the initial load and the current load can both damage a structure.

For snap-backs, the load control method and the load and damage control method both perform successfully. For displacement history, the load control method jumps over snap-backs while the load and damage control method follows snap-backs. For the damage history, both methods trace the whole damage process of snap-backs. According to the test results, the load control method delivers almost the same results as the load and damage control method, which means that damage history matters more than displacement history in the settlement test. However, displacement history cannot be ignored, such as the sequence of the point load and the settlement load, otherwise the problems of non-proportional loading in SLA remain.

Regarding constitutive modelling, the rotating smeared crack model (orthotropic damage model) was implemented in ISLA. This model plays an important role in the situation in this chapter in which the crack direction varies due to the point load and the settlement load. Fixed smeared crack models may be partially responsible for the fact that the initial load cannot be kept at 1.0 in SLA [131]. There are indications that fixed smeared crack models may induce stress locking, while rotating smeared crack models more smoothly accommodate principal stress rotations for non-proportional loads.

Mesh objectivity is an important topic in fracture mechanics. The theory of the crack band width addresses the mesh-size dependency, but the mesh-directional bias remains. This aspect of mesh-directional bias has not been studied here, but improvements can be achieved [151][152][153]. In this masonry settlement prob-

lem, the mesh bias may cause an unrealistic crack pattern at the corner of the opening. Random meshes with triangular elements [156] may partially solve this issue. Other reasons for the masonry settlement problem may relate to limitations of the smeared crack model, which is based on Mode-I fracture, to the lack of contact behaviour between the lintel and the masonry, or to the fact that in the current implementation, the material stiffness update is handled at the element level instead of the integration point level.

### 11.3.2. MASONRY HOUSE SUBJECTED TO DEAD LOAD AND PUSHOVER

ISLA robustly traces the whole crack propagation. The displacement of the diagram for ISLA overpasses the ultimate displacement of the experiment. The load control method with indirect displacement control loading robustly jumps over snap-backs. The in-plane vertical and diagonal cracks of the wide pier at the ground floor are successfully localized in ISLA, which governs the failure mechanism. The cracking mechanism, along with rocking of the masonry piers, determines the post-peak quasi-brittle response. There is no compression failure in ISLA for this case.

This matters when implementing interface elements into ISLA, which provides the possibility to consider realistic boundary conditions and connections.

The running bond is common and significant for masonry, which allows for a strong connection between the piers and the transversal walls, providing the flange effect. However, current ISLA analysis does not consider the running bond. ISLA fails to localize the cracks of the transversal walls. Possible solutions are to make discrete models with interface elements available in ISLA, to extend it to full 3D solid models that more accurately represent corner and flange effects as compared to shell elements, or to improve constitutive models, which can consider flange effects.



# 12

## CONCLUSIONS AND FUTURE WORK

### 12.1. CONCLUSIONS

Non-linear FEM analysis has been widely applied for quasi-brittle materials such as masonry, concrete and reinforced and prestressed concrete. However, the robustness of the algorithms remains a serious issue. The classical algorithm for solving non-linear mathematical equations is the N-R method. This method is robust if the load-displacement curve is continuous and smooth. The load-displacement curves of quasi-brittle materials have many little peaks related to initiation and propagation of numerous cracks. These peaks are only visible if one zooms in on a curve that is computed with very small load increments. Consequently, the tangent stiffness in the neighbourhood of these peaks has extreme variations and can lead to divergence of the N-R iterations. To enhance the robustness of solving non-linear problems, a total approach with secant stiffness and an “event-by-event” damage model is introduced by SLA, which is an alternative to the N-R method when bifurcation, snap-back or divergence problems arise. The incremental iterative procedure, adopted in non-linear finite element analysis, is replaced by a sequence of scaled linear finite element analyses with decreasing secant

stiffness, corresponding to local damage increments. However, SLA has difficulties in dealing with non-proportional loading as well as cases in which the displacement history matters, such as geometrically non-linear analysis, transient analysis and cyclic analysis with plastic unloading, since the damage history is traced in SLA rather than the displacement history.

To deal with the difficulties in SLA, this thesis improves SLA and proposes an incremental approach based on SLA called incremental sequentially linear analysis (ISLA).

### **Improvements to SLA:**

A simplified saw-tooth model is introduced, which is governed by the stiffness reduction factor. To make the fracture energy for SLA the same as that of a physical non-linear analysis, the initial tensile strength or the ultimate strain are rescaled [10]. In the simplified saw-tooth model, the rescaled strength of each cycle can be automatically computed based on the stiffness reduction factor used in the cycle. The proposed saw-tooth model provides the possibility to use varying stiffness reduction factors in cycles to balance the computational accuracy and efficiency.

An orthotropic damage model is introduced for SLA based on the rotating smeared crack model. Hereby, the difficulty of choosing a proper shear retention function is eliminated in this damage model compared with the previous damage model, which is based on fixed smeared cracks[129].

A new algorithm [132] for applying non-proportional load is implemented in SLA. An initial-load factor  $\nu$  is introduced to make the initial-load constant after scaling in each cycle. The stresses and strains caused by the initial load and the current load are computed based on the load combination of  $F_{ref}$  and  $F_{ini}/\nu$  for each damaged stiffness. The initial-load factor  $\nu$  is adjusted based on an interpolation or extrapolation procedure and applied in the pre-process to make  $\nu$  equal to  $\lambda$ . Instead of calculating the stresses from the initial load and the current load separately [12][131], they are computed simultaneously by the load combination [132]. In [132][131], the main difference from [12] is that the initial stresses are recomputed for the damaged stiffness rather than the initial undamaged stiffness. Without adding extra stresses in the post-process as in [12][131], the proposed algorithm is naturally suitable for different element types and failure criterion without additional modifications. This algorithm is demonstrated in non-proportional loading

of a 2D prestressed concrete beam and out-of-bending of a 3D masonry wall with overburden. This algorithm can be easily programmed in any commercial software since it only changes the load factor in pre-processing instead of operations on the fundamental code level in post-processing. Due to the interpolation or extrapolation procedure, the algorithm is not suitable for strong non-linear problems, which means the initial load cannot be very large or should have little influence on the critical element position.

#### **Development of incremental sequentially linear analysis:**

This thesis proposes ISLA. This method provides robust and accurate solutions for simulating the behaviour of structures based on damage cycles and load increments (Chapters 7, 8 and 9). The method is incremental; each increment begins and ends with an equilibrium state. The solution search path follows damage cycles sequentially with the secant stiffness, which traces both damage history (explicit) and displacement history (implicit). Note that the damage procedure is irreversible. Due to the stiffness reduction, the internal forces are updated based on the displacements of the previous load step, and the algorithm reaches a temporary equilibrium state. Afterwards, the incremental load is applied, and a linear analysis is performed for the current load step. ISLA is robust because all physical non-linearity is linearised in damage cycles with the explicit secant stiffness of the reduced elastic material model.

Just as in SLA, a utilisation value is defined. The utilisation value is determined at the local level by the stress state and the failure surface of an element with elastic material properties. Utilisation values are computed for each element. A utilisation function  $\mu$  is defined as the largest utilisation value of all elements, which is a function of the load factors and the stiffness matrix  $K$  at the global level. An equilibrium is reached when the stresses or strains of the critical element (i.e., the element that is the closest to the first or next damage event) lie either on or within the failure surface. Considering the calculation efficiency, the utilisation value of a material equilibrium state in ISLA is not purely 1 but has a tolerance (the stresses or strains of the critical element lie within the failure surface). In static analysis, this tolerance does not influence the results. After the structure slightly unloads due to the tolerance, it reloads with the next load increment.

ISLA employs the rotating smeared crack model (the damage model) and the

Mohr-Coulomb criterion with tension cut-off. The stiffness updating procedure is governed by damage. This damage follows the principal direction of the critical element of the current load step. The stiffness is reduced by a constant reduction factor. The default stiffness reduction factor is 0.9 for static analysis, which means that after an element becomes critical, its Young's modulus in the principal direction is reduced to 90% of the previous value. For one element, a stiffness reduction factor larger than 0.75 can guarantee accuracy. For a structure, a smaller stiffness reduction factor can be used, which depends on the number of potentially damaged elements in the structure. For the facade and the house tested in the thesis, the utilisation function is not sensitive, with a stiffness reduction factor of 0.25. Extra damage may be introduced when a small stiffness reduction factor is used for transient analysis. The stiffness reduction factor should be closer to 1, such as 0.99. However, a large stiffness reduction factor requires a large number of cycles in total. The crack band model based on the fracture energy is used to obtain mesh-independence.

Three control methods are proposed, namely the load control, damage control, and load and damage control methods. In the load control method, each load step can contain one increase or decrease of the load and several reductions of Young's modulus of various elements. In the damage control method, each load step can contain one reduction of Young's modulus and several changes of the load. In the load and damage control method, each load step can contain several changes of the load and several reductions of Young's modulus of various elements. The load and damage control method is optimized based on the utilisation values of ISLA. For the imposed displacement loads, the load control method is recommended. For force loads, this method can also be used, but the post-peak response cannot be obtained. The damage control method and the load and damage control method can be used to determine post-peak behaviour and snap-back behaviour of structures. The load and damage control method is much faster than the damage cycle. It is also robust and provides the same results. Based on efficiency, the load control method and the load and damage control method are suggested for large structures. For the notched beam test, objectivity has been achieved for these three methods. The results are not sensitive with different load steps and damage cycles.

Due to the different ways of updating the stiffness, ISLA does not deliver exactly identical results compared with the N-R method. Stiffness updating in ISLA

is based on the damage history while in the N-R method, it is based on the displacement history. The N-R method employs the current stiffness at the end of the current iteration for the next iteration while SLA and ISLA use the damaged stiffness, which is based on the saw-tooth model, at the end of the current cycle for the next cycle. In addition, the stiffness of a critical element is reduced cycle-by-cycle in ISLA while the stiffnesses of all damaged elements are updated simultaneously in the N-R method. Moreover, due to the failure criterion of SLA and ISLA that the stress-strain state of the critical element is on the failure surface, the stress-strain states of other damaged elements are within the failure surface. Therefore, ISLA has relatively smaller stiffness than that of the N-R method. For static analysis, the difference between ISLA and the N-R method is small. For transient analysis, the difference may be large.

The N-R method employs the current stiffness at the end of the current iteration for the next iteration while SLA and ISLA use the damaged stiffness, which is based on the saw-tooth model, at the end of the current cycle for the next cycle. The passive and proactive updating procedure results in the fact that SLA and ISLA have relatively smaller stiffness for the same displacements after one iteration. Furthermore, extra damage may be introduced when a small stiffness reduction factor is used, which can cause different equilibrium states to be found. In addition, the stress and strain are redistributed due to the stiffness reduction before applying the load increment of the next load step in ISLA, whereas they are not split in N-R, which may lead to different equilibrium states. Apart from this, in SLA and ISLA, critical elements are chosen cycle-by-cycle, which means that for each cycle, only one critical element is chosen, whereas the N-R method simultaneously updates the stiffnesses of multiple elements. Moreover, due to the failure criterion of SLA and ISLA that the stress-strain state of the critical element is on the material curve, the stress-strain states of other damaged elements are below the curve. Over all, SLA and ISLA have more flexible results than the exact solution while N-R has stiffer results than the exact solution. However, it is undetermined which method has a higher capacity because SLA and ISLA have smaller stiffnesses, for which the saw-tooth model is introduced, but stress and strain redistribution result in more elements carrying the load. These stiffness differences may cause large effects in transient analysis. As a result, ISLA and the N-R method may obtain different equilibrium states.

ISLA follows an incremental approach. The issue of non-proportional loading in SLA does not occur in ISLA since the initial load factor is not scaled. ISLA can also include geometrically non-linear effects because of the incremental approach. The proposed method can be easily implemented in commercial software. ISLA is validated for non-proportional loading of a prestressed concrete beam, out-of-plane bending of a masonry wall, settlement test of a masonry facade, and pushover of a masonry house. ISLA is demonstrated to be robust at the structural level. For snap-backs, the load control method and the load and damage control method both perform successfully. For the displacement history, the load control method jumps over snap-backs while the load and damage control method follows snap-backs. For the damage history, both methods trace the whole damage process of snap-backs.

Geometrical non-linearity can be included in ISLA due to its incremental procedure. When geometrical non-linearity is considered, the B matrix (the strain-displacement relation) and geometrically non-linear matrix (which is related to the 2nd Piola-Kirchhoff stress) are updated in each increment by the kinematic descriptions [110]. Only the material matrix is updated by ISLA in damage cycles with reduced secant stiffness. Similar to arc-length control, indirect displacement control is introduced in the load and damage control method to avoid or pass localized failure process zones when varying forces are applied to multiple nodes, for example in the case of pressure or other forms of distributed loadings. A control point is a selected node at a critical position (e.g., midspan of a simply supported beam or plate), the displacement of which is assumed to be always increasing. The unbalanced nodal force factor  $\lambda_r$  of the control point is defined as the difference of the nodal force between the control point loaded by the imposed displacement and the node loaded by the current load, the factor of which is  $\lambda_2$ . The current load factor  $\lambda_2$  is adjusted according to the unbalanced force. This procedure is repeated until  $\lambda_r$  is smaller than a tolerance value  $r_r$ , and then the next incremental imposed displacement is applied. ISLA is robust for the out-of-plane bending of a masonry wall with overburden. Strong geometrical non-linearity may cause divergence.

Transient non-linearity can be included in ISLA due to its incremental procedure. Transient non-linearity is considered by the Newmark time integration scheme while physical non-linearity is considered in damage cycles with reduced secant stiffness. Due to the fact that transient analysis is sensitive with the stiffness

change, ISLA follows both load steps (the relation between time and accelerations) and damage cycles (stiffness reductions). A modified damage control method is introduced, in which time is adjusted along with scaled acceleration during cycles, and a load schedule is added. The equilibrium states are searched for during each stiffness reduction until the load factor reaches the value of the current load step. Afterwards, the next load step is applied. The current load factor is scaled by the extrapolation procedure in the first 10 cycles and then by the bisection method in the next 10 cycles due to the strong non-linearity of the transient effect. Note that the utilisation value  $\mu$  cannot be 1 for the certain stiffness  $K$ . Extra damage can be introduced into the system with a constant stiffness reduction factor ( $\mu$  is smaller than 1). In addition, if a structure snaps back, the load needs to be reduced, which leads to a time decrement ( $\mu$  is larger than 1). When the number of cycles is larger than 20, the algorithm restarts from the previous equilibrium state and searches for the next equilibrium state of  $K'$ , in which the stiffness of the critical element is reduced. For static analysis, the damage control method can always find an equilibrium state for the certain stiffness when  $\mu$  is exactly 1. ISLA is validated for concrete in a multiple DOFs system. Note that ISLA follows the reduced secant stiffness for unloading while plastic material models follow the initial elastic stiffness. To this end, it is recommended that the reduced elastic material model is employed for brittle material to follow the secant stiffness for unloading, whereas the plastic material model should be used for ductile materials to follow the initial stiffness for unloading. However, ISLA cannot guarantee the robustness when a plastic material model is involved.

In Appendices A and B, ISLA has been extended for proportional cyclic analysis to demonstrate its possibility. Two types of unloading paths are considered, namely unloading with the secant stiffness (the damage model) in Appendix A and with the non-secant stiffness (the plastic model) in Appendix B. Firstly, the tensile unloading behaviour is simplified to follow the secant stiffness for the cyclic loading of quasi-brittle materials. Note that although tensile unloading can be simplified by following the secant stiffness, it is unrealistic to follow the secant stiffness for compressive unloading. Nevertheless, it is still worthwhile for the tensile failure of brittle materials, in which the compressive behaviour is elastic in FEM models due to the simplicity. Independent or correlative damage behaviour is considered for

reverse loading between tension and compression. Currently, this algorithm is suitable only for proportional loading since the stresses are assumed to be zero for the transition of tension and compression. Secondly, plastic unloading behaviour is introduced in ISLA and combined with reverse loading. The coupled damage-plastic material model is implemented in ISLA rather than the elastic material model to consider irreversible deformations. This is especially important for the unloading behaviour of metal materials and the compressive unloading behaviour of quasi-brittle materials. ISLA follows the damage model for loading while ISLA follows the plastic model for unloading. Plastic strain is recomputed when the reduced elastic modulus is changed to the unloading modulus for unloading. The damage model with reduced secant stiffness ensures computational robustness while the plastic model provides the possibility of unloading with non-secant stiffness. The unloading stiffness is defined as a constant value or a function to validate the algorithm, which needs to be adjusted based on the experiment. For repeating loading, the structure can be accurately unloaded to the state for which the total force is zero for proportional loading. However, for non-proportional repeating loading and cyclic loading, accuracy and robustness cannot be guaranteed when the load is reversed for a structure. The stresses of damaged elements are not reversed simultaneously at the state for which the total force is zero due to the residual stress. The solution is to perform iterations to update the stiffness, which results in the bifurcation that the stiffnesses of the damaged elements can be reduced by the damage of the loading, updated due to the unloading or updated due to the reverse loading. In addition, the isotropic hardening model used for unloading may cause divergence in ISLA.

## 12.2. FURTHER WORK

The following subjects for further research are suggested:

The saw-tooth model is employed in SLA and ISLA to represent the softening material model used in the N-R method. It is observed that ISLA and the N-R method do not produce identical results, especially for transient analysis. This is caused by the linearisation procedure of solving non-linear equations, in which one stiffness represents and replaces the varying stiffness over a period. When a constant stiffness reduction factor is used in SLA or ISLA, extra damage or imperfection may be introduced to the structure, which may cause the underestimation of a

structure. In addition, the utilisation function is not exactly 1 (i.e., smaller than 1). Although the difference is hardly observed at the global level (the load-displacement diagram), the distinctions can be seen at the local level (the stress-strain curve). According to the stress-strain curve, the capacity of non-critical elements is even more underestimated than the critical element based on the failure criterion used in SLA or ISLA. An improved saw-tooth model should be proposed for the stiffness reduction procedure. Investigation of a more realistic representative stiffness is suggested for non-linear problems. A possible solution may be to introduce a varying stiffness reduction factor based on the energy dissipation or the stiffness change rate. The improved saw-tooth model should be tested in not only static analysis but also transient analysis.

In this research, a local damage material model is used. Mesh objectivity should be further investigated, including mesh-size dependency and mesh-directional bias. Strange results are observed at the boundaries of forces and displacements of the facade and the house since connections or boundaries in the FEM model are simplified to enhance calculation efficiency. However, this simplification may cause mistakes in determining a critical element, which is more significant in ISLA than in other methods. Therefore, the definition of the critical element is suggested to include the influence of surrounding elements apart from the stress state itself (non-local damage model) in order to minimize the accuracy impact of certain strange stress states due to model simplification. Another solution is to implement ISLA in a strong discontinuity method, X-FEM or G-FEM. Further, the influence of different stiffness reduction factors to the critical element on the results should be investigated. Normally, a small stiffness reduction factor is chosen to boost calculation efficiency, but it may cause extra imperfections and unrealistic damage paths by reducing stiffness of one element by too much.

ISLA is programmed in ANSYS. The restart functionality in ANSYS is convenient for implementing ISLA. Other finite element programs do not have this versatile functionality. However, ANSYS restart cannot reuse the factorized stiffness matrix, which causes low efficiency of the stiffness regeneration. In other words, ANSYS needs to assemble the global stiffness matrix several times each cycle, specifically the same number of times as the number of damaged elements, which causes low efficiency for a large structure with a lot of damage. Therefore, the efficiency of the

ANSYS restart should be improved for assembling and updating the stiffness matrix. In addition, in ANSYS the material properties can be changed only at the element level, not at the integration point level. Several layers of shell elements with section offset are used to consider out-of-plain behaviour, which causes low efficiency. It is important to extend ISLA to update the stiffness at the integration point level.

ISLA can be used for not only continuum models as in this thesis but also discrete models such as interface elements or the lattice model, which are also based on damage cycles. The discrete crack model with interface elements is significant in simulating the behaviour of masonry structures. The smeared crack model cannot consider the behaviour of sliding or may overestimate the capacity of a structure, especially in the situation when cracks occur at the edges of structures. The discrete crack model with interface elements is suggested for implementation in ISLA, especially for the contact analysis, to consider sliding behaviour. Moreover, ISLA can be implemented to multiscale analysis, in which different scales are connected, averaged and transferred by a secant stiffness, which is governed by damage instead of tangent stiffness. Therefore, ISLA is proposed to combine the lattice model for multiscale analysis to improve the accuracy and robustness of multiscale analysis. The implementation algorithms should be tested on different types of FEM models and analyses.

When geometrical non-linearity, transient non-linearity and plastic non-linearity are included in ISLA, the Lagrange descriptions, the Newmark time integration scheme and isotropic hardening model are used, respectively. ISLA is robust for the examples tested in the thesis. However, further investigation should be conducted for more complicated examples. An orthotropic plastic model is suggested for implementation in ISLA, which is compatible with the orthotropic damage model in ISLA.

It is necessary to include robust iterations to determine loading and unloading states at the local level. In this thesis, ISLA considers only loading and unloading state changes at the global level to avoid iterations, which may cause divergences or bifurcations. In addition, ISLA is validated only for simple examples. Non-proportional loading is not considered. Cyclic loading with plastic unloading behaviour is tested for one element. Only repeating loading is tested for a beam. Cyclic loading has not yet been tested for a structure due to residual stresses. That

is to say, the reversing moment of each element cannot be predicted for a structure. The stresses of some elements are not reversed although the load is reversed at the global level. Meanwhile damage of some elements may begin when the stresses of other elements have not yet reversed. The algorithm for the structure level proposed in this thesis should be optimized to balance accuracy and efficiency. The major challenge is to define enough and proper unloading steps with iterations to change the stiffness of damaged elements when the stresses are reversed. Structural level tests are required to validate the algorithm.

In this thesis, the coupled damage-plastic model is employed for ISLA to consider unloading with the non-secant stiffness. However, the modified plastic model is simpler. The robustness and the accuracy of the modified plastic model are worthwhile for further investigation.



# BIBLIOGRAPHY

- [1] G. Houlsby, *A thermodynamic approach to constitutive modelling of concrete using damage mechanics and plasticity theory*, Ph.D. thesis, University of Oxford (2005).
- [2] R. De Borst and P. Nauta, *Non-orthogonal cracks in a smeared finite element model*, Engineering Computations **2**, 35 (1985).
- [3] J. G. Rots and R. De Borst, *Analysis of mixed-mode fracture in concrete*, Journal of Engineering Mechanics **113**, 1739 (1987).
- [4] J. G. Rots and J. Blaauwendraad, *Crack models for concrete, discrete or smeared? fixed, multi-directional or rotating?* HERON, 34 (1), 1989 (1989).
- [5] R. De Borst, M. A. Crisfield, J. J. Remmers, and C. V. Verhoosel, *Nonlinear finite element analysis of solids and structures* (John Wiley & Sons, 2012).
- [6] P. Ladevèze, *Nonlinear computational structural mechanics: new approaches and non-incremental methods of calculation* (Springer Science & Business Media, 2012).
- [7] P. Kerfriden, O. Allix, and P. Gosselet, *A three-scale domain decomposition method for the 3d analysis of debonding in laminates*, Computational mechanics **44**, 343 (2009).
- [8] B. Vandoren, K. De Proft, A. Simone, and L. J. Sluys, *A novel constrained large time increment method for modelling quasi-brittle failure*, Computer Methods in Applied Mechanics and Engineering **265**, 148 (2013).
- [9] J. Rots, *Sequentially linear continuum model for concrete fracture*, Fracture Mechanics of Concrete Structures **13** (2001).

- [10] J. G. Rots and S. Invernizzi, *Regularized sequentially linear saw-tooth softening model*, International Journal for Numerical and Analytical Methods in Geomechanics **28**, 821 (2004).
- [11] J. G. Rots, B. Belletti, and S. Invernizzi, *Robust modeling of rc structures with an “event-by-event” strategy*, Engineering Fracture Mechanics **75**, 590 (2008).
- [12] M. J. DeJong, M. A. Hendriks, and J. G. Rots, *Sequentially linear analysis of fracture under non-proportional loading*, Engineering Fracture Mechanics **75**, 5042 (2008).
- [13] C. Yu, P. Hoogenboom, and J. Rots, *Incremental sequentially linear analysis to control failure for quasi-brittle materials and structures including non-proportional loading*, Engineering Fracture Mechanics **202**, 332 (2018).
- [14] C. Yu, P. Hoogenboom, and J. Rots, *Incremental sequentially linear analysis of a notched beam*, in *Computational Modelling of Concrete Structures: Proceedings of the Conference on Computational Modelling of Concrete and Concrete Structures (EURO-C 2018), February 26-March 1, 2018, Bad Hofgastein, Austria* (CRC Press, 2018) p. 465.
- [15] J. G. Rots, *Computational modeling of concrete fracture*, Ph.D. thesis, Technische Hogeschool Delft (1988).
- [16] D. Ngo and A. Scordelis, *Finite element analysis of reinforced concrete beams*, in *Journal Proceedings*, Vol. 64 (1967) pp. 152–163.
- [17] A. Ingraffea and V. Saouma, *Numerical modeling of discrete crack propagation in reinforced and plain concrete*, in *Fracture mechanics of concrete: structural application and numerical calculation* (Springer, 1985) pp. 171–225.
- [18] J. G. Rots, *Smeared and discrete representations of localized fracture*, in *Current Trends in Concrete Fracture Research* (Springer, 1991) pp. 45–59.
- [19] Y. Rashid, *Ultimate strength analysis of prestressed concrete pressure vessels*, Nuclear engineering and design **7**, 334 (1968).

- [20] Z. P. Bavzant and B. H. Oh, *Crack band theory for fracture of concrete*, Matériaux et construction **16**, 155 (1983).
- [21] A. Hillerborg, M. Modéer, and P.-E. Petersson, *Analysis of crack formation and crack growth in concrete by means of fracture mechanics and finite elements*, Cement and concrete research **6**, 773 (1976).
- [22] R. Cope, P. Rao, L. Clark, and P. Norris, *Modelling of reinforced concrete behaviour for finite element analysis of bridge slabs*, Numerical Methods for Nonlinear Problems, Pineridge Press, Swansea **1980**, 457 (1980).
- [23] H. J. Herrmann, A. Hansen, and S. Roux, *Fracture of disordered, elastic lattices in two dimensions*, Physical Review B **39**, 637 (1989).
- [24] H. Schlangen, *Experimental and numerical analysis of fracture processes in concrete*, HERON, 38 (2), 1993 (1993).
- [25] J. Van Mier, A. Vervuurt, and E. Schlangen, *Boundary and size effects in uniaxial tensile tests: a numerical and experimental study*, Fracture and Damage in Quasibrittle Structures , 289 (1994).
- [26] W. Beranek and G. Hobbelman, *2d and 3d-modelling of concrete as an assemblage of spheres: revaluation of the failure criterion*, Fracture mechanics of concrete structures. Proc. FRAMCOS-2 , 965 (1995).
- [27] J. E. Bolander and N. Sukumar, *Irregular lattice model for quasistatic crack propagation*, Physical Review B **71**, 094106 (2005).
- [28] T. Belytschko, Y. Krongauz, D. Organ, M. Fleming, and P. Krysl, *Meshless methods: an overview and recent developments*, Computer methods in applied mechanics and engineering **139**, 3 (1996).
- [29] V. P. Nguyen, T. Rabczuk, S. Bordas, and M. Duflot, *Meshless methods: a review and computer implementation aspects*, Mathematics and computers in simulation **79**, 763 (2008).
- [30] T. Belytschko, Y. Y. Lu, and L. Gu, *Element-free galerkin methods*, International journal for numerical methods in engineering **37**, 229 (1994).

- [31] J. M. Melenk and I. Babuska, *The partition of unity finite element method: basic theory and applications*, Computer methods in applied mechanics and engineering **139**, 289 (1996).
- [32] T. Strouboulis, K. Coppers, and I. Babuska, *The generalized finite element method: an example of its implementation and illustration of its performance*, International Journal for Numerical Methods in Engineering **47**, 1401 (2000).
- [33] D. Sulsky and H. L. Schreyer, *Axisymmetric form of the material point method with applications to upsetting and taylor impact problems*, Computer Methods in Applied Mechanics and Engineering **139**, 409 (1996).
- [34] S. Bardenhagen, J. Brackbill, and D. Sulsky, *The material-point method for granular materials*, Computer methods in applied mechanics and engineering **187**, 529 (2000).
- [35] S. Bardenhagen and E. Kober, *The generalized interpolation material point method*, Computer Modeling in Engineering and Sciences **5**, 477 (2004).
- [36] N. Moës, J. Dolbow, and T. Belytschko, *A finite element method for crack growth without remeshing*, International journal for numerical methods in engineering **46**, 131 (1999).
- [37] T. Belytschko and T. Black, *Elastic crack growth in finite elements with minimal remeshing*, International journal for numerical methods in engineering **45**, 601 (1999).
- [38] N. Sukumar, N. Moës, B. Moran, and T. Belytschko, *Extended finite element method for three-dimensional crack modelling*, International Journal for Numerical Methods in Engineering **48**, 1549 (2000).
- [39] T.-P. Fries and T. Belytschko, *The extended/generalized finite element method: an overview of the method and its applications*, International Journal for Numerical Methods in Engineering **84**, 253 (2010).
- [40] M. Jirásek and T. Belytschko, *Computational resolution of strong discontinuities*, in *Proceedings of fifth world congress on computational mechanics, WCCM V, Vienna University of Technology, Austria* (2002).

- [41] M. Ortiz, Y. Leroy, and A. Needleman, *A finite element method for localized failure analysis*, Computer methods in applied mechanics and engineering **61**, 189 (1987).
- [42] T. Belytschko, J. Fish, and B. E. Engelmann, *A finite element with embedded localization zones*, Computer methods in applied mechanics and engineering **70**, 59 (1988).
- [43] J. C. Simo, J. Oliver, and F. Armero, *An analysis of strong discontinuities induced by strain-softening in rate-independent inelastic solids*, Computational mechanics **12**, 277 (1993).
- [44] M. Jirásek, *Comparative study on finite elements with embedded discontinuities*, Computer methods in applied mechanics and engineering **188**, 307 (2000).
- [45] G. N. Wells and L. Sluys, *A new method for modelling cohesive cracks using finite elements*, International Journal for Numerical Methods in Engineering **50**, 2667 (2001).
- [46] J. C. Simo and M. Rifai, *A class of mixed assumed strain methods and the method of incompatible modes*, International journal for numerical methods in engineering **29**, 1595 (1990).
- [47] G. Wells and L. Sluys, *Three-dimensional embedded discontinuity model for brittle fracture*, International Journal of Solids and Structures **38**, 897 (2001).
- [48] J. Alfaiate, G. Wells, and L. Sluys, *On the use of embedded discontinuity elements with crack path continuity for mode-i and mixed-mode fracture*, Engineering fracture mechanics **69**, 661 (2002).
- [49] J. Alfaiate, A. Simone, and L. Sluys, *Non-homogeneous displacement jumps in strong embedded discontinuities*, International Journal of Solids and Structures **40**, 5799 (2003).
- [50] J. Oliver, *On the discrete constitutive models induced by strong discontinuity kinematics and continuum constitutive equations*, International journal of solids and structures **37**, 7207 (2000).

- [51] J. Oliver, A. E. Huespe, M. Pulido, and E. Chaves, *From continuum mechanics to fracture mechanics: the strong discontinuity approach*, Engineering fracture mechanics **69**, 113 (2002).
- [52] J. Oliver, A. E. Huespe, E. Samaniego, and E. Chaves, *Continuum approach to the numerical simulation of material failure in concrete*, International journal for numerical and analytical methods in geomechanics **28**, 609 (2004).
- [53] D. Dias-da Costa, J. Alfaiate, L. Sluys, and E. Júlio, *A discrete strong discontinuity approach*, Engineering Fracture Mechanics **76**, 1176 (2009).
- [54] D. Dias-da Costa, J. Alfaiate, L. Sluys, and E. Júlio, *Towards a generalization of a discrete strong discontinuity approach*, Computer Methods in Applied Mechanics and Engineering **198**, 3670 (2009).
- [55] J. Oliver, A. E. Huespe, and P. J. Sánchez, *A comparative study on finite elements for capturing strong discontinuities: E-fem vs x-fem*, Computer methods in applied mechanics and engineering **195**, 4732 (2006).
- [56] D. Dias-da Costa, J. Alfaiate, L. Sluys, and E. Júlio, *A comparative study on the modelling of discontinuous fracture by means of enriched nodal and element techniques and interface elements*, International Journal of Fracture **161**, 97 (2010).
- [57] W.-F. Chen, *Plasticity in reinforced concrete* (J. Ross Publishing, 2007).
- [58] C. Comi and U. Perego, *Fracture energy based bi-dissipative damage model for concrete*, International journal of solids and structures **38**, 6427 (2001).
- [59] P. H. Feenstra, *Computational aspects of biaxial stress in plain and reinforced concrete*, PhD thesis, Delft University of Technology (1993).
- [60] P. H. Feenstra and R. De Borst, *A composite plasticity model for concrete*, International Journal of Solids and Structures **33**, 707 (1996).
- [61] P. B. LourenCco and J. G. Rots, *Multisurface interface model for analysis of masonry structures*, Journal of engineering mechanics **123**, 660 (1997).

- [62] P. B. LourenCco, J. G. Rots, and J. Blaauwendraad, *Continuum model for masonry: parameter estimation and validation*, Journal of structural engineering **124**, 642 (1998).
- [63] J. Lemaitre and J.-L. Chaboche, *Mechanics of solid materials* (Cambridge university press, 1994).
- [64] W. Brekelmans, P. Schreurs, and J. De Vree, *Continuum damage mechanics for softening of brittle materials*, Acta mechanica **93**, 133 (1992).
- [65] J. Mazars and J. Lemaitre, *Application of continuous damage mechanics to strain and fracture behavior of concrete*, in *Application of fracture mechanics to cementitious composites* (Springer, 1985) pp. 507–520.
- [66] J. Oliver, M. Cervera, S. Oller, and J. Lubliner, *Isotropic damage models and smeared crack analysis of concrete*, in *Proc. SCI-C Computer Aided Analysis and Design of Concrete Structures*, Vol. 945958 (1990).
- [67] M. Jirásek and T. Zimmermann, *Rotating crack model with transition to scalar damage*, Journal of engineering mechanics **124**, 277 (1998).
- [68] J. Mazars, *A description of micro-and macroscale damage of concrete structures*, Engineering Fracture Mechanics **25**, 729 (1986).
- [69] R. Faria, J. Oliver, and M. Cervera, *A strain-based plastic viscous-damage model for massive concrete structures*, International journal of solids and structures **35**, 1533 (1998).
- [70] D. Krajcinovic and G. Fonseka, *The continuous damage theory of brittle materials, part 1: general theory*, Journal of applied Mechanics **48**, 809 (1981).
- [71] S. Murakami and N. Ohno, *A continuum theory of creep and creep damage*, in *Creep in structures* (Springer, 1981) pp. 422–444.
- [72] J.-L. Chaboche, *Continuous damage mechanics—a tool to describe phenomena before crack initiation*, Nuclear Engineering and Design **64**, 233 (1981).
- [73] J. Mazars and G. Pijaudier-Cabot, *Continuum damage theory—application to concrete*, Journal of Engineering Mechanics **115**, 345 (1989).

- [74] Z. P. Bazant and P. C. Prat, *Microplane model for brittle-plastic material: I. theory*, Journal of Engineering Mechanics **114**, 1672 (1988).
- [75] E. Kuhl and E. Ramm, *On the linearization of the microplane model*, Mechanics of Cohesive-frictional Materials **3**, 343 (1998).
- [76] Z. P. Bazant, *Nonlocal damage theory based on micromechanics of crack interactions*, Journal of engineering mechanics **120**, 593 (1994).
- [77] G. Pijaudier-Cabot and Z. P. Bazant, *Nonlocal damage theory*, Journal of engineering mechanics **113**, 1512 (1987).
- [78] Z. P. Bazant, *Instability, ductility, and size effect in strain-softening concrete*, Journal of the engineering mechanics division **102**, 331 (1976).
- [79] R. P. R. DE and J. DE VREE, *Gradient enhanced damage for quasi-brittle materials*, International Journal for numerical methods in engineering **39**, 3391 (1996).
- [80] L.-Q. Chen, *Phase-field models for microstructure evolution*, Annual review of materials research **32**, 113 (2002).
- [81] C. V. Verhoosel and R. de Borst, *A phase-field model for cohesive fracture*, International Journal for numerical methods in Engineering **96**, 43 (2013).
- [82] R. de Borst and C. V. Verhoosel, *Gradient damage vs phase-field approaches for fracture: Similarities and differences*, Computer Methods in Applied Mechanics and Engineering **312**, 78 (2016).
- [83] P. Grassl and M. Jirásek, *Damage-plastic model for concrete failure*, International journal of solids and structures **43**, 7166 (2006).
- [84] O. Omidi and V. Lotfi, *Continuum large cracking in a rate-dependent plastic-damage model for cyclic-loaded concrete structures*, International Journal for Numerical and Analytical Methods in Geomechanics **37**, 1363 (2013).
- [85] M. Ortiz, *A constitutive theory for the inelastic behavior of concrete*, Mechanics of materials **4**, 67 (1985).

- [86] G. Meschke, R. Lackner, and H. A. Mang, *An anisotropic elastoplastic-damage model for plain concrete*, International journal for numerical methods in engineering **42**, 703 (1998).
- [87] A. D. Jefferson, *Craft—a plastic-damage-contact model for concrete. i. model theory and thermodynamic considerations*, International Journal of Solids and Structures **40**, 5973 (2003).
- [88] P. Grassl, D. Xenos, U. Nyström, R. Rempling, and K. Gylltoft, *Cdpm2: A damage-plasticity approach to modelling the failure of concrete*, International Journal of Solids and Structures **50**, 3805 (2013).
- [89] P. Feenstra, J. Rots, A. Arnesen, J. Teigen, and K. Hoiseth, *A 3d constitutive model for concrete based on a co-rotational concept*, (1998).
- [90] J. Rots, P. Nauta, G. Kuster, and J. Blaauwendraad, *Smeared crack approach and fracture localization in concrete*, (1985).
- [91] T. Massart, P. Bouillard, M. Geers, R. Peerlings, *et al.*, *Multi-scale modeling of damage in masonry structures*, (2003).
- [92] I. Gitman, H. Askes, and L. Sluys, *Coupled-volume multi-scale modelling of quasi-brittle material*, European Journal of Mechanics-A/Solids **27**, 302 (2008).
- [93] V. P. Nguyen, O. Lloberas-Valls, M. Stroeven, and L. J. Sluys, *Homogenization-based multiscale crack modelling: from micro-diffusive damage to macro-cracks*, Computer Methods in Applied Mechanics and Engineering **200**, 1220 (2011).
- [94] R. Hill, *On macroscopic effects of heterogeneity in elastoplastic media at finite strain*, in *Mathematical Proceedings of the Cambridge Philosophical Society*, Vol. 95 (Cambridge University Press, 1984) pp. 481–494.
- [95] V. Kouznetsova, W. Brekelmans, and F. Baaijens, *An approach to micro-macro modeling of heterogeneous materials*, Computational mechanics **27**, 37 (2001).

- [96] V. V. Kouznetsova, *Computational homogenization for the multi-scale analysis of multi-phase materials*, Ph.D. thesis, Technische Universiteit Eindhoven (2002).
- [97] R. Smit, W. Brekelmans, and H. Meijer, *Prediction of the mechanical behavior of nonlinear heterogeneous systems by multi-level finite element modeling*, Computer methods in applied mechanics and engineering **155**, 181 (1998).
- [98] C. Miehe, J. Schotte, and J. Schröder, *Computational micro–macro transitions and overall moduli in the analysis of polycrystals at large strains*, Computational Materials Science **16**, 372 (1999).
- [99] F. Feyel and J.-L. Chaboche, *Fe2 multiscale approach for modelling the elasto-viscoplastic behaviour of long fibre sic/ti composite materials*, Computer methods in applied mechanics and engineering **183**, 309 (2000).
- [100] K. Terada and N. Kikuchi, *A class of general algorithms for multi-scale analyses of heterogeneous media*, Computer methods in applied mechanics and engineering **190**, 5427 (2001).
- [101] R. Hill, *Elastic properties of reinforced solids: some theoretical principles*, Journal of the Mechanics and Physics of Solids **11**, 357 (1963).
- [102] P. Squire, *Local and global aspects in the mathematical theory of plasticity*, Plasticity today , 279 (1985).
- [103] I. Gitman, H. Askes, and L. Sluys, *Representative volume: existence and size determination*, Engineering fracture mechanics **74**, 2518 (2007).
- [104] V. P. Nguyen, O. Lloberas-Valls, M. Stroeven, and L. J. Sluys, *On the existence of representative volumes for softening quasi-brittle materials—a failure zone averaging scheme*, Computer Methods in Applied Mechanics and Engineering **199**, 3028 (2010).
- [105] I. M. Gitman, H. Askes, and E. C. Aifantis, *The representative volume size in static and dynamic micro-macro transitions*, International Journal of Fracture **135**, L3 (2005).

- [106] V. Kouznetsova, M. G. Geers, and W. M. Brekelmans, *Multi-scale constitutive modelling of heterogeneous materials with a gradient-enhanced computational homogenization scheme*, International Journal for Numerical Methods in Engineering **54**, 1235 (2002).
- [107] I. M. Gitman, *Gradient elasticity with internal length and internal inertia based on the homogenisation of a representative volume element*, Journal of the Mechanical Behavior of Materials **18**, 1 (2007).
- [108] O. C. Zienkiewicz, R. L. Taylor, O. C. Zienkiewicz, and R. L. Taylor, *The finite element method*, Vol. 3 (McGraw-hill London, 1977).
- [109] W. Alnaas, *Nonlinear finite element analysis of quasi-brittle materials*, Ph.D. thesis, Cardiff University (2016).
- [110] R. d. Borst and L. Sluys, *CIE 5142 Computational Methods in Non-linear Solid Mechanics* (TU Delft, Delft University of Technology, 2015) Chap. 4.4, pp. 65–75.
- [111] M. Crisfield, *Accelerated solution techniques and concrete cracking*, Computer methods in applied mechanics and engineering **33**, 585 (1982).
- [112] G. A. Wempner, *Discrete approximations related to nonlinear theories of solids*, International Journal of Solids and Structures **7**, 1581 (1971).
- [113] E. Riks, *An incremental approach to the solution of snapping and buckling problems*, International Journal of Solids and Structures **15**, 529 (1979).
- [114] E. Ramm, *Strategies for tracing the nonlinear response near limit points*, in *Nonlinear finite element analysis in structural mechanics* (Springer, 1981) pp. 63–89.
- [115] T. Pohl, E. Ramm, and M. Bischoff, *Adaptive path following schemes for problems with softening*, Finite Elements in Analysis and Design **86**, 12 (2014).
- [116] M. Crisfield, *A fast incremental/iterative solution procedure that handles “snap-through”* , in *Computational Methods in Nonlinear Structural and Solid Mechanics* (Elsevier, 1981) pp. 55–62.

- [117] E. Ramm, *The riks/wempner approach-an extension of the displacement control method in nonlinear analysis*, Recent Advance in Non-linear Computation Mechanics (1982).
- [118] R. De Borst, *Computation of post-bifurcation and post-failure behavior of strain-softening solids*, Computers & Structures **25**, 211 (1987).
- [119] R. De Borst, *Non-linear analysis of frictional materials*, Ph.D. thesis, TU Delft, Delft University of Technology (1986).
- [120] C. V. Verhoosel, J. J. Remmers, and M. A. Gutiérrez, *A dissipation-based arc-length method for robust simulation of brittle and ductile failure*, International Journal for Numerical Methods in Engineering **77**, 1290 (2009).
- [121] M. Crisfield, *Difficulties with current numerical models for reinforced concrete and some tentative solutions*, in *Int. Conf. on Computer-Aided Analysis and Design of Concrete Structures* (1984) pp. 331–358.
- [122] A. Carpinteri, *Mechanical damage and crack growth in concrete: plastic collapse to brittle fracture*, Vol. 5 (Springer Science & Business Media, 2012).
- [123] J. G. Rots and R. De Borst, *Analysis of concrete fracture in “direct” tension*, International journal of solids and structures **25**, 1381 (1989).
- [124] D. A. Hordijk, *Local approach to fatigue of concrete* (TU Delft, Delft University of Technology, 1991).
- [125] J. Rots, *Settlement damage predictions for masonry*, in *Maintenance and re-strengthening of materials and structures: Brick and brickwork. Proc. Int. Workshop on urban heritage and building maintenance* (2000) pp. 47–62.
- [126] M. Boonpichetvong, *Settlement damage of masonry buildings in soft-ground tunnelling*, The Structural Engineer **83**, 32 (2005).
- [127] J. G. Rots, S. Invernizzi, and B. Belletti, *Saw-tooth softening/stiffening-a stable computational procedure for rc structures*, Computers and Concrete **3**, 213 (2006).

- [128] J. Rots, S. Invernizzi, B. Belleti, and M. Hendriks, *Circumventing bifurcations in structural softening*, in *Workshop on Computational Modeling on Concrete, Masonry and Fiber-reinforced Composites, Delft 17-18 June* (Delft University of Technology, 2009).
- [129] A. Slobbe, M. Hendriks, and J. Rots, *Sequentially linear analysis of shear critical reinforced concrete beams without shear reinforcement*, Finite Elements in Analysis and Design **50**, 108 (2012).
- [130] L. Voormeeren, *Extension and Verification of the Sequentially Linear Analysis to Three-Dimensional Cases*, Master's thesis, Delft University of Technology (2011).
- [131] A. Van de Graaf, J. Rots, and M. Hendriks, *Sequentially linear analysis for simulating brittle failure*, (2014).
- [132] C. Yu, P. Hoogenboom, and J. G. Rots, *Algorithm for non-proportional loading in sequentially linear analysis*, 9th International Conference on Fracture Mechanics of Concrete and Concrete Structures (2016).
- [133] M. Pari, M. A. Hendriks, and J. G. Rots, *Non-proportional loading in sequentially linear analysis for 3-d stress states*, International Journal for Numerical Methods in Engineering .
- [134] G. Giardina, A. V. Van de Graaf, M. A. Hendriks, J. G. Rots, and A. Marini, *Numerical analysis of a masonry facade subject to tunnelling-induced settlements*, Engineering structures **54**, 234 (2013).
- [135] J. Oliver, A. Huespe, S. Blanco, and D. Linero, *Stability and robustness issues in numerical modeling of material failure with the strong discontinuity approach*, Computer Methods in Applied Mechanics and Engineering **195**, 7093 (2006).
- [136] J. Oliver, A. Huespe, and J. Cante, *An implicit/explicit integration scheme to increase computability of non-linear material and contact/friction problems*, Computer Methods in Applied Mechanics and Engineering **197**, 1865 (2008).

- [137] W. Alnaas and A. D. Jefferson, *A smooth unloading–reloading approach for the nonlinear finite element analysis of quasi-brittle materials*, Engineering Fracture Mechanics **152**, 105 (2016).
- [138] F. Cazes, G. Meschke, and M.-M. Zhou, *Strong discontinuity approaches: An algorithm for robust performance and comparative assessment of accuracy*, International Journal of Solids and Structures **96**, 355 (2016).
- [139] R. GraCca-e Costa, J. Alfaia, D. Dias-da Costa, and L. Sluys, *A non-iterative approach for the modelling of quasi-brittle materials*, International Journal of Fracture **178**, 281 (2012).
- [140] A. S. Al-Sabah and D. F. Laefer, *Use of negative stiffness in failure analysis of concrete beams*, Engineering Structures **126**, 187 (2016).
- [141] R. GraCca-e Costa, J. Alfaia, D. Dias-da Costa, P. Neto, and L. Sluys, *Generalisation of non-iterative methods for the modelling of structures under non-proportional loading*, International Journal of Fracture **182**, 21 (2013).
- [142] J. Alfaia and L. J. Sluys, *On the use of non-iterative methods in cohesive fracture*, International Journal of Fracture **210**, 167 (2018).
- [143] J. Eliávs, P. Frantík, and M. Vovrechovský, *Improved sequentially linear solution procedure*, Engineering fracture mechanics **77**, 2263 (2010).
- [144] J. Eliávs, *Generalization of load–unload and force-release sequentially linear methods*, International Journal of Damage Mechanics **24**, 279 (2015).
- [145] 4.5.2 *Damaged plasticity model for concrete and other quasi-brittle materials*, ABAQUS software manual (ABAQUS Theory Manual) Chap. 4.5.2.
- [146] 13 *Element library* (ANSYS Theory Manual) Chap. 13.183.
- [147] R. Esposito, F. Messali, and J. G. Rots, *TESTS FOR THE CHARACTERIZATION OF REPLICATED MASONRY AND WALL TIES*, Tech. Rep. (Delft University of Technology, 2016).
- [148] G. Ravenshorst and F. Messali, *OUT-OF-PLANE TESTS ON REPLICATED MASONRY WALLS*, Tech. Rep. (Delft University of Technology, 2016).

- [149] G. Giardina, A. Marini, M. A. Hendriks, J. G. Rots, F. Rizzardini, and E. Giuriani, *Experimental analysis of a masonry facade subject to tunnelling-induced settlement*, Engineering Structures **45**, 421 (2012).
- [150] E. Buckingham, *On physically similar systems; illustrations of the use of dimensional equations*, Physical Review **4**, 345 (1914).
- [151] M. Cervera and M. Chiumenti, *Mesh objective tensile cracking via a local continuum damage model and a crack tracking technique*, Computer Methods in Applied Mechanics and Engineering **196**, 304 (2006).
- [152] M. Jirasek and P. Grassl, *Evaluation of directional mesh bias in concrete fracture simulations using continuum damage models*, Engineering Fracture Mechanics **75**, 1921 (2008).
- [153] A. T. Slobbe, *Propagation and band width of smeared cracks*, (2015).
- [154] R. Esposito, S. Jafari, G. Ravenshorst, H. Schipper, and J. Rots, *Influence of the behaviour of calcium silicate brick and element masonry on the lateral capacity of structures*, in *Australasian Masonry Conference, Sydney, Australia* (2018).
- [155] R. Esposito, K. Terwel, G. Ravenshorst, H. Schipper, F. Messali, and J. Rots, *Cyclic pushover test on an unreinforced masonry structure reseambling a typical dutch terraced house*, in *16th World Conference on Earthquake, WCEE* (2017) pp. 9–13.
- [156] M. DeJong, M. Hendriks, and J. Rots, *Shear retention and mesh alignment during fracture using sequentially linear analysis*, (2009).



# ACKNOWLEDGEMENTS

Life is strange. Looking back on my PhD journey, I am surprised about how this thesis on a numerical solver and a constitutive model has been accomplished, as there were a lot of challenges: programming was an unfamiliar task for me before I came to the Netherlands, and performing fundamental research seemed like a toilsome effort. At the end of writing this thesis, I would like to express my appreciations to those who have helped and supported me, and especially to people who have changed me.

First of all, my most profound gratitude goes to my promotor, Prof. Jan Rots, who gave me the chance to start and continue my PhD career. I will be forever grateful for his help, patient guidance, encouragement and persistent support, which motivated me to finish this thesis. This thesis is my present for him in honor of his achievements on the occasion of his 60th birthday. ISLA (incremental sequentially linear analysis) in this thesis inherits Jan's "children": the smeared crack model and SLA (sequentially linear analysis). In addition, he shared his knowledge and experience of fracture mechanics, structural mechanics and computational mechanics with me. Apart from the academic help, Jan has taught me how to present my work and to communicate with others. With his guidance on how to catch the common interests amongst researchers, ISLA is better presented in the academic society. Also, I feel really grateful that he provided me with a research position and shared his network with me after my PhD project. I will never forget that he worked in the evening to give me comments on papers and the thesis and to write a reference letter. Personally, I admire his courage to shoulder the responsibilities of initializing seismic research in the Netherlands.

Meanwhile, my deep and special appreciation extends to my copromotor Dr. Pierre Hoogenboom for his suggestions, patient guidance, help and continuous support throughout my research and my personal life. He has spent a lot of time on helping me to present my work from the perspective of readers and checking my

grammar mistakes patiently. Moreover, I can always get academic inspirations from the talks with him. It provided me with a brand-new point of view, which is significant to push the boundaries of research. Besides, I will always remember that he helped me a lot on Dutch daily life. He has used much of his personal time to read the Dutch letters and make a phone call in Dutch, even though this is not his duty at all. The most important thing he has taught me is to hold the bottom line for research and not to lose faith or integrity due to reputation or money.

I would particularly like to acknowledge Prof. Bert Sluys, Prof. Max Hendriks and Dr. Yuguang Yang, who were not my copromotors or supervisors, for all their help during my research. I was an impolite person who always knocked on their doors and tried asking a question or a lot of questions without appointment, but each of them treated me politely and answered my questions patiently. I had quite a few meetings and talks with Bert. I have learned plenty about geometrical non-linearity, transient non-linearity, searching paths, solution objectivity, multiscale schemes and other ISLA related methods from Bert. I have received a large amount of information about fracture models, structural modeling and use of DIANA FEA from Max. Yuguang has also taught me a lot about concrete behavior and experimental research especially on shear retention.

I am really indebted to my doctoral committee members, Prof. dr. T. Jefferson, Prof. ir. S.N.M. Wijte, Dr. J. Alfaiaate, Prof. dr. ing. habil. J. Ozbolt, Prof. dr. ir. L. J. Sluys and Prof. dr. ir. Z. Li, for taking the time and effort to carefully review my work and attend my PhD defense.

Many thanks go to my current and former colleagues in TU Delft. I appreciate all the help and the cheerful memories with the colleagues from Structural mechanics group, namely Anneke Meijer, Jaap Meijer, Manimaran Pari, Rita Esposito, Francesco Messali, Samira Jafari, Arthur Slobbe, Anindya Roy, Qingpeng Li, Yi Xia, Meng Gao, Langzi Chang, Michele Longo, Marianthi Sousamli, Edwin Meulman, Paul Korswagen Eguren, Roel Schipper, Lucia Licciardello and Suman Bhattacharai. Anneke was proactive to help me, taking my problems seriously, nevertheless humbling to tell me what she has done. A special gratitude goes to Mani, Rita, Francesco, Samira and Arthur for their great help on my research. Appreciation goes to the colleagues of the Computational mechanics group such as Frans van der Meer, Jaap Weerheijm, Yaolu Liu, Kai Li, Mingzhao Zhuo, Liting Qiu, Yueye Caoyang, Jitang Fan,

Erik Simons, Lars Voormeeren, Tiziano li Piani, Fanxiang Xu, Zheng Yang, Lu Ke, Dongyu Liu, Mohsen Goudarzi, Richard Dekker and Ali Paknahad. Special thanks go to Yaolu Liu, Frans van der Meer, Jaap Weerheijm, Erik Simons, Fanxiang Xu and Mingzhao Zhuo for advancing my research. I would like to express my appreciations to the colleagues from Dynamic group including Prof. Andrei Metrikine, Tao Lv, Mingjuan Zhao, Yang Qu, Yaxi Peng and Andrei Faragau, from whom I have learned a lot about dynamic mechanics. I also feel fortunate to know Prof. Erik Schlangen, Guang Ye, Branko Savija, Zhiwei Qian, Xu Ma, Shizhe Zhang, Xuliang Hou, Shi Xu, Hongzhi Zhang, Wenjuan Lv, Xiaowei Ouyang, Yu Chen, Zhuqing Yu, Dong Hua, Jiayi Chen, Tianshi Lu and Hao Huang of the Microlab. Special thanks go to Erik, Branko, Zhiwei Qian, Xu Ma and Hongzhi Zhang who share their knowledge about the lattice model. I feel glad that Prof. Cheng Su, Prof. Jing Ji, Dr. Qingjun Chen and Dr. Zhiliang Zuo from South China University of Technology, where I have finished my Msc study, have visited here to refresh our old memories and build new memories. The conference experience is also unforgettable. I cherish these memories with Jan, Bert, Erik, Jaap, Mani, Branko, Tiziano, Xu Ma and Hongzhi Zhang.

Appreciations go to the colleagues from DIANA FEA. First, I would like to express my deepest appreciation to Gerd-Jan Schreppers who offered me a position, feels interested in ISLA and wrote a reference letter for me. In particular, I would like to acknowledge Gerd-Jan, Wijtze Peter Kikstra, Jos Jansen, Manimaran Pari, Evangelos Goulas, Panos Evangelou, Angelo Garofano, Anne van de Graaf and Kesio Palacio for their academic help. I really appreciate that Gerd-Jan, Wijtze Pieter, Jos, Mani, Panos and Tanvir Rahman have spent time on my method. I would also like to express special gratitude to Jan Kortschot who gave me lots of help and funny moments. Thanks also go to the other colleagues: Ab van den Bos, Wouter, Sander van den Broek, Arno Wolthers, Lisa Biddlecombe, Yonhyeon Bae, William, Boyuan Yang, Hee-Jeong Kang, Maziar Partovi, Michel van Batenburg, Jantine van Steenbergen-Hubert, Sascha van Vliet, Emile van Varsseveld, Xander Burgerhout, Martijn Aarden, Pim van der Aa, Andreas Buykx and Chantal Frissen for the lunch time, cake time, coffee break and all the great moments that we shared. It would be my great pleasure if ISLA can be implemented into DIANA FEA.

I feel really grateful for all enjoyable memories and great help from Bin Hu, Yuguang Yang, Chong Li, Ye Fan, Xiangyu Zheng, Xu Ma, Lei Zhang, Ziyong Yi, Tao

Lv, Mingjuan Zhao, Yang Qu, Zhen Yang, Lin Xiao, Shizhe Zhang, Xun Gong, Fei Yan, Peiyao Luo, Jiakun Gong, Xinyuan Mao and Lizuo Xin. I also feel appreciated and pleased to travel with Chong Li, Ye Fan, Xiangyu Zheng, Xu Ma, Lei Zhang and Fei Yan. I cannot enjoy my colorful life in the Netherlands without them. I also feel lucky to know other friends and colleagues including Anqi Fu, Yue Dai, Fengqiao Zhang, Tianxiang Wang, Hong Zhang, Haopeng Wang, Tianchi Tang, Silong Luo, Long Wu, Qingqing Ye, Bowei Huang, Xiangming Liu, Xin Tian, Hengqian Yi, Xiangyun Deng, Chengcheng Du, Zhe Hou, Jiawei Lai, Nan Lin, Ding Luo, Yang Lv, Yunyao Luo, Na Chen, Yanxin Tan, Boyuan Shi, Qu Wang, Xialu Wang, Xiangrong Wang, Lizuo Xin, Yu Xin, Tianqi Xu, Boyuan Yang, Hao Yang, Kaiyue Yang, Chi Zhang, Weiyuan Zhang, Shiwei Bao, Juanjuan Cai, Jia Xu, Jieying Ding, Zhijie Li, Xiaoling Liu, Hongde Luo, Qi Wang, Zihong Xie, Mengshi Yang, Yipei Zeng, Xin Zhang, Debo Zhao, Min Zhi, Nan Zhong, Ye Zhou, Shuai Yi, Yuanxing Xu, Yinrong Wen, Xiaolu Sun, Keran Rong, Xueli Jia, Xu Gao, Ying Dai, Xuecan Cui, Xin Chen, Hai Gong, Yuming He, Qian Liu, Yuling Li and Yang Li.

Last but not least, I would like to express my deepest gratitude and love to my parents for their unconditional love, unconditional support, unconditional patience, unconditional understanding and unconditional encouragement through my whole life. Many thanks go to my grandpa, my granduncles, my grandaunts, my aunts, my uncles, my sister, my brother and all relatives for their great love and support. Special appreciation goes to my girlfriend Quanxin Jiang for her love, patient understanding and continuous support especially in the dark period of my life. Love you forever!

爸爸妈妈，感谢你们对我的无条件付出，我永远爱你们，我会尽我所能孝顺你们！

# A

## EXTENSION OF ISLA TO PROPORTIONAL CYCLIC LOADING FOR BRITTLE MATERIALS

ISLA employs the smeared crack model with the secant stiffness. At the local level, an elastic material model is used to ensure computational robustness. This behaviour is realistic for the tensile unloading of brittle materials. However, it is unrealistic to continue to follow the secant stiffness when the loading state switches from tensile unloading to compressive loading for the cyclic loading. Normally, a damage-plastic model is used for the cyclic loading, but the robustness issue remains[83]. In this chapter, two damage models, namely the correlative damage model and the correlative-independent damage model, are proposed to consider the stiffness change of the loading state switch in the cyclic loading. Although these two models still follow the secant stiffness for unloading, they are simple, robust and realistic for the cyclic loading of brittle materials with the tensile failure due to the elastic compressive behaviour used in FEM models.

This chapter merely shows the possibilities of ISLA for cyclic loading. Only proportional loading is considered to avoid iterations, so the transition of tension and

compression of all elements is the moment when the load factor is zero at the global level. If non-proportional loading is considered, iterations are necessary to determine the transition of tension and compression at the local level with iterations, which may induce difficulties when determining the proper stiffness of each element.

## MATERIAL MODEL

In both damage models, the secant stiffness is reduced for loading when  $\mu$  is larger than 1. The secant stiffness is followed for both tensile and compressive unloading, which is the same as the standard damage model. Nevertheless, the stiffness is changed when the loading state switches from tension to compression, or vice versa. Two stiffnesses are considered for each element, namely  $d^t D_0^{el}$  for the tensile stiffness and  $d^c D_0^{el}$  for the compressive stiffness, instead of one stiffness  $d D_0^{el}$  in the standard damage model of ISLA, where  $D_0^{el}$  is the initial (undamaged) elastic stiffness of the material and  $d$  is the scalar stiffness degradation variable for the isotropic damage model, the value of which is between 0 and 1. For the orthotropic damage model,  $d$  is the tensor stiffness degradation variable based on the principal directions of the rotating smeared crack model or the fixed smeared crack model, which can be computed by

$$d = [T]^{-1} (E_n / E_0) [R] \quad (\text{A.1})$$

where  $[T]$  is the rotation matrix of the strain tensor to the principal directions,  $[R]$  is the rotation matrix of the stress tensor to the principal directions,  $E_n$  is the Young's modulus of the maximum principal direction for tensile failure or the minimum principal direction for compressive failure, and  $E_0$  is the initial Young's modulus (Section 3.6).

In the correlative damage model, the stiffness is changed by a certain function related to the previous stiffness when the loading state switches. The stiffness degradation variables in the correlative damage model are

$$d_n^t = f(d_{n-1}^c) \quad (\text{A.2})$$

$$d_m^c = g(d_{m-1}^t) \quad (\text{A.3})$$

where  $n$  is a load step in which the loading state switches from the previous compressive unloading to the current tensile loading and  $m$  is a load step in which the

loading state switches from the previous tensile unloading to the current compressive loading.  $f(\cdot)$  and  $g(\cdot)$  are two functions to describe the stiffness change due to the loading state switch and are explained in the next section.

In the correlative-independent damage model, the damage to compression is independent, while the damage to tension is influenced by both tension and compression. The stiffness degradation variables in the correlative-independent damage model are

$$d_n^t = \min(d_{n'}^t, d_{n-1}^c) \quad (\text{A.4})$$

$$d_m^c = d_{m'}^c \quad (\text{A.5})$$

where  $n'$  is the last load step of the tensile loading before  $n$  and  $m'$  is the last load step of the compressive loading before  $m$ .

Figures A.1 and A.2 show different loading paths of the original damage model, the correlative damage model and the correlative-independent damage model when the loading state switches. In Figure A.1, all models follow the secant stiffness for tensile unloading. The stiffness recovers to the initial stiffness in the correlative-independent damage model and to the value between the secant stiffness and initial stiffness in the correlative damage model while the compressive loading still follows the secant stiffness in the original damage model. In Figure A.2, all models also follow the secant stiffness for compressive unloading, which indeed is unrealistic. However, it is realistic for brittle materials if there is no compressive damage. The stiffness follows the secant stiffness for the tensile loading in the original damage model and the correlative-independent damage model while the stiffness is reduced in the correlative damage model. Note that if the secant stiffness of the last tensile load step is smaller than the secant stiffness of the last compressive load step, the stiffness follows the secant stiffness of the last tensile load step in the correlative-independent damage model.

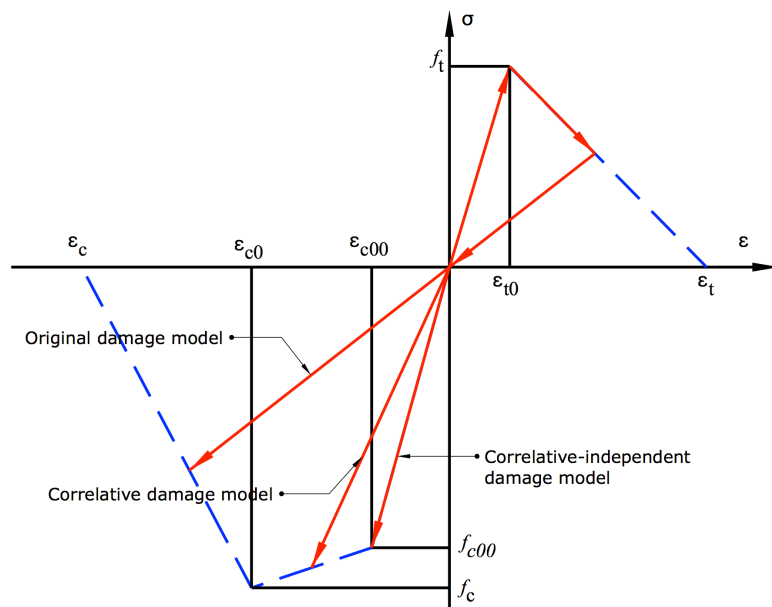


Figure A.1: Different compressive loading paths of the original damage model, the correlative damage model and the correlative-independent damage model when the loading state switches from tension to compression

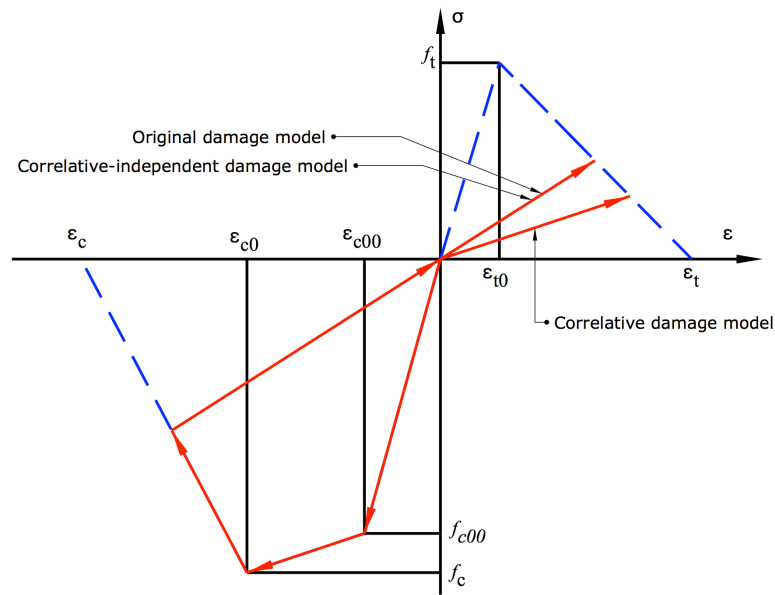


Figure A.2: Different tensile loading paths of the original damage model, the correlative damage model and the correlative-independent damage model when the loading state switches from compression to tension

## FUNCTION STUDY FOR THE CORRELATIVE DAMAGE MODEL

In correlative damage model, the stiffness is changed by a certain function related to the previous stiffness when the loading state switches. Therefore, the damage due to the loading of the other direction is considered in this model. For instance, the stiffness is reduced to consider the influence of the compressive damage to tensile loading when the loading state of the certain element changes from compression to tension. Permanent strain is still ignored owing to the limitation of the damage model. Nevertheless, the correlative damage model is realistic and applicable for tensile failure of concrete and masonry.

The second-order polynomial function ( $y = ax^2 + bx + c$ ) is used to describe the stiffness change.

$$d_n^t = f(d_{n-1}^c) = a(d_{n-1}^c)^2 + b(d_{n-1}^c) + c \quad (\text{A.6})$$

where  $f(0) = 0$  and  $f(1) = 1$

$$d_m^c = g(d_{m-1}^t) = a(d_{m-1}^t)^2 + b(d_{m-1}^t) + c \quad (\text{A.7})$$

where  $g(0) = 0$  and  $g(1) = 1$ , so for both function  $f(\cdot)$  and  $g(\cdot)$

$$c = 0$$

$$a + b = 1$$

When the loading state switches from compression to tension, the stiffness should decrease monotonically and sharply, which means

$$-\frac{b}{2a} \leq 0$$

$$a \geq 0$$

So

$$0 \leq a \leq 1$$

The function can be defined as

$$d_n^t = f(d_{n-1}^c) = (d_{n-1}^c)^2 \quad (\text{A.8})$$

When the loading state switches from tension to compression, the stiffness should monotonically and dramatically increase, which means

$$-\frac{b}{2a} \geq 1$$

$$\alpha \leq 0$$

So

$$-1 \leq \alpha \leq 0$$

The function can be defined as

$$d_m^c = g(d_{m-1}^t) = -(d_{m-1}^t)^2 + 2(d_{m-1}^t) \quad (\text{A.9})$$

A more realistic way is to regress from the experiment results.

Similarly, the function  $f(\cdot)$  for the stiffness change from compression to tension can be also defined by higher-order polynomial functions. When the function is, for example  $d_n^t = f(d_{n-1}^c) = (d_{n-1}^c)^4$ , the tensile stiffness drops faster due to the compressive damage.

Importantly, when one function is defined, whether it is from tension to compression or the other way around, the other function is determined, which actually **must be the inverse function**. For example, when the loading state switches from tension to compression, the stiffness increases. However, when the loading state switches back to tension again without compressive damage, the tensile stiffness should be the same as the previous tensile stiffness. Two groups of inverse functions are tested in the next section.

Firstly, if the stiffness change function  $g(\cdot)$  (from tension to compression) is

$$d_m^c = g(d_{m-1}^t) = -(d_{m-1}^t)^2 + 2(d_{m-1}^t) \quad (\text{A.10})$$

the stiffness change function  $f(\cdot)$  (from compression to tension) is

$$d_n^t = f(d_{n-1}^c) = 1 - \sqrt{1 - (d_{n-1}^c)} \quad (\text{A.11})$$

Secondly, if the stiffness change function  $f(\cdot)$  (from compression to tension) is

$$d_n^t = f(d_{n-1}^c) = (d_{n-1}^c)^4 \quad (\text{A.12})$$

the stiffness change function from tension to compression is

$$d_m^c = g(d_{m-1}^t) = (d_{m-1}^t)^{1/4} \quad (\text{A.13})$$

## UNIAXIAL TEST FOR CONCRETE

All damage models are tested with the identical FEM model in Section 6.4 for the cyclic loading test. Apart from the same tensile behaviour, the non-linear compressive behaviour is considered with strength of -14.3 MPa and ultimate strain of -0.01 (Figure A.3). The loading schedule of the nodal imposed displacement is shown in Figure A.4, the exact displacement factors of which are shown in Table A.1.

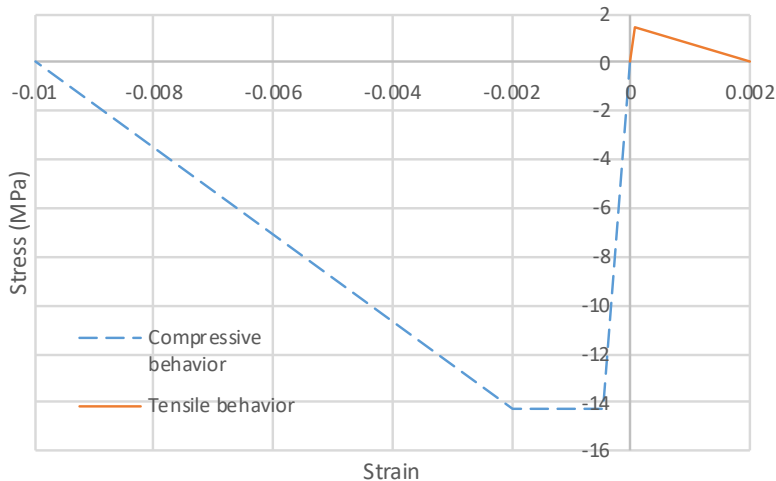


Figure A.3: Concrete tensile and compressive material model

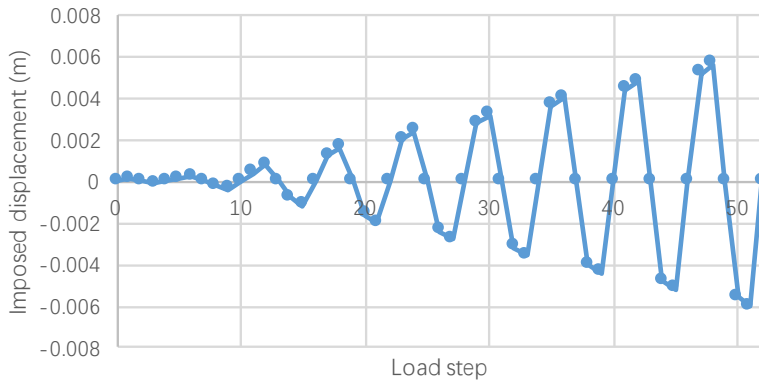


Figure A.4: Loading schedule a (imposed displacement)

Initially, the original damage model is tested for comparison. The stress-strain curve for the cyclic analysis is shown in Figure A.5. It can be seen that the tensile

Load step	1	2	3	4	5	6	7	8	9	10	11	12	13	14	15
Imposed displacement (m)	0.0001	0	-0.0001	0	0.0001	0.0002	0	-0.0002	-0.0004	0	0.0004	0.0008	0	-0.0008	-0.0012
Load step	16	17	18	19	20	21	22	23	24	25	26	27	28	29	30
Imposed displacement (m)	0	0.0012	0.0016	0	-0.0016	-0.002	0	0.002	0.0024	0	-0.0024	-0.0028	0	0.0028	0.0032
Load step	31	32	33	34	35	36	37	38	39	40	41	42	43	44	45
Imposed displacement (m)	0	-0.0032	-0.0036	0	0.0036	0.004	0	-0.004	-0.0044	0	0.0044	0.0048	0	-0.0048	-0.0052
Load step	46	47	48	49	50	51	52								
Imposed displacement (m)	0	0.0052	0.0056	0	-0.0056	-0.006	0								

Table A.1: The exact values of imposed displacements

stress and strain align well with the linear softening behaviour of 1.43 MPa tensile strength and 0.002 ultimate strain while the stiffness for compressive loading follows the secant stiffness of the previous tensile load step. Due to large load steps, the stress-strain curve is discontinuous. However, it can be continuous by post-scaling to include the results of cycles when the utilisation function is larger than 1 (Figure A.6), which is allowed because of the proportional static analysis. It also indicates how overshot results get corrected cycle-by-cycle to compare the curves with and without post-scaling. For compressive loading, there is no further damage from compression due to the tension damage. Compressive loading and unloading follow the secant stiffness of the previous tensile load step. As for non-proportional analysis, post-scaling cannot be performed. Sufficient numbers of load steps are required to obtain a continuous curve.

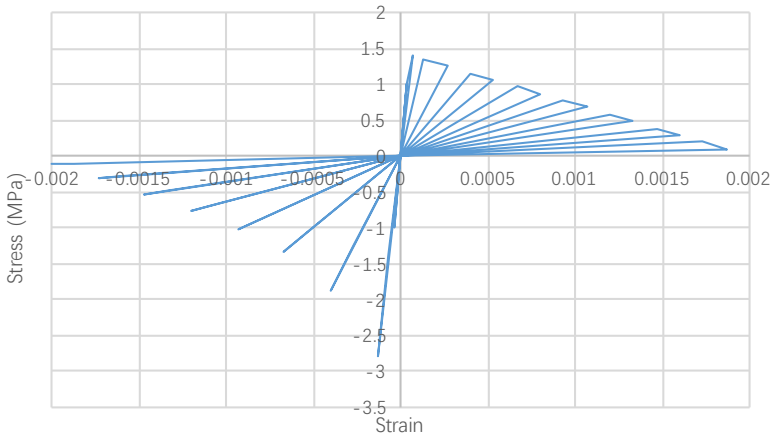


Figure A.5: Stress-strain curve for concrete cyclic analysis

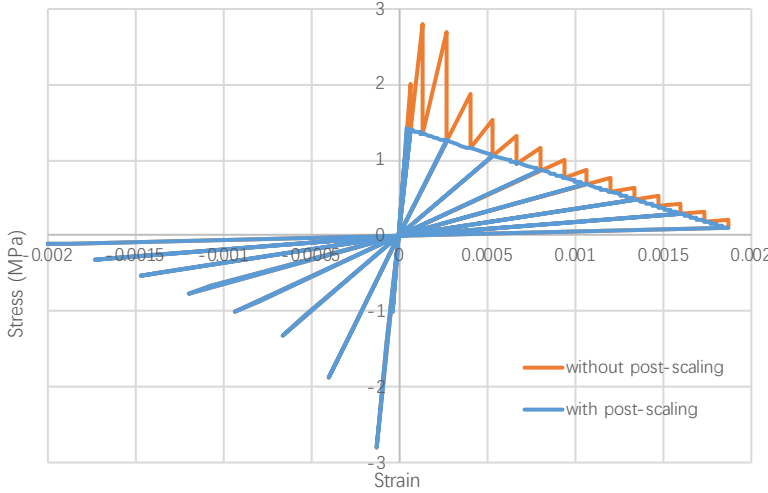


Figure A.6: Stress-strain curves for concrete cyclic analysis, including all cycle results with and without post-scaling

## CORRELATIVE DAMAGE MODEL

In the correlative damage model, the stiffness is changed by a certain function related to the previous stiffness when the loading state switches. Two groups of functions are used for testing. Group one is Eq. (A.10) and Eq. (A.11). Group two is Eq. (A.12) and Eq. (A.13).

### GROUP ONE OF THE INVERSE FUNCTIONS

Figure A.7 shows the stress-strain curve for the same loading schedule, which indicates that there is no further compressive damage after the stiffness recovers from the previous tensile loading. The tensile curve is continuous since there is no compressive damage. To be exact, the tensile stiffness changes back to that of the previous tensile load step shown in Table A.2, in which the results of only the first and last cycles are outputted after load step 10 and the results of load steps from 27 to 50 are hidden. Moreover, compressive stiffness is larger than the previous tensile stiffness due to triggering of the recovery function. In addition, the initial stiffness remains if there is no damage when the loading state switches.

The reason why the structure cannot go to a compressive damage state is that the capacity of concrete for compression is much higher than that of tension. Even though the stiffness is increased, the stress cannot exceed the strength of the current compressive stiffness when concrete is pulled to the same displacement value for

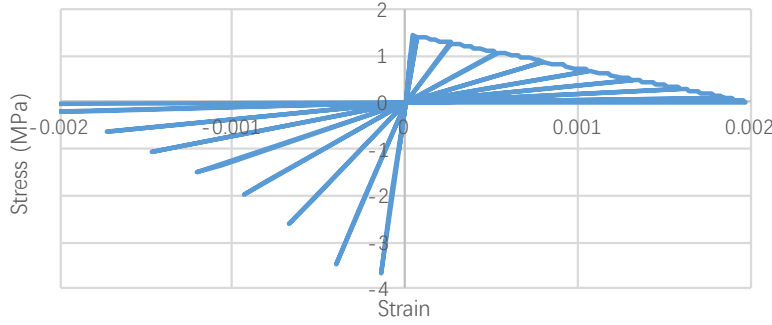


Figure A.7: Stress-strain curve of the correlative damage model (Group one), including all cycle results with scaling procedure for the loading schedule b

Load step	1	2	3	4	5	6	6	6	6	6
Load state	tension	tension	compression	compression	tension	tension	tension	tension	tension	tension
Stress	1	0	-1	0	1	1.42959257	1.42630745	1.42230026	1.41690962	1.41650638
Strain	3.3333E-05	0	-3.333E-05	0	3.3333E-05	4.7653E-05	5.2826E-05	5.8531E-05	6.4788E-05	6.5424E-05
Stiffness	30000.3	30000.3	30000.3	30000.3	30000.3	29999.85	26999.865	24299.8785	21869.8907	21651.1917
Load step	6	6	7	8	9	10	11	11	12	12
Load state	tension	tension	tension	compression	compression	compression	tension	tension	tension	tension
Stress	1.41623984	1.414696	0	-1.82871	-3.657419	0	1.41611211	1.359878	1.36671206	1.262215
Strain	6.6072E-05	6.6667E-05	0	-6.667E-05	-0.0001333	0	6.6733E-05	0.00013333	0.000134	0.00026667
Stiffness	21434.6828	21220.3339	21220.3339	27430.5128	27430.7111	27430.7111	21220.4931	10199.1105	10199.076	4733.30033
Load step	13	14	15	16	17	17	18	18	19	20
Load state	tension	compression	compression	compression	tension	tension	tension	tension	compression	
Stress	0	-2.325281	-3.487922	0	1.26898257	1.169515	1.17156499	1.070245	0	-2.068901
Strain	0	-0.0002667	-0.0004	0	0.0002681	0.0004	0.0004007	0.00053333	0	-0.0005333
Stiffness	4733.30033	8719.79285	8719.805	8719.805	4733.305	2923.7875	2923.7887	2006.71063	2006.71063	3879.1918
Load step	21	22	23	23	24	24	25	26	...	...
Load state	compression	compression	tension	tension	tension	tension	tension	compression	...	...
Stress	-2.586126	0	1.07281957	0.970209	0.97426862	0.870188	0	-1.708825	...	...
Strain	-0.0006667	0	0.00053462	0.00066667	0.00066946	0.0008	0	-0.0008	...	...
Stiffness	3879.18706	3879.18706	2006.708	1455.31277	1455.31375	1087.735	1087.735	2136.03125	...	...
Load step	51	52	53	53	54	55	56	57	58	59
Load state	compression	compression	tension	tension	tension	compression	compression	compression	compression	compression
Stress	-0.209086	0	0.09770433	0.012199	0	-0.041002	-0.057403	-0.073804	-0.09204	-0.106605
Strain	-0.002	0	0.00186755	0.00198333	0	-0.0033333	-0.0046667	-0.006	-0.0073333	-0.0086667
Stiffness	104.543	104.543	52.3169836	6.15075734	6.15075734	12.3006012	12.300642	12.3006667	12.300546	12.3005764
Load step	60	60								
Load state	compression	compression								
Stress	-0.12219	-0.029769								
Strain	-0.0099337	-0.0099833								
Stiffness	12.3006014	2.98186988								

Table A.2: Stiffness change procedures for the correlative damage model (Group one)

pushing. Therefore, a new loading schedule is applied to the structure, in which the compressive imposed displacements are exaggerated, as shown in Figure A.8. Meanwhile, apart from changing the loading schedule, the compressive stress may overpass the strength by following Group two of functions to dramatically recover the stiffness from tension to compression.



Figure A.8: Loading schedule b for concrete compressive failure test with increased imposed compressive displacement

Figures A.9 and A.10 show the stress-strain curves of the correlative damage model for loading schedule b, which align well with the material properties. It can be seen that the curves of both tensile and compressive parts are discontinuous because damages occur in both loading states. As a matter of fact, the stiffness cannot be fully recovered when the structure is damaged in the opposite loading. Table A.3 shows parts of stiffness change procedures, in which the results of only the first and the last cycles are outputted after load step 10 and the results of load steps from 22 to 41 are hidden. For both tension and compression, the stiffness is lower than the value of the previous load step, which has the same loading state because of damage from the opposite loading. Meanwhile, the tensile stiffness is smaller than the previous compressive value while the compressive stiffness is larger than the previous tensile value. In addition, the stiffness remains unchanged if there is no damage from the opposite loading.

#### GROUP TWO OF THE INVERSE FUNCTIONS

When loading schedule b (Figure A.8) is applied, Figure A.11 shows the stress-strain curve for the correlative damage model (Group 2). The enlargement results

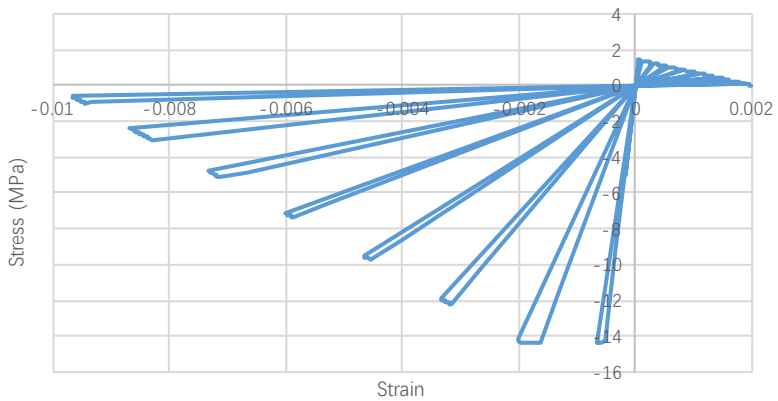


Figure A.9: Stress-strain curve of the correlative damage model (Group one), including all cycle results with the scaling procedure for the loading schedule b

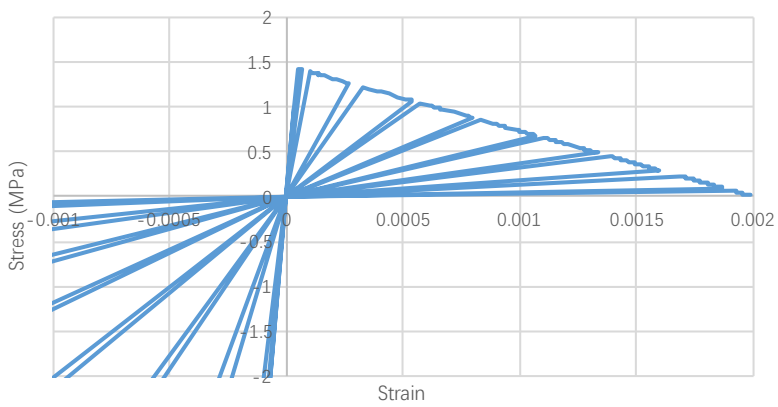


Figure A.10: Enlargement results of tension part for Figure A.9

	1	2	3	4	5	6	6	6	6	6
tension	tension	compression	compression	tension						
1.00	0.00	-5.00	0.00	1.00	1.43	1.43	1.42	1.42	1.42	1.42
3.33E-05	0.00E+00	-1.67E-04	0.00E+00	3.33E-05	4.77E-05	5.28E-05	5.85E-05	6.48E-05	6.54E-05	
30000.30	30000.30	29999.94	29999.94	30000.30	29999.85	26999.87	24299.88	21869.89	21651.19	
	6	6	7	8	9	9	9	9	9	9
tension	tension	tension	compression							
1.42	1.41	0.00	-9.14	-14.31	-14.31	-14.31	-14.31	-14.30	-14.32	
6.61E-05	6.67E-05	0.00E+00	-3.33E-04	-5.22E-04	-5.80E-04	-6.44E-04	-6.50E-04	-6.57E-04	-6.64E-04	
21434.68	21220.33	21220.33	27430.67	27430.63	24687.57	22218.81	21996.62	21776.66	21558.89	
	9	10	11	11	12	12	13	14	15	15
compression	compression	tension	tension	tension	tension	tension	compression	compression	compression	compression
-14.23	0.00	1.39	1.36	1.37	1.26	0.00	-11.60	-14.32	-14.16	
-6.67E-04	0.00E+00	1.00E-04	1.33E-04	1.34E-04	2.67E-04	0.00E+00	-1.33E-03	-1.65E-03	-2.00E-03	
21343.30	21343.30	13884.81	10171.31	10171.27	4720.39	4720.39	8698.06	8698.06	7079.73	
	16	17	17	18	18	19	20	21	21	...
compression	tension	tension	tension	tension	tension	compression	compression	compression	compression	...
0.00	1.23	1.16	1.17	1.07	0.00	-10.30	-12.22	-11.88	-11.88	...
0.00E+00	3.25E-04	4.00E-04	4.02E-04	5.33E-04	0.00E+00	-2.67E-03	-3.17E-03	-3.33E-03	-3.33E-03	...
7079.73	3777.72	2909.99	2909.99	1997.24	1997.24	3861.51	3861.51	3563.19	3563.19	...
	42	42	43	44	45	45	46	47	47	48
tension	tension	tension	compression	compression	compression	compression	tension	tension	tension	
0.39	0.29	0.00	-2.90	-3.01	-2.37	0.00	0.23	0.19	0.19	
1.47E-03	1.60E-03	0.00E+00	-8.00E-03	-8.31E-03	-8.67E-03	0.00E+00	1.68E-03	1.73E-03	1.73E-03	
263.82	181.89	181.89	362.68	362.68	273.72	273.72	137.18	112.20	112.20	
	48	49	50	51	51	52	53	53		
tension	tension	compression	compression	compression	compression	tension	tension			
0.10	0.00	-0.97	-0.99	-0.59	0.00	0.06	0.01			
1.87E-03	0.00E+00	-9.33E-03	-9.45E-03	-9.67E-03	0.00E+00	1.92E-03	1.98E-03			
52.27	52.27	104.45	104.45	61.32	61.32	30.67	6.14			

Table A.3: Stiffness change procedures of the correlative damage model (Group one) for loading schedule b

for the tensile loading part are shown in Figure A.12. Compared to the curve in Figure A.9, the compressive loading cycles are continuous rather than discontinuous while the gaps between the tensile loading cycles become larger and there is no damage in several tensile loading cycles. Table A.4 shows the stiffness change procedure for the correlative damage model (Group 2). Even though the tensile stiffness is damaged to 4,708 MPa in load step 12, the initial compressive stiffness recovers to 18883 MPa in load step 14, which is close to the last compressive stiffness (21,353 MPa) in load step 9. On the other hand, the initial tensile stiffness is damaged to 85 MPa in load step 17 from the last tensile stiffness (4,708 MPa) in load step 12 due to the compressive damage in load steps 14 and 15, which causes no damage in load steps 17 and 18.

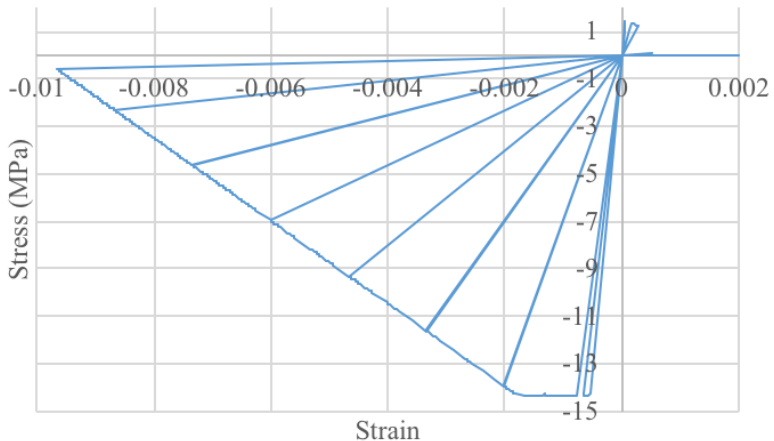


Figure A.11: Stress-strain curve of the correlative damage model (Group two), including all cycle results with scaling procedure for the loading schedule c

### CORRELATIVE-INDEPENDENT DAMAGE MODEL

In the correlative-independent damage model, the tensile damage has no influence on compressive loading, which means the stiffness fully recovers to the value of the last compressive loading state when the loading state switches from tension to compression. On the other hand, there is no recovery and there even be further damage when the loading state switches from compression to tension, which means the tensile stiffness is the minimum value of the previous compres-

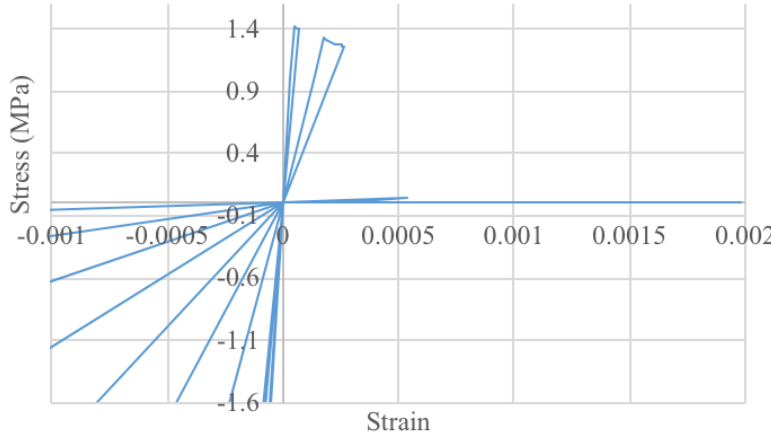


Figure A.12: Enlargement results of the tension part for Figure A.11

Load step	1	2	3	4	5	6	6	6	6
Load state	tension	tension	compression	compression	tension	tension	tension	tension	tension
Stress	1	0	-5	0	1	1.41643059	1.41287284	1.40869565	1.40462428
Strain	3.3333E-05	0	-0.0001667	0	3.3333E-05	4.7215E-05	5.2329E-05	5.7971E-05	6.4226E-05
Stiffness	30000.3	30000.3	29999.94	29999.94	30000.3	29999.85	26999.865	24299.8785	21869.8907
Load step	6	6	6	7	8	9	9	9	9
Load state	tension	tension	tension	tension	compression	compression	compression	compression	compression
Stress	1.40371906	1.40346825	1.400549	0	-9.147809	-14.304627	-14.30587	-14.318309	-14.31342
Strain	6.5488E-05	6.6138E-05	6.6667E-05	0	-0.0003333	-0.005212	-0.0005792	-0.006441	-0.0006504
Stiffness	21434.6828	21220.3339	21008.13	21008.13	27443.4544	27443.4133	24699.0717	22229.1639	22006.873
Load step	9	9	10	11	12	12	13	14	14
Load state	compression	compression	compression	tension	tension	tension	tension	compression	compression
Stress	-14.307759	-14.235505	0	1.026671	1.32559264	1.255677	0	-14.313345	-14.281055
Strain	-0.0006634	-0.0006667	0	0.00013333	0.00017215	0.00026667	0	-0.000758	-0.0013333
Stiffness	21568.9362	21353.2468	21353.2468	7700.05175	7700.02662	4708.78286	4708.78286	18882.8845	10710.7939
Load step	15	16	17	18	19	20	20	21	21
Load state	compression	compression	tension	tension	tension	compression	compression	compression	compression
Stress	-13.842082	0	0.033992	0.045323	0	-13.939659	-12.795099	-12.805343	-11.599141
Strain	-0.002	0	0.0004	0.00053333	0	-0.0020141	-0.0026667	-0.0026688	-0.0033333
Stiffness	6921.041	6921.041	84.98	84.9806781	84.9806781	6921.04001	4798.16153	4798.16268	3479.74265
Load step	23	24	25	26	26	27	27	28	29
Load state	tension	tension	tension	compression	compression	compression	compression	tension	tension
Stress	0.00362	0.004344	0	-11.628211	-10.40336	-10.445141	-9.300923	0	0.000545
Strain	0.0006667	0.0008	0	-0.0033417	-0.004	-0.0040161	-0.0046667	0	0.00093333
Stiffness	5.42999729	5.43	5.43	3479.74225	2600.84	2600.84	2600.83996	1993.05479	1993.05479
Load step	31	32	32	33	33	34	35	36	37
Load state	tension	compression	compression	compression	compression	compression	tension	tension	compression
Stress	0	-9.3079046	-8.14561	-8.1456107	-6.952115	0	0.00008	0.000089	0
Strain	0	-0.0046702	-0.0053333	-0.0053333	-0.006	0	0.0012	0.00133333	0
Stiffness	0.58406232	1993.05519	1527.30197	1527.302	1158.68583	1158.68583	0.06666667	0.06675002	0.06675002
Load step	38	39	39	40	41	42	43	44	44
Load state	compression	compression	compression	compression	tension	tension	tension	compression	compression
Stress	-5.801636	-5.8069154	-4.626679	0	0.00009	0.00009	0	-4.6347897	-3.479847
Strain	-0.0066667	-0.0066727	-0.0073333	0	0.00146667	0.0016	0	-0.0073462	-0.008
Stiffness	870.245356	870.245494	630.910801	630.910801	0.00613636	0.005625	0.005625	630.91075	434.980875
Load step	45	46	47	48	49	50	50	51	51
Load state	compression	compression	tension	tension	tension	compression	compression	compression	compression
Stress	-2.327081	0	0	0	0	-2.3269155	-1.155863	-1.1566609	-0.580604
Strain	-0.0086667	0	0.00173333	0.00186667	0	-0.008666	-0.0093333	-0.0093398	-0.0096667
Stiffness	268.509336	268.509336	0	0	0	268.509438	123.842469	123.842478	60.0624807

Table A.4: Stiffness change procedures of the correlative damage model (Group two) for the loading schedule c

sive and tensile stiffnesses.

When loading schedule b is applied (Figure A.8), Figure A.13 shows the stress-strain curve. When the loading state switches, no stiffness change is observed since the tensile stiffness is damaged faster than the compressive stiffness.

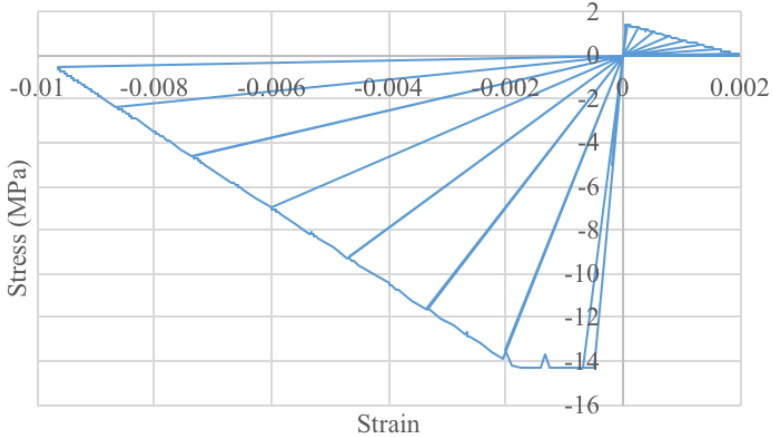


Figure A.13: Stress-strain curve of the correlative-independent damage model, including all cycle results with the scaling procedure for loading schedule b

In loading schedule c (Figure A.14), the imposed negative displacement is twice as large as that in loading schedule b (Figure A.8) for the same load step until the displacement increases to 0.0295 m to validate the compression damage to the tensile stiffness. Figure A.15 shows the stress-strain curve of the correlative-independent damage for loading schedule c, the enlargement results of which for the tensile loading part are shown in Figure A.16. It can be observed that the compressive loading part is continuous even though there are several cycles of tensile damage. For the tensile loading part, it can be seen that the results are discontinuous and even remain linear for several loading cycles. Table A.5 shows the detailed stiffness change procedure. Only the results of the first and the last cycles are shown after load step 12, and results after load step 31 are not displayed. The compressive stiffness recovers to the initial value in load step 8 although the tensile stiffness is damaged to 21,008 MPa in load step 6. On the other hand, the beginning tensile stiffness in load step 11 follows the final compressive stiffness in load step 9 rather than the stiffness of the last tensile loading step (load step 7). Similar phenomena can be observed in the subsequent load steps. For example, the initial compressive stiffness in load

step 14 (10,252 MPa) is the same as the last one in load step 9, and initial tensile stiffness (2,619 MPa) in load step 17 is the same as the compressive stiffness in load step 15 rather than the last tensile stiffness in load step 12. There is even no tensile damage due to the previous compressive damage in load steps 17, 23 and 24.

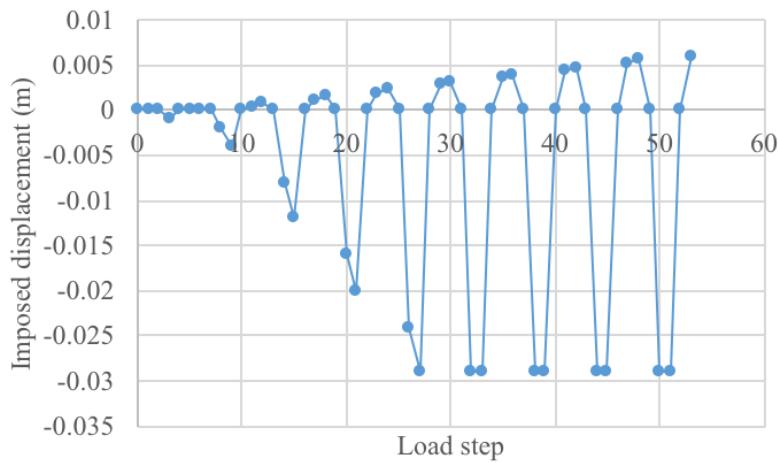


Figure A.14: Modified loading schedule d for concrete compressive failure test with increased imposed compressive displacement

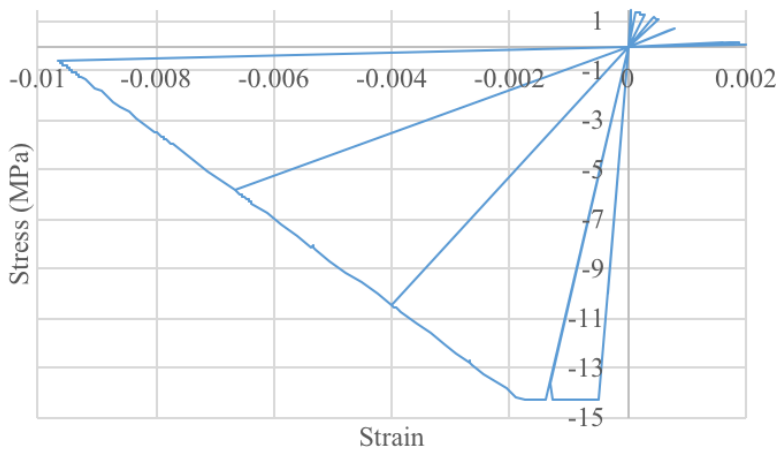


Figure A.15: Stress-strain curve of the correlative-independent damage model, including all cycle results with the scaling procedure for loading schedule d

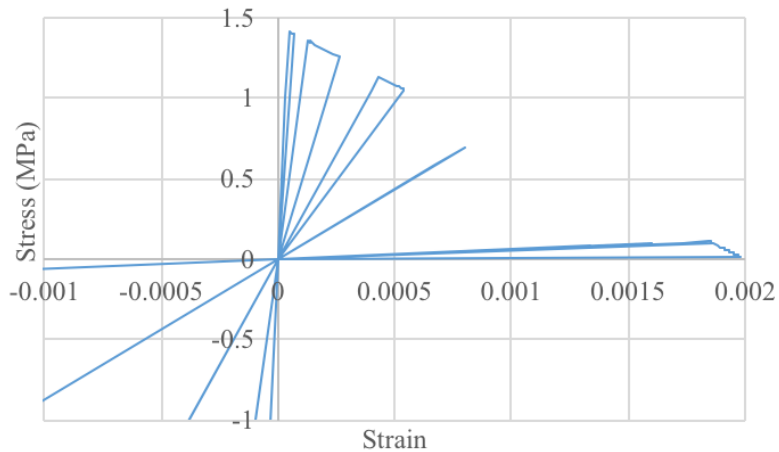


Figure A.16: Enlargement results of the tension part for Figure A.15

Load step	1	2	3	4	5	6	6	6	6	6
Load state	tension	tension	compression	compression	tension	tension	tension	tension	tension	tension
Stress	1	0	-10	0	1	1.41643059	1.41287284	1.40869565	1.40462428	1.40410506
Strain	3.3333E-05	0	-0.0003333	0	3.3333E-05	4.7215E-05	5.2329E-05	5.7971E-05	6.4226E-05	6.4851E-05
Stiffness	30000.3	30000.3	30000.3	30000.3	30000.3	29999.85	26999.865	24299.8785	21869.8907	21651.1917
Load step	6	6	6	7	8	8	8	8	8	8
Load state	tension	tension	tension	tension	compression	compression	compression	compression	compression	compression
Stress	1.40371906	1.40346825	1.400549	0	-14.306152	-14.306152	-14.308426	-14.310954	-14.308145	-14.305451
Strain	6.5488E-05	6.6138E-05	6.6667E-05	0	-0.0004769	-0.0004769	-0.0005299	-0.0005889	-0.0006542	-0.0006607
Stiffness	21434.6828	21220.3339	21008.13	21008.13	29999.85	29999.85	26999.865	24299.8785	21869.8907	21651.1917
Load step	8	9	9	9	9	9	9	9	9	10
Load state	compression									
Stress	-14.2899	-14.311317	-14.313689	-14.316388	-14.319313	-14.313893	-14.313825	-14.315174	-13.6696	0
Strain	-0.0006667	-0.0006677	-0.000742	-0.0008246	-0.0009164	-0.0010178	-0.0011309	-0.0012567	-0.0013333	0
Stiffness	21434.7428	21434.8286	19291.3232	17362.2434	15625.9891	14063.4352	12657.0316	11391.3285	10252.2256	10252.2256
Load step	11	11	12	12	12	12	12	12	12	12
Load state	tension									
Stress	1.35476611	1.353289	1.35396648	1.34432726	1.3327228	1.32156463	1.30861164	1.29409555	1.27856622	1.26174269
Strain	0.00013214	0.00013333	0.0001334	0.00014717	0.00016211	0.00017861	0.00019651	0.00021592	0.00023704	0.00025991
Stiffness	10252.2181	10149.6929	10149.6586	9134.69233	8221.22347	7399.10075	6659.18918	5993.27251	5393.94451	4854.54893
Load step	12	12	12	13	14	14	15	15	16	17
Load state	tension	tension	tension	tension	compression	compression	compression	compression	compression	tension
Stress	1.26017994	1.25871726	1.256099	0	-14.321215	-12.6879	-12.77302	-10.4746	0	1.047463
Strain	0.00026221	0.00026455	0.00026667	0	-0.0013969	-0.0026667	-0.0026846	-0.004	0	0.0004
Stiffness	4806.00524	4757.9453	4710.36536	4710.36536	10252.1872	4757.95655	4757.95	2618.65	2618.65	2618.6575
Load step	18	18	19	20	20	21	21	22	23	24
Load state	tension	tension	tension	compression	compression	compression	compression	compression	tension	tension
Stress	1.13638568	1.054409	0	-10.477269	-8.08277	-8.115261	-5.81699	0	0.581699	0.698038
Strain	0.00043396	0.00053333	0	-0.004001	-0.0053333	-0.0053548	-0.0066667	0	0.00066667	0.0008
Stiffness	2618.66039	1977.01811	1977.01811	2618.66414	1515.52032	1515.52424	872.548064	872.548064	872.548064	872.5475
Load step	25	26	26	27	27	28	29	30	31	...
Load state	tension	compression	compression	compression	compression	compression	tension	tension	tension	...
Stress	0	-5.8169833	-3.47448	-3.4783181	-0.57787	0	0.055794	0.063765	0	...
Strain	0	-0.0066667	-0.008	-0.0080088	-0.0096667	0	0.00093333	0.00106667	0	...
Stiffness	872.5475	872.5475	434.31	434.30985	59.7796346	59.7796346	59.7793071	59.7796688	59.7796688	...

Table A.5: Stiffness change procedures of the correlative-independent damage model for loading schedule d

## CYCLIC LOADING TEST FOR THE NOTCHED CONCRETE BEAM

The experiment by Hordijk [124] is used for testing and simply involves a supported concrete beam with a notch in the middle (Figure A.17). All the material properties are the same as in Section 4.5. The test setup is modified for the application of cyclic loading.

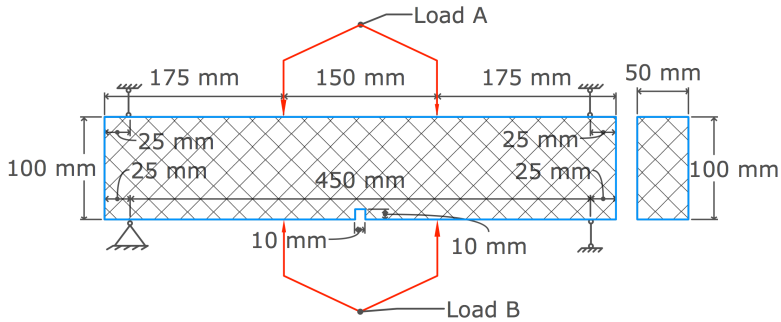


Figure A.17: Test model

The load schedule is shown in Figure A.18. The negative imposed displacements are applied at the position of Load A while the positive ones are added at the position of Load B. When the load is applied at either Load A or Load B, the previous load at the other position is removed. Therefore, two types of boundaries can be seen in Figure A.19.

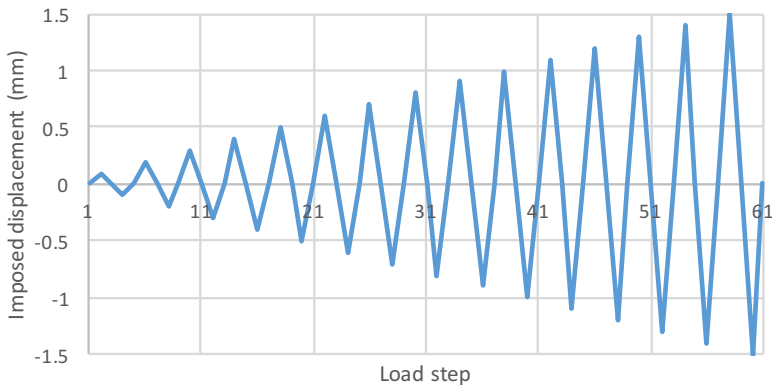


Figure A.18: Load schedule for the cyclic loading test of the notched beam

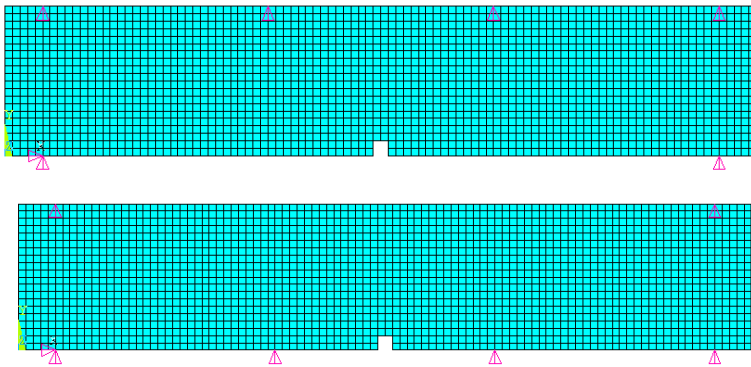


Figure A.19: FEM model

As for reverse loading, two models are considered: the correlative-independent damage model and the correlative damage model (group one of inverse functions). Due to the elastic compressive behaviour, the compressive stiffness of the correlative-independent damage model is kept initial for all load steps. Here, unloading stiffness recovery of tension is ignored since the unloading stiffness is almost the secant stiffness for tensile unloading. If group 2 of inverse functions is used in the correlative damage model, the behaviour is similar to that of the correlative-independent damage model.

## TEST RESULTS OF THE CORRELATIVE-INDEPENDENT DAMAGE MODEL

It can be seen in Figure A.20 that the slope changes instead of following the secant stiffness when the load is reversed. Actually, the slope recovers to the initial state if there is no damage in the loading of this direction. Afterwards, the slope changes back to the previous value of this direction when the structure is loaded again in this direction. That is to say, step 4 does not follow the secant stiffness of step 3 (green line) while step 7 follows the secant stiffness of step 3 instead of the secant stiffness of step 6 (orange line) in Figure A.21. The capacity for negative loading is slightly smaller than for positive loading due to the notch at the bottom.

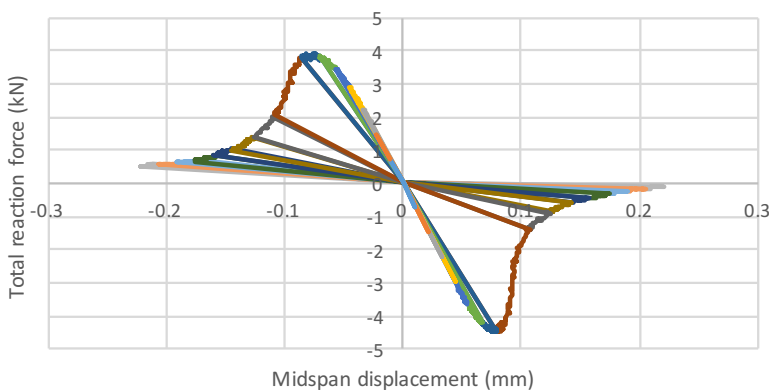


Figure A.20: Displacement-reaction force curve for cyclic behaviour of the concrete beam with a notch (independent damage)

Figure A.22 indicates the whole process of loading and unloading in the negative and positive directions. In general, only brittle failure can be seen for the negative loading due to the notch. However, the structure suffers from ductile to brittle failure since the influence of the notch is smaller for positive loading. As for the negative loading, the structure cracks earlier for the same imposed displacement. Subsequently, two columns of elements crack before the reaction force meets the peak. However, cracks develop in only one column of elements while the others are closed after the peak. A similar procedure can be seen in the positive direction. The major distinction is the cracks occur only along the notch for the negative loading whereas cracks occur at nearly whole parts of the top of the beam midspan before the peak for the positive loading. As a matter of fact, the cracks along the notch are still larger than others for the positive loading.

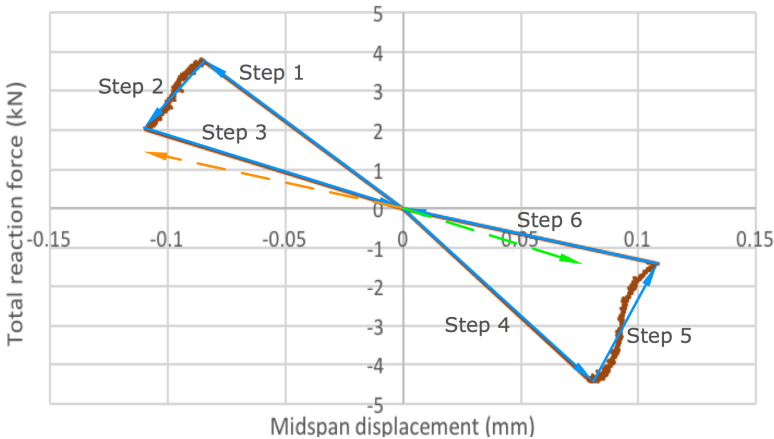


Figure A.21: One loop of the notched beam cyclic loading test

## TEST RESULTS OF THE CORRELATIVE DAMAGE MODEL

Figure A.23 shows the load-displacement diagram of the correlative damage model while the maximum principal strain contours can be seen in Figure A.24. Since the initial loading is in the negative direction, the damage in this direction is dominant for the structure. As a matter of fact, the damage of this direction causes an even lower capacity of the positive direction than that of the negative direction whereas it is higher for the correlative-independent damage model. In addition, the curve gaps between adjacent loading loops result from the damage of the previous loading steps, which are in the other direction. When the load is reversed, the stiffness cannot fully recover, determined by the reversing load function of the correlative damage model. The major distinction for the two directions is that there are several “slides” in the positive loading direction. A slide is a sudden reduction of the stiffness. This is due to the fact that cracks in the negative loading direction develop faster than in the other direction. The reason for this is that the load schedule starts from the negative loading direction and the notch also has a larger influence. When cracks develop to the mid-height of the beam, some elements will convert from compression to tension. Nevertheless, the stiffness cannot recover to the initial state due to the heavy damage in the other direction. Therefore, an abrupt change can be seen when the stiffness of the element close to mid-height is smaller than that of the element near the bottom. Speaking of the negative loading direc-

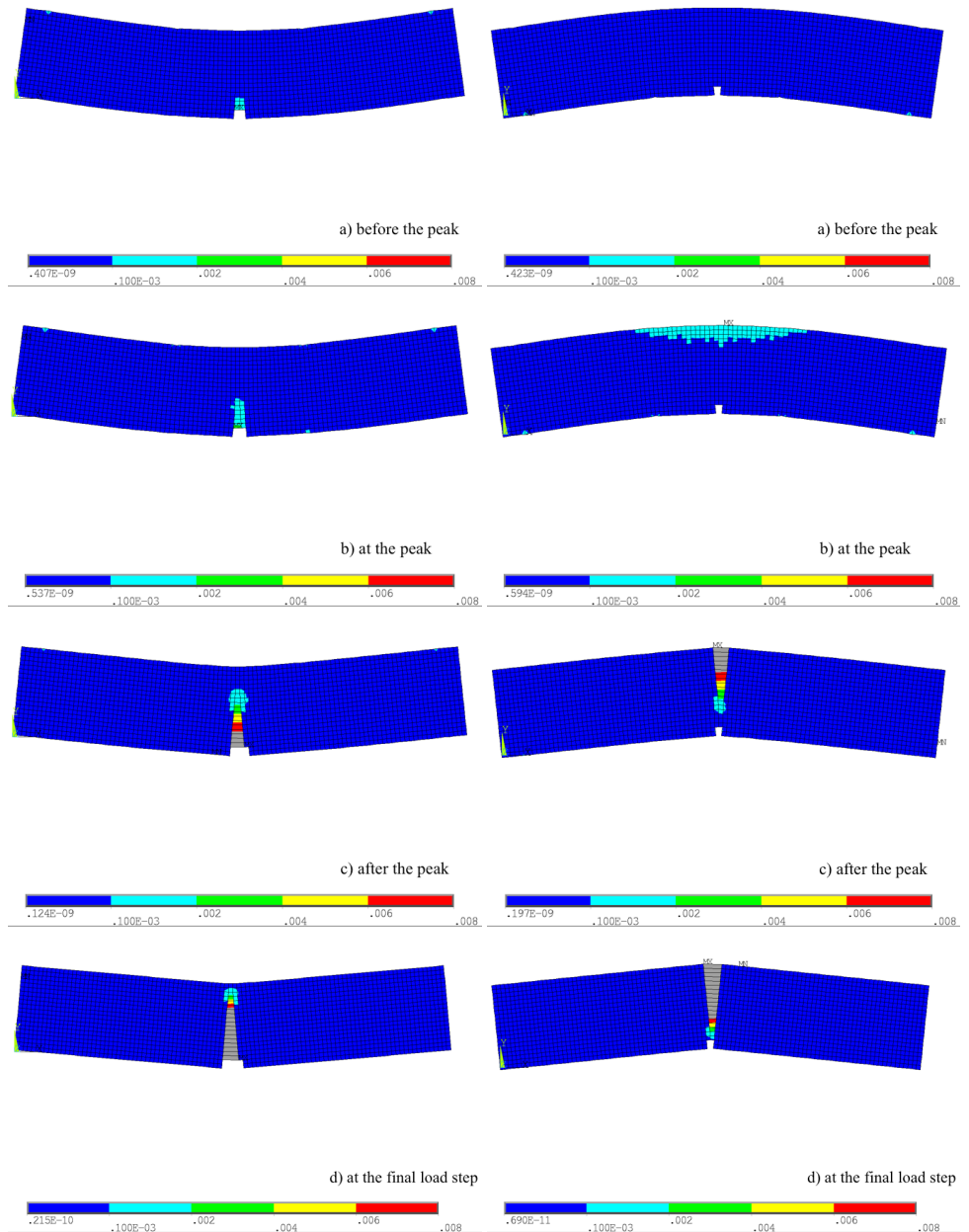


Figure A.22: Maximum principal strain contours of the cyclic loading test for the correlative-independent damage model: (a) before the peak of the reaction force, b) at the peak, c) after the peak and d) at the final step in the negative and positive directions)

tion, these curves are much smoother than those in the positive loading direction because of the slower crack development in the negative loading direction. In other words, the stiffness of the damaged element closer to the bottom is basically always smaller than the stiffness near mid-height. Moreover, the final crack length in the positive loading direction is much shorter than in the other direction. This is also due to the heavier damage in the negative loading direction.

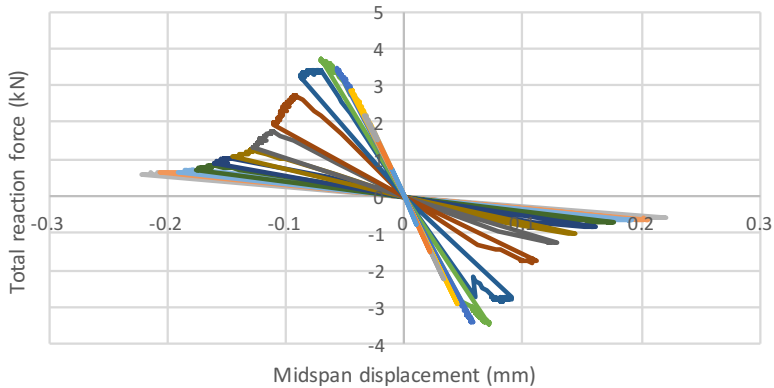


Figure A.23: Displacement-reaction force curve for cyclic behaviour of the notched concrete beam (correlative damage)

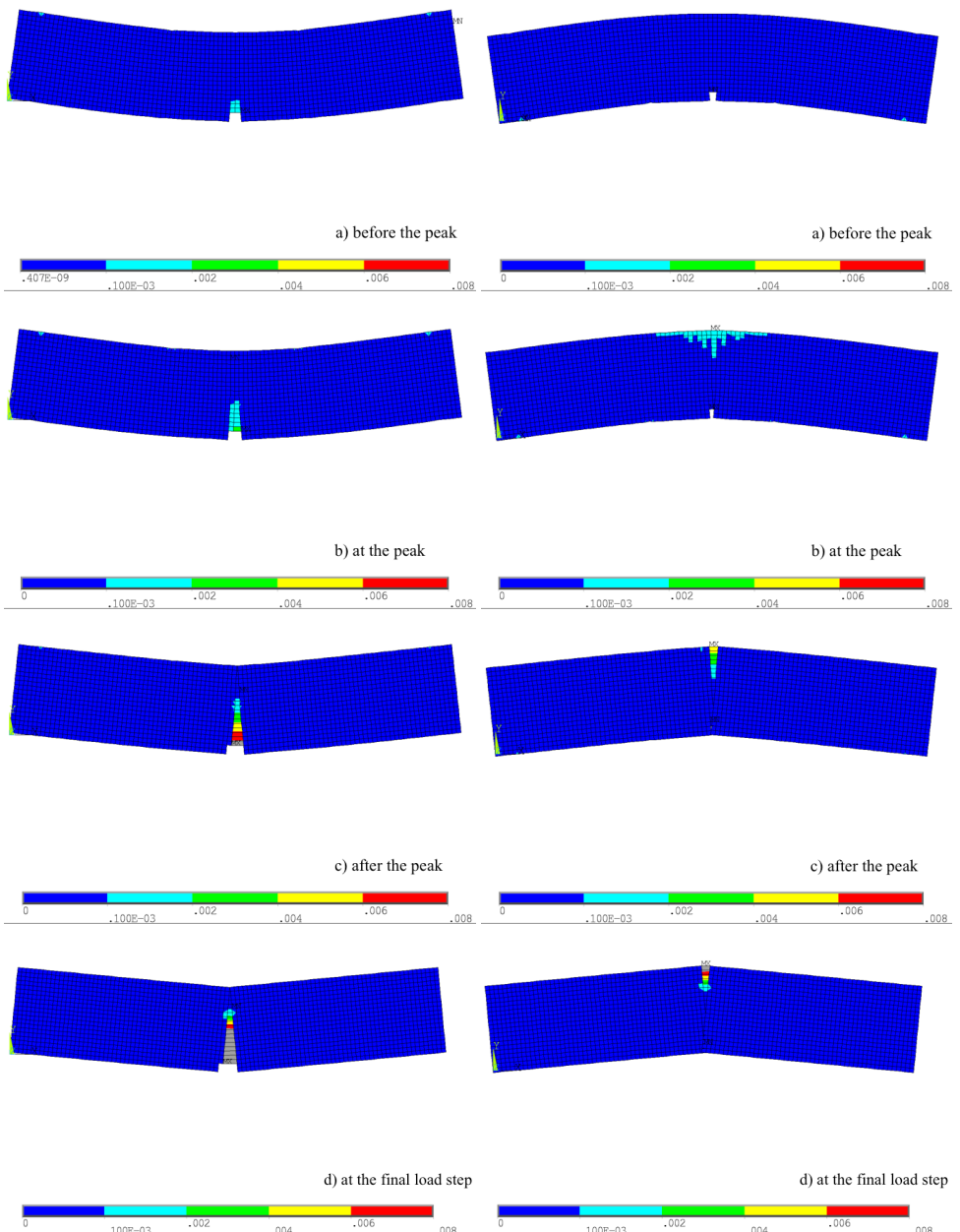


Figure A.24: Subsequent maximum principal strain contours: a) before the peak of the reaction force, b) at the peak, c) after the peak and d) at the final step in the negative and positive directions (the correlative damage model)

## DISCUSSION

The correlative damage model and the correlative-independent damage mode are introduced to consider cyclic loading in ISLA. The stiffness change in two models are validated by a uniaxial test. Compared with the correlative-independent damage model, the correlative damage model is more realistic. More realistic and complicated functions can be implemented, but the two functions for both sides must be inverse. The correlative-independent damage model is similar to the correlative damage model with group 2 of inverse functions when the compressive behaviour is elastic in FEM models.

For the cyclic loading test of the notched beam, the correlative-independent damage model and the correlative damage model are robust and accurate. It is shown that full open and closure of cracks can be traced in ISLA. Meanwhile, the correlative damage model can also consider mutual impacts for cyclic loading.

Note that although the tensile unloading can be simplified by following the secant stiffness, it is unrealistic to follow the secant stiffness for the compressive unloading. Nevertheless, it is still worthwhile for the tensile failure of brittle materials, as the compressive behaviour is elastic in FEM models due to the simplicity. In Chapter B, the unloading behaviour with the non-secant stiffness is considered in ISLA, but limitations remain.

Currently, this algorithm is suitable only for proportional loading since the stresses are assumed to be zero for the transition of tension and compression.

The load control method is used in this chapter. Basically, the load scaling control method is designed for cases in which the N-R method with arc-length control is used. However, it is still possible to use the load scaling control method in cyclic loading analysis by changing the loading direction. The solution is to define several unit loads, positive and negative, determined by the loading schedule. Some conditions can be set to trigger the algorithm to run the next unit load when the current load factor meets certain values in the loading schedule. The stiffness should also be changed when the loading state switches.

In addition, it is possible to implement the load control method for a total approach such as SLA since the unloading behaviour still follows the secant stiffness. The only difference from the algorithm in ISLA is that the procedure is restarted from the origin for every load step rather than the previous load step. The equilib-

rium is determined by the utilisation function  $\mu$  rather than a unit load with the load factor  $\lambda$  in the standard SLA.

# B

## COUPLED DAMAGE-PLASTIC MATERIAL MODEL IN ISLA FOR PROPORTIONAL LOADING

In Appendix A, the material model is unloaded to the origin of the stress-strain curve (the elastic material model with the secant stiffness). This material model can describe the damage procedure but is not allowed for unloading with the non-secant stiffness, which is a limitation of the damage model and the smeared crack model. However, in the plastic model, the plastic modulus cannot drop below a critical value based on effective stress, which may diverge, and may not be negative based on nominal stress [83]. The damage model has been coupled with the plastic model for the N-R method [83][84][85][86][87][88].

In this appendix, the coupled damage-plastic material model rather than the elastic material model is implemented in ISLA to consider irreversible deformations, which can be applied for modelling materials such as metals and also cyclic loaded concrete and masonry. ISLA follows the damage model for loading and the plastic model for unloading. Plastic strain is recomputed when the reduced elastic modulus is changed to the unloading modulus for unloading. The damage model

with reduced secant stiffness ensures computational robustness while the plastic model provides the possibility of unloading with the non-secant stiffness.

Note that iterations are not considered to determine loading or unloading at the local level. Non-proportional loading is also not considered. The coupled damage-plastic material model still follows the secant stiffness for possibly local unloading when a structure is globally loaded. In the discussion section, a material model called the modified plastic model is proposed, which follows the non-secant stiffness for possible local unloading when a structure is globally loaded. However, both material models need to be further investigated compared with experimental results.

## MATERIAL DEFINITION

Figure B.1 shows a concrete compressive stress-strain curve with three load cycles, which is used to explain the material model. It has the same material properties for monotonic loading as Figure 3.9. Initially, there is no stress and no strain. Curve A shows that the material is first linearly elastic without plastic strain. After damage, the stress-strain curve follows Curve B for unloading. Subsequently, the load is increased again, and Curve B is followed up to Curve C, at which moment unloading occurs again. Finally, the load is increased again, and the material follows Curve C until no strength is left.

The reduced linear elastic stiffness is used to represent the damage for ISLA in previous chapters. If the elastic modulus of the element is still used to define the damage, when the damaged structure is loaded again after unloading, the origin should be shifted by the plastic strain. For calculation of the utilisation function, Figure B.1 indicates that there are three types of stress-strain curves of material properties (A, B and C), which are marked as three colours when the plastic strain augments. Actually, material property values of all damaged elements may be totally distinctive from each other because of various plastic strains, even for the same type of stress-strain curve. It is not convenient to calculate the utilisation function in this way.

Instead, the total strain  $\epsilon_{to}$  is used to represent the damage (Figure B.2(a)). Only in this way are the material properties for distinguished elements fixed. Although only the elastic modulus  $E_{el}$  can be defined and modified, the virtual total modulus

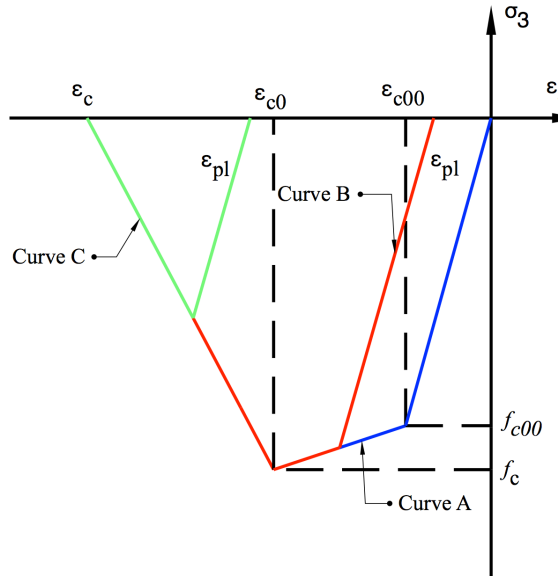
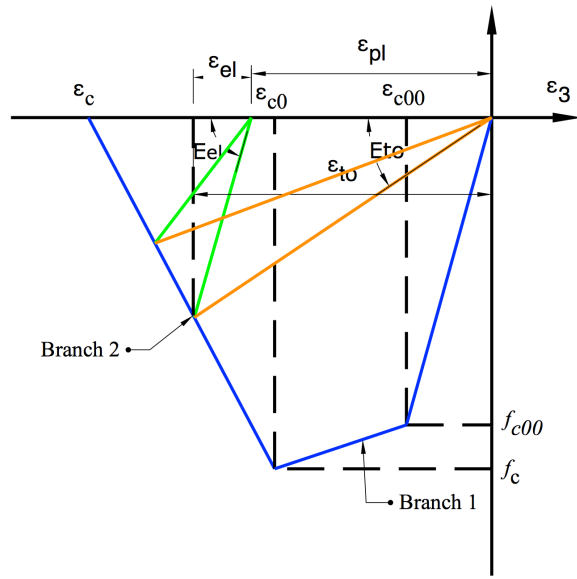


Figure B.1: Material properties based on different plastic strains

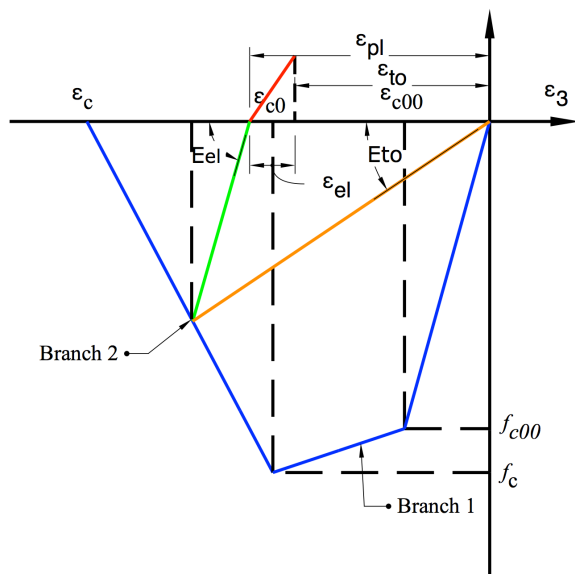
$E_{to}$  is also changed along with  $E_{el}$ . However, when the unloading procedure of concrete has passed the transition point of tension and compression, the origin should be shifted by the plastic strain  $\epsilon_{pl}$  such that  $(\epsilon_{to} - \epsilon_{pl})$  is used to represent the damage in the other direction (Figure B.2(b)).

## MATERIAL MODELLING

To consider plastic deformations and ensure robustness of the algorithm, the elastic material model is replaced by a plastic material model (isotropic hardening model) for all materials, regardless of whether they are metal or a brittle material such as concrete or masonry. The Following is the implementation of the algorithm. The algorithm consists of the loading procedure and the unloading procedure. Initially, the loading procedure is performed. The yield stress is set to a very large value such as 100 times the strength. Therefore, the loading procedure is basically the same as ISLA for the elastic material model without unloading (Figure B.3). The dots above the stress-strain curve are scaled cycle-by-cycle onto the curve by reducing the elastic modulus. The dashed red arrow line represents the elastic modulus of the current cycle. The dashed green line represents the virtual total modulus  $E_{to}$ ,



(a)



(b)

Figure B.2: Damage definition and the origin updating procedure

which is the same as the elastic modulus when there is no plastic strain. The incremental cycle-by-cycle procedure is shown in Section 5.5, which is hidden in this figure due to a concise indication.

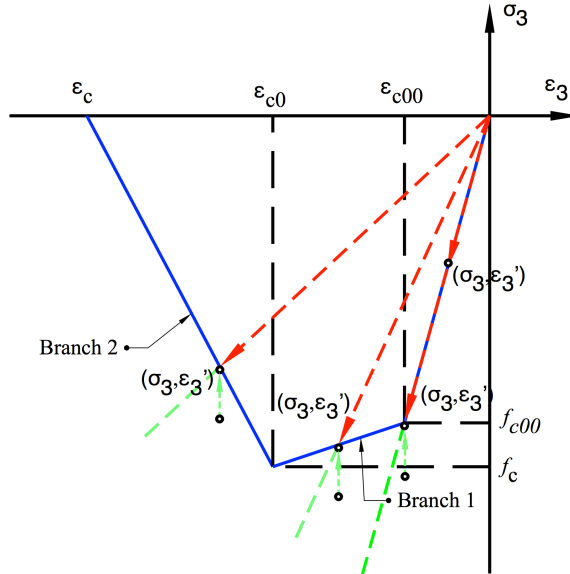


Figure B.3: Initial loading procedure of sequentially non-linear iterative implicit method before unloading

When the algorithm detects that the next load step is unloading, the unloading procedure is activated. The yield stress of the material model is set to the stress of the last cycle in the current load step for all damaged elements whereas the elastic modulus (the solid orange arrow line) is defined as the unloading modulus (the dot-dash blue arrow line) of the next load step, which can be any value (not only the initial Young's modulus) or derived from a certain function. The material model of Route A is converted to that of Route B, as shown in Figure B.4. Therefore, part of the elastic strain is converted to plastic strain.

It is important to change the material model before the unloading load step to guarantee the accuracy of the unloading result. In ISLA, the elastic modulus is reduced to increase elastic strain rather than plastic strain in order to render total strain the same as that of the plastic material model from non-linear N-R analysis to avoid divergence problems. From Eq. (B.1), the plastic strain from ISLA would be smaller than that from the non-linear N-R analysis due to various elastic moduli.

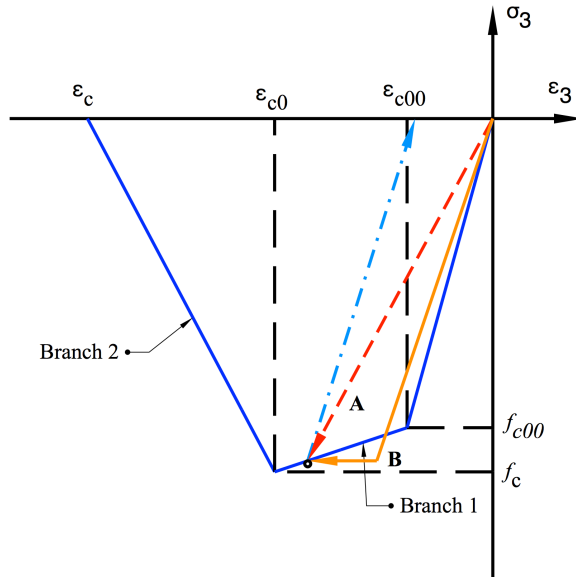


Figure B.4: Procedure for ISLA when the algorithm detects that the next step is unloading

Without unloading, there is no plastic strain for ISLA. Therefore, it is important to correct elastic and plastic strain before the unloading load step so that the loading procedure is connected with the unloading procedure at an identical strain state without an abrupt change at the beginning of the unloading load step. Otherwise, the curve unloads to the incorrect position.

$$\epsilon_{to} = \epsilon'_{to}$$

$$\epsilon_{el} + \epsilon_{pl} = \epsilon'_{el} + \epsilon'_{pl} \quad (\text{B.1})$$

As for the tangent modulus of the material model, it should be sufficiently small, otherwise the unloading path may be like Route D instead of Route C (Figure B.5). It can be seen that part of the elastic strain (Part E) is converted to plastic strain when unloading, which also causes a stress value ( $\sigma''_3$ ) larger than the correct one ( $\sigma'_3$ ). The unloading procedure performs the unloading load step after changing the model's yield stress, elastic modulus and tangent modulus.

Subsequently, when the algorithm detects the next load step is loading, the loading procedure is activated, and the yield stress of all damaged elements is increased to a very large value. If the material model remains the same as that in Route

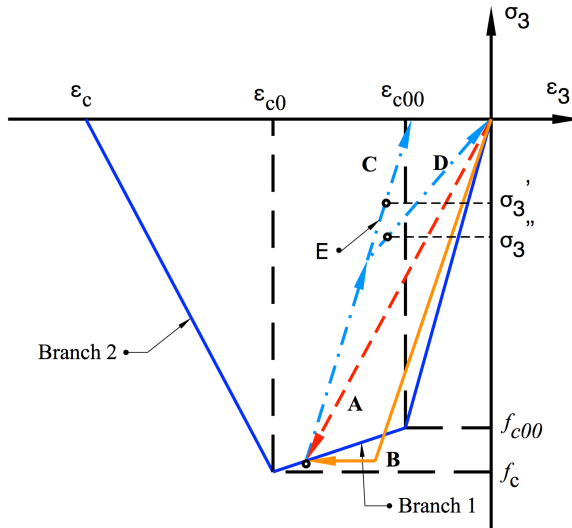


Figure B.5: The unloading procedure of ISLA during unloading

B and C, the loading path will continue in Route F rather than Route G (Figure B.6). Consequently, the utilisation function will be mistakenly smaller than 1 for the next load step because the stress of Route F is not larger than the strength of the material properties. This mistake may also occur for steel behaviour but not for the softening part of concrete or masonry behaviour. However, for the softening part, this change in material properties is still necessary for the next loading procedure.

When the utilisation function is larger than 1, the algorithm restarts from the last cycle of the previous load step (equilibrium state). Afterwards, elastic modulus reduction is performed as part of the loading procedure until the utilisation function is not larger than 1 (Figure B.7). The beginning elastic modulus is equal to the unloading modulus, which is larger than that of the previous loading step. However, there is no recovery from the damage due to the increase of plastic strain. Actually, the damage is identical and is measured by  $E_{t0}$  if the curve is reloaded to the same position before unloading.

It is recommended that the algorithm restarts from the state where the stress is zero during loading, otherwise the plastic strain can be negative when the elastic modulus is reduced to Route J (Figure B.8).

When the algorithm detects that the next step is unloading, the unloading procedure previously explained is activated. Otherwise, the algorithm performs the

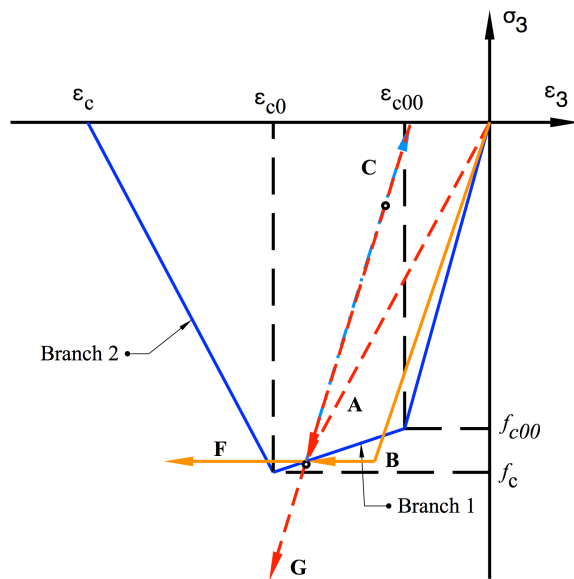


Figure B.6: The loading procedure of ISLA when the algorithm detects that the next step is loading

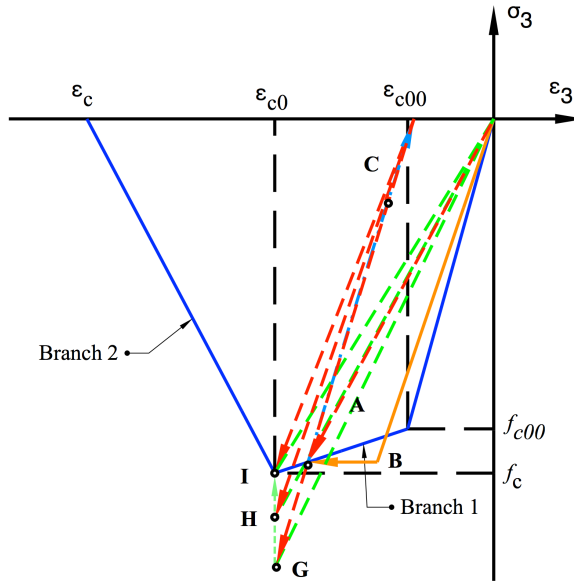


Figure B.7: The loading procedure of ISLA during loading

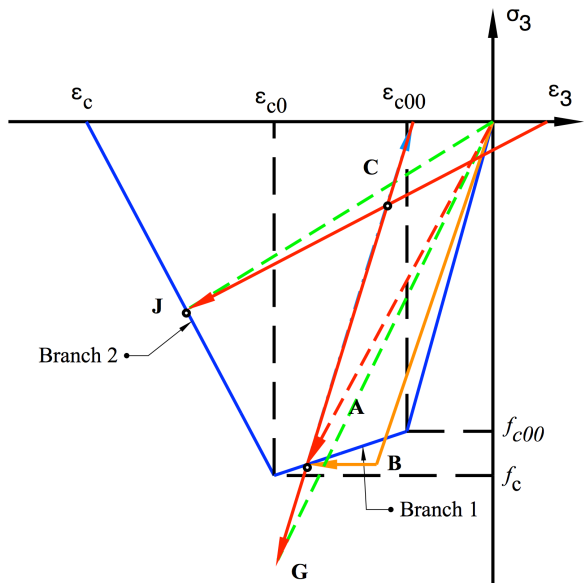


Figure B.8: The restart point of the equilibrium state for loading

loading procedure.

## ALGORITHM IMPLEMENTATION

"Find the origin" is defined to ensure the structure unloads to the moment when the total reaction force is zero. The program structure diagram for this is shown in Figure B.9. Figure B.10 shows the program structure diagram to consider plastic unloading behaviour. Not until all the load steps are finished or the whole structure totally fails is this algorithm terminated. Compared with the algorithm for secant unloading behaviour, the main disparities are that several condition checks are added, and the corresponding material model updates to convert from "basically" elastic material (very high yield strength) to a plastic material model.

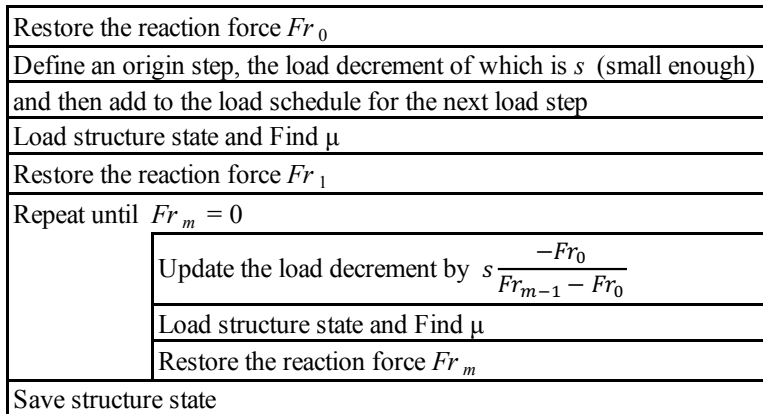


Figure B.9: Program structure diagram of "Find the origin"

When reverse loading is included in ISLA, the major distinction is that the start point of the material property curve should be moved instead of the origin due to the plastic unloading strain from loading in the other direction. For example, the new origin shifts left by  $\epsilon_{pl}$  to consider tensile damage after compressive unloading in Figure B.2(b).

At the local level, the shifting distance of the origin is clear, which is the plastic strain of loading in the other direction. However, it is complicated at the global level. Due to the residual stress, not all damaged elements are reverse loaded simultaneously. Hereby, it is impossible to define a certain reversing moment to change the stiffness for all damaged elements. To be exact, there is a reversing period instead of a reversing moment for the global level. The start point of this reversing period is the moment when the reaction force becomes zero. There is no damage when

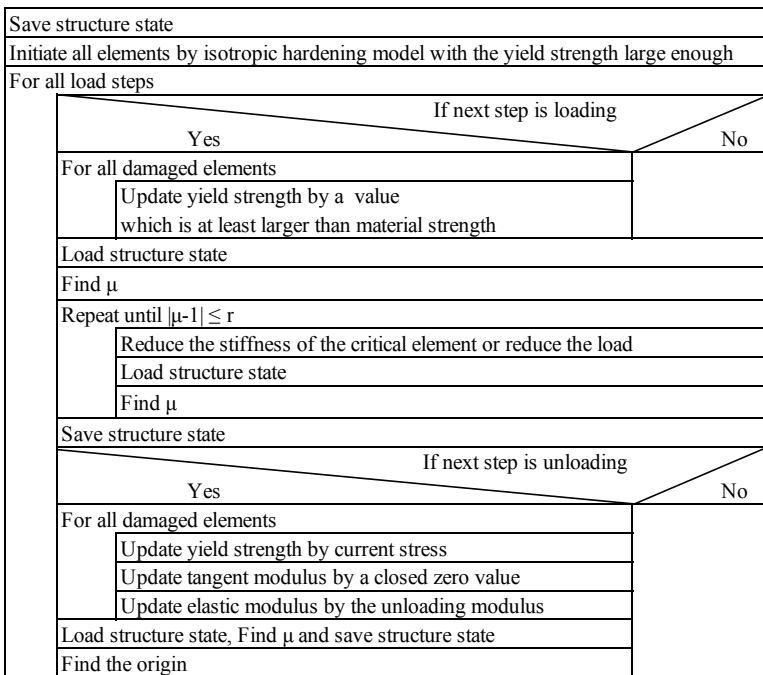


Figure B.10: Program structure diagram of ISLA with the coupled damage-plastic material model, including plastic unloading

unloading and thus the moment of no reaction force is predictable. Then origin can be updated for the damaged elements, the stresses of which are almost zero. Meanwhile, the stiffness is also updated by the reversing function introduced in Chapter A. However, for the elements with the residual stress, the solution is to ensure the load increment is small enough so the moment when the reaction force is zero the origin is updated and the stiffnesses change, which leads to inaccuracy. Figure B.11 shows the program structure diagram of ISLA with the coupled damage-plastic material model for the combination of plastic unloading and reverse loading. This PSD is suitable for brittle materials and metal materials. However, for metal materials, it is unnecessary to define a group of reverse loading steps since the stiffness does not change during reversing.

In addition, when plastic unloading stiffness is a non-linear function instead of a certain value, presently the solution is to define sufficiently small load increments from the moment of starting unloading to the moment when the reaction force is zero. Therefore, the stiffness is adjusted at certain load steps when the stress is lower than the certain value determined by the defined non-linear function.

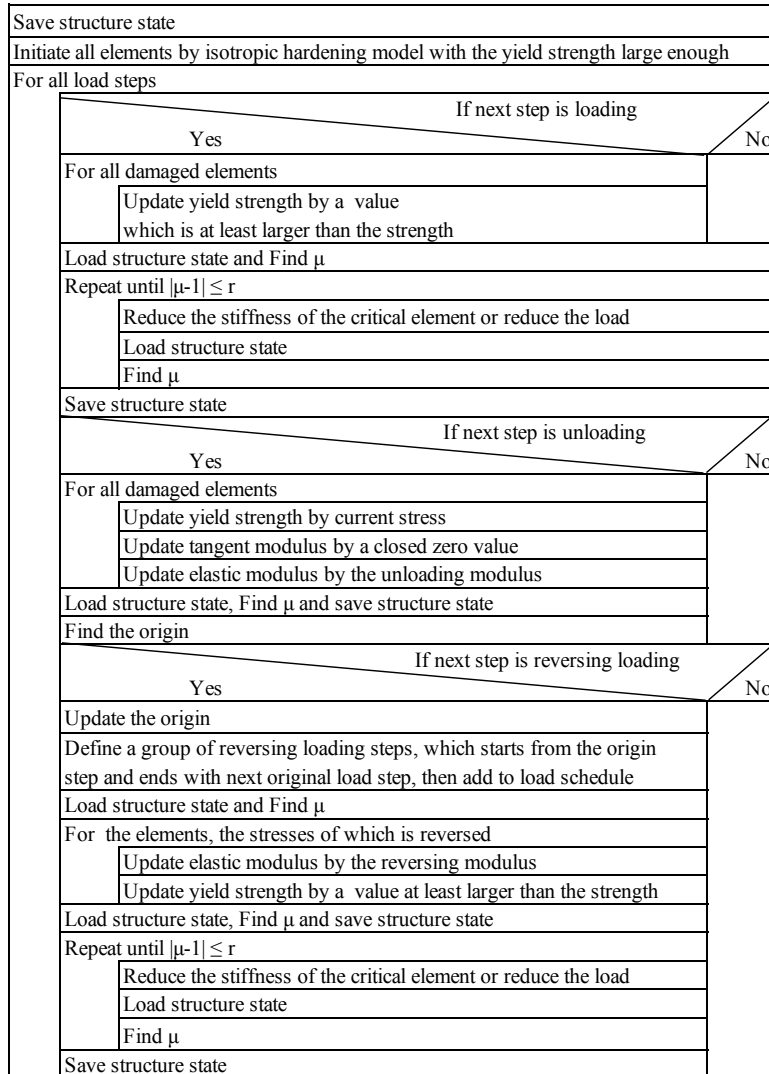


Figure B.11: Program structure diagram of ISLA with the coupled damage-plastic material model for the combination of plastic unloading and reverse loading

## COMBINATION TEST OF PLASTIC UNLOADING AND REVERSE LOADING FOR STEEL

Consider one element test for steel. The yield strength is 429 MPa, Young's modulus is 210 GPa and Poisson's ratio is 0.3. The elastic modulus is set back to the initial Young's modulus for unloading. The geometric dimensions and FEM model are the same as in Section 6.4. The load schedule is designed in Figure B.12 based on steel's plastic behaviour. The main purpose is to test the unloading procedure when the stress is lower than the yield stress. Except for Load step 1 (elastic step) and Load steps 2 and 6 (loading steps), the others are all unloading steps.

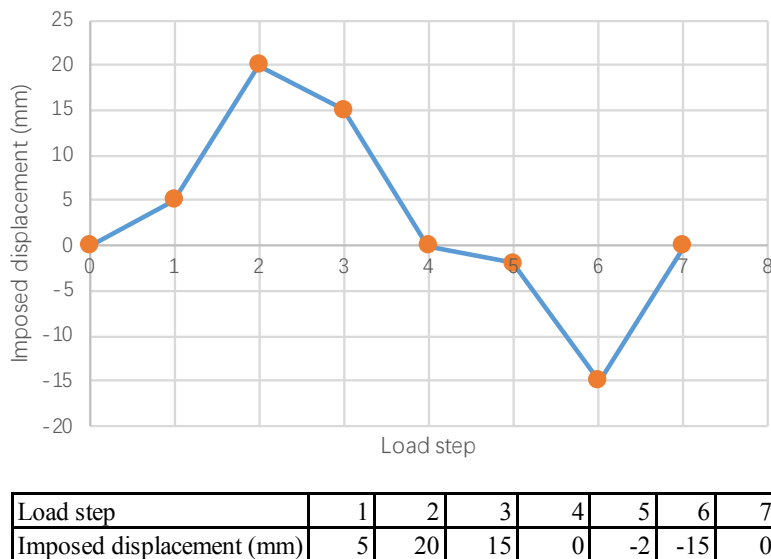


Figure B.12: Loading schedule for testing steel's plastic behaviour

It can be seen in Figure B.13 that the whole loading damage process can be obtained by post-scaling. The results of this process show that the utilisation function is larger than 1 and the corresponding utilisation value, which is the same as in SLA. Compared with non-linear analysis in Figure B.14, ISLA can include plastic behaviour when unloading instead of going back to the origin zero. Currently, results of four quadrants can be obtained by ISLA. A missing corner can be seen at the third quadrant when total strain is scaled, which demonstrates that the origin needs to be updated when the load is reversed. Meanwhile, it is notable that there is still

stress for two load steps with zero strain (Load steps 4 and 7). Speaking of the error of the selected load steps, ISLA is accurate of which errors are almost zero, as shown in Table B.1. The reason why the error of Load step 7 is relatively large is because the utilisation value of Load step 6 is not exactly 1. The difference of 3 MPa is relatively much larger for 96 MPa than for 429 MPa. Figure B.15 shows that elastic strain follows with the loading schedule while plastic strain nearly remains, with the exception of two loading steps. The abrupt strain change at two damage steps due to increased elastic strain by reducing the elastic modulus is converted to plastic strain at the end of the loading step to prepare for the next unloading step.

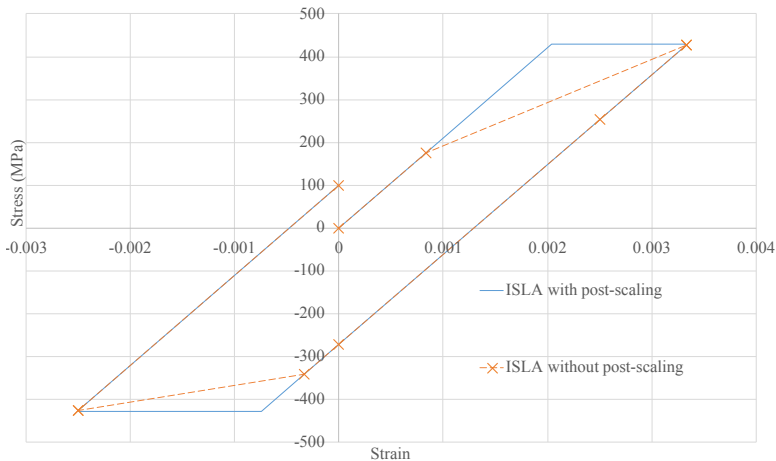


Figure B.13: Stress-strain curves for the cyclic analysis of steel without and with post-scaling, including all cycle results

Table B.1: Stress comparison for the cyclic analysis of steel

Load step	1	2	3	4	5	6	7
ISLA	175.00001	428.069678	253.069678	-271.93032	-341.93032	-425.58356	99.416438
N-R	175	429	254	-271	-341	-429	96
error	0.00%	0.22%	0.37%	0.34%	0.27%	0.80%	3.56%

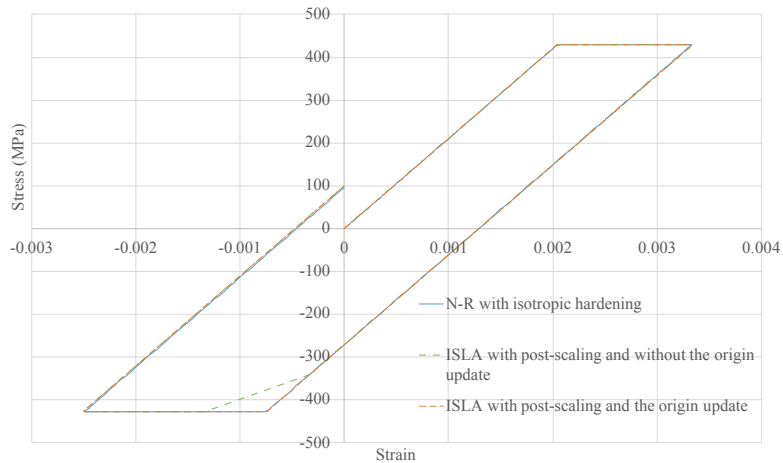


Figure B.14: Stress-strain curves for the cyclic analysis of steel comparing ISLA and N-R analysis

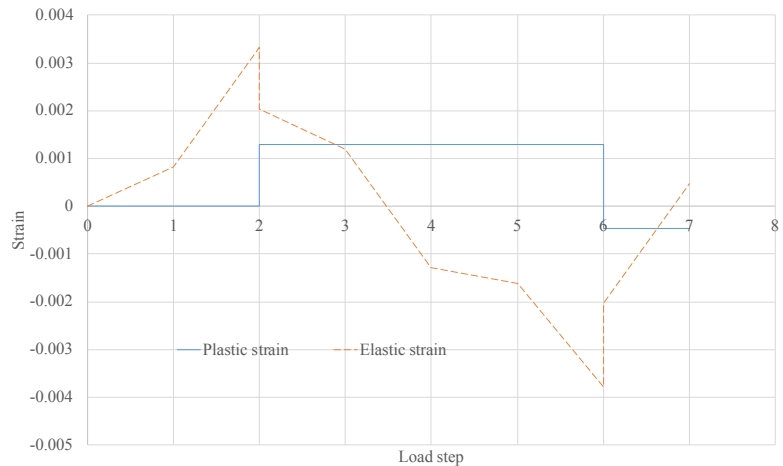


Figure B.15: Elastic strain versus plastic strain for the cyclic analysis of steel

## PLASTIC UNLOADING BEHAVIOUR TEST FOR CONCRETE

Consider one element test of steel. All the material properties, geometric dimensions and FEM model are the same as in Section 6.4. The unloading elastic modulus is set as 20,000 MPa which is 2/3 of the initial Young's modulus. Twelve points are selected from the concrete compressive stress-strain curve, for which the unloading procedure enables the stress to drop to zero (Figure B.16). Figure B.17 shows the imposed displacements for every load step. Note that the imposed displacements for unloading are adjusted by the algorithm to ensure the stress is zero. The designed strain of unloading is compared with the strain when the stress unloads to zero.

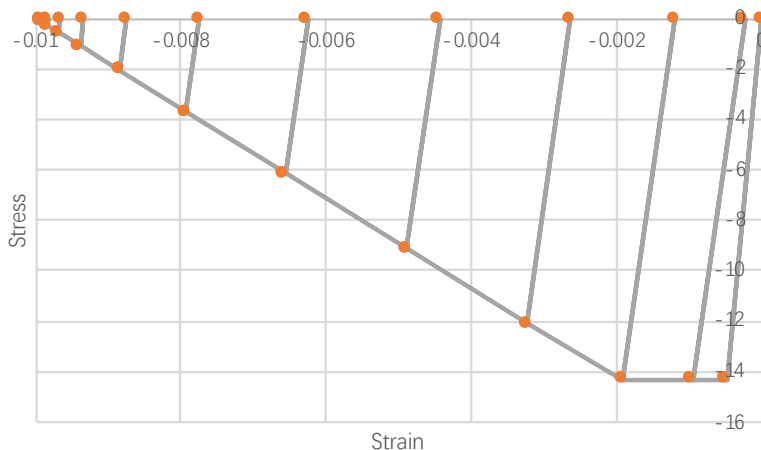
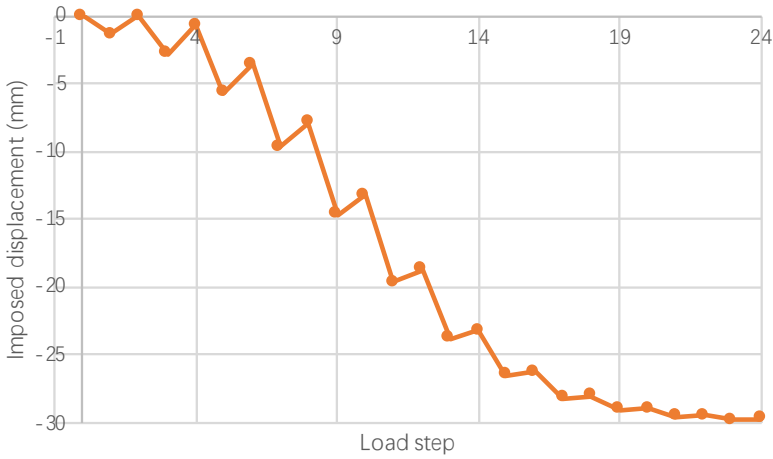


Figure B.16: Selected points from compressive material properties

Figure B.18 shows the stress-strain curves of ISLA and the designed curve. It can be seen that the curve of ISLA with post-scaling and the designed curve overlap with each other while the point of Load step 3 from the curve of ISLA without post-scaling is lower than that of the designed curve. According to Table B.2, the stress error of Load step 3 is 4.34% (maximum) followed by Load step 5 (1.43%) while the rest are lower than 1%. This is because the utilisation function of Load step 3 is not exactly 1 but 0.956, which can be corrected by post-scaling. The error of Load step 3 also causes the strain of Load step 4 (unloading procedure) to be larger than the strain of the point on the designed curve whereas errors of the others are almost zero, as shown in Table B.3. Therefore, the errors do not accumulate. As for the



Load step	1	2	3	4	5	6	7	8	9	10
Imposed displacment (mm)	-1.430	0.000	-2.860	-0.715	-5.720	-3.575	-9.684	-7.868	-14.642	-13.269
Load step	11	12	13	14	15	16	17	18	19	20
Imposed displacment (mm)	-19.679	-18.756	-23.767	-23.210	-26.522	-26.212	-28.154	-27.989	-29.048	-28.963
Load step	21	22	23	24						
Imposed displacment (mm)	-29.516	-29.473	-29.756	-29.734						

Figure B.17: Loading schedule for testing concrete plastic unloading behaviour (imposed displacements)

unloading elastic modulus, the errors are less than 0.01%, as shown in Table B.4. Further, elastic strain fluctuates along with the material properties in Figure B.19, which means it increases with the reduction of elastic modulus during loading and then decreases to zero during unloading. Eventually, the elastic strain drops to zero. In addition, Figure B.20 shows the plastic strain remains unchanged during loading and unloading but abruptly ascends at the transition point of loading and unloading. Finally, the plastic strain augments to the ultimate strain when the elastic strain is zero.

Based on two tests, it can be seen that elastic strain represents the relationship between the loading procedure and structure capacity while plastic strain indicates the position of the origin for load steps. The proper stiffness for the plastic model in the sequentially non-linear iterative implicit method is obtained by a sub-step iteration procedure. Overall, the sequentially non-linear iterative implicit method combines ISLA with a plastic unloading procedure.

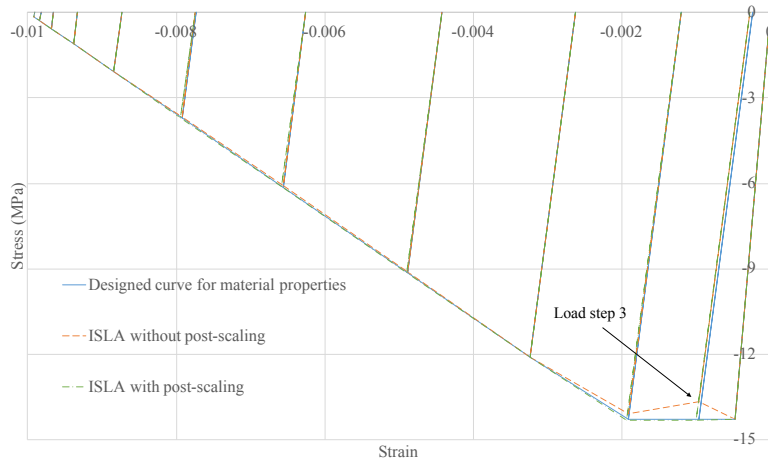


Figure B.18: Stress-strain curves for the repeating analysis of concrete comparing ISLA and material properties

Table B.2: Stress comparison for the repeating analysis of concrete

Load step	1	2	3	4	5	6	7	8	9	10
Designed stress (MPa)	-14.300	0.000	-14.300	0.000	-14.300	0.000	-12.105	0.000	-9.151	0.000
Actual stress (MPa)	-14.300	0.000	-13.679	0.000	-14.096	0.000	-12.093	0.000	-9.110	0.000
Error	0.00%		-4.34%		-1.43%		-0.10%		-0.45%	
Load step	11	12	13	14	15	16	17	18	19	20
Designed stress (MPa)	-6.150	0.000	-3.714	0.000	-2.072	0.000	-1.100	0.000	-0.567	0.000
Actual stress (MPa)	-6.094	0	-3.684	0	-2.064	0	-1.096	0	-0.565	0
Error	-0.91%		-0.80%		-0.39%		-0.34%		-0.41%	
Load step	21	22	23	24						
Designed stress (MPa)	-0.288	0.000	-0.145	0.000						
Actual stress (MPa)	-0.286	0	-0.144	0						
Error	-0.78%		-0.89%							

Table B.3: Strain comparison for the repeating analysis of concrete

Load step	1	2	3	4	5	6	7	8	9	10
Designed strain ( $10^{-3}$ )	-0.477	0.000	-0.953	-0.238	-1.907	-1.192	-3.228	-2.623	-4.881	-4.423
Actual strain ( $10^{-3}$ )	-0.477	0.000	-0.953	-0.269	-1.907	-1.202	-3.228	-2.623	-4.881	-4.425
Error	0.00%	0.00%	0.00%	13.02%	0.00%	0.86%	0.00%	0.02%	0.00%	0.05%
Load step	11	12	13	14	15	16	17	18	19	20
Designed strain ( $10^{-3}$ )	-6.560	-6.252	-7.922	-7.737	-8.841	-8.737	-9.385	-9.330	-9.683	-9.654
Actual strain ( $10^{-3}$ )	-6.560	-6.255	-7.922	-7.738	-8.841	-8.737	-9.385	-9.330	-9.683	-9.654
Error	0.00%	0.05%	0.00%	0.02%	0.00%	0.00%	0.00%	0.00%	0.00%	0.00%
Load step	21	22	23	24						
Designed strain ( $10^{-3}$ )	-9.839	-9.824	-9.919	-9.911						
Actual strain ( $10^{-3}$ )	-9.839	-9.824	-9.919	-9.911						
Error	0.00%	0.00%	0.00%	0.00%						

Table B.4: Unloading modulus comparison for the repeating analysis of concrete

Load step	2	4	6	8	10	12
Designed unloading modulus (MPa)	30000	20000	20000	20000	20000	20000
Actual unloading modulus (MPa)	29999.979	19999.6491	19999.9149	19999.5369	19999.3414	20001.5098
Error	0.000%	-0.002%	0.000%	-0.002%	-0.003%	0.008%
Load step	14	16	18	20	22	24
Designed unloading modulus (MPa)	20000	20000	20000	20000	20000	20000
Actual unloading modulus (MPa)	19997.8287	19995.9311	20007.6672	20007.7906	20000	19988.8951
Error	-0.011%	-0.020%	0.038%	0.039%	0.000%	-0.056%

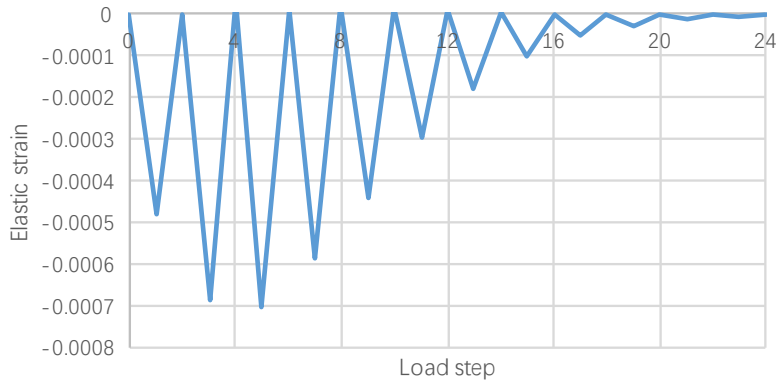


Figure B.19: Elastic strain versus load step for the repeating analysis of concrete

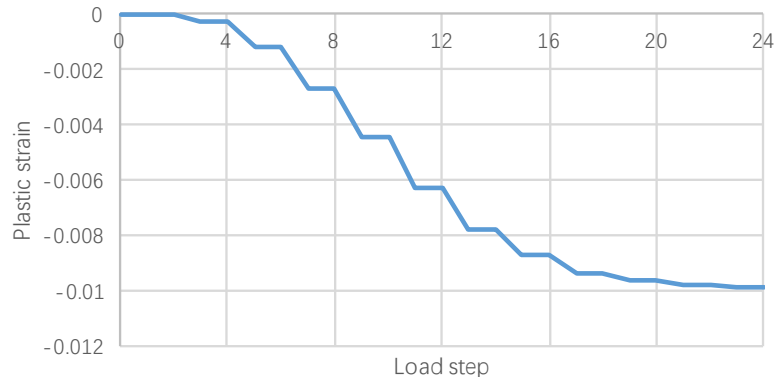


Figure B.20: Plastic strain versus load step for the repeating analysis of concrete

## COMBINATION TEST OF PLASTIC UNLOADING AND REVERSE LOADING FOR CONCRETE

In this section, one element test starts from tensile damage to compressive damage. All the material properties, geometric dimensions and FEM model are the same as in Section 6.4. Eq. B.2 is used to define the tensile plastic unloading behaviour, which is the relationship of the secant stiffness and unloading stiffness. When the test goes to compression, the stiffness recovers to the initial stiffness (30000 MPa).

$$y = f(x) = -x^2 + 2x \quad (\text{B.2})$$

where  $y$  and  $x$  are the relative unloading and secant stiffness to the initial stiffness, respectively, which is between 0 and 1.

The imposed displacements are defined in Figure B.21. Load step 5 is a nominal zero step. Actually, it is the moment when the reaction force is zero, which is automatically calculated and replaced with the corresponding displacement by the proposed method.

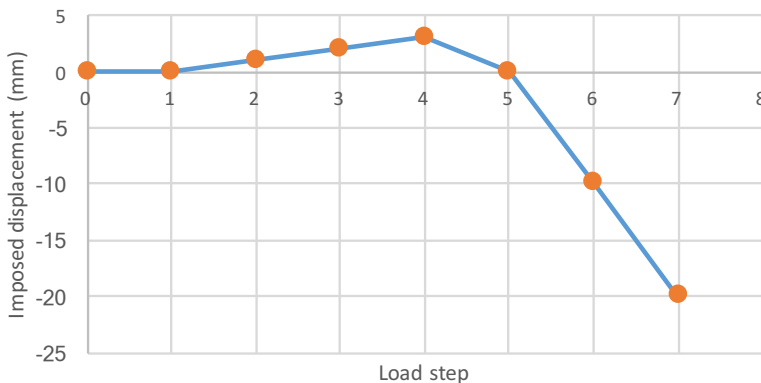


Figure B.21: Load schedule of the imposed displacements

Figure B.22 shows the stress-strain curve for this cyclic loading schedule. Compared with the material properties, the tensile elastic and softening parts overlap, and those for compressive behaviour are shifted right. The shifting value is the plastic strain caused by tensile plastic unloading. Table B.5 shows the detailed results of these seven load steps. It can be seen that the stiffness is damaging from 30,030.03 MPa to 724.86 MPa during tensile loading, then recovers to 1,432.21 MPa. The stiff-

ness recovery value is correct based on Eq. B.2. Moreover, the imposed displacement is adjusted to 1.482 mm when the reaction force is zero for Load step 5. Subsequently, Load steps 6 and 7 are compression damage steps. Table B.6 shows parts of cycle results from Load steps 4 through 6. It is important to mention three cycles. First, there is no stiffness damage at cycle 16 of Load step 4 because this transition cycle is used to convert part of the elastic strain to plastic strain to prepare for plastic unloading. Second, cycle 1 of Load step 5 is used to calculate the global stiffness, so the reversing moment can be predicted for the next load step. Third, the stiffness recovers to the initial stiffness 300,000 MPa at cycle 1 of Load step 6. Finally, the stiffness is damaged to 2,809.52 MPa, as shown in table B.5.

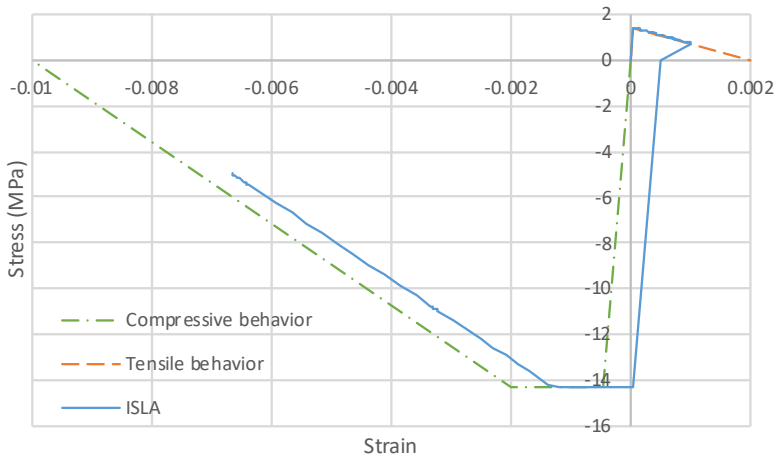


Figure B.22: Stress-strain curve for one-element cyclic loading test

Table B.5: Stress-strain curve for one-element cyclic loading test

Load step	Strain	Stress (MPa)	Stiffness (MPa)	Imposed displacement (mm)
1	3.33E-07	0.01	30030.03003	0.001
2	0.00033333	1.203609	3610.830611	1
3	0.00066667	0.965828	1448.741276	2
4	0.001	0.72486	724.8607249	3
5	0.00049389	0	1432.206973	1.482
6	-0.00333333	-10.752656	2809.522005	-10
7	-0.00666667	-4.936075	689.3438638	-20

Table B.6: Stress-strain curve for one-element cyclic loading test

Load step	Cycle	Strain	Stress (MPa)	Stiffness (MPa)
4	14	0.000995	0.728538308	732.181
4	15	0.001	0.72486	724.86
4	16	0.001	0.72486	724.8607249
5	1	0.0009	0.581639	1432.206228
5	2	0.0004939	0	1432.206228
6	1	1.672E-05	-14.30914357	29987.94656
6	2	-3.632E-05	-14.3103325	26990.39154
6	3	-9.519E-05	-14.31011232	24292.35567
6	4	-0.0001607	-14.31280404	21863.93431

## NOTCHED BEAM TEST, INCLUDING PLASTIC UNLOADING

All the material properties, geometric dimensions and FEM model are the same as in Chapter 7. Two types of unloading modulus are defined, namely a constant value of 20,000 MPa (the initial Young's modulus is 32,000 MPa) and the secant stiffness. The monotonic loading schedule in Chapter 7 is modified to a repeating loading schedule, as shown in Figure B.23.

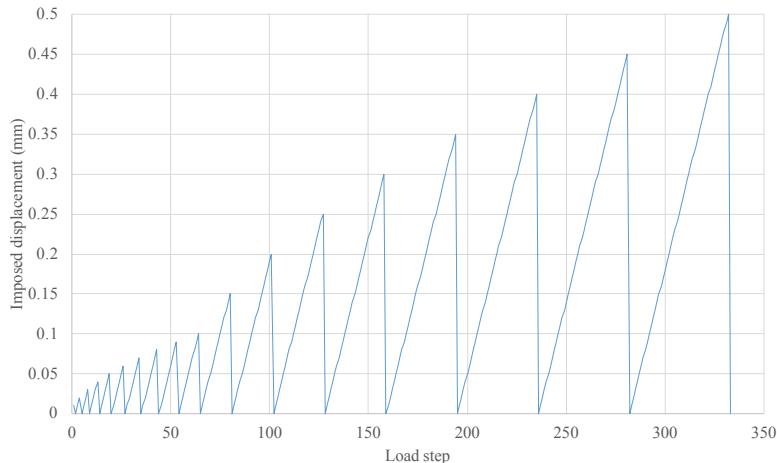
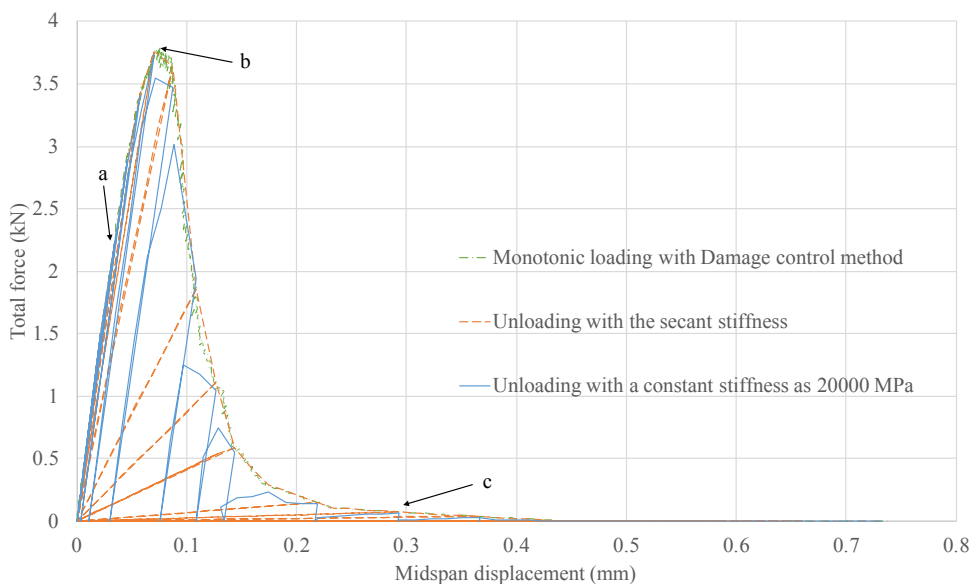


Figure B.23: Loading schedule for repeating loading of the notched beam

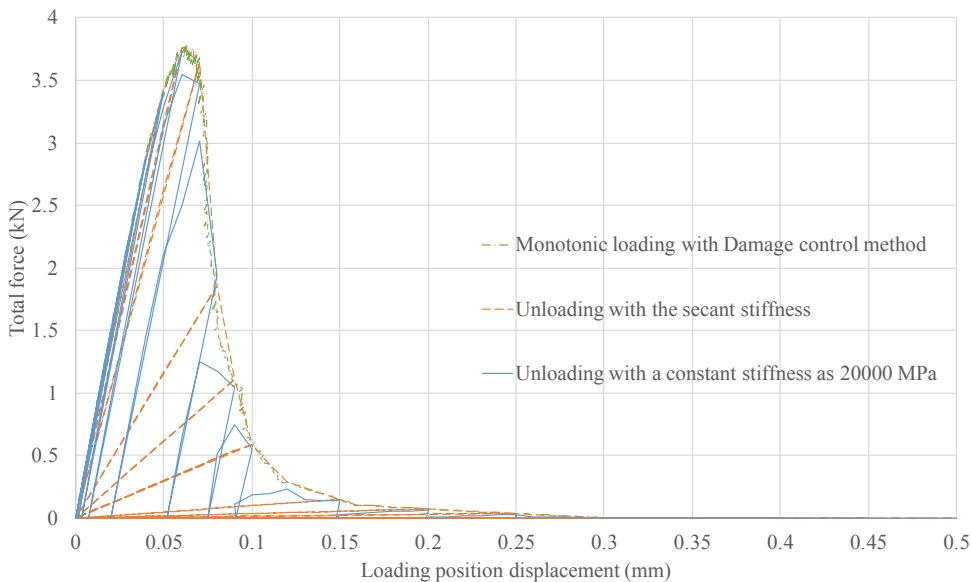
Figure B.24 shows the displacement-force diagrams for the midspan and the loading position separately. Three load steps are marked for post-processing. The backbones of two types of unloading modulus align well with the curve of the mono-

tonic loading with the damage control method. When the secant stiffness is used, the beam is unloaded to the origin without any permanent deformation for all unloading steps. Afterwards, the beam can be reloaded to the position of the previous loading step. On the contract, when the constant stiffness (20,000 MPa) is used, the permanent deformation related to the plastic strain accumulates step-by-step and can be regarded as permanent damage. In addition, the beam cannot be reloaded to the position of the previous loading step due to the permanent damage. The peaks of the two curves align well with each other, and the total forces of both are 3.87 kN.

Figure B.25 shows the crack patterns of the pre-peak, the peak and the post-peak marked in Figure B.24 when the beam is unloaded by the secant stiffness. The crack starts from the notch and propagates to the top of the beam. The beam meets the peak when the three elements are damaged. The total force drops to nearly zero when eight elements are damaged. The beam is unloaded to the states where there is nearly no strain (less than 1e-9). Figure B.25 shows the crack patterns when the beam is unloaded by the constant stiffness (20000 MPa). For position a, the beam is unloaded to the state where there is no crack. For positions b and c, the crack almost remains when the beam is unloaded to the state for which the total force is zero.



(a) Selected displacements from the bottom of the beam midspan



(b) Selected displacements from the loading position

Figure B.24: Load-displacement diagrams of the notched beam for the repeating loading test: (a) total force versus midspan displacement and (b) total force versus loading position displacement

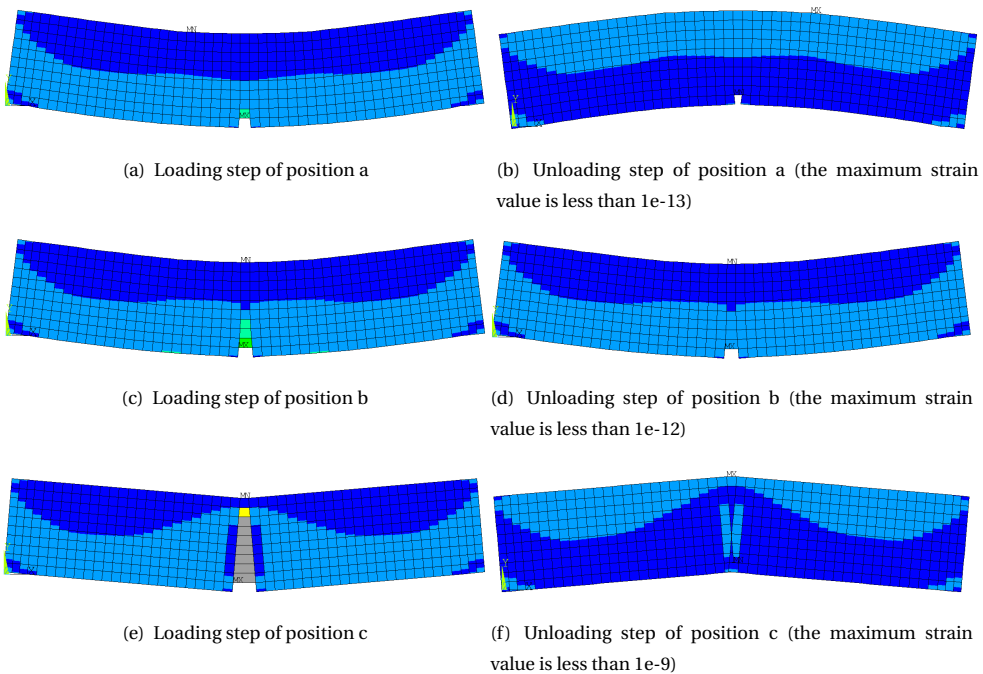


Figure B.25: Horizontal tensile strains (x-direction, strain contour) for the loading and unloading of the three positions marked in Figure B.24 when the secant stiffness is used for unloading

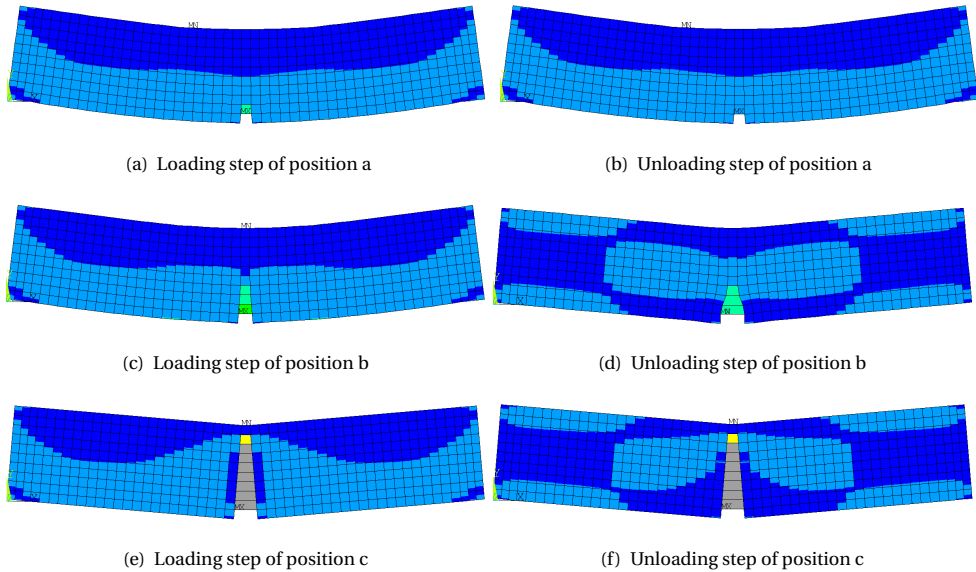


Figure B.26: Horizontal tensile strains (x-direction, strain contour) for the loading and unloading of the three positions marked in Figure B.24 when the constant stiffness (20.000 MPa) is used for unloading

## DISCUSSION

To sum up, the coupled damage-plastic material model has been implemented in ISLA, as shown in Figure B.27, which is a varying isotropic hardening model that includes yield strength, elastic modulus and tangent modulus. ISLA consists of the loading procedure and unloading procedure. It should be noted that the dashed red arrow line represents the reduced elastic modulus and the dashed green line represents the virtual total modulus, but the actual incremental path is shown in Section 5.5. When the loading procedure is performed, the reduced elastic modulus is "basically" determined by the standard ISLA to obtain the correct virtual total modulus, the procedure of which still reduces the stiffness or scales the load cycle-by-cycle (the double dot-dash green arrow line) from one equilibrium state to another until the utilisation function is not larger than 1. Here, "basically" means the original elastic material model in ISLA is replaced by the isotropic hardening model with very large yield strength. When the next load step is unloading, the unloading procedure is performed. It is important that after the elastic modulus of the loading procedure has been reduced, the plastic strain is corrected based on the unload-

ing modulus (the dot-dash blue arrow line) of the next load step for all damaged elements. The yield strength is determined by the stress of the current load step, and the elastic modulus, which can be certain constant values or functions and is not restrained by initial Young's modulus (the solid orange arrow line), depends on the unloading recovery behaviour. Here, an almost zero tangent modulus is recommended to ensure the accuracy of the unloading stress. When the next load step is loading, the loading procedure is performed. The yield strength is set to a very large value.

For the proportional repeating loading, the structure can be accurately unloaded to a state at which the total force is zero. The unloading stiffness can be a constant stiffness, the secant stiffness or a function. However, for non-proportional repeating loading and cyclic loading, accuracy and robustness cannot be guaranteed when the load is reversed for a structure. The stresses of damaged elements are not reversed simultaneously at the state for which the total force is zero due to the residual stress. The solution is to perform iterations to update the stiffness, which results in the bifurcation that the stiffnesses of the damaged elements can be reduced by the damage of loading, updated due to the reverse loading, or updated due to the unloading.

Another possible material model, called the modified plastic model (Figure B.28), considers plastic unloading. In this model, for loading, the yield strength is continually reduced until the utilisation function is equal to or is smaller than 1, rather than the elastic modulus in the coupled damage-plastic material model. The elastic modulus is determined by the unloading modulus. The advantage is that the material model does not need to switch from the "basically" damage model to the plastic model for unloading. The modified plastic model follows the non-secant stiffness for possible local unloading when a structure is globally loaded. For the previous test, the elastic modulus is constant, the material model of which is shown in Figure B.29. The modified plastic model aligns well with the designed curve for the one-element test (Figure B.30) while the peak and post-peak behaviour of the backbone in the modified plastic model do not fit well with the curve of monotonic loading in the damage control method for the notched beam test (Figure B.31). In the modified plastic model, when the yield strength of the critical element is reduced, the stresses of other elements also become smaller since the stiffness does

not change. On the other hand, in the coupled damage-plastic model, when the elastic modulus of the critical element is reduced, the stresses of other elements increases. Based on comparison of the one-element test and the notched beam test, although the modified plastic model is simple, the coupled damage-plastic model is more reliable. Moreover, the damage model and the smeared crack model are widely used and are accepted in solid mechanics. Therefore, the coupled damage-plastic model was chosen for ISLA. The principle, robustness and accuracy of the modified plastic model need to be further investigated.

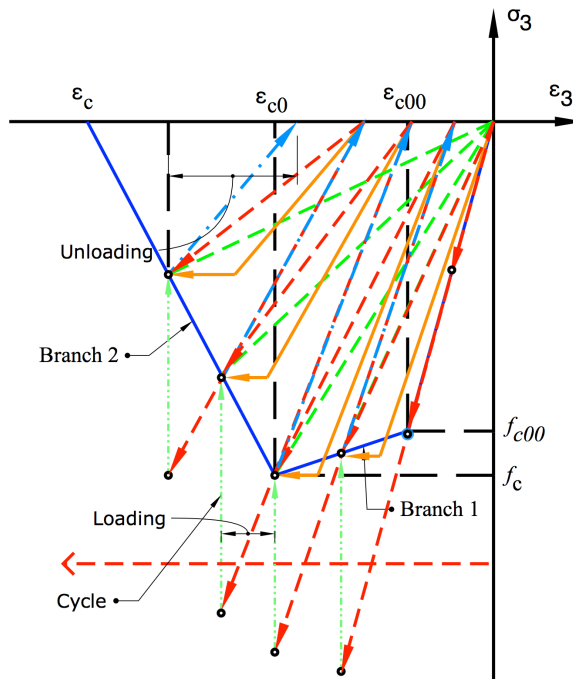


Figure B.27: Coupled damage-plastic material model in ISLA

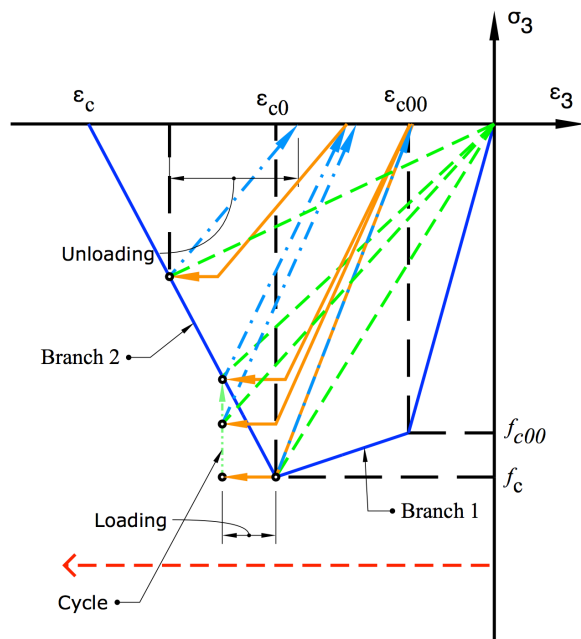


Figure B.28: Modified plastic model in ISLA with varying unloading modulus

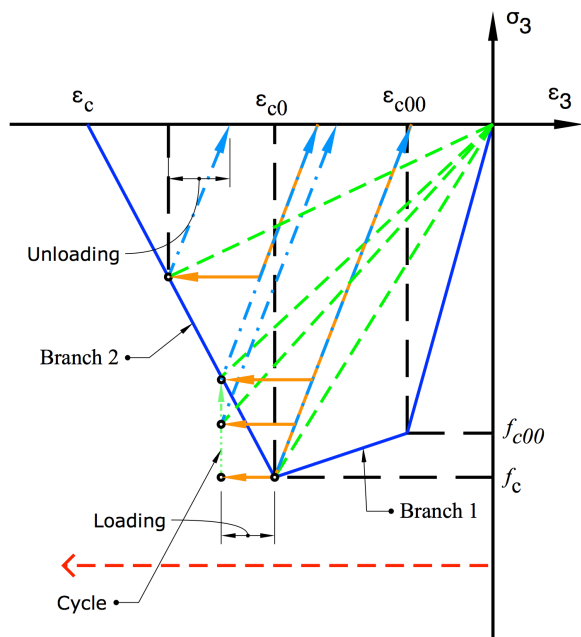


Figure B.29: Modified plastic model in ISLA with constant unloading modulus

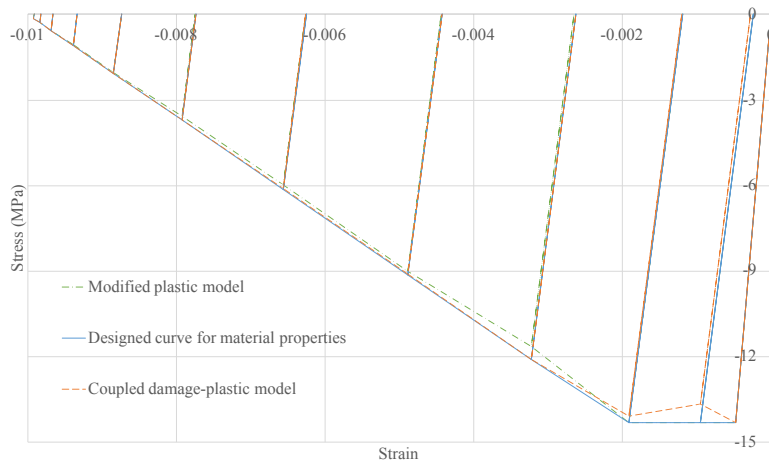


Figure B.30: Comparison of the coupled damage-plastic model and the modified plastic model for the one-element test

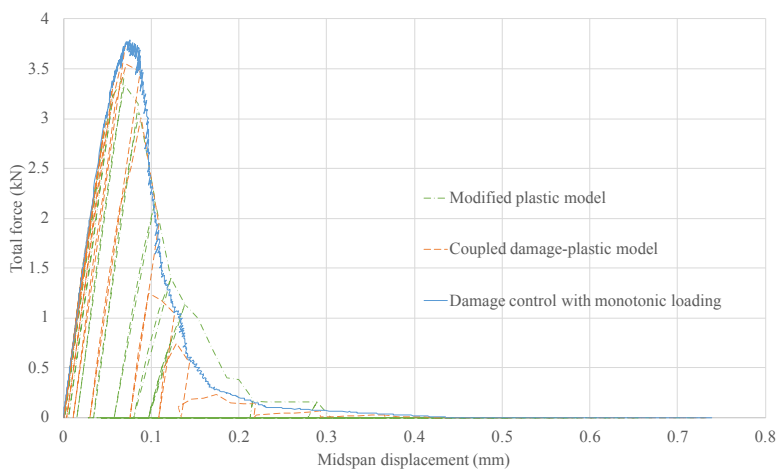


Figure B.31: Comparison of the coupled damage-plastic model and the modified plastic model for the notched beam test



# CURRICULUM VITÆ

**Chenjie Yu**

15-04-1988 Born in Wuhan, China.

## EDUCATION

Sep 2013–Sep 2017	Ph.D. Candidate Department of Structural Engineering, Delft University of Technology, The Netherlands <i>Thesis:</i> From sequentially linear analysis to incremental sequentially linear analysis <i>Promotor:</i> Prof. dr. ir. J.G. Rots
Sep 2010–Jun 2013	MSc student in Structural Engineering Department of Structural Engineering, South China University of Technology, China
Sep 2006–Jul 2010	BSc student in Structural Engineering Department of Structural Engineering, Tongji University, China

## WORKING EXPERIENCE

Sep 2018–Mar 2019	Software development engineer DIANA FEA BV (formerly TNO DIANA BV), The Netherlands
Sep 2017–Sep 2018	Researcher Department of Structural Engineering, Delft University of Technology, The Netherlands
e-mail	ycjrt@icloud.com Chenjie.Yu@tudelft.nl

# LIST OF PUBLICATIONS

## JOURNAL PUBLICATIONS

2. **Chenjie Yu**, P.C.J. Hoogenboom, J.G. Rots, *Incremental Sequentially Linear Analysis to control failure for quasi-brittle materials and structures including non-proportional loading*. Engineering Fracture Mechanics, 202, 332-349 (2018).
1. P.C.J. Hoogenboom, **Chenjie Yu**, K. Taneja. *Moments due to concentrated loads on thin shell structures*. Heron, 61(3), 153 (2016).

## CONFERENCE PUBLICATIONS

2. **Chenjie Yu**, P.C.J. Hoogenboom, J.G. Rots, *Incremental Sequentially Linear Analysis of a Notched Beam*. Computational Modelling of Concrete and Concrete Structures (EURO-C), Bad Hofgastein, 2018.
1. **Chenjie Yu**, P.C.J. Hoogenboom, J.G. Rots, *Algorithm for non-proportional loading in sequentially linear analysis*. 9th International Conference on Fracture Mechanics of Concrete and Concrete Structures, UC Berkeley, 2016.